COLLOIDAL SYNTHETIC PATHWAYS OF ATOMICALLY-FLAT COMPLEX NANOCRYSTAL HETEROSTRUCTURES

A DISSERTATION SUBMITTED TO

THE GRADUATE SCHOOL OF ENGINEERING AND SCIENCE

OF BILKENT UNIVERSITY

IN PARTIAL FULFILLMENT OF THE REQUIREMENTS FOR

THE DEGREE OF

DOCTOR OF PHILOSOPHY

IN

MATERIALS SCIENCE AND NANOTECHNOLOGY

By

Farzan Shabani

January 2024

COLLOIDAL SYNTHETIC PATHWAYS OF ATOMICALLY-FLAT COMPLEX NANOCRYSTAL HETEROSTRUCTURES

By Farzan Shabani

January 2024

We certify that we have read this thesis and that in our opinion it is fully adequate,in scope and in quality, as a thesis for the degree of Doctor of Philosophy.

Hilmi Volkan Demir (Advisor)

Evren Mutlugün

Bilge Baytekin

Andrey L. Rogach

Emine Yegan Erdem

Approved for the Graduate School of Engineering and Science:

Orhan Arıkan
Director of the Graduate School

ABSTRACT

COLLOIDAL SYNTHETIC PATHWAYS OF ATOMICALLY-FLAT COMPLEX NANOCRYSTAL HETEROSTRUCTURES

Farzan Shabani
Ph.D. in Materials Science and Nanotechnology
Advisor: Hilmi Volkan Demir
January 2024

Colloidal semiconductor nanocrystals (NCs) constitute one of the most important branches of nanoscience, with an increasingly high research interest, culminating with a Nobel Prize most recently. The nanometric size of these NCs allows for size-dependent optical properties, which provides an extra tool besides the composition to fine-tune these properties. Recent advancements in NC synthesis have been enabling important developments in the design and engineering of different shapes, compositions, and heterostructures of NCs. Accompanied by a deeper physical understanding and more sophisticated fabrication techniques, the NCs are now being integrated into many of the optoelectronic devices and are of prime importance for the next-generation optoelectronics. Despite all the progress, however, the full potential and synthesis dynamics of the NCs still need further investigation. Here, we addressed specifically four key aspects of the semiconductor NCs: shape engineering, electronic heterostructures, doping, and surface modification. In this thesis research, the synthesis dynamics, especially nucleation, growth and diffusion, were investigated in depth for different synthetic routes and conditions, and some of the important challenges were resolved. With the scarce number of proper emitters at longer wavelengths, in this thesis, a complex and thick heterostructure based on group II-VI nanoplatelets (NPLs) with relaxed quantum confinement was developed. The multi-shell design of the proposed NPLs helps overcome the unfavorable growth in the thickness direction, which, together with the cation dissolution/recrystallization and cation reorganization at high temperatures, relaxes the strain between the domains. The final NPLs, emitting in the deep-red region close to the bulk bandgap of CdSe, were used as an active layer in a light-emitting diode (LED) device and exhibited an exceptionally high external quantum efficiency (EQE) of 6.8% at electroluminescence peak wavelength of 701 nm, one of the best reported for colloids in this spectral range in the literature. Additionally, a novel heterostructure

of multi-crown NPLs was designed and demonstrated, where several direct and indirect recombination pathways give rise to photoluminescence with both type-I and type-II characteristics. The design of these NPLs, especially the size of the domains, was shown to significantly impact the final optical properties that can activate/deactivate the recombination channels alongside the temperature. These multi-crown type-II NPLs exhibit an extremely high two-photon absorption cross-section with the highest value of 12.9×10^6 GM and low dark-bright exciton splitting energy critical for optoelectronic applications, including photodetectors, bioimaging and quantum devices. Next, we showed silver doping dynamics of core/shell NPLs, which previously proved challenging due to the self-purification after the shell growth. Here, the composition of the shell was shown to be an important factor in the destruction mechanism of the NPLs in the irreversible doping regime at high doping temperatures. The Ag:CdSe/CdZnS core/shell NPLs exhibit only dopant emission with superior paramagnetic properties compared to CdS-shelled NPLs thanks to better lattice preservation and higher dopant content. At last, a surface modification method was suggested and demonstrated for group I-III-VI NCs to enhance their electronic properties. Replacing the long-chain organic ligands with a S^{2-} layer, injection of a negative charge and passivation of donor sites changed the behavior of the field-effect transistors (FETs) based on these NCs from *p*-type to *n*-type with more than a 10^5-fold enhancement in the carrier mobility. This method allowed fine-tuning of the optical properties of the NCs by the diffusion of the cations and shell formation. The findings of this thesis shine light on some of the important challenges in the field of semiconductor NCs while drawing a guideline for future research on the synthetic routes and optoelectronic properties. The thesis paves the way for future device integration of the developed NCs to fully realize their potential, while the demonstration of the more elaborated properties, including nonlinear absorption, paramagnetism and dark-bright exciton splitting, encourages further fundamental studies focusing on the physics of the semiconductor NCs.

Keywords: colloidal semiconductor nanocrystals, colloidal quantum dots, colloidal quantum wells, nanoplatelets, electronic heterostructures

ÖZET

ATOMİK OLARAK DÜZ KARMAŞIK NANOKRİSTAL HETERO YAPILARIN KOLOİDAL SENTETİK YOLLARI

Farzan Shabani
Malzeme Bilimi ve Nanoteknoloji, Doktora
Tez Danışmanı: Hilmi Volkan Demir
Ocak 2024

Kolloidal yarı iletken nanokristaller (NK'lar), giderek artan araştırma ilgisiyle nanobilimin en önemli dallarından biri haline gelmiş ve yakın zamanda en son Nobel Ödülü ile taçlandırılmıştır. NK'ların nanometrik boyutu, boyuta bağlı optik özelliklere izin vermekle birlikte, bu özelliklere ince ayar yapmak için bileşimin yanı sıra fazladan bir araç sağlamaktadır. NK sentezindeki son gelişmeler, NK'ların farklı şekillerinin, bileşimlerinin ve heteroyapılarının tasarımında ve mühendisliğinde önemli geliştirmelere olanak sağlamaktadır. Daha derin bir fiziksel anlayış ve daha karmaşık üretim teknikleriyle birlikte, NK'lar artık birçok optoelektronik aygıta entegre edilebilmekte ve yeni nesil optoelektronik için birincil öneme sahip hale gelmeye başlamıştır. Ancak tüm bu ilerlemelere rağmen, NK'ların tüm potansiyelini çıkarabilmek ve sentez dinamiklerini anlamak için hala daha fazla araştırmaya ihtiyaç duyulmaktadır. Burada yarı iletkenNK'ların özellikle dört temel yönü ele alınmıştır: şekil mühendisliği, elektronik heteroyapılar, katkılama ve yüzey modifikasyonu. Bu tez araştırmasında, sentez dinamikleri, özellikle çekirdeklenme, büyüme ve difüzyon, farklı sentez yolları ve koşulları için derinlemesine araştırılmış ve bazı önemli zorluklar çözülmüştür. Daha uzun dalga boylarında uygun ışıyıcıların az sayıda olması nedeniyle, bu tezde, gevşetilmiş kuantum sınırlamasına sahip grup II-VI nanolevhalara (NL'ler) dayanan karmaşık ve kalın bir heteroyapı geliştirilmiştir. Önerilen NL'lerin çok kabuklu tasarımı, kalınlık yönündeki olumsuz büyümenin üstesinden gelmeye yardımcı olur; bu, katyon çözünmesi/yeniden kristalleşmesi ve yüksek sıcaklıklarda katyonun yeniden düzenlenmesiyle birlikte alanlar arasındaki gerilimi rahatlatmaktadır. CdSe'nin yığın bant aralığına yakın derin kırmızı bölgede ışıyan son NL'ler, ışık yayan diyot (LED) cihazında aktif bir katman olarak kullanılmış ve 701 nm'lik elektrolüminesans tepe dalga boyunda %6.8'lik olağanüstü yüksek bir harici kuantum verimliliği (EQE) sergilemiştir. Bu değer, literatürde koloitler için bu spektral aralıkta bildirilen en yüksek değerlerden

biridir. Ek olarak, çeşitli doğrudan ve dolaylı rekombinasyon yollarının hem tip-I hem de tip-II özelliklere sahip fotolüminesansa yol açtığı, çok taçlı NL'lerin yeni bir heteroyapısı tasarlanmış ve gösterilmiştir. Bu NL'lerin tasarımının, özellikle alan boyutlarının, sıcaklıkla birlikte rekombinasyon kanallarını etkinleştirebilen/devre dışı bırakabilen nihai optik özellikleri önemli ölçüde etkilediği gösterilmiştir. Bu çok taçlı tip-II NL'ler, en yüksek değeri 12.9 x 106 GM olan son derece yüksek iki fotonlu soğurma kesiti ve fotodetektörler, biyogörüntüleme ve kuantum cihazları dahil olmak üzere optoelektronik uygulamalar için kritik olan düşük karanlık-parlak eksiton bölme enerjisi sergilemektedirler. Bir sonraki aşamada, kabuk büyümesinden sonra kendi kendini temizlemesi nedeniyle daha önce zorlu olduğu kanıtlanan çekirdek/kabuk NL'lerinin gümüş katkı dinamikleri gösterilmiştir. Burada kabuk bileşiminin, geri dönüşü olmayan katkılama rejimindeki yüksek katkılama sıcaklıklarında NL'lerin yok etme mekanizmasında önemli bir faktör olduğu gösterilmiştir. Ag:CdSe/CdZnS çekirdek/kabuk NL'ler, daha iyi örgü koruması ve daha yüksek katkı içeriği sayesinde CdS kabuklu NL'lere kıyasla yalnızca üstün paramanyetik özelliklere sahip katkı ışıması sergilerler. Son olarak grup I-III-VI NK'ların elektronik özelliklerini geliştirmek için bir yüzey modifikasyon yöntemi önerilmiş ve gösterilmiştir. Uzun zincirli organik ligandların S2- katmanıyla değiştirilmesi, negatif yük enjeksiyonu ve donör bölgelerin pasifleştirilmesi, bu NK'lara dayalı alan etkili transistörlerin (FET'ler) davranışını p tipinden n tipine, taşıyıcı hareketliliğinde 105 kattan daha fazla artış ile değiştirmiştir. Bu yöntem, katyonların difüzyonu ve kabuk oluşumu yoluyla NK'ların optik özelliklerinin hassas bir şekilde ayarlanmasına izin vermiştir. Bu tezin bulguları, yarı iletken NK'lar alanındaki bazı önemli zorluklara ışık tutarken, sentetik yollar ve optoelektronik özellikler üzerine gelecekteki araştırmalar için bir kılavuz çizmektedir. Tez, geliştirilen NK'ların potansiyellerini tam olarak gerçekleştirmeleri için gelecekteki aygıt entegrasyonunun yolunu açarken, doğrusal olmayan soğurma, paramanyetizma ve karanlık-parlak eksiton bölünmesi dâhil daha ayrıntılı özelliklerin gösteren, yarı iletken NK'ların fiziğine odaklanan daha ileri temel çalışmaları teşvik etmektedir.

Anahtar sözcükler: koloidal yarıiletken nanokristaller, kolloidal kuantum noktaları, koloidal kuantum kuyuları, nanolevhalar, elektronik heteroyapılar

Acknowledgement

First, I want to express my deepest gratitude to my advisor Prof. Hilmi Volkan Demir for his great scientific and personal guidance throughout my PhD years. I was more than lucky to work in his research group and benefit from his deep knowledge, scientific endeavor and warm attitude, which will be always a source of inspiration in my life.

I like to thank my thesis monitoring committee members Prof. Evren Mutlugün, Prof. Bilge Baytekin and Professor Dönüş Tuncel for their scientific feedback and discussions that helped me to better develop the ideas. Also, I sincerely thank the jury members Prof. Andrey L. Rogach and Prof. Emine Yegan Erdem for their time and consideration to read the thesis and attend the defense presentation.

I am also happy to thank all the colleagues and collaborators for their helps and inputs that made writing this thesis possible. Especially, I would like to thank Dr. Savaş Delikanlı for his fondness and scientific contribution, and all the past and present members of Demir Research Group, including Özgün Akyüz, Emre Ünal, Rabia Önen, Dr. Aysan Khaligh Vazirabadi, Dr. Betül Canımkurbey, Dr. Negar Gheshlaghi, Hamed Dehghanpour Baruj, Dr. Muhammad Hamza Humayun, Dr. Pedro Ludwig Hernandez Martinez, Rumon Miah, Hüseyin Bilge Yağcı, Furkan Işık, İklim Yurdakul, İlayda Özkan, Mohsin Waris, Taha Haddadifiam, Ahmet Tarık Işık, Dr. Emek G. Durmusoglu, Dr. Merve Izmir, Dr. Onur Erdem, Dr. Kıvanç Güngör, Dr. Tatiana Lastovina, Dr. Mojtaba Sadeghi, Dr. Zahra Adelpour, Dr. Andriy Budnyk, Bülent Kanmaz, Dr. Nina Sheremet, Dr. Volodymyr Sheremet, Muhammad Ahmad, Sina Foroutan, Taylan Bozkaya, Dr. Zeynep Dikmen, Ulviyya Quliyeva, Dr. Yemliha Altıntas, Dr. Satish Kumar, Dr. Fırat Karaboğa, İrfan Selim Bozdoğan, Yavuz Selim Aydın, Alkim Gokbayrak, Melis Ece Tatar and Tunç Bektaş. I will always remember their friendship and good times we spent together. I would like to express my gratitude to the professors and graduate students, as well as the technical and administrative personnel at UNAM, especially Duygu Kazancı and Ayşegül Torun. Also, I like to extend my thanks to Prof. Athos Petrou, Prof. Baiquan Liu, Prof. Emrah Ozensoy, Prof. İbrahim Sarpkaya and their group members for their contribution and scientific inputs.

I would like to thank all the friends from Bilkent University and outside, whose companionship, affection and tenderness empowered me throughout the years. I will always remember the times I had with Farzad, Hadi, Mirali, Ata, Peyman, Hamid, Sadegh, Abbas, Saman, Mohammad, Pedram, Matthew, Justin, Anıl, Richard, Hakan, and Sena.

Finally, I cherish the warm and unconditional support of my family throughout my life, which I will be always thankful. My father Nemat, my mother Farideh, and my brother Farid were always beside me through the good and bad times, for which I owe all my life to them.

Contents

CHAPTER 1 ..... **1**

Introduction **1**

1.1. Organization and scope of the Thesis 4

CHAPTER 2 ..... **6**

Colloidal Semiconductor Nanocrystals **6**

2.1. Basic Concepts of Semiconductor Nanocrystals 7

2.2. Colloidal Synthesis of Semiconductor Nanocrystals 10

2.3. Electronic Heterostructures of Colloidal Nanocrystals 15

2.3.1. Nanoplatelets with Type-I Heterostructure 17

2.3.2. Nanoplatelets with Quasi Type-II Heterostructure 18

2.3.3. Nanoplatelets with Type-II Heterostructure 21

2.4. Doping of Semiconductor Nanocrystals 23

2.4.1. Doped Nanoplatelets 24

2.5. Group I-III-VI Nanocrystals 28

CHAPTER 3 ..... **33**

Core/Crown/Double Shell Heteronanoplatelets **33**

3.1. Motivation 33

3.2. Experimental 36

3.3. Results and Discussion 41

3.4. Summary 59

CHAPTER 4 ..... **61**

Gradient Multi-crown Type-II Heteronanoplatelets **61**

4.1. Motivation 61

4.2. Experimental 64

4.3. Results and Discussion 68
4.4. Summary 102

CHAPTER 5 104

Thermodynamic Doping of Core/Shell Heteronanoplatelets 104

5.1. Motivation 104
5.2. Experimental 107
5.3. Results and Discussion 110
5.4. Summary 140

CHAPTER 6 141

Surface-Modified Group I-III-VI Nanocrystals 141

6.1. Motivation 141
6.2. Experimental 144
6.3. Results and Discussion 147
6.4. Summary 161

CHAPTER 7 162

Conclusion 162

7.1. Concluding Remarks 163
7.2. Future Outlook 167
7.3. Thesis Contributions to the Literature 174

Bibliography 178

List of Figures

Figure 2.1. A schematic of the quantum confinement effect. The bulk semiconductor demonstrates continuous energy levels in the conduction and valance band with the lowest band gap compared to the NCs. As the size of the NC becomes smaller than the Bohr radius, both conduction and valance bands exhibit discretized energy levels with the band gap widening. 8

Figure 2.2. a) A schematic of the photoexcitation and exciton generation of the NCs followed by heat dissipation and photoemission. b) A representative drawing of 0D NCs, known as QDs, passivated with organic ligand. The hollow circles show the functional group of the ligand, in which the ligands are attached to the NCs surface with these functional groups. c) A TEM image of CdSe-based NCs with the lattice fringes visible in the image. 10

Figure 2.3. A schematic of the LeMar growth model consists of three main stages: First, a spike in the monomers' concentration brings the system to the supersaturation, close to the homogeneous nucleation phase. In the second stage, small crystallites start to randomly nucleate in the solution, which also causes a decrease in the concentration of the free monomers. In the third stage, the small nuclei undergo inhomogeneous nucleation and growth, increasing the size of the NCs and decreasing the concentration of the free monomers. Ostwald ripening also happens in this stage, in which one crystal may dissolve in the solution at the expense of the growth of another crystal. b) The Gibbs free energy and the two surface and volume terms that affect the system's overall energy. With increasing the size of the NCs, the volume energy per volume decreases while the surface energy per area decreases. The Gibbs free energy starts to decrease at a critical radius of the sphere (r_c). 12

Figure 2.4. A schematic of three different planes of FCC cubic crystal and the representative bonds. 13

Figure 2.5. a) CdSe NPLs with terminating facets from {100} planes. b) Normal growth scheme, in which first a nucleus forms on the lateral or basal plane and then it grows. c) A schematic of the Ostwald ripening of the NPLs. The smaller NPLs dissolve and produce monomers for thicker and larger NPLs. 15

Figure 2.6. The band alignment for three electronic heterostructures of a) type-I, b) quasi type-II and c) type-II. 16

Figure 2.7. a) Sketch of CdSe/CdS core/crown NPLs along with the corresponding electron and hole wavefunction distributions in the domains. b) Absorption and c) PL spectra of the CdSe core and CdSe/CdS core/crown NPLs. 18

Figure 2.8. Schematics of the (a) c-ALD method and (b) hot-injection method. 21

Figure 2.9. Schematics of the doping mechanisms: (a) kinetic control and (b) thermodynamic control doping of NCs. The red and green small dots denote the dopant and host. 24

Figure 2.10. (a) A macroscopic model of Ag-doping for CdSe NCs with three different stages of doping: (i) At low Ag concentration, Ag_{int}^{+} with high interstitial mobility diffuse to the center of the NC, and later, are pushed to the surface and partially replace the Cd ions. (ii) The Ag_{Cd}^{-} and Ag_{int}^{+} ions form a bond, initiating the nucleation of Ag_2Se, and (iii) with increasing the Ag concentrations, Cd^{2+} ions are totally replaced with Ag on the surface..... 26
Figure 2.11. A classification of hard and soft metal and ligands..... 30
Figure 3.1. Absorption and PL spectra of (a) 4.5 ML CdSe core, and (b) 4.5 ML CdSe/CdS core crown NPLs. (c) TRF decay curve of CdSe core and CdSe/CdS core/crown NPLs. Copyright 2022 WILEY-VCH Verlag GmbH & Co. KGaA, Weinheim. 42
Figure 3.2. (a) A schematic of the synthesis pathway toward the final hetero-NPLs. First, bare CdSe core was laterally passivated with CdS crown, and then the c-ALD buffer layers were grown in the thickness direction to prepare the seeds. These seeds were used for the final HI shell coating. The thick NPLs were treated for longer times and using higher precursor concentrations during the hot injection. (b) Band alignment of CdSe, CdS and ZnS. The numbers were extracted from ref. [146] and ref. [31]. (c) Absorbance and PL spectra, and (d) TRF decay curves of (CdSe/CdS)@(1-4 CdS) (core/crown)@(c-ALD shell) seed NPLs. Copyright 2022 WILEY-VCH Verlag GmbH & Co. KGaA, Weinheim..... 44
Figure 3.3. (a) Absorbance and photoluminescence spectra and (b) TRF decay curves of HI shell NPLs with a generic heterostructure of (CdSe/CdS)@(1-4 CdS/ZnS) (core/crown)@(c-ALD/HI shell). (c) TEM image of the NPLs with 4 MLs of CdS buffer layers capped with ZnS HI shell showing a rectangular shape. (d) Absorbance and PL spectra and (e) TRF decay curves of HI shell NPLs with a generic heterostructure of (CdSe/CdS)@(1-4 CdS/CdZnS) (core/crown)@(c-ALD/HI shell). (f) TEM image of NPLs with 4 MLs of CdS buffer layers and final CdZnS HI shell. The shape of the NPLs is generally rectangular with less defined edges compared to the NPLs capped with ZnS HI shell. For both sets of samples, the growth time at 300 ˚C was between 1-2 h and the amount of Cd, Zn and injected S precursors were limited. Copyright 2022 WILEY-VCH Verlag GmbH & Co. KGaA, Weinheim. 47
Figure 3.4. TEM images of thick NPLs that were treated with higher concentrations of the precursors for a prolonged time: (a) NPLs with 3 ML of CdS buffer layer, with a heterostructure of (CdSe/CdS)@(3CdS/CdZnS) (core/crown)@(c-ALD shell/(HI shell), (b) and (c) NPLs with 4 MLs of CdS buffer layer, with a heterostructure of (CdSe/CdS)@(4CdS/CdZnS) (core/crown)@(c-ALD shell/(HI shell). For both of the samples the shape has become more symmetric compared to the previous rectangular NPLs. (d) Absorbance and PL spectra, (e) TRF decay curves, and (f) X-ray diffraction patterns of thick (core/crown)@(c-ALD/HI shell) NPLs. All of the samples

were treated between 3-4 h for the shell growth at 300 ˚C and the amount of Cd and Zn precursors were doubled in comparison to thin shell NPLs. Copyright 2022 WILEY-VCH Verlag GmbH & Co. KGaA, Weinheim. 51
Figure 3.5. Absorbance and photoluminescence spectra of thick-shell (CdSe/CdS)@(2CdS/CdZnS) (Core/Crown)@(c-ALD/HI Shell) NPLs. Copyright 2022 WILEY-VCH Verlag GmbH & Co. KGaA, Weinheim. 53
Figure 3.6. XPS spectra of thick (core/crown)@(4CdS/CdZnS) NPLs. The spectra for Cd, Se, Zn and S were fitted according to the orbital splitting of Cd3d, Se3d, Zn2p and S2p. Elemental binding energies were measured, showing no participation of the elements in other unwanted states. Copyright 2022 WILEY-VCH Verlag GmbH & Co. KGaA, Weinheim. 55
Figure 3.7. (a) LED device structure and flat band energy level diagram. The values for NPLs energy levels were measured directly from the XPS measurement according to the method used previously [148]. The energy levels for ZnO were extracted from the literature [147] and those of other layers were taken from the catalogs of their materials. (b) Cross-sectional scanning electron microscopy image of the device showing the layers with different contrasts. (c) Electroluminescence spectrum at an applied bias of 8 V, (d) current density and luminance versus voltage, and (e) EQE versus driving voltage, all for the deep-red emitting CQW-LED with (core/crown)@(4CdS/CdZnS) NPLs as the active material. Copyright 2022 WILEY-VCH Verlag GmbH & Co. KGaA, Weinheim. 57
Figure 3.8(a) Electroluminescence spectrum (λ_{EL} = 689 nm) at V_{app} of 10 V, (d) Current density versus voltage, and (e) EQE versus driving voltage, for deep-red emitting CQW-LEDs with (C/C)@(4CdS/ZnS) NPLs as active material. Copyright 2022 WILEY-VCH Verlag GmbH & Co. KGaA, Weinheim. 58
Figure 4.1. (a) Band alignment of the NPLs with the general heterostructure of CdSe/CdSeTe/CdTe core/crown/crown and all the possible direct band-edge transitions happen in one domain. (b) Same as (a) for the possible indirect type-II transitions between two different domains. (c) A schematic of the synthetic route of CdSe/CdSeTe/CdTe core/crown/crown NPLs. Starting with 4.5 ML CdSe core, two consecutive crowns were grown through a single-pot procedure where a mixture of Se-Te was injected for the first crown and then only Te was introduced to the NPLs. (d) TEM image of 4.5 ML CdSe core and (e and f) multi-crown NPLs with r equal to 3 and 0.33, respectively. All scale bars are 20 nm. Copyright 2023 WILEY-VCH Verlag GmbH & Co. KGaA, Weinheim. 69
Figure 4.2. XPS spectra of CdSe/:1 CdSeTe/:3 CdTe core/crown/crown NPLs. The elemental binding energies of Cd, Se and Te, presented in the NPLs heterostructure, are measured, and the curves are fitted to the peaks to ensure the nature of the binding. Copyright 2023 WILEY-VCH Verlag GmbH & Co. KGaA, Weinheim. 70

Figure 4.3. XRD patterns of CdSe/:3 CdSeTe/:1 CdTe and CdSe/:1 CdSeTe/:3 CdTe core/crown/crown NPLs with zinc blende crystal structure. The XRD peaks of bulk zinc blende CdTe (black lines at the top) and CdSe (red lines at the bottom) are included as references. As the ratio of the final crown increases, the peaks are shifted to the lower diffraction angles, which suggests a higher ratio of the final crown to the middle crown. Copyright 2023 WILEY-VCH Verlag GmbH & Co. KGaA, Weinheim. 71

Figure 4.4. EDX mapping of CdSe/$CdSe_{0.5}Te_{0.5}$/CdTe multi-crown NPLs with r=1/3. The top left image shows the mapping of all the elements and the inset shows the TEM image. The respected element mappings are indicated for other images. The scale bars are 100 nm. Copyright 2023 WILEY-VCH Verlag GmbH & Co. KGaA, Weinheim. 73

Figure 4.5. TEM-line EDX of two multi-crown NPLs with the same D=1 and different r of (a) 3/1 and (b) 1/3. The EDX line is drawn in the respective TEM images above the graphs and only the region corresponding to the actual place of the NPLs is plotted. Se and Te fractions were first calculated and then normalized between 0 and 1 to differentiate different domains. The core region was expected to have Se above 0.75 and the boundary between the intermediate crown and final crown was supposed to have 0.75 of Te (or 0.25 Se). The scale bars are 10 nm in the TEM images. Copyright 2023 WILEY-VCH Verlag GmbH & Co. KGaA, Weinheim. 74

4.6. TEM images of CdSe/$CdSe_{0.5}Te_{0.5}$ core/crown NPLs after injection of 0.5 mL of Se-Te-TOP crown precursor at two different magnifications. The scale bars are 50 nm in (a) and 10 nm in (b). 75

Figure 4.7. (a) Absorption and (b) emission spectra of CdSe/$CdSe_{0.5}Te_{0.5}$ core/crown NPLs after different annealing times at the synthesis temperature of 215 ˚C. The inset in (d) shows the magnified PL spectra at the peak. Copyright 2023 WILEY-VCH Verlag GmbH & Co. KGaA, Weinheim. 76

Figure 4.8. (a) Absorption profile of CdSe/CdSeTe/CdTe core/crown/crown NPLs with constant composition of the intermediate crown (Se/Te = 1) and changing ratio of intermediate to final crown, r. (b) PL profile of the same samples. The dotted curves are the deconvoluted peaks for each graph. (c) TRF decay curves at the emission peak wavelength of the NPLs. (d) PLE profile of the NPLs with r = 1 sweeping from the beginning (570 nm) to the end (670 nm) of the emission spectra. Copyright 2023 WILEY-VCH Verlag GmbH & Co. KGaA, Weinheim. 78

Figure 4.9. PL spectra and deconvoluted peaks for (a) CdSe/:3 $CdSe_{0.5}Te_{0.5}$/:1 CdTe, (b) CdSe/:1 $CdSe_{0.5}Te_{0.5}$/:1 CdTe and (c) CdSe/:3 $CdSe_{0.5}Te_{0.5}$/:1 CdTe core/crown/crown NPLs. Copyright 2023 WILEY-VCH Verlag GmbH & Co. KGaA, Weinheim. 79

Figure 4.10. TRF decay curves of CdSe/:1 $CdSe_{0.5}Te_{0.5}$/:3 CdTe core/crown/crown NPLs recorded at two emission wavelengths of T1 = 577 nm and T2 = 627 nm. Copyright 2023 WILEY-VCH Verlag GmbH & Co. KGaA, Weinheim. 82

Figure 4.11. (a and b) Three-dimensional representations of hole wavefunction for CdSe/CdSeTe/CdTe core/crown/crown NPLs with rectangular and square shapes after photoexcitation, respectively. (c) 2D in-plane representations of hole wavefunction for the same rectangular (up) and square (down) NPLs. (d and e) Three-dimensional representation of electron wavefunction for rectangular and square multi-crown NPLs, respectively, and (f) same wavefunctions for rectangular (up) and square (down) in a 2D in-plane representation. The electron wavefunction is centered around the core for both sets of NPLs. (g) Sketches of the NPLs with the size of different domains used for the theoretical calculations. Both sets of rectangular and square NPLs have an intermediate crown with x = 0.50 and r = 1/1. Copyright 2023 WILEY-VCH Verlag GmbH & Co. KGaA, Weinheim. 84
Figure 4.12. (a) Higher-state electron and hole energies for rectangular CdSe/CdSeTe/CdTe core/crown/crown NPLs. (b and c) A few representations of electron and hole wavefunction, respectively. Copyright 2023 WILEY-VCH Verlag GmbH & Co. KGaA, Weinheim. 86
Figure 4.13. (a) Electron (purple) and hole (red) wavefunctions of the NPLs with x = 0.5 and changing r. (b) The e-h overlap extracted from the corresponding heterostructures with different r and x. (c) Absorption and (d) PL spectra of the CdSe/$CdSe_{1-x}Te_x$/CdTe core/crown/crown NPLs with different intermediate compositions. (e) Absorption and (f) PL spectra of the CdSe/:1 $CdSe_{0.5}Te_{0.5}$/:1 CdTe core/crown/crown NPLs with different collective sizes of the crowns, $D = d_{int} + d_f$. Copyright 2023 WILEY-VCH Verlag GmbH & Co. KGaA, Weinheim. 88
Figure 4.14. TRF decay curves of the CdSe/:1 $CdSe_{1-x}Te_x$/:1 CdTe core/crown/crown NPLs with different compositions of the intermediate crown. Copyright 2023 WILEY-VCH Verlag GmbH & Co. KGaA, Weinheim. 91
Figure 4.15. TRF decay curves of the CdSe/:1 CdSe0.5Te0.5/:1 CdTe core/crown/crown NPLs with different sizes of the collective crowns, D. Copyright 2023 WILEY-VCH Verlag GmbH & Co. KGaA, Weinheim. 93
Figure 4.16. Deconvolution of the PL spectra for CdSe/:1 $CdSe_{0.75}Te_{0.25}$/:1 CdTe and CdSe/:1 $CdSe_{0.25}Te_{0.75}$/:1 CdTe core/crown/crown NPLs. Copyright 2023 WILEY-VCH Verlag GmbH & Co. KGaA, Weinheim..... 95
Figure 4.17. Temperature-dependent PL spectra at different temperatures and (b) emission peak position versus temperature extracted from the PL spectra for CdSe/:3 $CdSe_{0.5}Te_{0.5}$/:1CdTe core/crown/crown NPLs. (c) PL decay curves for the same samples. The inset shows the evolution of the lifetime with temperature. (d) Open-aperture z-scan graphs comparing two samples of multi-crown NPLs with the same composition (x = 0.5) and r = 1 and different collective crown sizes, D. The black scatter dots correspond to the measurement for only hexane, and the solid lines are the fittings for the samples. An increase in the size of the NPLs gives a huge rise in the two-photon absorption cross-section from 1.6×10^6 to 12.9×10^6 GM. Copyright 2023 WILEY-VCH Verlag GmbH & Co. KGaA, Weinheim. 97

Figure 4.18. Emission peak position (scattered squares) fitted with (a) Varshni and (b) Bose−Einstein type equation for CdSe/:3 CdSe0.5Te0.5/:1 CdTe core/crown/crown NPLs. 99
Figure 4.19. PL spectra of CdSe/:3 $CdSe_{0.5}Te_{0.5}$/:1 CdTe core/crown/crown NPLs presented in black line for three temperatures of (a) 295 K, (b) 250 K and (c) 200 K, and peaks deconvoluted (red and blue lines) for 295 and 250 K. Copyright 2023 WILEY-VCH Verlag GmbH & Co. KGaA, Weinheim. 100
Figure 4.20. Evolution of the FWHM of the PL peak with temperature for CdSe/:3 $CdSe_{0.5}Te_{0.5}$/:1 CdTe core/crown/crown NPLs. Copyright 2023 WILEY-VCH Verlag GmbH & Co. KGaA, Weinheim. 101
Figure 4.21. Evolution of the decay lifetimes with temperature for CdSe/:3 $CdSe_{0.5}Te_{0.5}$/:1 CdTe core/crown/crown NPLs. Copyright 2023 WILEY-VCH Verlag GmbH & Co. KGaA, Weinheim. 102
Figure 5.1. Schematics of (a) reversible non-destructive doping and (b) irreversible destructive doping. Under both regimes, increasing the driving force would decrease the in-solution dopant concentration and increase the host concentration. However, for a reversible process, the NPLs retrieve their original composition upon a decrease in the driving force through a reverse exchange reaction, while for an irreversible process, the NPLs cannot regain their initial form (composition, shape, etc.). Copyright 2023 American Chemical Society..... 112
Figure 5.2. (a) Absorption and PL spectra of the initial 4.5 ML CdSe core seeds used for the proceeding shell coatings. Absorption and PL spectra of (b) CdSe/ZnS, (c) CdSe/CdS and (d) CdSe/CdZnS core/thin-shell NPLs, which were mainly used in this study for silver doping. Copyright 2023 American Chemical Society..... 113
Figure 5.3. (a) Absorption profile for aliquot samples of Ag:CdSe/ZnS core/shell NPLs after complete injection of Ag precursor at 160 ˚C, taken while the doping temperature was increased from 160 to 240 ˚C. TEM images of the samples at four different temperatures of (b-c) 25 ˚C (before the injection of the doping precursor), (d-e) 170 ˚C, (f-g) 240 ˚C and (h-i) 260 ˚C. Scale bars are 50 nm. The black and white arrows show the silver selenide islands and etching sites on the NPLs, respectively. (j) Emission spectra of the aliquot samples corresponding to the NPLs in (a). The inset is a schematic showing the dependency of the position of the mid-gap states on the Ag concentration. (k) Evolution of dopant/band-edge emission ratio with increasing temperature. (l) ICP-MS analysis of Ag concentration. Copyright 2023 American Chemical Society. 114
Figure 5.4. Absorption and PL evolution of (a, b) CdSe/ZnS, (c, d) CdSe/CdS and (e, f) CdSe/CdZnS core/shell NPLs doped with Ag(OAc)-ethanol (0.016 M) precursor at room temperature. Although the total amount of Ag is two times higher than the high-temperature method, the dopant emission remained insignificant after 24 h. The highest D/BE ratio achieved was 0.54 for CdSe/CdS core/shell NPLs. Copyright 2023 American Chemical Society. 116
Figure 5.5. TEM-EDS maps of Cd, Zn, S, and Ag for CdSe/ZnS NPLs after doping with no washing. The silver ions are distributed homogenously in the bulk of the NPLs and the Ag concentration is much higher for brighter

islands in the TEM image. The mapping shows the islands predominantly consist of Ag with some Cd alloying. Copyright 2023 American Chemical Society. 117
Figure 5.6. Absorption spectra of CdSe/ZnS core/thin-shell NPLs doped with Ag at 250 and 260 ˚C. Copyright 2023 American Chemical Society. 118
Figure 5.7. Band-edge and dopant emission peak wavelength evolution with increasing the temperature for CdSe/ZnS core/thin-shell NPLs. Copyright 2023 American Chemical Society. 119
Figure 5.8. TEM images of CdSe/CdS core/shell NPLs at (a) 160 ˚C, before the injection of Ag precursor and (b, c) at 210 and 250 ˚C, respectively, after the injection of Ag precursor. Scale bars are 50 nm. (d) Evolution of PL spectra of Ag:CdSe/CdS core/shell NPLs within the temperature range of 160 (green line) to 240 ˚C (red line). The inset follows the red shift in the dopant emission with increasing the temperature. (e) D/BE emission ratio. The inset is a schematic showing the decrease in the band-edge with increasing the shell thickness. The thick-shelled samples show negligible dopant emission as the Ag-activated states are no longer inside the bandgap. (f) Ag concentration measured via ICP-MS from aliquots taken during the synthesis. For thick-shelled samples, the core/shell synthesis was prolonged and its emission was red-shifted compared to the thin-shelled NPLs due to the confinement relaxation. Copyright 2023 American Chemical Society. 121
Figure 5.9. (a) PL spectra evolution between 160 ˚C (green line) and 240 ˚C (red line) and (b) D/BE emission ratio for extra-thick CdSe/CdS core/shell NPLs. Copyright 2023 American Chemical Society. 124
Figure 5.10. (a) PL emission spectra of CdSe/CdZnS core/shell NPLs after injection of the Ag precursor from 160 ˚C (green line) to 240 ˚C (red line). The inset follows the red shift of dopant emission with increasing temperature. (b) D/BE emission ratio for thin- and thick-shelled NPLs. The inset is the Eyring plot for the same data. (c, d) TEM images of the samples for thin CdZnS-shelled NPLs taken at 240 and 260 ˚C, respectively. (e) Concentration of Ag and (f) Cd and Zn for CdZnS-shelled samples obtained via ICP-MS analyses. Copyright 2023 American Chemical Society. 126
Figure 5.11. PLQY of CdSe/CdZnS core/thin-shell NPLs at different temperatures and the share of the dopant emission, in which $PL_DQY = PLQY \times D/(D+BE) \times 100$. Copyright 2023 American Chemical Society. 127
Figure 5.12. X-ray diffraction patterns of CdSe/CdZnS core/shell NPLs before and after silver doping. Copyright 2023 American Chemical Society. 128
Figure 5.13. High-resolution X-ray photoelectron spectroscopy (XPS) spectra of host elements of Cd 3d, Zn 2P, Se 3d, S 2P, and dopant Ag 3d states for a representative sample of CdSe/CdZnS core/thick-shell NPLs doped with silver at 240 ˚C, along with the elemental composition extracted from the XPS measurement. Copyright 2023 American Chemical Society. 129

Figure 5.14. (a) Absorption (black) and emission spectra (red) of Ag-doped CdSe/CdZnS: core/thin-shell NPLs. OLA was introduced to the reaction flask just before quenching in water. (b, c) TEM images of the same NPLs with EDS analysis of the corresponding elements given below. Copyright 2023 American Chemical Society. 132
Figure 5.15. (a) Absorption (black) and emission spectra (red) of Ag:CdSe/CdZnS core/thin-shell NPLs. The flask was quenched just after addition of OA. (b, c) TEM images of the same NPLs with EDS analysis of the corresponding elements given below. Copyright 2023 American Chemical Society. 133
Figure 5.16. TRF decay curves of thin-shelled NPLs with respective heterostructures of CdSe/ZnS, CdSe/CdS and CdSe/CdZnS core/shell. All three samples were half-doped with Ag, in which the dopant to band-edge PL peak intensity ratio equals one: (a) band-edge emission decay after doping and (b) dopant emission decay curve. Copyright 2023 American Chemical Society. 135
Figure 5.17. (a) Right circularly polarized (RCP) and left circularly polarized (LCP) components of photoluminescence for partially silver-doped CdSe/CdZnS core/shell NPLs at 3 K and in the absence of magnetic field. The circular polarization, shown in blue line, is almost zero in the band-edge emission vicinity. (b) Same measurement at an increased magnetic field of 7 T. The bound exciton feature, at energy P_X, demonstrates negative circular polarization. (c) P_X vs. the magnetic field (B) for a temperature range from 3 to 15 K. (d) Bound exciton Zeeman splitting (ΔE_Z) as a function of B at T = 3 K. Copyright 2023 American Chemical Society. 137
Figure 5.18. Temperature-dependent PL of partially doped CdSe/CdZnS core/shell NPLs in the band-edge vicinity. The emission peak broadening with decreasing temperature can be attributed to the strain variation and interaction of band-edge excitons with the silver impurities. The only prominent feature is coming from the bound excitons while the absence of free exciton is probably originated from the high dopant concentration. Copyright 2023 American Chemical Society. 138
Figure 5.19. (a) RCP and LCP components in the vicinity of the band-edge emission for partially silver-doped CdSe/CdS core/shell NPLs at 3 K and in the absence of magnetic field. The circular polarization, shown in blue line, is almost zero in this vicinity. (b) Same measurement at an increased magnetic field of 7 T. The bound exciton feature at energy P_X exhibits weak circular polarization compared to the CdSe/CdZnS core/shell NPLs. (c) P_X vs. magnetic field for a temperature range between 3 and 15 K. (d) Bound exciton Zeeman splitting (ΔE_Z) as a function of B at T = 3 K. Both P_X and ΔE_Z follow the same behavior shown for CdSe/CdZnS core/shell NPLs; however, the circular polarization is smaller and ΔE_Z is slightly shifted to higher. Copyright 2023 American Chemical Society. 139
Figure 6.1. Real images of the QDs and a schematic of the half-reactions. For each step of the surface treatment, the QDs are either dispersible in the polar or non-polar solvent based on the surface polarity and ligands on the surface of the QDs. 148

Figure 6.2. (a) Absorption and (b) PL spectra of CIS QDs before and after the shell treatment. (c) TRF decay curves and the corresponding three-exponential fits for the same samples. (d) XRD pattern of CIS and CIS/3ZnS QDs. (e) Concentration of Cu and Zn for each cycle of shell treatment. (f) TEM images of CIS/3ZnS QDs.... 149
Figure 6.3. TRF decay curve of CIS QDs after the S^{2-} half-reaction. The red line is the tri-exponential fit of the curve. 150
Figure 6.4. TEM image of untreated CIS QDs. 151
Figure 6.5. (a) Absorption and (b) PL spectra of CIS QDs before and after CdS-treatment. (c) TRF decay curve of the samples. (d) Concentration of Cd and Cu for each cycle of shell treatment..... 152
Figure 6.6. (a) Absorption and (b) emission spectra for AIS QDs, respectively, before and after surface treatment. (c) Absorption spectra of CISe QDs before and after surface treatment. (d) TEM images of AIS/3ZnS and (e) CISe/3ZnS QDs. (g and h) Real images of the AIS and CISe QDs during different stages of the surface treatment, respectively..... 155
Figure 6.7. TEM images of (a) AIS and (b) CISe core QDs before the treatment..... 156
Figure 6.8. (a) QDs-FET device structure and (b) SEM image of the cross-section of this CIS-FET device. (c) I_{DS} vs I_{Gs} transfer curves for CIS-based FETs with V_{DS} = 20 V. (d) I_{DS} vs V_{DS} output characteristic curves of CIS-FETs, (e) CIS(1S)-FETs, (f) CIS(1/ZnS/S)-FETs and (g) CIS(2ZnS/S)-FETs. (h and i) AFM images for CIS and CIS/1S films, respectively. (j) Time-dependent CIS-FET measurement..... 157
Figure 6.9. (a) Transfer characteristics of pristine and surface-treated AIS-based FETs at V_{DS} = 20 V. (b-e) Output characteristics of AIS-, AIS(1S)-, AIS(ZnS/S)- and AIS(2ZnS/S)-FETs, respectively..... 159
Figure 6.10. (a and b) Output characteristics of surface-treated CIS-based FETs after CdS-treatment at V_{DS} = 20 V. (c) Transfer characteristics of CIS QDs before and after CdS-treatment..... 160
Figure 7.1. TEM images of CS NPLs (a) before and (b) after the In treatment. (c) Absorption spectra of CS and CIS NPLs. Adapted from ref. [285]. Copyright 2023 American Chemical Society. (d) A proposed schematic of the energy transfer system consisting CdSe/CdS core/crown NPLs donor and CIS NPLs acceptor. (e and f) PL spectra of the donor and the absorption spectra of the CS and CIS NPLs acceptor, respectively. 173

List of Tables

Table 3.1. The summary of the optical properties of the CdSe core and CdSe/CdS core/crown NPLs. 43

Table 3.2. Optical properties of (CdSe/CdS)@(1-4 CdS) (Core/Crown)@(c-ALD Shell) NPLs. Copyright 2022 WILEY-VCH Verlag GmbH & Co. KGaA, Weinheim. 45

Table 3.3. Optical properties of (CdSe/CdS)@(1-4 CdS/ZnS) (Core/Crown)@(c-ALD/HI Shell) and (CdSe/CdS)@(1-4 CdS/CdZnS) (Core/Crown)@(c-ALD/HI Shell) NPLs. Copyright 2022 WILEY-VCH Verlag GmbH & Co. KGaA, Weinheim. 48

Table 3.4. TRF decay components of (CdSe/CdS)@(1-4 CdS/ZnS) (Core/Crown)@(c-ALD/HI Shell) NPLs (blue shade) and (CdSe/CdS)@(1-4 CdS/CdZnS) (Core/Crown)@(c-ALD/HI Shell) NPLs (red shade). Copyright 2022 WILEY-VCH Verlag GmbH & Co. KGaA, Weinheim. 49

Table 3.5. TRF decay components of thick-shell NPLs. Copyright 2022 WILEY-VCH Verlag GmbH & Co. KGaA, Weinheim. 54

Table 3.6. List of the LEDs based on the colloidal nanocrystals emitting in the vicinity of 700 nm. Copyright 2022 WILEY-VCH Verlag GmbH & Co. KGaA, Weinheim. 59

Table 4.1. A summary of the peaks deconvolution results 80

Table 4.2. Decay Components and numerical analysis of time-resolved fluorescence from NPLs with general heterostructure of CdSe/:d_{int} $CdSe_{0.5}Te_{0.5}$/:d_f CdTe core/crown/crown for different ratios of crown sizes, r. Copyright 2023 WILEY-VCH Verlag GmbH & Co. KGaA, Weinheim. 81

Table 4.3. A summary of the decay components. 82

Table 4.4. The summary of the decay components in Figure 4.14. 92

Table 4.5. The summary of the decay components of the CdSe/:1 CdSe0.5Te0.5/:1 CdTe core/crown/crown NPLs with different sizes of the collective crowns, D. 94

Table 4.6. Summary of the peak deconvolution shown in Figure 4.16. 95

Table 4.7. The Varshni and Bose−Einstein fitting parameters. 99

Table 5.1. The summary of the emission peak wavelength and FWHM with increasing the temperature for CdSe/ZnS core/thin-shell NPLs. 119

Table 5.2. Band-edge and dopant emission peak wavelength and FWHM for CdSe/CdS core/thin-shell NPLs. FWHM for the band-edge emission is not reported as the samples demonstrate two band-edge emission peaks due to NPLs breakage. Copyright 2023 American Chemical Society. 123
Table 5.3. Band-edge and dopant emission peak wavelength and FWHM for CdSe/CdZnS core/thin-shell NPLs. Copyright 2023 American Chemical Society. Copyright 2023 American Chemical Society. 125
Table 5.4. TRF decay components of half-doped thin-shelled NPLs for (a) band-edge emission and (b) dopant emission. Copyright 2023 American Chemical Society. 136
Table 6.1. Decay components for CIS QDs before and after the shell treatment. 150
Table 6.2. Decay components for CIS QDs before and after treatment with CdS shells. 153
Table 6.3. Device characteristics of FETs based on pristine and surface-treated QDs. 161

Chapter 1

Introduction

Since the first report of successful synthesis and quantum mechanical formulations [1]–[3], colloidal semiconductor nanocrystals (NCs) have become one of the major pillars of nanoscience and nanotechnology. The quantum size effect of these NCs paved the way for a new paradigm in materials science where the light-matter interaction is highly dependent on the size beside the conventional composition and phase [1]. This simple new tool has fully restructured the scientific endeavor from all the disciplines and brought the formal branches of science ever closer together to explore the consequences. The rise of NCs was later recognized by display technologies, where the distinguished properties of these immensely small materials enhanced our ability to cope with the evergrowing market demands. The full potential is yet to be contrived but the signs are ubiquitous. From simple wall painting to advanced screens of home televisions, NCs are becoming an indispensable part of our lives [4]–[7]. The recent Nobel Prize in chemistry awarded to the first pioneers in the synthesis of the NCs cherished this conceivable future [8]. In hindsight, however, the quest is far from over.

Colloidal semiconductor NCs provide an exceptionally interesting ground for future optoelectronic applications. The ease of synthesis enables large-scale output of meticulously engineered NCs with desired properties at a very low cost [7]. More importantly, the strong light-matter interaction of the NCs is essential for most optoelectronic applications [9], [10]. Spherical semiconductor NCs, known as quantum dots (QDs), allow high absorption of the light resulting in the generation of an electron-hole pair (exciton). The exciton generation can be used for a vast range of applications either benefiting from the recombination of electron-hole pair, such as light-emitting diode (LED), laser and luminescence solar concentrator (LSC), or from the extracted photoexcited electron such as photocatalyst and solar cell. The most critical feature of the NCs is their high tunability [11], [12]. The light-matter interaction can be tuned through size, shape, compositions and heterostructures, ultimately expanding our control over a broad range of electromagnetic spectrum from the ultraviolet (UV) to the near-infrared [13]–[15].

Besides the spectral coverage and tunability, the photogenerated light can also be tailored for different applications. The intrinsic properties of the photogenerated light, including the Stokes shift and lifetime, and reducing the unwanted phenomena such as the Auger recombination and electron/hole trapping are critical for different applications. For some applications requiring distinct properties such as paramagnetism, ferromagnetism, nonlinear light-matter interaction, etc., further engineering is also needed [16]–[19]. The complex envelope of the requirements brings about complex strategies in the design and synthesis of the NCs, in which engineering the NCs is not bounded to the size or composition anymore as the only factors.

The past two decades observed numerous strategies to answer these needs. In particular, the shape engineering of the NCs proved critical to tune and enhance the optoelectronic

properties [20], [21]. So far, NCs with different compositions can be synthesized in different shapes each of which comes with their own sets of properties. Aside from NCs with high aspect ratios, such as 1D nanorods and 2D nanoplatelets (also known as nanosheets or nanoplates), more elaborate shapes including pyramids, tetrapods, rings and the like have been also realized [6], [22]. The confinement regime and geometry can be changed through engineering the shape, enhancing the color purity by reducing the inhomogeneous broadening [23]. These "shaped" NCs also enable the prospect of geometrical heterostructure beyond the conventional core/shell for the isotropic QDs and also bring the prospect of NCs coupling [24], [25].

In this thesis, we demonstrate different synthetic strategies to develop semiconductor NCs with tailor-made properties. We focus on four main characters, namely, shape, heterostructure, composition and surface, and investigate the properties based on each of these four. For 2D nanoplatelets (NPLs) preserving the shape while constructing elaborated heterostructures is one of the prime aims, as the shape is the root cause of the superior properties of the NPLs. The CdSe NPLs are used as the base material in three chapters, to further grow different heterostructure and modify the composition. The high-temperature synthesis protocol can change the anisotropic shape toward spherical, or even worse, damage the shape, which hinders the realization of the heterostructure. Here, the control over the synthesis parameters is important to grow the domains of crown and shell and not to diminish the shape anisotropy. The heterostructure of the NCs is a powerful tool to extend the emission coverage, tune the PL properties and overcome the dissimilarity between the domains. By designing a logical combination of type-I, type-II and quasi type-II heterostructures, the possibility of new PL properties is shown. Moreover, impurity doping of the NPLs can further enhance our ability to realize the properties that are impossible to achieve via conventional methods. The silver doping of

the NPLs can induce paramagnetic properties while giving the power to tune the emission in the near-infrared region. As doping requires high temperature for a better diffusion of the impurity, again, the preservation of the shape is challenging and needs to be addressed by the synthesis parameters. Finally, modification of the surface of the semiconductor NCs is imperative for optoelectronic applications that need high carrier mobility. A universal approach is proposed for that, which addresses three barriers to carrier mobility: hopping distance, charge balance and acceptor sites. The final aim of the thesis is to propose a combination of techniques critical for the real-world application of the semiconductor NCs and provide a better understanding of the synthesis dynamic of the NCs under different conditions.

1.1. Organization and scope of the Thesis

In Chapter 2, we present an overview of the semiconductor QDs from the basic synthesis concepts resulting in the nucleation and growth of the QDs and their 2D NPLs counterparts. The size-dependent optical properties and various electronic/geometrical heterostructures of type-I, type-II and quasi-type-II in the core/crown or core/shell geometries are discussed. An overview of doping of the QDs is provided, mostly focusing on the silver doping of the NPLs. Finally, the optoelectronic properties of group I-III-VI QDs are reviewed.

In Chapter 3, we show the synthesis and properties of the CdSe-based core/crown/double shell NPLs with extended emission in the near-infrared region. This heterostructure demonstrates enhanced properties at relatively longer wavelengths (ca. 700 nm), most preferable for electroluminescence applications.

In Chapter 4, we investigate the excitonic properties of the convoluted system of CdSe/CdSeTe/CdTe core/crown/crown NPLs. The multi-channel recombination pathway of the NPLs is shown to be tunable with different shares of direct and indirect recombinations. We also show that these NPLs are best for applications requiring nonlinear absorption of the light due to the high charge-transfer channels at lower energies.

In Chapter 5, we demonstrate the silver-doping of the core/shell NPLs at high temperatures and follow the thermodynamic pathway in the reversible and irreversible doping regimes. The shell of the NPLs is shown to greatly change the doping mechanism of the NPLs, with the CdSe/CdZnS core/shell exhibiting the highest doping capability.

In Chapter 6, we present a surface modification method of group I-III-VI QDs to tune their optical and electronic properties. The surface-modified QDs demonstrate a 10^5-fold increase in carrier mobility due to the decreased hopping distance, electron injection and donor site passivation.

In Chapter 7, we conclude with the final remarks of the thesis and give an overview of some of the ongoing studies with possible future research directions.

Chapter 2

Colloidal Semiconductor Nanocrystals

In this thesis, we study different aspects of the colloidal semiconductor nanoplatelets from the synthesis, heterostructures and application point of view. With the possibility to tune the resulting properties through engineering their composition and structure, we will show that these NPLs provide a solid ground for a vast range of optoelectronic and magnetic properties critical for electronic devices. Before we get into our findings, in this chapter, we will present the fundamentals governing the optical properties of the nanocrystals, including the quantum confinement effect and size-dependent optical properties of the NCs. The colloidal synthesis of semiconductor NCs will be explained in detail, in which the nucleation and growth of the NCs play a central role in the size, shape and composition of the NCs. Moreover, the effect of the ligands on the colloidal stability and emission quality will be discussed. Finally, the underlying reason behind the different growth schemes of the 2D NPLs will be investigated, in which the surface energy of the planes overhauls the isotropic growth scheme common for 0D quantum dots.

2.1. Basic Concepts of Semiconductor Nanocrystals

Semiconductor NCs are a group of materials systems with at least one of their dimensions in the nanoscale range of 2-20 nm [26]. These NCs can be synthesized using different methods, including colloidal synthesis in a solvent and epitaxial growth at high temperatures [26]. Through optimized colloidal synthesis of these materials, it is possible to form small NCs, consisting of hundreds to thousands of atoms, easily dispersible in polar or nonpolar solvents [27]. Colloidal semiconductor NCs possess interesting properties due to a phenomenon known as the quantum confinement effect [26]. While for bulk materials, continuous energy levels in both the conduction band (CB) and valance band (VB) separated by a band gap exist due to a large density of the bonded atoms, in semiconductor NCs, the CB and VB demonstrate discretized energy levels originating from a limited number of atoms (Figure 2.1) [28]. These energy levels and the band gap of the NCs can be tuned through the size and shape of the NCs. As a result, the quantum confinement effect substantially expands the control over the properties of NCs with the same composition, while for the bulk semiconductors, changing the properties is only possible with changing the composition.

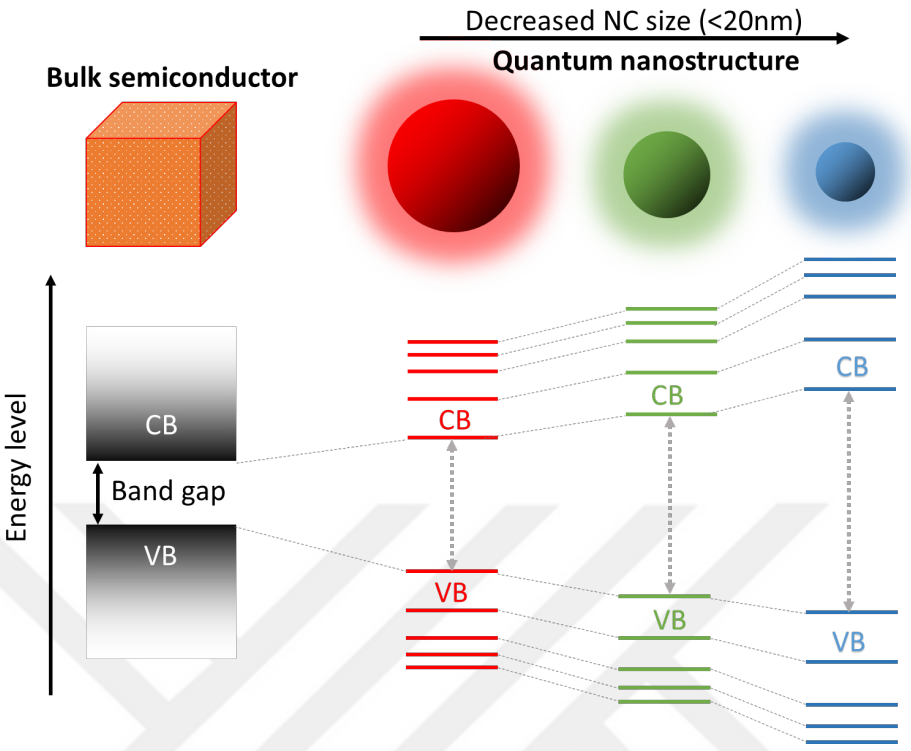

Figure 2.1. A schematic of the quantum confinement effect. The bulk semiconductor demonstrates continuous energy levels in the conduction and valance band with the lowest band gap compared to the NCs. As the size of the NC becomes smaller than the Bohr radius, both conduction and valance bands exhibit discretized energy levels with the band gap widening.

Exciting the NCs with a photon of higher energy than the band gap energy, a phenomenon known as photoexcitation, produces a pair of electron and hole (e-h, exciton). In NCs with sizes smaller than the Bohr radius, the electron and hole are bounded together with a strong Coulombic binding energy, which is not as strong for bulk materials. The high e-h binding energy induces a high absorption of the NCs compared to the bulk materials [28].

Through photoexcitation, an electron and hole pair is generated above the energy levels away from the band edge of the materials (Figure 2.2a). The excess of the incident photon energy than the band gap dissipates rapidly in the form of heat, and the electron and hole relax down to the band edge [29]. The strong binding energy can also open up new relaxation channels in the form of ionization of an electron in the valance band, which produces an extra e-h pair on rare occasions [30].

The excited electron and hole pair then recombines and generates a photon with an energy equal to the bandgap energy of the NCs. The process of photoexcitation and photoemission is the root cause of the observed absorption and emission of the NCs [31]. As mentioned before, changing the size of the NCs causes a change in the effective band gap of the material and, hence, the absorption and emission spectra. The photoluminescence (PL) emission linewidth of the semiconductor NCs is narrow due to the quantized energy level and the photoluminescence quantum yield (PLQY) is high due to surface passivation with organic ligands (Figure 2.2b), which also provide high chemical and colloidal stability of the NCs in the solution [32]. The polarity of the ligand determines the solubility of the NCs in the polar or non-polar solvent. For organic ligands, the polarity can be tuned by the length of the ligand, while NCs capped with inorganic ligands are only dispersible in polar solvents due to their high surface polarity [33], [34]. Depending on the composition of the NCs and the synthesis condition, the surface of the NCs can be terminated with a specific set of crystal planes, with lattice fringes visible in the TEM images (Figure 2.2c) [23].

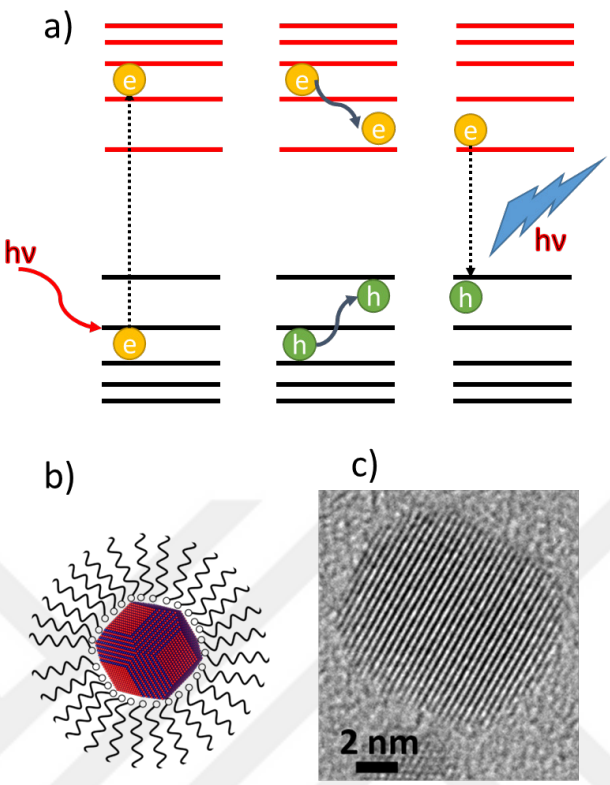

Figure 2.2. a) A schematic of the photoexcitation and exciton generation of the NCs followed by heat dissipation and photoemission. b) A representative drawing of 0D NCs, known as QDs, passivated with organic ligand. The hollow circles show the functional group of the ligand, in which the ligands are attached to the NCs surface with these functional groups. c) A TEM image of CdSe-based NCs with the lattice fringes visible in the image.

2.2. Colloidal Synthesis of Semiconductor Nanocrystals

The solution-based synthesis, also known as colloidal synthesis, of the semiconductor NCs is one of the most versatile methods to produce high-quality semiconductor NCs and achieve distinct properties for many applications. The method is based on the

nucleation and growth of the NCs in a non-coordinating solvent, through which the synthesis condition can produce a vast range of NCs with different compositions, shapes and heterostructures [7], [16], [25], [35]–[38]. In this section, first, the general nucleation and growth scheme of the colloidal synthesis of semiconductor QDs will be discussed and then the anisotropic growth of the 2D nanoplatelets will be investigated.

To synthesize QDs with a quasi-isotropic growth scheme, three essential elements are needed: the anion and cation precursors, the non-coordinating solvent and the ligand[7], [39]. The precursors provide the building block for the NCs, which upon activation, for example, by increasing the temperature and concentration of the free anions and cations in the solution, react with each other and form the NCs. The non-coordinating solvent provides the medium for the reaction to take place without participating in it and the ligands interact with the surface of the QDs to increase the colloidal stability and enhance the optical properties.

One prominent model in predicting the nucleation and growth scheme of the NCs is the La Mer model shown in Figure 2.3a [40]. In the basic interpretation, upon increasing the concentration of the free monomers and supersaturation of the solution, small crystallites nucleate spontaneously and homogeneously all through the solution medium. Followed by this nucleation stage, the nanocrystals undergo a growth stage, in which the free monomers nucleate on the surface of the small crystallites and more monomers attach to the surface, enlarging the size of the NCs [40]. The fundamental reason behind the nucleation and growth of the NCs lies behind the thermodynamic equilibrium governing the total energy of the system. Defining the Gibbs free energy for a spherical cluster as

$$\Delta G = -\frac{4}{3}\pi r^3|\Delta G_V| + 4\pi r^2\gamma \qquad (2.1)$$

where r is the radius of the sphere, ΔG_V is the Gibbs free energy per unit volume and γ is the surface energy per unit area. The Gibbs free energy starts to decrease at a critical radius onward. The first term of the equation is negative, which favors the formation of bigger spheres; however, the second term is positive due to the increase in the surface area with increasing the size of the sphere (Figure 2.3b) [40].

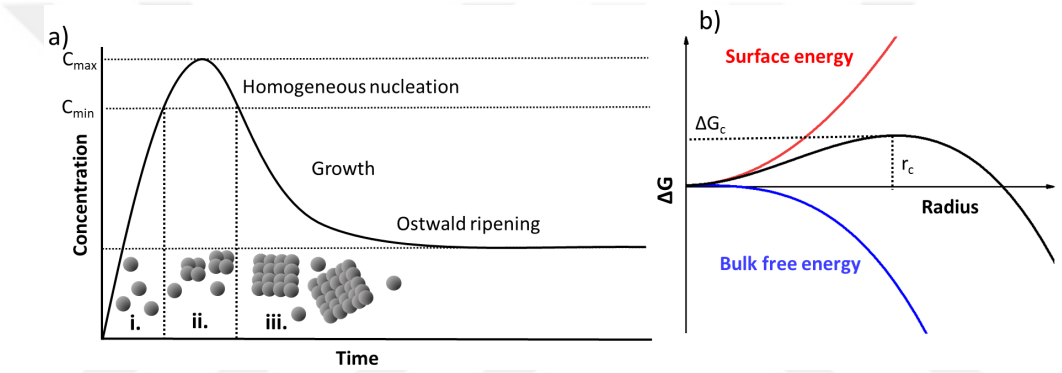

Figure 2.3. A schematic of the LeMar growth model consists of three main stages: First, a spike in the monomers' concentration brings the system to the supersaturation, close to the homogeneous nucleation phase. In the second stage, small crystallites start to randomly nucleate in the solution, which also causes a decrease in the concentration of the free monomers. In the third stage, the small nuclei undergo inhomogeneous nucleation and growth, increasing the size of the NCs and decreasing the concentration of the free monomers. Ostwald ripening also happens in this stage, in which one crystal may dissolve in the solution at the expense of the growth of another crystal. b) The Gibbs free energy and the two surface and volume terms that affect the system's overall energy. With increasing the size of the NCs, the volume energy per volume decreases while the surface energy per area decreases. The Gibbs free energy starts to decrease at a critical radius of the sphere (r_c).

While the isotropic growth scheme of the LeMar model gives a good grasp of the colloidal synthesis of the NCs, it does not explain the anisotropic growth of 1D nanorods/nanowires and 2D NPLs. In fact, even for 0D QDs, the shape of the NCs is not spherical and is terminated by specific planes, as shown in Figure 2.2b. The anisotropy in the shape originates from the energy difference between different facets, which causes some planes to grow faster than the other facets and anisotropic enlargement of the NCs [40]. Fast growing facets continue growing and slow facets are exposed.

The preretirement for anisotropic growth is first to activate the energy difference of the planes. In a crystalline structure, each terminating plane has a different number of broken bonds, which contributes to the surface energy of that plane [41]. As an example, Figure 2.4 shows the broken bonds for three different planes of (100), (110) and (111) of a face centered cubic (FCC) crystal structure. Here, the (110) planes with five broken bonds have the highest energy and the (111) planes have the lowest number of broken bonds. The final crystal, grown under free conditions, will be mostly terminated by (111) planes compared to (100) and (110) planes.

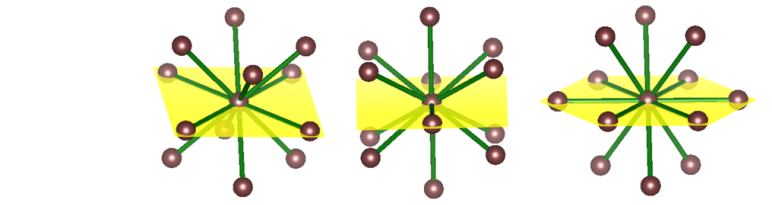

Terminated plane	(100)	(110)	(111)
Broken bonds	4	5	3

Figure 2.4. A schematic of three different planes of FCC cubic crystal and the representative bonds.

While the abovementioned criterion plays a central role in the growth of any kind of nanocrystals, the first synthesized CdSe NCs had a quasi-spherical shape due to the synthesis condition [3]. If the energy difference between the terminated planes is negligible, this criterion also predicts a quasi-spherical shape. As the CdSe QDs are synthesized at relatively high temperatures, the surface energy of the planes converges and the difference is negligible, which amplifies isotropic growth. Moreover, using bulky precursors such as $Cd(oleate)_2$ covers the surface of the NCs, which means the limiting growth factor is the transfer of the monomers to the surface (and not the surface reaction rate) [41].

As will be discussed later, the synthesis temperature of the CdSe NPLs is much lower than the QDs counterparts (240 ˚C compared to 300 ˚C). Also, for the CdSe NPLs, the small-chain precursor of $Cd(OAc)_2$ reduces the transfer distance of the monomers to the surface. These two changes in the synthesis condition activate the role of the surface energy in the growth of the NPLs, resulting in the anisotropic growth scheme [42]. The zinc blende CdSe NPLs are terminated with (100) planes on all sides. The same crystal planes have the same surface energy, and in principle, the zinc blende crystal should have a cubic shape instead of a flat shape. Although the growth mechanism of the NPLs is not fully understood, this anomaly in the growth is discussed in the literature [42], and is correlated to the growth instability of the NPLs, in which the inhomogeneous nucleation on the facets requires higher energy with increasing the size of the plane [42]. NPLs also undergo Ostwald ripening at high temperatures, in which the thinner NPLs dissolve and provide monomers for the growth of thicker NPLs. The atomically precise thickness of the NPLs inhibits the defocusing of the thickness size distribution of the NPLs, and instead, Ostwald ripening is another factor in realizing thicker NPLs [43].

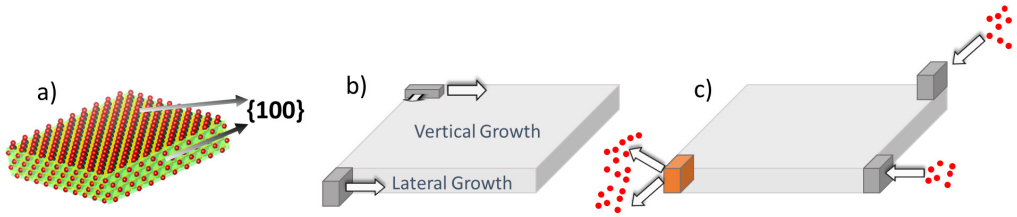

Figure 2.5. a) CdSe NPLs with terminating facets from {100} planes. b) Normal growth scheme, in which first a nucleus forms on the lateral or basal plane and then it grows. c) A schematic of the Ostwald ripening of the NPLs. The smaller NPLs dissolve and produce monomers for thicker and larger NPLs.

2.3. Electronic Heterostructures of Colloidal Nanocrystals

Colloidal NCs can be composed of more than one domain with different compositions and configurations, which paves the way for different electronic heterostructures. Tuning and enhancing the optical properties of NCs is possible through engineering the electronic heterostructure, which expands our ability beside the conventional tuning tools including the size, composition and shape of the NCs. The three most common electronic heterostructures of the NCs are type-I, quasi-type-II and type-II. Other heterostructures in the literature, such as inverted type-I and inverted type-II, refer to the same electronic heterostructures with complementary geometries, which will be discussed in this chapter.

The electronic band-alignment of the type-I heterostructure is depicted in Figure 2.6a. In this structure, a second domain with a deeper conduction and valance band than the first domain (core) is deposited around the core [44]. The heterostructure is mainly used to boost the optical performance of the NCs by passivating the surface and preventing the excitons from reaching the surface [44]. As the colloidal NCs possess a high surface-to-

bulk ratio, the number of surface atoms is significantly higher in comparison to the bulk materials. These surface atoms are not completely saturated in terms of the chemical bonds while having the same coordination number with the bulk atoms. The broken bonds mean that the surface atoms (like the lattice defects) possess an electrical charge that can attract the electron or hole and diminish the optical properties by capturing the carrier (charge trap) instead of the exciton recombination [45]. To reduce the adverse effects, the ligands are introduced to the NCs, usually at the end of the synthesis, which can saturate the surface to some degree [45]. However, even for a ligand-capped NC, some broken bonds exist and the surface atoms do not reach their coordination number. To counter this effect, a layer of an inorganic domain with a higher bandgap can be coated on the NCs that prevent the carriers from reaching the surface [46]. The type-I electronic structure lays a recombination pathway in which the excitons are first transferred to the core band-edge and recombination happens there [46], [47]. The inverted type-I heterostructure has the same electronic structure but the position of the domains (core and shell) are exchanged [48].

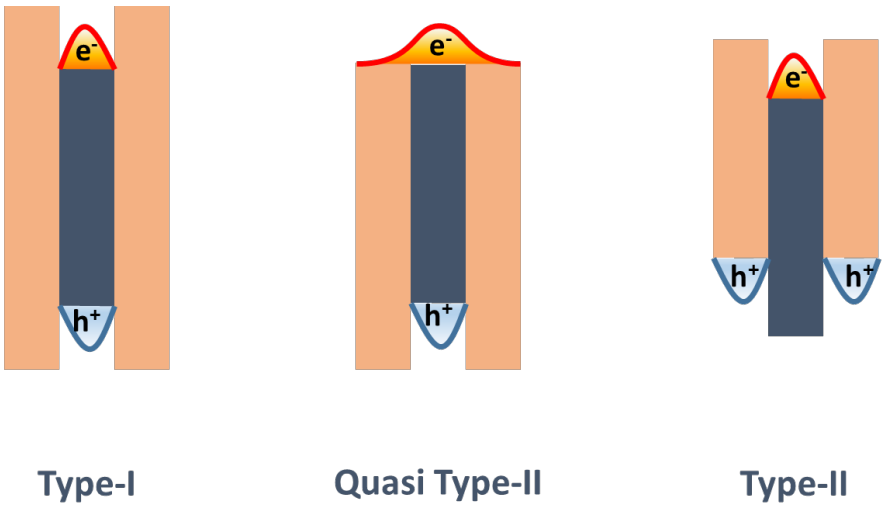

Figure 2.6. The band alignment for three electronic heterostructures of a) type-I, b) quasi type-II and c) type-II.

The quasi-type-II electronic heterostructure (Figure 2.6b) has a very similar band structure to type-I, except the band offset for the conduction band is much smaller than type-I [49]. This electronic heterostructure can also passivate the surface of the NCs, but most importantly, it is a powerful tool for tuning the emission wavelength of the NCs [50]. While the hole, with a much higher effective mass than the electron, mostly resides in the core, the electron demonstrates a wavefunction distribution across all the domains. This relaxed confinement on the electron induces a red shift in the absorption and emission spectra of the NCs and can be tuned through the size of the shell [50].

In the type-II electronic heterostructure, the valance and conduction band of the second domain (shell) is in a staggered configuration with the core (Figure 2.6c) [51]. The configuration implies that the electron and hole wavefunction are spatially separated from each other and the recombination happens at the interface of the domains [51]–[53]. Moreover, as the new recombination pathway has a lower energy than the band gap of the separate domains, the observed emission is red-shifted even more than the quasi-type-II electronic heterostructure [54]. Type-II band alignment is powerful in realizing emission at low energies and is usually used for emission below the band gap energy of the domains. For the inverted type-II heterostructures, the position of the core and shell is reversed, which can be used for suppressed Auger recombination [55].

2.3.1. Nanoplatelets with Type-I Heterostructure

The type-I electronic heterostructure of the NPLs can be best realized in the core/crown geometry. In this architecture, the crown with a wider bandgap than the core is deposited on the peripheral sides of the NPLs, passivating the lateral sides of the NPLs [44]. The synthesis of core/crown NPLs is usually carried out using a two-pot procedure, in which first, the core is synthesized and then, in a separate synthesis, the crown is deposited on

the lateral sides. The anisotropic growth scheme needed for the crown formation implies that the synthesis should be performed at relatively lower temperatures to maintain the thickness and 2D shape of the NPLs [44].

4 monolayers (MLs) CdSe/CdS core/crown NPLs are one of the most common type-I heterostructures known for their high PLQY and chemical stability (Figure 2.7a). The crown made of CdS prevents the carriers to reach the lateral sides of the NPLs, which causes an instant increase in the PLQY from ca. 30% for the CdSe core to more than 90% after crown deposition [56]. As the thickness of the core does not change with crown deposition, the electron and hole confinement remain the same and the spectral shift is limited to 2 nm (Figure 2.7b and Figure 2.7c).

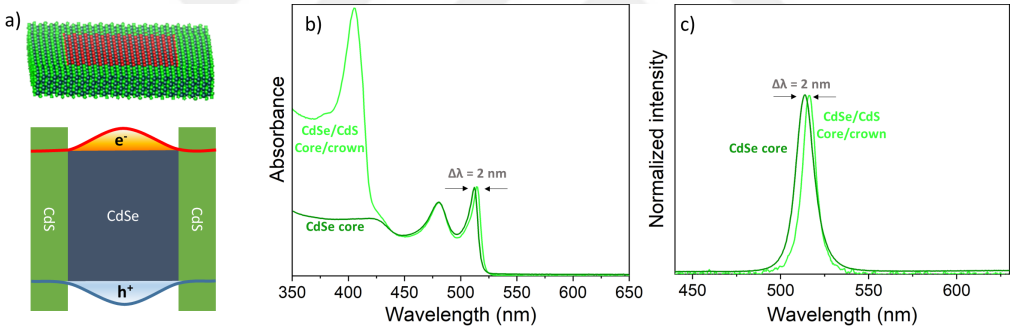

Figure 2.7. a) Sketch of CdSe/CdS core/crown NPLs along with the corresponding electron and hole wavefunction distributions in the domains. b) Absorption and c) PL spectra of the CdSe core and CdSe/CdS core/crown NPLs.

2.3.2. Nanoplatelets with Quasi Type-II Heterostructure

Quasi type-II band alignment of the semiconductor NCs is probably the most common heterostructure in the literature. This heterostructure is sometimes referred to as type-I due to the wider bandgap of the second domain; however, the diffusion of the electron

wavefunction into the second domain of wider bandgap relaxes the confinement and the electron and hole wavefunctions do not remain in the narrower bandgap domain [57]. In the QDs, quasi type-II heterostructure can best be realized by the coating of a shell around the core, resulting in a spectral red shift of absorption and emission and enhancing the PLQY due to the passivation of the surface [57]. Research on the development of core/shell heterostructures of the QDs started after sufficient realization of the synthetic routes for the core QDs [46]. In the early reports, the core/shell QDs with CdSe core were coated with CdS or ZnS to boost the PLQY and provide spectral tunability [58]–[60].

The seed-mediated method provides enough control over the radius of the core and shell and, hence, the optical properties of the QDs. With increasing the core size or the shell's thickness, the electron and hole confinement relaxes, resulting in a red shift in the absorption and emission spectra [57]. In the common synthesis protocol of the core/shell QDs, first, high-quality core is synthesized and purified, and then, it is used for a second pot synthesis to grow the shell. In some procedures, one-pot synthesis of the core/shell QDs was also developed, in which the precursors for the shell are injected right after the growth of the core [61]. For both synthetic routes, the chance of renucleation and size defocusing exist, diminishing the performance of the QDs [61]. The successive ion layer adsorption and reaction (SILAR) technique is an alternative pathway based on the biphasic growth of the shell, preventing the renucleation of other species [62]. In this method, the shell precursors are alternatively introduced to the QDs and cleaned from the synthesis medium to achieve atomically precise control over the thickness of the shell. While a powerful method for precise deposition of the shell, core/shell QDs synthesized via the SILAR method do not have the same quality as the high-temperature grown QDs due to the higher chance of point defects and incomplete surface passivation.

Following the same path of QDs, the core/shell synthesis protocol for NPLs was developed to enhance the quality and tune the emission. In the early reports, the CdS, ZnS or alloyed CdZnS shell was coated on the NPLs through the colloidal-atomic layer deposition (c-ALD) technique, which is very similar to the SILAR method [56]. A schematic of the c-ALD synthesis protocol is shown in Figure 2.8. Here, the long-chain capped NPLs are first transferred from the original non-polar to a polar solvent by replacing the ligands with a layer of S^{2-}/Se^{2-} anion. The electrostatic repulsion due to the negative charge of the NPLs prevents precipitation and contributes to the colloidal stability in the polar solvent. Then, after precipitation of the anion-terminated NPLs and redispersion, the unreacted sulfur is removed and a metal precursor of Cd, Zn or a mixture of Cd/Zn is introduced to the NPLs, completing the first CdS, ZnS or CdZnS layer. The process can be repeated as many times as needed and the thickness of the NPLs can be tuned with an atomistic precision. In the end, the NPLs are transferred back to the non-polar solvent by ligation.

While c-ALD is a powerful method to control the shell reaction and thickness, it does not provide high-quality NPLs due to incomplete ligation and possible high density of the defects. Another method of coating a shell on the NPLs is hot injection (HI), known for high-performance final NPLs, versatility and tunability. In the HI method, the seed NPLs are mixed with the cation precursor and the shell is grown at high temperatures (ca. 300 ˚C) by controlled injection of the sulfur precursor (Figure 2.8). The high growth temperature of the shell causes better growth with fewer number of defects in the structure. The emission peak wavelength of the NPLs can be tuned by three factors of cation precursor composition and amount and the growth time.

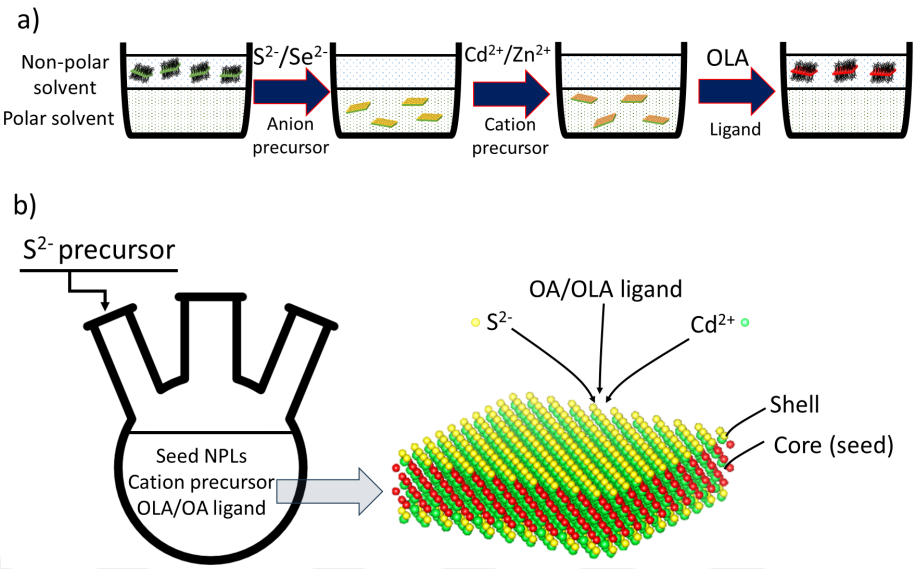

Figure 2.8. Schematics of the (a) c-ALD method and (b) hot-injection method.

Growing the shell red-shifts the absorption and emission spectra of the NPLs due to the relaxed confinement [63]. Quasi type-II electronic heterostructure is especially important in overcoming the discrete energy jumps of the NPLs originating in the vertical confinement of the NPLs in the red region [50]. For shorter wavelengths, the composition of the starting core can be modified by the addition of alloying elements such as S, which widens the bandgap. The strategy is especially important in realizing high-performance NPLs emitting in the green region [50].

2.3.3. Nanoplatelets with Type-II Heterostructure

In the type-II electronic heterostructure of the NPLs, two domains of different compositions with staggered electronic band structure configuration are put adjacent to each other, where the conduction and valance bands of one domain are higher (or lower) than the other one. In this electronic structure, the electron and hole are transferred to two different domains and the recombination occurs at the interface of the domains [64]. The spatial separation of the electron and hole increases the recombination lifetime and

causes indirect recombination with a relatively broad PL spectrum that are the characteristics of the type-II heterostructure [64]. These heterostructures are especially important for long-wavelength emission with lower energy than the bulk bandgap of the domains [35]. Moreover, the long emission lifetime paves the way for applications including photocatalysis and solar energy harvesting, where a long exciton lifetime is necessary to extract the electron [51], [65].

In the colloidal NCs, the heterostructure can be engineered in core/shell architecture for the QDs [66], dot-on-platelets [67] or dot-on-rod [68]. For NPLs, CdSe/CdTe core/crown is the most commonly used structure for type-II band alignment [51]. As the synthesis of the CdSe core NPLs is thoroughly understood and well-established, growing a crown of CdTe results in a type-II electronic structure. Previously it was shown that for CdSe/CdTe core/crown NPLs, the indirect emission can be tuned through the size of the crown or by alloying the crown with Se [69], [70]. Although CdSe/CdTe core/crown NPLs are the most widely studied type-II heterostructure in the literature, other architectures and compositions such as CdTe–CdSe inverted type-II, CdSe/ZnSe dots-on-plates and CdS/ZnSe core/crown NPLs have also been demonstrated in the literature [51].

More recently, complex heterostructures of the type-II NPLs have been developed where the number of the domains is increased and, hence, the number of interfaces between the domains contributing to the final emission is increased. Among these heterostructures, CdSe/CdS/CdTe [64], CdSe/CdSeTe/CdTe [51], CdSe/$CdSe_{1-x}Te_x$/CdSe/CdS [52] and CdSe/CdTe/CdSe [53] core/multi-crown NPLs suggest further control over the excitonic behavior by changing the size and composition of the domains and resulted in different emission profiles from one peak emission to many peaks emissions. One similar factor in all these heterostructures is the possibility of many direct and indirect recombination

pathways, which can be activated/deactivated due to the different recombination rate of each channel.

2.4. Doping of Semiconductor Nanocrystals

In simple words, doping is the process of introducing new elements in small quantities in the lattice of a host NCs [71]. The dopant ions can introduce new properties, including optical, electronic and magnetic, that are otherwise not possible to achieve with pure original composition [71]. Doping of the NPLs can be undertaken using two different methods [72]: in situ doping, in which the dopant ions are introduced to the reaction pot while the nucleation and growth of the NCs take place (Figure 2.9a). In this method, the dopant ions are kinetically trapped in their position due to the fast cooling of the reaction and will not diffuse out of the NPLs due to the high activation energy of the diffusion. Second, diffusion doping, in which the NPLs are first synthesized and then the dopant ions are introduced to the already formed NPLs (Figure 2.9b). Here, dopant ions diffuse in the lattice of the NPLs and stay there as the result of the thermodynamic equilibrium between the dopant content in the solution and the NPLs [72]. So far, many studies have investigated doping of the NPLs with Mn, Ag, Cu and Hg and the doping dynamics and the final dopant-induced properties of each system [71]. Here, we mostly focus on doping the NPLs with Ag, which is one of the main topics of this thesis in the coming chapters.

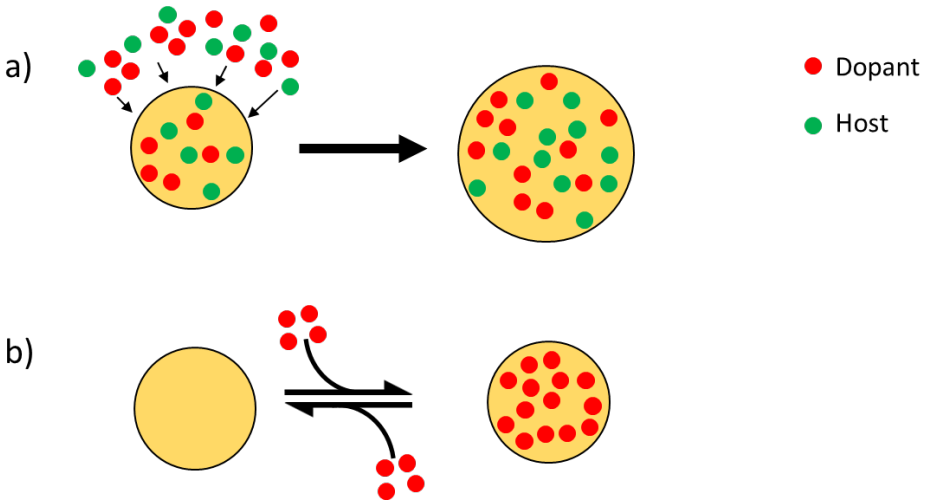

Figure 2.9. Schematics of the doping mechanisms: (a) kinetic control and (b) thermodynamic control doping of NCs. The red and green small dots denote the dopant and host.

2.4.1. Doped Nanoplatelets

The previous studies focusing on the silver doping of the group II-VI NCs are comparatively fewer in number than Mn- and Cu-doping. The challenge primarily arises due to the softer Lewis acid of Ag^{+}, which promotes the formation of lattice Ag_2E (E: chalcogenide) through diffusion and exchange with the host atoms. The reaction occurs rapidly within a time frame of 100 ms without any noticeable long-lasting intermediates. [73]–[75]. Under extreme conditions with high ion concentrations, a distinct Ag_2S phase begins to nucleate [76]. The strong affinity of silver to form lattice bonds enables the doping process at room temperature, mitigating potential drawbacks, including Ostwald ripening and damage to the structure. In one of the initial studies detailing the exchange between Ag and Cd in CdSe QDs, the Alivisatos group showcased the feasibility of a complete exchange reaction of Ag with CdSe. [77]. The resulting NCs maintained their shape and crystalline structure owing to the preservation of the intact anion sublattice. However, for the reverse exchange reaction, a 50-fold increase in the initial concentration

of Cd precursor was necessary, which led to a disrupted lattice. An intriguing finding from their experiment was that the exchange reaction does not affect or harm the original QDs above a certain size threshold, while below that size, the QDs experience fragmentation or dissolution. [77]. The soft nature of Ag as a Lewis acid facilitates its exchange with the host divalent ions, which together with a soft base, enables a reverse exchange reaction [78].

The exchange reaction triggered many research studies focusing on shape engineering, heterostructure building, and composition modification of the NCs [79], including ZnTe, Ag_2Te, CdTe, PbTe and $PtTe_2$ nanowires [80] Ag_2S/CdS dots-in-rods [81], [82], CdSe/Se, ZnSe/Se, and PbSe/Se core/shell QDs, [83] and CdS and TiS_2–Ag_2S toroid QDs [84]. Furthermore, CdE QDs exhibit significant potential for applications demanding high chemical sensitivity, wherein CdSe quantum dots can readily absorb Ag and Ag_2S QDs can absorb Cd and Zn [85]–[87]. The soft lattice of Ag_2E also provides a versatile template to synthesize a range of group I-III-VI NCs, including $AgInSe_2$ and $AgInS_2$ QDs, through partial exchange [88], [89].

The mechanism of Ag-doping and exchange reactions is most accurately described by the interstitial diffusion of ions within the lattice and subsequent exchange with the host ions, in contrast to the vacancy-mediated diffusion observed in the case of Zn, Cd, and Pb [90], [91]. According to a study by Otto et al. [90], the density-function theory (DFT) calculation suggests that the Ag_{int}^{+} ions (interstitial Ag^+) diffuse rapidly to the center of the NCs. As the positive charge accumulates, the Ag^+ ions repulse each other, which ultimately triggers an exchange reaction with the Cd^{2+} ions. Then, a pair of lattice Ag^+ and Ag_{int}^{+} ions around the Se^{2-} forms initiating a rapid full exchange of the NC (Figure 2.10). Then, a pair of lattice Ag^+ and Ag_{int}^{+} ions around the Se^{2-} forms and initiate a rapid

full exchange of the NC. According to the model, at lower dopant concentrations, Ag^+ ions tend to occupy interstitial sites positioned at the center of the QDs. However, at higher concentrations, whether alloyed or fully exchanged, these ions predominantly occupy Ag_{Cd}^- sites located on the surface. This occupation led to the displacement and removal of Cd from the lattice [90]. The formation of surface-bound Ag^+ ions was also noted in other studies, particularly when the dopant concentration fell between levels insufficient for complete exchange and not low enough to confine Ag^+ ions solely to the QD centers [92], [93].

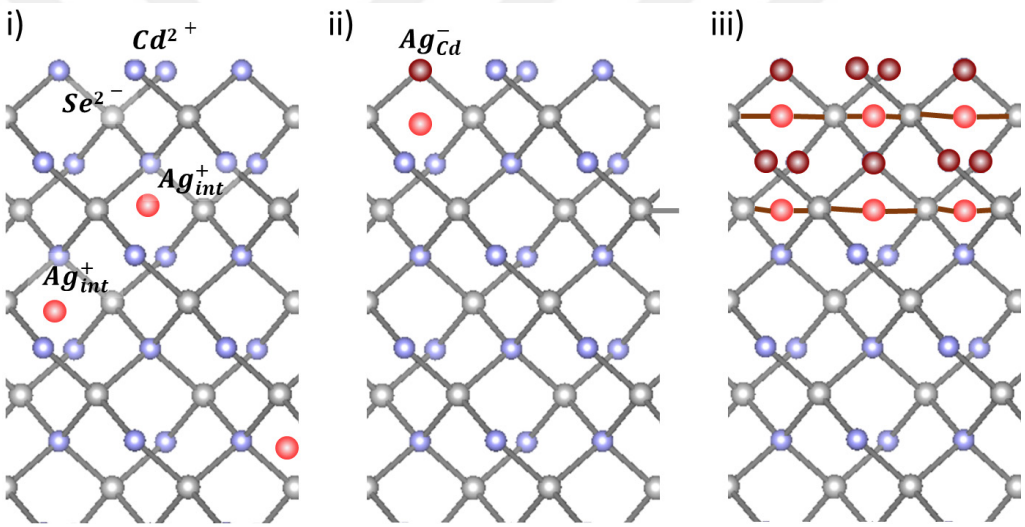

Figure 2.10. (a) A macroscopic model of Ag-doping for CdSe NCs with three different stages of doping: (i) At low Ag concentration, Ag_{int}^+ with high interstitial mobility diffuse to the center of the NC, and later, are pushed to the surface and partially replace the Cd ions. (ii) The Ag_{Cd}^- and Ag_{int}^+ ions form a bond, initiating the nucleation of Ag_2Se, and (iii) with increasing the Ag concentrations, Cd^{2+} ions are totally replaced with Ag on the surface.

The rapid and efficient exchange reaction necessitates a slower and controlled cation exchange process, which avoids completely altering the host composition. To synthesize

doped QDs, limitations on dopant concentration are imposed, and in certain approaches, an excess of ligand is introduced. The additional ligand serves as Ag-scavenger, facilitating the doping process while preventing excessive alteration of the composition [91], [94]. An ideal doping process entails the preservation of the NC shape, which is important for the post-doping routes. Also, with the low concentration of the dopant, the XRD pattern does not exhibit a huge change, which points to the retention of the crystalline structure [94]–[96]. The dominance of the ME (M: metal) sublattice over Ag_2E results in unchanged binding energies for M and E in the XPS spectra, while the presence of Ag^+ can be confirmed through the appearance of Ag3d peaks [97].

The concentration of Ag in the NCs determines the optical properties. For the low-doped NCs, the emission and absorption spectra do not show much change compared to undoped NCs; however, these lightly-doped NCs demonstrate enhanced photoluminescence due to activation of the dark excitons [94], [96], [98]. For highly doped NCs, the mid-gap states within the bandgap are activated, which results in lower energy emission [99]–[101]. The excitonic features, including the electron-heavy hole and electron-light hole for CQWs, remain in their position after heavy silver doping but a low energy tail due to Ag^{2+} photoconversion forms [101]. The NCs exhibit enhanced dopant emission with a relatively longer lifetime while the band-edge emission decreases. The recombination process for doped NCs involves the deeply localized hole recombining with free electrons in the conduction band, resulting in dopant emission. However, the bonding nature differs fundamentally between Cu^+:CdSe NCs and Ag^+:CdSe NCs. In Cu^+:CdSe NCs, the bonding follows a conventional oxidation pattern, while in Ag^+:CdSe NCs, an "inverted" bonding mechanism is observed. Despite this difference, the ultimate spectroscopic properties appear similar for both cases [102].

Ag-doping paves the way for tuning the PL of the NCs in the NIR region [103]. Introducing silver oleate precursor to CdSe NPLs at room temperature was shown to be effective in doping the NPLs while preserving the 2D shape, and results in strong dopant emission for high-dopant regimes. The emission is tunable by changing the concentration of Ag, covering a broad region from green to orange and deep-red [92].

Post-Ag doping of 3.5, 4.5 and 5.5 ML NPLs with silver acetate precursor was shown to yield highly doped NPLs with high PLQY [104]. Upon growing 1-5 MLs of CdS shell on the doped NPLs with the c-ALD technique, the emission and absorption spectra can be further red-shifted; however, the concentration of Ag in the core decreases due to the self-purification during the shell growth. [44], [63], [104]. Ag-doped CdSe NPLs can also be synthesized by in-situ technique, in which the silver precursor is introduced during the nucleation and growth of the CdSe NPLs. In this approach, Ag precursor is added to the reaction solution before CdSe starts to nucleate, and silver is trapped in the lattice due to the fast quench of the reaction in a water bath [105], [106].

2.5. Group I-III-VI Nanocrystals

With the advancement in the synthesis of colloidal NCs, the quest to realize and engineer other groups of colloidal NCs has been initiated. Group I-III-VI semiconductor NCs are one of the emerging fluorescence materials with a synthetic pathway closely correlating with the group II-VI NCs. The soft and defective crystalline lattice of these NCs allows heavy alteration in the composition, which opens the way for more complex systems [107]. $Cu_{2-x}S$ NCs are one of the conventional base materials that other compositions can be realized by cation exchange with Cu or vacancy filling [108]. Considering $Cu_{2-x}S$ NCs as the base material, it is possible to further implement other elements in the vacancy sites or through cation exchange with Cu. $Cu_{2-x}S$ is a polymorphous material that,

depending on the vacancy density and temperature, can form different crystalline structures, from djurleite for Cu-rich to covellite for CuS [109]. The high number of vacancy sites in the structure causes localized surface plasmon resonance (LSPR) in the near-infrared region, which can also be tuned by healing these sites through cation exchange [109].

$CuInS_2$ (CIS) NCs are one of the most studied compositions of the group I-III-VI colloidal NCs due to the ease of synthesis [110]. These NCs can either be synthesized through one-pot synthesis where both cations are introduced at the beginning of the synthesis [110]. Or, they can be synthesized in a two-pot procedure where first $Cu_{2-x}S$ or In_2S_3 NCs are synthesized and then the second cation is introduced for cation exchange [110]. As the chemical reactivity of Cu is higher than In, even in the one-pot synthesis, $Cu_{2-x}S$ NCs are first formed at the beginning of the synthesis at relatively lower temperatures, and then In exchange reaction occurs.

Similar to the group II-IV NCs, group I-III-VI NCs are predominantly synthesized by colloidal approach; however, other synthetic routes including hydrothermal/solvothermal, template-directed and cation exchange methods are also utilized for engineering the shape or narrowing the size distribution of the NCs [37]. The LaMer model, describing the three stages of NCs formation, is also applicable for group I-III-VI NCs. The nucleation stage caused by the supersaturation of the active precursor can be shortened by the hot-injection method where the anion precursor is rapidly introduced at high temperature to prevent continuous nucleation typical of the heat-up method. The nucleation stage takes place at relatively lower temperatures for group I-III-VI NCs (180-250 °C) compared to Cd chalcogenide NCs (250-300 °C), which is due to the faster and easier formation of the cationic complex of Cu than Cd. Moreover, the vast number of cation precursors and NCs compositions emphasis the importance of the

precursor selection. To ensure the balance of the precursors' reactivity the hard-soft acid-base theory is widely employed in the synthesis of group I-III-VI NCs, which helps avoid the formation of two separate compositions [111], [112]. Based on this theory, ions are categorized to behave as acid or base depending on their electron donating or accepting behavior, respectively. These ions are further classified as soft, borderline and hard, in which the soft acid and soft base have higher affinity to form a bond with covalent nature and, similarly, the hard acid and hard base better form an ionic bond with each other. On the contrary, the hard-soft combinations tend to form weaker bonds that is ideal for nucleation as it provides a high concentration of free monomers [112]. Figure 2.11 shows the classification of some of the hard and soft metal/ligands that are extensively used in the synthesis of NCs.

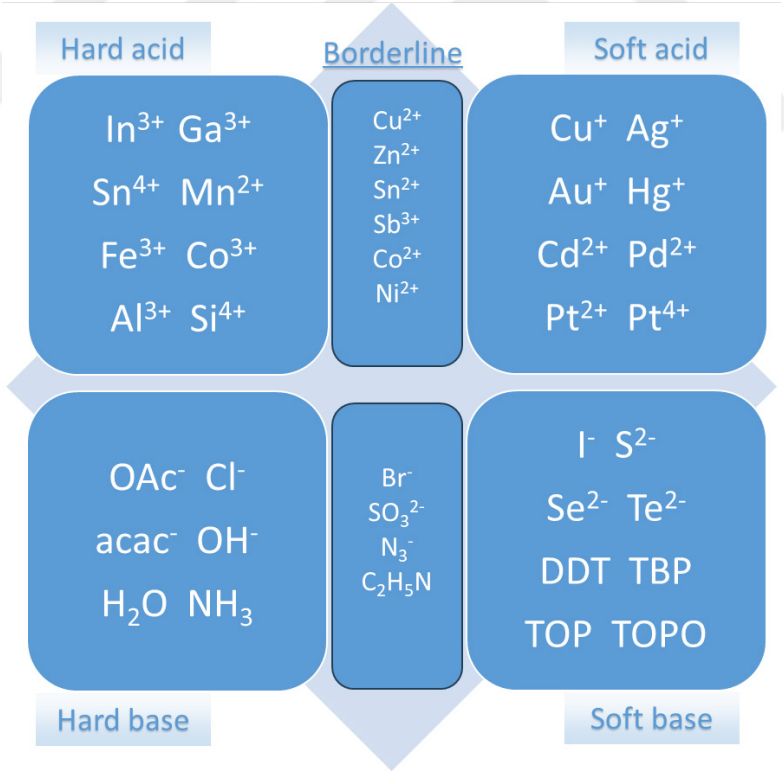

Figure 2.11. A classification of hard and soft metal and ligands.

Depending on the synthesis procedure, different crystal shapes, from 2D nanosheets to 0D pyramidical QDs, can be synthesized [37]. Moreover, the flexible lattice of the NCs allows alloying with other elements, which yields other compositions such as $AgInS_2$ (AIS), $CuInSe_2$ (CISe) or quaternary systems, including AgInSSe, $ZnCuInS_2$ and so on [37], [113]. Implementing a core/shell heterostructure, usually consisting of a shell with a wider bandgap than the base material, such as ZnS, is a common strategy to further confine the electron and hole in the core and enhance the optical properties [113].

The optical properties of group I-III-VI NCs can be tuned by changing the size and composition of the NCs covering a relatively broad range of the spectrum from green to near-infrared; however, the PL profile is usually broad due to the defective nature of the NCs [113]. Compared to Cd-based NCs, group I-III-VI NCs demonstrate a broad and featureless absorption profile with no sharp absorption transition or excitonic peaks, which is due to the size, shape and composition inhomogeneity of the NCs. The PL peak of these NCs is also broader than Cd-based NCs for the same inhomogeneities, while the defective nature of the PL and unequal bond length between metal-chalcogenide also contribute to the broad PL peak [37].

Group I-III-VI NCs demonstrate a broad range of functional properties, which opens the way for many optoelectronic applications. The ability to fine-tune the properties by adjusting the composition and size of these NCs makes them especially interesting as absorber in photovoltaic (PV) devices [114]. These materials are extensively used in luminescent solar concentrator (LSC) due to their high PLQY and relatively large stokes shift, and more recently, they have been employed in light-emitting diode (LED) for their broad spectral coverage [112]. The facile synthesis route, low cost and high chemical yield alongside the high structural versatility put group I-III-VI NCs as one of the most

appealing materials for other applications including field-effect transistors, photocatalysis, battery and storage applications, sensors and bioapplications [37], [112].

Chapter 3

Core/Crown/Double Shell Heteronanoplatelets

This chapter of the thesis is based on the publication “Deep-Red-Emitting Colloidal Quantum Well Light-Emitting Diodes Enabled through a Complex Design of Core/Crown/Double Shell Heterostructure” F. Shabani, H. Dehghanpour Baruj, I. Yurdakul, S. Delikanli, N. Gheshlaghi, F. Isik, B. Liu, Y. Altintas, B. Canımkurbey, H. V. Demir, Small 18 (8), 2106115 (2022). Reprinted with permission from [44]. Copyright 2023 WILEY-VCH Verlag GmbH & Co. KGaA, Weinheim.

3.1. Motivation

CdSe NPLs are among the most studied CQWs, offering a suitable platform as a base material to further design and synthesize complex heterostructures. Theoretically, the band-edge emission of these NPLs can be extended beyond 700 nm; however, the complications arising from the synthesis of these NPLs largely inhibit further increase the thickness and relaxing the confinement. In its zinc blend crystalline structure,

increasing the thickness along [001] direction, normal to the basal planes [42], can be performed mainly through one of the two strategies: (i) one/two-pot synthesis of thick NPLs [115], [116], and (ii) deposition of a shell with a different composition. While direct synthesis of CdSe NPLs with 2.5-7.5 monolayers (MLs) have so far been reported in the literature, increasing the thickness above 7.5 MLs with maintained purity is only possible through colloidal atomic layer deposition (c-ALD) [115]–[119]. Deposition of each layer decreases the electron and hole confinement, and is a possible way to tune the emission peak between discrete energy levels [56] . However, the final material obtained from c-ALD usually suffers from low PLQY and in some cases the emission even dies out [118], [120], [121]. Covering the lateral sides of CdSe NPLs with a higher bandgap material, a heterostructure, which is known as core/crown, can increase the PLQY of bare CdSe core up to around 90% without changing the emission peak position [56], [122]. On the other hand, the second material can be grown in the thickness direction, which unlike the core/crown, gives rise to extended leakage of electron's wavefunction into the shell [123]. Recently, hot injection (HI) method has been proposed and developed for the NPLs, which yields much higher PLQYs with ease of synthesis [124], [125]. HI is a powerful technique that enables the synthesis of high-quality NPLs with a spectral coverage from 550 to 650 nm, which may be obtained conventionally through shell thickness or alloying the core, shell or both [50].

In contrast to all of the aforementioned strategies to tune the emission peak of the CdSe-based NPLs, it is yet a major challenge to further extend the emission coverage to longer wavelengths, while keeping the 2D shape of the NPLs intact. Having the bulk bandgap energy of CdSe to be around 1.712 eV, theoretically it is possible to exceed the emission peak of 700 nm [126]. There are several reports of CdSe/CdS core/shell in the literature for giant quantum dots, in which the emission peak can be pushed up to around 640 nm

[127]–[129]. For the 4.5 ML CdSe core NPLs, the thick shell of CdS, corresponding to 14 MLs, gives an emission peak of 670 nm with moderate PLQY of 50-60% [124]. However, when the shell is alloyed with zinc, the PLQY can boost up to unity at the expense of emitting below 655 nm [130]–[132]. Herein, it is of primary importance to extend the emission peak of these high-quality NPLs to longer wavelengths without compromising their properties. This is especially important as the emitters in this region have poor PLQY and large full-width at-half-maximum (FWHM) [133], or are chemically unstable [134], which diminishes their performance in optoelectronic applications. In the recent years, colloidal NPLs have shown excellent performance with superior properties for laser and light-emitting diode (LED) applications, which is originated from their visible range tunability, photostability and high PLQY [50], [135], [136]. Developing high-performance CdSe-based NPLs can compensate the lack of good emitters for electroluminescence (EL) applications at longer wavelengths by employing their excellent properties as active material in LEDs. The deep-red to near infrared light is important for applications of telecommunications and light vision devices [137], [138]. Moreover, because of the weak light absorption and scattering from biological tissues at longer wavelengths, this light is particularly useful for biosensing and biomedical applications [139].

In this chapter, we propose and show a meticulous synthesis pathway toward the best optimized heterostructure to address the pivotal requirements of a CdSe-based emitter with the lowest possible energy. The seeds for the final HI are designed to be laterally large and passivated, and enable a relatively large vertical thickness, so that through the final HI shell coating the thickness can be effectively increased. This strategy yields very thick NPLs, emitting closer to the theoretical bulk bandgap energy of CdSe. These thick NPLs were implemented in LEDs as active material, emitting above 700 nm with

excellent external quantum efficiency (EQE) of 6.8 %, which is in close competition with other types of semiconductor NCs [134].

3.2. Experimental

Materials. Cadmium acetate ($Cd(OAc)_2$, 99.995%), cadmium acetate dihydrate ($Cd(OAc)_2 \times 2H_2O$, 98%), cadmium nitrate tetrahydrate ($Cd(NO_3)_2 \cdot 4H_2O$, ≥99.0%), zinc acetate ($Zn(OAc)_2$, 99.99%), zinc acetate dihydrate ($Zn(OAc)_2 \times 2H_2O$, 98%), sodium myristate (≥99.0%), sulfur (99.98%), ammonium sulfide solution ($(NH_4)_2S$, 40-48 wt. % in H_2O), selenium (99.99%), 1- octanethiol (≥98.5%), oleic acid (OA, 90%), oleylamine (OLA, 70%), ethanolamine (EA, ≥99%), 1-octadecene (ODE, 90%), n-hexane (≥97.0%), ethanol (absolute), methanol (≥99.7%), N-methylformamide (NMF, 99%), toluene (≥99.5%), acetonitrile (≥99.9 %), dimethyl sulfoxide anhydrous (DMSO, ≥99.9%), ethyl acetate (≥99.7%), poly (N, N′-bis(4-butylphenyl)-N,N′-bis(phenyl)-benzidine) (p-TPD) (Lumtec), poly(9-vinylcarbazole) (PVK), tetramethylammonium hydroxide (TMAH, 98%) and chlorobenzene (>98%), m-xylene (>98%) were obtained from Sigma Aldrich, and used with no further change. Poly (ethylene dioxythiophene): polystyrene sulfonate (PEDOT: PSS) was purchased from Osilla (AI 4083).

Cadmium myristate synthesis. Cadmium myristate was synthesized according to the previous recipes in the literature with no modification [140].

4.5 ML CdSe core NPLs synthesis. 4.5 ML CdSe core NPLs were synthesized according to a modified recipe reported in the literature [56]. First, 800 mg of cadmium myristate, 67 mg of Se and 60 mL of ODE were mixed in a three-neck flask, and the temperature was increased to 95 ˚C under vacuum. The flask maintained under vacuum for 30 minutes to remove oxygen and other volatile species. Then, under argon atmosphere, the

temperature was set to 237.5 ˚C and when the solution turned into golden yellow, at around 195 ˚C, 250 mg of $Cd(OAc)_2.2H_2O$ was swiftly added to the flask. The reaction maintained at high temperature for 7 min, and then 5 mL of OA was injected into the flask while the flask was quickly quenched in water. The solution was collected and mixed with hexane, and 4.5 ML CdSe core NPLs were separated from QDs and other populations of NPLs by addition of ethanol and centrifugation at 6000 rpm for 6 min. The final NPLs were redispersed in hexane and kept for further use.

4.5 ML CdSe/CdS core/crown NPLs synthesis. 4.5 ML CdSe/CdS core/crown NPLs were synthesized according to the published report in the literature with slight modifications [56]. First, the crown solution was made by mixing of 2.4 g of $Cd(OAc)_2.2H_2O$, 10 mL of ODE and 1.7 mL of OA. The solution was sonicated and stirred at high temperature of 150 ˚C, consecutively, until a milky and homogeneous solution was obtained.

For lateral growth of CdSe core with CdS crown, 4 mL of 4.5 ML CdSe core (with optical density (OD) of one at wavelength of 350 nm, when 100 µL of it is diluted in 3 mL of hexane) was precipitated via ethanol and centrifugation, and again redispersed in 1 mL of hexane. The core solution was put in a 50 mL flask alongside with 20 mL of ODE and 400 µL of OA, and the mixture was degassed at 90 ˚C for 30 min. Then, the flask was flushed with argon gas, and a mixture of 2.4 mL of crown solution and 400 mL of S-ODE (0.1 M) was injected into the flask. The temperature was set to 225 ˚C, with heating rate of 10 ˚C/min. When the temperature reached 225 ˚C, the flask was immediately quenched in water and the NPLs were collected and mixed with 15 mL of hexane. The solution was first centrifuged at 6000 rpm for 6 min to remove unstable and unwanted species, and later the NPLs were precipitated by the addition of ethanol and centrifugation. At the end, the CdSe/CdS core/crown NPLs were redispersed in hexane and kept for later use.

(CdSe/CdS)@(1-4 CdS) (core/crown)@(c-ALD shell) NPLs synthesis. c-ALD shelling of the NPLs has been carried out in accord with the reports in the literature and some minor modifications [56]. First, the batch of core/crown NPLs, which was produced from one crown synthesis, was precipitated by addition of ethanol and centrifugation, and then redispersed in 1 mL of hexane. The process was repeated for six times to remove all of the unreacted chemicals, especially cadmium acetate. Then, 1 mL of NMF was added to the solution, causing phase separation between NMF and hexane. After that, 75 μL of ammonium sulfide was added to the solution in order to cover the outer layer of the NPLs with S, leading to transfer of the NPLs to NMF. After 3 min of stirring, hexane was removed with a pipette, and the NPLs were precipitated by addition of extra toluene, acetonitrile and centrifugation. The NPL were redispersed in NMF, and the precipitation/redispersion has been carried out for extra 2 times. For growth of the cation, 2 mL of a solution of $Cd(NO_3)_2{\cdot}4H_2O$ in NMF (1 M) were added to the NPLs solution, and the solution was stirred for 15-30 min. Later, the NPLs were precipitated by addition of extra toluene, acetonitrile and centrifugation, and redispersed in NMF for 3 times. The procedure was repeated for each layer in order to obtain the desired number of c-ALD shells. The last precipitate was transferred to hexane by addition of 2 mL of OLA and stirring at 50 ˚C for 2 min, for a better ligand passivation.

(CdSe/CdS)@(1-4 CdS/ZnS, CdZnS) (core/crown)@(c-ALD shell/HIS) NPLs synthesis. The (CdSe/CdS)@(1-4 CdS) (core/crown)@(c-ALD shell) NPLs were used as seed for the final hot-injection shell (HIS). For each synthesis, 1 OD of the seed, 500 μL of OA, 3.5 mL of ODE, and 0.2 mmol of $Zn(OAc)_2$+$Cd(OAc)_2$ (with the $Zn(OAc)_2$/ $Cd(OAc)_2$ ratio of 4 to 1, for CdZnS HI shell, or 5 to zero for ZnS HI shell) was added to a three-neck 50 mL flask. The solution was degassed at room temperature for 1 h, and further degassed at 85 ˚C for 30 min. Then, 500 μL of OLA was added under N_2 gas, and the

temperature was set to 300 ˚C. When the temperature reached 160 ˚C, 4 mL of the solution of octanethiol-ODE (0.1 M) was started to be injected with the rate of 10 mL/h which was decreased to 4 mL/h after 240 ˚C. The flask was kept at 300 ˚C for 60-120 min, and then quenched in water. The solution was diluted with hexane and centrifuged to remove the unstable particles. The NPLs were isolated by addition of extra ethanol and centrifugation, and redispersed in hexane.

For thick shell NPLs, the whole process is the same except that the initial amount of cation was doubled, and the injected octanethiol-ODE was increased to 10 mL. The shell growth time was increased to 3-4 h with no further modification on the procedure.

ZnO synthesis. ZnO nanocrystal were synthesized according to the published protocol with slight modifications [132]. In a typical synthesis, 3 mmol of $Zn(OAc)_2 \times 2H_2O$ was dissolved in 30 mL of DMSO at room temperature. Then, 10 mL of a solution of TMAH-ethanol (0.55 M) was injected at the rate of 40 mL/h. The solution was kept on stirring at ambient temperature for 24 h. Afterward, ZnO NCs were precipitated by adding ethyl acetate and redispersed in ethanol. In order to improve the stability of NCs, 200 µL of EA were added to the solution, and it kept stirring for an hour. Finally, the ZnO NCs capped with EA ligands were precipitated by adding ethyl acetate, and then redispersed in ethanol.

LED fabrication. Prepatterned indium tin oxide (ITO) glass substrates with a sheet resistance of ≈20 $\Omega\ sq^{-1}$ washed by detergent, deionized water, acetone and isopropanol, sequentially in an ultrasonic bath for 15 min each. Then ozone plasma treatment carried out for 15 min in order to remove the remained organic residuals and modification of ITO's work-function. The PEDOT: PSS solution filtered through a 0.22 µm PTFE filter, then spin-coated in air at 4000 rpm for 45 s and baked at 140 ˚C for 30 min. Then, the

substrates were transferred to a nitrogen-filled glove box with O_2 < 0.1 ppm and H_2O < 0.1 ppm. Poly-TPD (in chlorobenzene, 8 mg/mL), PVK (in m-xylene, 5 mg/mL), NPLs (in toluene, 15 mg/mL) and ZnO (in ethanol, 25 mg/mL) were deposited layer by layer using spin-coating. Both poly-TPD and PVK were spin-coated at 3000 rpm for 45 s and baked at 110 ℃ for 20 min and 140 ˚C for 30 min, respectively. NPLs and ZnO were spin-coated at 2000 rpm for 45 s, baked at 60 ˚C for 20 min and then 90 ˚C for 20 min, respectively. Finally, in a thermal evaporator chamber at 3×10^{-6} mbar, 100 nm of Al was deposited with a shadow mask in order to create a 4.5 mm^2 active area. Then, inside the glovebox, the devices were encapsulated using UV-curable resin and encapsulation coverslips. All of measurements took place outside the glovebox.

NPLs characterizations. In solution optical characterizations performed in quartz cuvettes, and NPLs were diluted in hexane. Absorption and PL spectra were collected via Agilent Cary 60 UV-Vis Spectrophotometer and Varian Cary Eclipse at the excitation wavelength of 400 nm, respectively. Time-resolved photoluminescence (TRF) measurement carried out at excitation wavelength of 375 nm and repetition rate of 2.5 MHz, via Pico Quant FluoTime 200. Absolute PLQY of the NPLs were measured by the methodology reported previously in the literature at the excitation wavelength of 400 nm. Transmission Electron Microscopy (TEM) imaging has been carried out at 300 kV voltages using Tecnai G2 F30 microscope. The XRD diffraction pattern was obtained via drop casting and evaporation of the NPLs solution for a couple of time, and the measurement has been done with Panalytical Xpert Pro MPD.

Device characterization. EQE measurement was carried out by integrated sphere (Newport 819D-IS-5.3), computer-controlled source-meter (Agilent U3606A), and spectrometer (Ocean optics-QE Pro). Luminance measurement was carried out using

spectroradiometer (Konica-Minolta CS-2000) in air at room temperature. Cross-sectional images of the LEDs were obtained by cutting out a vertical slice of the device with focused ion beam (FIB), and scanning electron imaging.

3.3. Results and Discussion

First, we demonstrate the synthesis of the seed NPLs needed for the final HI shell coating. The seed needs to lead to the best possible performance in terms of PLQY and low defect sites and to be thick enough so that they can endure the harsh reaction conditions at high temperatures, which is necessary for boosting up the thickness effectively for longer emission peak wavelengths. Starting with 4.5 ML CdSe core as the base material, all the forthcoming peripheral or vertical layers would be grown upon it. The core would be in a sandwich-like structure in which it is surrounded by crown and shells with different compositions and band alignments.

The absorption and emission spectra of CdSe core and CdSe/CdS core/crown are depicted in Figure 3.1a and b, respectively, with their fluorescence decay curve presented in Figure 3.1c (The properties are summarized in Table 3.1). The first and second excitonic absorption peaks of the core are located at 510 and 479 nm corresponding to heavy and light hole transitions, respectively, with the emission peak is centered at 512 nm. A multiexponential decay function was fitted for each decay curve and the lifetime components were extracted from the best fit. CdSe/CdS core/crown NPLs exhibit an amplitude-averaged fluorescence lifetime (τ_{av}) of ≈ 3.6 ns, which is more than one order of magnitude longer than that of CdSe core. The multi-exponential decay behavior is an indicative of different channels with the fastest component usually attributed to the nonradiative decay pathway [141]. Addition of the CdS crown also causes a slight red-shift of the emission and absorption of CdSe core, which is due to the change in the

dielectric constant and increase of the lateral size of the NPLs. The outermost layers of NPLs are passivated with a metal layer [43]. Incomplete passivation of the surface causes the charge carrier to be trapped and reduces emission, which decreases the PLQY [123]. For the CdSe/CdS core/crown NPLs, the peripheral surface of the core is effectively passivated with the crown, which in turn reduces the trapping and increases the PLQY. It is known that direct growth of shell layers on top of the core leads to reduced PLQY of the NPLs, while the lateral passivation with a wider bandgap crown enhances PLQY [56]. For this reason, before c-ALD coating, the lateral sides of the CdSe core is passivated with a layer of CdS crown [56], [142]. Deposition of a medium-sized crown leads to a three-fold increase in the PLQY of the NPLs, which also manifests itself in longer recombination lifetime. Moreover, the growth of CdS crown increases the absorption cross-section of the NPLs at shorter wavelengths that act as an antenna for enhanced exciton formation, contributing to radiative recombination through exciton funneling into the core [143], [144].

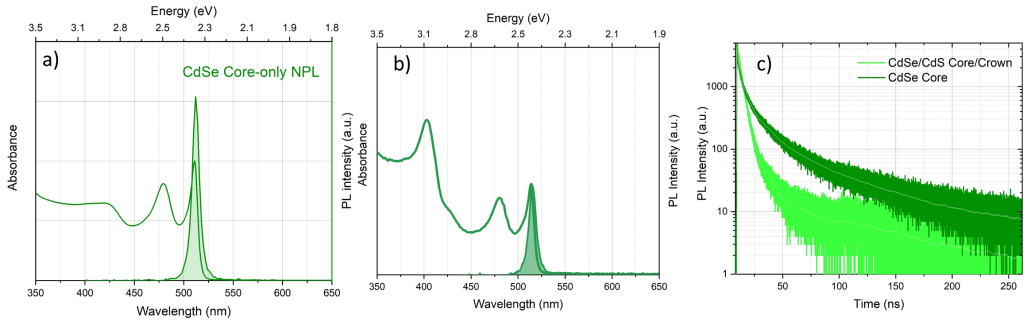

Figure 3.1. Absorption and PL spectra of (a) 4.5 ML CdSe core, and (b) 4.5 ML CdSe/CdS core crown NPLs. (c) TRF decay curve of CdSe core and CdSe/CdS core/crown NPLs. Copyright 2022 WILEY-VCH Verlag GmbH & Co. KGaA, Weinheim.

Table 3.1. The summary of the optical properties of the CdSe core and CdSe/CdS core/crown NPLs.

Sample	PL emission wavelength (nm)	FWHM (nm)	PLQY (%)	Amplitude average lifetime (ns)
CdSe Core	512.3	8.3	31.0	0.2
CdSe/CdS Core/Crown	515.1	9.1	92.2	3.6

Figure 3.2a depicts a schematic of all the steps with the main chemicals that are involved in formation of crown or shells. The size and alignment of the domains determine the wavefunctions of the electron and hole, which is critical for tuning the peak emission wavelength. Figure 3.2b demonstrates the bulk band alignment of CdSe, CdS and ZnS, three compounds that participate in the formation of the final targeted heterostructure. The carrier wavefunctions leak into the shell, however, as it is centered around the core and all of the other layers have wider bandgaps, which energetically drives electron and hole pair to recombine through the lowest energy route, it is still expected that the final electron and hole recombination to occur in the core.

It was shown previously that with the growth of CdS or ZnS HI shell on 4ML CdSe core reaching emission peak above 670 nm is not possible [124], [125]. This in part is due to the lattice mismatch between different domains, which increases upon thickening of the shell. At the high growth temperature of 300 ˚C, the extra energy induced by lattice mismatch may be reduced, however the tendency for growth decreases. To overcome the thickness limitation, it is possible to include a buffer layer of CdS shell using c-ALD method, which has a much smaller lattice mismatch of 3.9%, compared to 12% for ZnS [145]. Moreover, the carriers wavefunction, especially of electron with a lower effective mass and a smaller band offset, relaxes into the CdS shell and causes a huge red-shift upon deposition of each layer. The red-shift in the case of (core/crown)@shell is larger than the core/shell, which is due to the change in dielectric constant [56]. The small band

offset between the conduction band of CdSe and CdS also facilitates the electron wavefunction propagation leading to a quasi-Type-II structure (Figure 3.2b). However, passivation of the outermost layers of NPLs with ZnS effectively increases the PLQY [125] owing to the enhancement of exciton confinement.

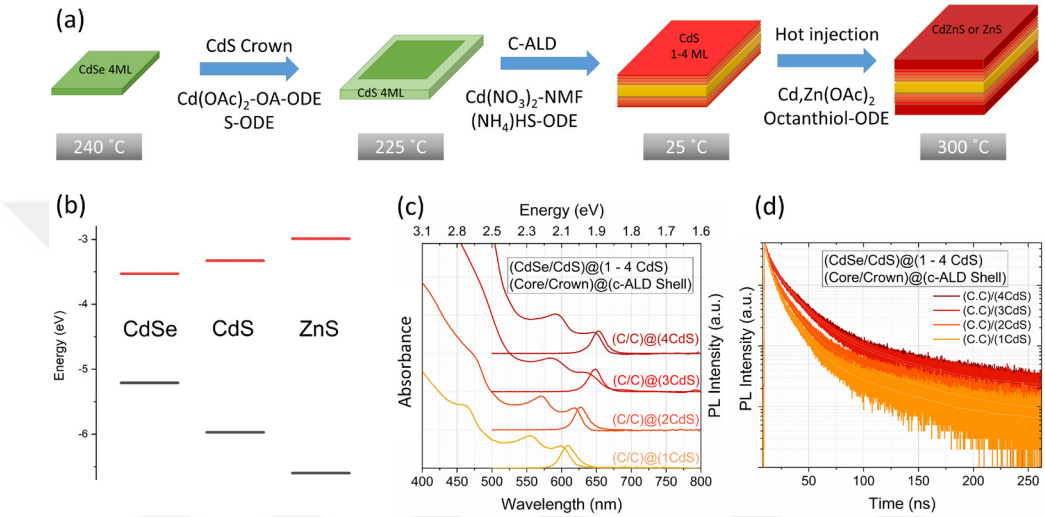

Figure 3.2. (a) A schematic of the synthesis pathway toward the final hetero-NPLs. First, bare CdSe core was laterally passivated with CdS crown, and then the c-ALD buffer layers were grown in the thickness direction to prepare the seeds. These seeds were used for the final HI shell coating. The thick NPLs were treated for longer times and using higher precursor concentrations during the hot injection. (b) Band alignment of CdSe, CdS and ZnS. The numbers were extracted from ref. [146] and ref. [31]. (c) Absorbance and PL spectra, and (d) TRF decay curves of (CdSe/CdS)@(1-4 CdS) (core/crown)@(c-ALD shell) seed NPLs. Copyright 2022 WILEY-VCH Verlag GmbH & Co. KGaA, Weinheim.

Herein, for the next step of the seed preparation, 1 to 4 monolayers of CdS shell were deposited on top of the core/crown NPLs with c-ALD method. This (core/crown)@(c-ALD shell) was later treated as the seed for hot injection, so that the thickness increases

effectively and the core was passivated from all sides. Figure 3.2c and d show the absorption and emission spectra and decay curves of (CdSe/CdS)@(1-4 CdS) (core/crown)@(c-ALD shell) NPLs, respectively. The absorption peak of CdS crown, which is originally located at 406 nm, red-shifts and disappears upon further c-ALD CdS shell growth, while the relaxation time increases from 3.6 ns for CdSe/CdS core/crown to 12.2 ns after deposition of 3 and 4 MLs of c-ALD CdS shell (Table 3.2) owing to the higher spatial freedom of the excitons. The PLQY of the NPLs drops upon increasing the number of the c-ALD shells, which is due to poor passivation and defected structure of the NPL during the room temperature process. This also shows its effect in the same τ_{av} for 3 and 4 ML of CdS. However, the thickest NPLs exhibit a large red-shift to 652 nm in the emission peak with a FWHM of 22.1 nm.

Table 3.2. Optical properties of (CdSe/CdS)@(1-4 CdS) (Core/Crown)@(c-ALD Shell) NPLs. Copyright 2022 WILEY-VCH Verlag GmbH & Co. KGaA, Weinheim.

Sample	PL emission wavelength (nm)	FWHM (nm)	PLQY (%)	Amplitude average lifetime (ns)
(C/C)@(1CdS)	609.0	25.6	41.7	7.2
(C/C)@(2CdS)	627.3	22.2	46.8	9.4
(C/C)@(3CdS)	648.0	22.3	43.0	12.2
(C/C)@(4CdS)	652.6	22.1	31.2	12.2

In the next step, the (CdSe/CdS)@(1-4 CdS) (core/crown)@(c-ALD shell) NPLs were used as the seed for the upcoming hot injection shell growth, in order to increase the thickness. For the hot injection shell layer, two compositions of ZnS and CdZnS were chosen. As CdS has a narrower bandgap than ZnS, tuning the emission peak over longer wavelengths seems to be easier. However, CdS shell yields a lower PLQY than ZnS and would compromise the performance of the NPLs [125].

Figure 3.3a and d present the absorption and emission spectra of (CdSe/CdS)@(1-4 CdS/ZnS) and (CdSe/CdS)@(1-4 CdS/CdZnS) (core/crown)@(c-ALD shell/HIS) heterostructures, respectively. For all of the samples, the first and second excitonic peaks are in place, while their position is red-shifted compared to the initial seeds. This was predictable as the vertical growth of the shell would further loosen the tight confinement in the NPLs. The characteristic absorption peak of CdS crown also red-shifts toward higher wavelengths. This peak is obvious for the first two monolayers of c-ALD CdS shell when the HI shell is ZnS, but starts to fade away for CdZnS HIS even for 1 monolayer of CdS. The CdS crown peak is more prominently obvious for (CdSe/CdS)@(1-2 CdS/ZnS) NPLs than those of the (CdSe/CdS)@(1-2 CdS/CdZnS) NPLs, which is due to a sequence of events: During the hot injection shell growth, the outermost layers of the NPLs tend to etch in the initial stages [130], which is mainly due to incomplete decomposition of $Cd(OAc)_2$ or $Zn(OAc)_2$ in the presence of oleylamine (OLA) that accelerates the process [146].

Prior to the activation temperature of 1-octanthiol at around 260 ˚C, the extra dissolved Cd atoms with much higher chemical activity than Zn, will grow laterally on the seed NPLs, enlarging the lateral size and increasing its absorption in the blue region, at the cost of decreasing the thickness. Moreover, at higher temperatures (>280 ˚C), Cd atoms can contribute to the shell formation faster than Zn atoms, hence making a thicker shell that covers the crown. While the peak absorbance ratio (A_{crown}/A_{core}) for CdSe/CdS core/crown and (CdSe/CdS)@(1CdS) (core/crown)@(c-ALD shell) is approximately 1.7, the ratio significantly increases to 6 for (CdSe/CdS)@(1CdS/ZnS) (core/crown)@(c-ALD shell/HI shell) NPLs and drops to 5.5 for 2 MLs of buffer layer. This observation further emphasizes the role of the CdS crown which, alongside with side passivation, can act as the protective layer that prevents etching of the core during the hot injection shell growth at the expense of its partial dissolution.

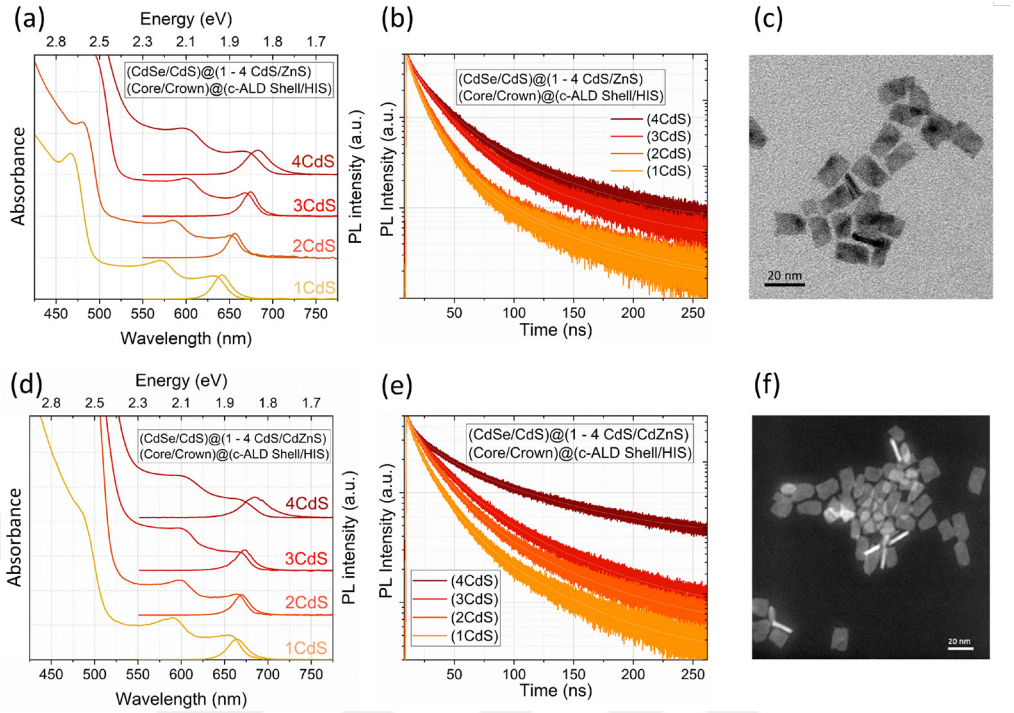

Figure 3.3. (a) Absorbance and photoluminescence spectra and (b) TRF decay curves of HI shell NPLs with a generic heterostructure of (CdSe/CdS)@(1-4 CdS/ZnS) (core/crown)@(c-ALD/HI shell). (c) TEM image of the NPLs with 4 MLs of CdS buffer layers capped with ZnS HI shell showing a rectangular shape. (d) Absorbance and PL spectra and (e) TRF decay curves of HI shell NPLs with a generic heterostructure of (CdSe/CdS)@(1-4 CdS/CdZnS) (core/crown)@(c-ALD/HI shell). (f) TEM image of NPLs with 4 MLs of CdS buffer layers and final CdZnS HI shell. The shape of the NPLs is generally rectangular with less defined edges compared to the NPLs capped with ZnS HI shell. For both sets of samples, the growth time at 300 ˚C was between 1-2 h and the amount of Cd, Zn and injected S precursors were limited. Copyright 2022 WILEY-VCH Verlag GmbH & Co. KGaA, Weinheim.

Table 3.3 list the emission peaks, FWHM and PLQY of the samples with CdZnS and ZnS HI shell. With larger conduction band offset energy of ZnS, the red-shift for ZnS HI shell is less prominent than the CdZnS HI shell. Moreover, the tendency for ZnS to grow

is weaker than that of CdS, which means that under the same conditions (precursor concentration, growth time, etc.), a thinner shell of ZnS will be deposited, a problem that would be further amplified by a higher lattice mismatch between CdSe core and ZnS shell in contrast to CdS shell. For the samples that are coated with ZnS, the emission wavelength covers a broad range from 641 to 679 nm while for CdZnS HI shell the emission peak is between 665 and 686 nm. The convergence of the emission peak wavelength for two different HI shells for the increasing number of CdS buffer layers implies that the growth rate of ZnS enhances as a result of the lower lattice mismatch. PLQY for ZnS HI shell remains above 80% (at a maximum of 97%) but it drops for CdZnS HI shell, which is an indicative of low cation diffusion at this growth time/temperature scale that maintains the outer shell layer for both set of NPLs. For ZnS HI shell NPLs, the outer shell layer is covered with ZnS that has a higher conduction band offset and prevents the electron wavefunction to reach the surface.

Table 3.3. Optical properties of (CdSe/CdS)@(1-4 CdS/ZnS) (Core/Crown)@(c-ALD/HI Shell) and (CdSe/CdS)@(1-4 CdS/CdZnS) (Core/Crown)@(c-ALD/HI Shell) NPLs. Copyright 2022 WILEY-VCH Verlag GmbH & Co. KGaA, Weinheim.

Sample	PL emission wavelength (nm)	FWHM (nm)	PLQY (%)
(C/C)@(1CdS/ZnS)	641.2	23.7	97.0
(C/C)@ (2CdS/ZnS)	656.3	20.2	94.8
(C/C)@ (3CdS/ZnS)	674.7	20.4	83.5
(C/C)@ (4CdS/ZnS)	679.3	26.8	80.0
(C/C)@(1CdS/CdZnS)	664.6	25.7	81.5
(C/C)@(2CdS/CdZnS)	669.9	21.5	70.8
(C/C)@(3CdS/CdZnS)	672.8	23.0	46.6
(C/C)@(4CdS/CdZnS)	685.6	34.6	36.4

Figure 3.3b and e show the decay curve of the samples. The average lifetimes (Table 3.4) of both samples increase with the shell thickness due to the expansion of electron-hole

distance, with ZnS HI shell NPLs exhibiting lower τ_{av} than CdZnS HIS NPLs. This confirms the retention of ZnS outer layer with an increased spatial overlap of the carriers due to the large band offsets. The TEM images (Figure 3.3c and f) for NPLs with 4 ML CdS buffer layer show that they maintained their 2D shape, with one of the facets usually grown to a higher extend that prohibits the NPLs to have a perfect rectangular shape. CdZnS HI shell NPLs have a larger lateral size of 10.8±0.7 × 19.7±0.7 nm^2 with a thickness of 3.8±0.3 nm than ZnS HIS NPLs of 9.9±0.8 × 16.5±0.4 nm^2 with a lower thickness of 2.8±0.2 nm. The imperfect shape of NPLs is due to the limited growth time and the chemicals in the reaction that inhibits the shape focusing of the NPLs. For the thick shell samples, we will see that by providing enough time and reactants the shape evolves toward a more uniform rectangle.

Table 3.4. TRF decay components of (CdSe/CdS)@(1-4 CdS/ZnS) (Core/Crown)@(c-ALD/HI Shell) NPLs (blue shade) and (CdSe/CdS)@(1-4 CdS/CdZnS) (Core/Crown)@(c-ALD/HI Shell) NPLs (red shade). Copyright 2022 WILEY-VCH Verlag GmbH & Co. KGaA, Weinheim.

Sample	τ_1 (ns)	τ_2 (ns)	τ_3 (ns)	$\frac{A_1.\tau_1}{\sum A_i.\tau_i}$ (%)	$\frac{A_2.\tau_2}{\sum A_i.\tau_i}$ (%)	$\frac{A_3.\tau_3}{\sum A_i.\tau_i}$ (%)	Amplitude average lifetime $\frac{\sum A_i.\tau_i}{\sum A_i}$ (ns)
(1CdS)	5.0	15.6	67.8	13.8	62.6	23.6	14.1
(2CdS)	5.4	16.5	73.1	11.2	65.7	23.1	15.7
(3CdS)	5.2	18.7	56.6	4.1	54.6	41.3	22.6
(4CdS)	2.8	18.1	55.6	2.1	41.7	56.1	24.6
(1CdS)	4.9	16.5	53.8	5.5	51.9	42.7	22
(2CdS)	9.4	22	63.5	8.2	46.5	45.4	27.1
(3CdS)	3.9	21.5	62.9	1.9	38.3	59.9	31.2
(4CdS)	3.2	17.5	79.2	1.4	15.6	83	42.2

The abovementioned heterostructure allows for the extension of emission peak to around 680 nm with acceptable properties. However, in order to reach a peak emission of 700

nm or above, extra addition of cation and anion precursors and extended growth time are required. In this regard, the same (core/crown)@(c-ALD Shell) seeds that were used before were prepared while the growth time was increased to 180-240 min, in comparison to 60-120 min for the previous samples. The recipe was also modified with the same composition of the hot injection shell, but the amount of the initial Zn and Cd precursors were doubled. Moreover, the anion precursor of 1-octanthiol was continued to be injected up until 10 mL (See the Experimental for the details).

The first effect of the altered recipe is modification of the shape of the NPLs, shown in Figure 3.4a and c. Compared to thin hot injection shell NPLs, the thick NPLs have much sharper edges with a well-defined square shape. The lateral size of the NPLs decreases along the longer dimension as a result of etching while it increases along the shorter one. For (CdSe/CdS)@(4CdS/CdZnS) (core/crown)@(c-ALD shell/(HI shell) NPLs, the lateral size is 13±1 × 13±1 nm^2 and the vertical thickness is 4.8 nm. Compared to thin shell NPLs, TEM images of thick shell NPLs show partial dissolution of the longer dimension that can recrystallize on the shorter sides, if enough time is given. Comparatively, the lateral size distribution increases for an ensemble of the NPLs, as the recrystallization also happens in vertical direction, due to Ostwald ripening [43]. This suggests a dual shell growth mechanism, in which part of the cations and anions are provided from the precursor and the other part is the result of opening windows during each cycle of Ostwald ripening, as was discussed elsewhere [43]. Figure 3.4b shows a TEM side image of the thick NPLs, with an obvious contrast between the core and the shell. The CdSe core and CdS crown contain heavy element of Cd which has a higher contrast than ZnS such that, even with partial disintegration of periphery of the NPLs, the core remains intact in its place.

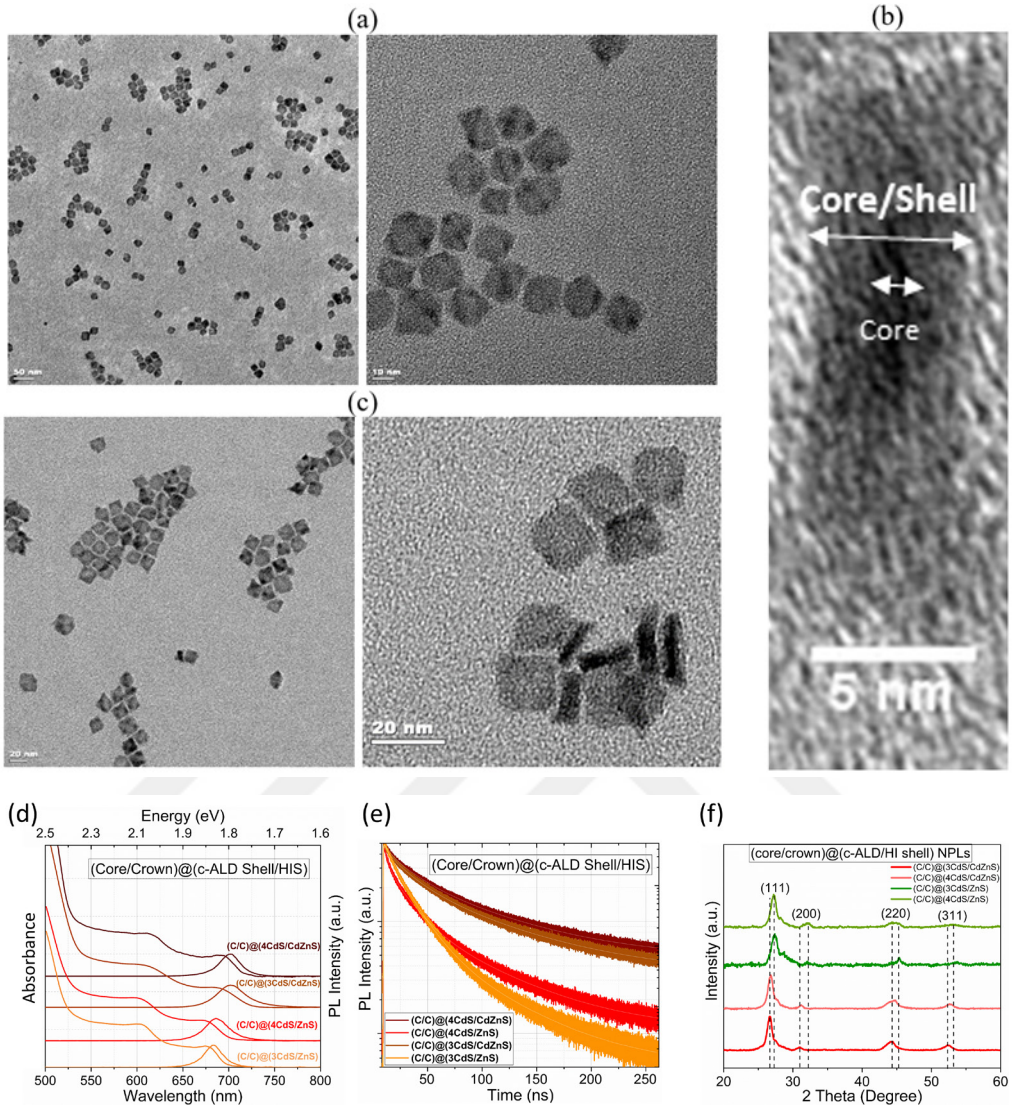

Figure 3.4. TEM images of thick NPLs that were treated with higher concentrations of the precursors for a prolonged time: (a) NPLs with 3 ML of CdS buffer layer, with a heterostructure of (CdSe/CdS)@(3CdS/CdZnS) (core/crown)@(c-ALD shell/(HI shell), (b) and (c) NPLs with 4 MLs of CdS buffer layer, with a heterostructure of (CdSe/CdS)@(4CdS/CdZnS) (core/crown)@(c-ALD shell/(HI shell). For both of the samples the shape has become more symmetric compared to the previous rectangular NPLs. (d) Absorbance and PL spectra, (e) TRF decay curves, and (f) X-ray diffraction patterns of thick (core/crown)@(c-ALD/HI shell) NPLs. All of the samples were treated

between 3-4 h for the shell growth at 300 ˚C and the amount of Cd and Zn precursors were doubled in comparison to thin shell NPLs. Copyright 2022 WILEY-VCH Verlag GmbH & Co. KGaA, Weinheim.

Figure 3.4d shows the absorption and emission spectra of (core/crown)@(c-ALD shell/thick HIS) for samples that have 3 or 4 monolayers of CdS c-ALD shell, and thick HIS of either ZnS or CdZnS. While reaching longer wavelength emissions is not feasible with hot injection shell growth on mere CdSe core, it is possible to go beyond 700 nm emission peak, closer to the theoretical bulk bandgap of CdSe, if the hot injection is performed on (core/crown)@(c-ALD shell) seeds. As the shell grows bigger, the emission bandwidth broadens and PLQY decreases. The loosened exciton confinement due to the increased thickness is partially responsible for this broadening. However, due to Ostwald ripening, the lateral/thickness size distribution may increase and result in small inhomogeneous broadening. Also, as the thickness increases the probability of formation of defects with surface or strain nature is increasing, which suppresses the PLQY. Figure 3.5 shows the absorption and emission spectra of a test sample with 2 MLs of intermediate c-ALD shell. The sample was treated with the same thick HI shell growth process; however, the growth time was substantially increased to 360 min so that an emission peak near 700 nm becomes achievable. The emission spectrum is extremely broadened with a FWHM of 52 nm, and the PLQY also drops below 2%. This is a further emphasis on the role of the intermediate c-ALD shell, which would alleviate the lattice mismatch strain between different domains. The long shell growth time at high temperature also facilitates the diffusion and reorganization of the cations, as was previously shown [130]. During this time, the distribution of Zn and Cd changes and makes a gradient alloyed structure in the shell, where the strain is reduced and the outermost layer is composed of mostly ZnS.

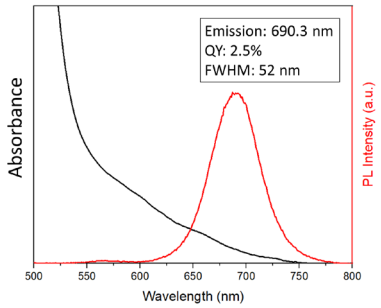

Figure 3.5. Absorbance and photoluminescence spectra of thick-shell (CdSe/CdS)@(2CdS/CdZnS) (Core/Crown)@(c-ALD/HI Shell) NPLs. Copyright 2022 WILEY-VCH Verlag GmbH & Co. KGaA, Weinheim.

Figure 3.4e shows the decay curve of the thick NPLs (for which the decay components are listed in Table 3.5). Two sets of NPLs that are coated with final CdZnS HIS have a slower decay rate than the ZnS coated NPLs, in accordance with their longer emission wavelength and thickness. For thick ZnS HIS NPLs, the average lifetime does not show a significant change in spite of their thicker shell, which confirms the diffusion and reorganization of Zn to outer layers. Moreover, the pure ZnS shell is more susceptible to generating defect sites because of its lower affinity to bind to the surface, which also reflects its effect on lower PLQY. The best optimized sample that emits at 701 nm is (core/crown)@(4CdS/CdZnS) NPLs with a PLQY of 88 % and a FWHM of 26 nm. Its average lifetime is higher than thin NPLs of the same class but yet almost equal to NPLs with 3 ML of buffer layer. In this sample, the interplay among the shell growth, surface passivation and cation reorganization preserve the properties and thickness. The multi-exponential decay behavior of this sample mainly originates from a possible nonradiative channel, with usually the fastest decay rate. It was previously shown that even for core/shell NPLs possessing near-unity PLQY (close to but less than 100%) it has not been possible to reach a mono-exponential decay, however for these samples the share of the fast decay channel would be very low [125]. In our best sample, less than 1% of

the recombination share is coming from the fastest channel (4.4 ns) which has a value in the order of previously reported nonradiative channel of core/shell NPLs [31]. The rest 99% of the emission contribution is coming from the two longest components (78.3 ns and 19.8 ns) (Table 3.5), which have far higher characteristic lifetime rates than the usual nonradiative channels. This indicates reasonably high surface passivation, suppressing otherwise strong nonradiative channels possibly originating from the surface traps to a good extent.

Table 3.5. TRF decay components of thick-shell NPLs. Copyright 2022 WILEY-VCH Verlag GmbH & Co. KGaA, Weinheim.

Sample	τ_1 **(ns)**	τ_2 **(ns)**	τ_3 **(ns)**	$\frac{A_1.\tau_1}{\sum A_i.\tau_i}$ **(%)**	$\frac{A_2.\tau_2}{\sum A_i.\tau_i}$ **(%)**	$\frac{A_3.\tau_3}{\sum A_i.\tau_i}$ **(%)**	**Amplitude average lifetime** $\frac{\sum A_i.\tau_i}{\sum A_i}$ **(ns)**
(C/C)@ (3CdS/ZnS)	9.1	19.5	57.1	4.8	51.6	43.4	25.3
(C/C)@ (3CdS/CdZnS)	4.9	23.5	87.3	0.9	19.9	79.2	51.7
(C/C)@ (4CdS/ZnS)	5.2	18.7	56.6	4.0	54.6	41.3	22.6
(C/C)@ (4CdS/CdZnS)	4.4	19.8	78.3	0.8	13.7	85.5	50.8

The X-ray diffraction pattern in Figure 3.4f shows that the diffraction peak position of the NPLs match with bulk CdS and ZnS, with a slight increase in the diffracted angle when the ZnS shell is coated, which is due to shell alloying. Since all of the domains have the same crystalline structure of zinc blende and all the NPLs consist of a dominantly thick shell, all of the NPLs have a similar diffraction pattern with a slight shift of the peaks. ZnS has the smallest lattice constant compared to CdSe and CdS, hence the ZnS HIS NPLs show a small emergence of ZnS peak at approximately 2θ of 29˚,

near to the bulk peak of ZnS for stronger plane of (111), because of their higher probability of pure and thicker ZnS shell formation. X-ray photoelectron spectroscopy (XPS) presented in Figure 3.6 provides information about the binding energy of cadmium, zinc, selenium and sulfur and their chemical states. No other species is formed through thick shelling, or otherwise they were successfully filtered out through standard cleaning procedure. Neither Se nor S is oxidized after the synthesis, as may be the case for the chalcogenides.

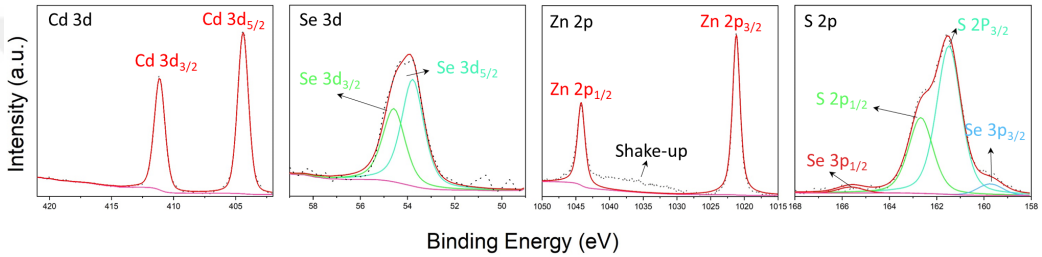

Figure 3.6. XPS spectra of thick (core/crown)@(4CdS/CdZnS) NPLs. The spectra for Cd, Se, Zn and S were fitted according to the orbital splitting of Cd3d, Se3d, Zn2p and S2p. Elemental binding energies were measured, showing no participation of the elements in other unwanted states. Copyright 2022 WILEY-VCH Verlag GmbH & Co. KGaA, Weinheim.

As discussed above, the synthesized CdSe-based NPLs present a high PLQY and a narrow FWHM in the deep-red spectral region. In the final section, CQW-LEDs based on these NPLs were prepared to confirm their outstanding electroluminescence properties. The CQW-LEDs were fabricated using our deep-red NPLs in the device configuration of indium tin oxide (ITO)/ poly(3,4-ethylenedioxythiophene) polystyrene sulfonate (PEDOT:PSS) / Poly(N,N'-bis-4-butylphenyl-N,N'-bisphenyl)benzidine (poly-TPD)/Poly(9-vinylcarbazole) (PVK)/NPLs/zinc oxide (ZnO)/Al (Figure 3.7a). In Figure 3.7a, the energy levels for ZnO were extracted from the literature [147] and for the CQWs

were calculate directly from the XPS measurement based on a published method (the details of which is given in the Experimental Section) [148].

Figure 3.7b shows the cross-sectional image of the resulting LED device. Due to poor contrast between ZnO and thick NPLs layer, they cannot be distinguished from each other. In this device structure, ITO is employed as the anode, PEDOT: PSS as the hole injection layer (HIL), poly-TPD, PVK as the co-hole transport layer (co-HTL), NPLs as the emitting layer (EML), ZnO as the electron transport layer (ETL), and Al as the cathode contact. The co-HTL, consisting of poly-TPD/PVK, is designed to benefit from both the high hole mobility provided by poly-TPD (1×10^{-4} $cm^2 V^{-1} s^{-1}$), and deep highest-occupied-molecular-orbital (HOMO) energy level (-5.8 eV) provided by PVK [149]. Using this architecture, the stepwise energy level alignment between ITO and HIL/HTL ensures an efficient hole injection into the EML (Figure 3.7a).

In an all-in-solution LED structure, ZnO nanocrystals are commonly used as ETL. It is synthesized via easy in-solution process at ambient temperature and without the need of any specific condition. Their relatively high electron mobility and proper energy level allow efficient electron injection into the EML [150], [151]. However, when only poly-TPD or PVK is used as the HTL, the hole injection would not be as high as that of the electrons through ZnO layer, which may cause charge imbalance in the EML lead to increased nonradiative Auger recombination [152]. To address this problem, we used poly-TPD/PVK as the stepwise co-HTLs, which allows for a better charge balance.

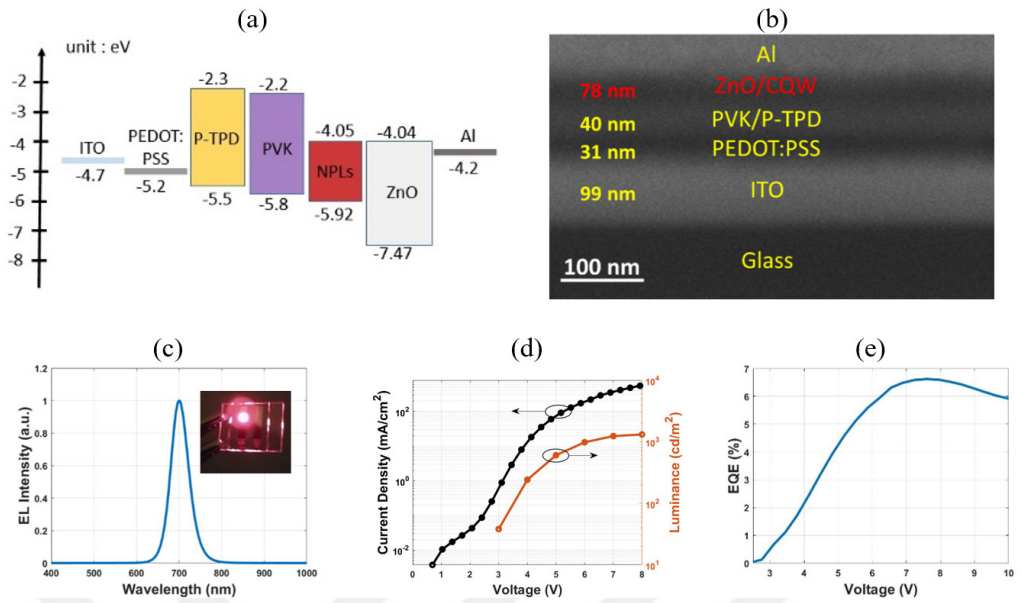

Figure 3.7. (a) LED device structure and flat band energy level diagram. The values for NPLs energy levels were measured directly from the XPS measurement according to the method used previously [148]. The energy levels for ZnO were extracted from the literature [147] and those of other layers were taken from the catalogs of their materials. (b) Cross-sectional scanning electron microscopy image of the device showing the layers with different contrasts. (c) Electroluminescence spectrum at an applied bias of 8 V, (d) current density and luminance versus voltage, and (e) EQE versus driving voltage, all for the deep-red emitting CQW-LED with (core/crown)@(4CdS/CdZnS) NPLs as the active material. Copyright 2022 WILEY-VCH Verlag GmbH & Co. KGaA, Weinheim.

Figure 3.7c presents the normalized electroluminescence of the deep-red CQW-LED with one symmetric peak centered around 701 nm, which is the deepest red CQW-LED reported in the literature to our knowledge. The device performance of the CQW-LED are shown in Figure 3.7d and e. The turn-on voltage (Von) of our CQW-LED is ~2.4 V and the maximum power efficiency of it is 21.3 lm/W. The current density-voltage (black) and luminance-voltage (orange) graphs show steady increase with a maximum

brightness level of 1300 cd m^{-2} at the operating voltage of 8 V, and the maximum EQE of 6.8 % was achieved at the applied voltage of 7.5 V. Another CQW-LED devices that was fabricated from the heterostructure of (core/crown)@(4CdS/ZnS) exhibits an EL peak centered around 689 nm with an EQE of 5.3% (Figure 3.8). The results are a clear proof of capability of these NPLs as the active material for longer wavelength electroluminescent LEDs.

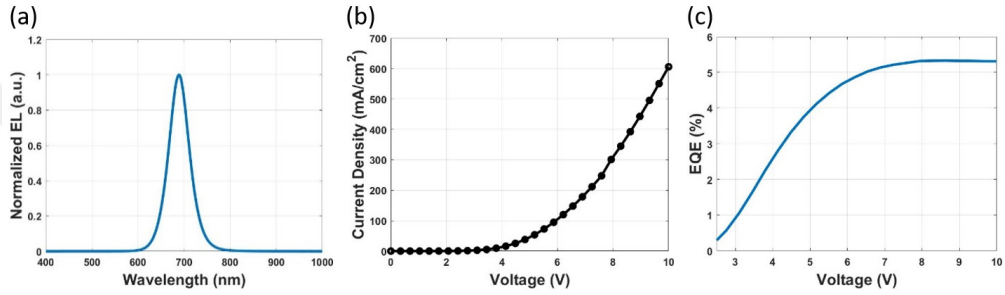

Figure 3.8(a) Electroluminescence spectrum (λ_{EL} = 689 nm) at V_{app} of 10 V, (d) Current density versus voltage, and (e) EQE versus driving voltage, for deep-red emitting CQW-LEDs with (C/C)@(4CdS/ZnS) NPLs as active material. Copyright 2022 WILEY-VCH Verlag GmbH & Co. KGaA, Weinheim.

As discussed before, the NPLs reported to date emit in the visible range of the light; hence no report of the electroluminescence properties of NPLs at longer wavelengths can be found. However, the peak EQE of our device surpasses many of the best reported nanomaterials emitting in the vicinity of 660 nm to 740 nm [134], [153]. Table 3.6 lists the performance of other types of LEDs with different active materials of mainly perovskites. Considering our previous report on CdSe-based CQW-LEDs [50]. our device in this current work demonstrates widely extended spectral tunability into the deep-red region, along with an excellent EQE, which outcompetes the perovskite-LEDs in terms of the performance in this spectral range.

Table 3.6. List of the LEDs based on the colloidal nanocrystals emitting in the vicinity of 700 nm. Copyright 2022 WILEY-VCH Verlag GmbH & Co. KGaA, Weinheim.

Emitting layer	λ_{EL} (nm)	Turn on voltage (V)	Luminance (cd m^{-2})	EQE (%)	Ref.
PEO: $(BA)_2(Cs)_{n-1}Pb_nI_{3n+1}$	680	3	1392	6.23	[154]
$CsPb_{0.64}Zn_{0.36}I_3$	682	2	2202	15.1	[155]
$CsPbI_3$	682	2.8	210	8.65	[156]
$CsPbI_3$	683	-	1100	7.3	[157]
$CsPbI_3$	686	3.9	14725	13.7	[158]
$CsPbI_3$	688	4.5	748	5.02	[159]
$CsPbI_3$	688	1.9	435	7.25	[160]
$NCPI_6Cl$	689	2	440	3.7	[161]
$CsPbI_3$	690	2.1	<600	<6	[155]
$CsPbI_3$	690	>3	1444	14.08	[162]
Sr^{2+} doped $CsPbI_3$	691	8	1152	13.5	[163]
$CsPbI_3$/PbS	691	1.9	1050	11.8	[164]
$PA_2CsPb_2I_7$-$CsPb(Br,Cl)_3$	693	-	-	0.22	[165]
$(NMA)_2Cs_{n-1}PbnI_{3n+1}$	694	1.9	732	7.3	[166]
$CsPbI_3$	698	2.2	206	5.7	[167]
$(BA)_2(MA)_2Pb_3I_{10}$	700	2.7	214	2.29	[168]
$Cs_xFA_{1-x}Pb(Br_{1-y}I_y)_3$	735	3	-	5.9	[153]
PhPr-Si QD	735	2.2	-	6.2	[169]
(CdSe/CdS)@(4CdS/CdZnS) (core/crown)@(c-ALD/HIS)	701	2.4	1300	6.8	This work

3.4. Summary

In summary, a systematic pathway was designed to increase the thickness of NPLs and push the emission peak wavelength to extend the range of tunability while maintaining the excellent properties of the NPLs. Unlike the conventional HI method where CdSe core is used directly as the seed, here we first synthesized thick NPLs seeds that contain a passivating medium-size CdS crown, and then through consecutive c-ALD cycles, CdS shell was grown on top of them. This strategy is proved to be effective for the growth of final HI shell, as it can overcome the barrier that may hinder the deposition of extra shell

layers with a minimum increase of the defect density and incoherent shell growth. The interplay between the lower bandgap CdS and the surface passivation of ZnS make it possible to find the best tradeoff between the tunability and properties. It was shown that by alloying the HI shell from ZnS to CdZnS it is possible to reach longer wavelengths while reducing the surface passivation effect through the high bandgap ZnS. Our best performance NPLs emits at 701 nm with PLQY of 88 % and FWHM of 26 nm. At the end, the LED device with mentioned structure was fabricated with the thick NPLs as the active material, which exhibits the highest EQE of 6.8 % at the emission wavelength of 701 nm. These results should encourage further investigation of such advanced heterostructures of NPLs into the deep-red to near-infrared high-performance LEDs based on II-VI semiconductors, which can possibly compete with other types of semiconductor LEDs.

Chapter 4

Gradient Multi-crown Type-II Heteronanoplatelets

This chapter of the thesis is based on the publication "Gradient Type-II CdSe/CdSeTe/CdTe Core/Crown/Crown Heteronanoplatelets with Asymmetric Shape and Disproportional Excitonic Properties" F. Shabani, P. L. H. Martinez, N. Shermet, H. Korkut, I. Sarpkaya, H. Dehghanpour Baruj, S. Delikanli, F. Isik, E. G. Durmusoglu, H. V. Demir, Small 19 (11), 2205729 (2023). Reprinted with permission from [51]. Copyright 2023 WILEY-VCH Verlag GmbH & Co. KGaA, Weinheim.

4.1. Motivation

Type-II heterostructures of the semiconductor NPLs are an interesting electronic group of NPLs that provide an excellent platform for exceptional properties, such as long lifetime PL, huge stokes shift, PL wavelength tunability, and broad emission spectra, that are not possible to achieve through type-I heterostructures [20], [170]. The fundamental feature of these type-II NPLs originates from the spatial separation of the carriers to

distinct domains, in which the emission happens through radiative recombination of the electrons and holes at the interface [49], [171]. To obtain this electronic structure, both the valance and conduction band of one domain must be either on a higher or lower energy level than the adjacent domain [172], [173]. In this regard, electron wavefunction mostly resides in one domain while the wavefunction of the hole is separated into the other one. The nature of this separation, alongside with this special band alignment, causes a decrease in the recombination energy compared to the band edge energy, which shows its effect in the red-shifted emission [174].

For the semiconductor NPLs, the predominant Type-II heterostructure is core/crown geometry, in which the second semiconductor is laterally grown on the seed NPLs. The first type-II colloidal NPLs were synthesized via seed-mediated growth of CdTe crown on CdSe core [69]. This chemical approach is still widely used for crown growth of either type-I or type-II core/crown NPLs, for its versatility and precision [65], [122], [175]–[177]. Although CdSe/CdTe core/crown is the common heterostructure of interest among the type-II NPLs [55], [69], other compositions such as CdSe/CdSeTe [55], CdS/ZnSe [67], CdTe–CdSe inverted type-II [55] and CdSe/ZnSe dots-on-plates [67] have also been investigated as potential heterostructures. Recently, more sophisticated heterostructures have been developed for type II nanoplatelets with two crowns being grown on the seed core [178]. Khan et al. [64] proposed a two-crown heterostructure in which the intermediate crown of CdS acts as an electron barrier that inhibits the propagation of the electrons into the outermost CdTe crown. These multi-crown heterostructures are especially interesting as they offer multiple tunable recombination channels, which can be further modified toward cascade structure with bi- and tri-emission characteristics.

The characteristic feature of type-II heterostructures is the long-lived emission [50], [179]–[183], which is induced by the charge separation that slows down the recombination at the interface of the domains. In this way, the strong Coulombic attraction between electron and hole pair is alleviated and the fast exciton decay is hindered, which is crucial for light-harvesting or photocatalytic applications [173], [184]. Moreover, the origin of the emission that determines the emission wavelength depends on the heterostructure's design, such as the volume, shape and composition of the domains, and the environmental condition, such as the solvent, temperature and external charge injection [185]–[187]. Numerous studies have been conducted on the physics that governs the carrier dynamics in type-II heterostructures [188]. Most of these studies investigate the carrier's dynamics through the time-correlated photon counting absorption and emission and the active radiative and non-radiative channels that determine the optical behavior [181].

In this chapter, a novel heterostructure of core/crown/crown NPLs with a step-wise band alignment was designed and synthesized through a seed-mediated one-pot technique. An analogy was drawn between the theoretical and experimental results where the geometry of the heterostructure was shown to have a critical role in the final properties of the NPLs. The intermediate crown with a staggered configuration with the core and final crown enables squeezing or loosening of the hole wavefunction and shapes the electron-hole (e-h) overlap of spatially separated charges. The recombination channel(s) can be activated by adjusting the geometry, which determines the distinguished type-II characteristics of each set of NPLs. The excitonic properties of the multi-crown type-II NPLs were shown to be sensitive to the temperature through not only the electron-phonon interaction but also the lattice contraction at low temperatures, which affects the direct recombination channels more than the indirect ones. The multi-channel gradient

heterostructure exhibits a very low onset of lifetime prolongation temperature of ca. 9 K, which indicates low excitons splitting energy promising for quantum devices. Moreover, the smooth transition between the domains facilitates lower energy photon absorption and gives rise to an extremely high two-photon absorption cross-section (δ_{2PA}) with superlinear behavior.

4.2. Experimental

Materials. Selenium (99.99%), tellurium (99.99%), 1-octadecene (ODE, 90%), cadmium acetate dihydrate (98%), trioctylphosphine (TOP, 90%), 1-octanethiol (≥98.5%), n-hexane (≥97.0%), absolute ethanol, toluene (≥99.5%), oleic acid (OA, 90%), sodium myristate (≥99.0%) and cadmium nitrate tetrahydrate (≥99.0%) were purchased from Sigma Aldrich.

Preparation of cadmium myristate Cadmium myristate. was prepared according to a previously published recipe in the literature [140]. In a typical synthesis, 6.26 mg of sodium myristate and 2.46 mg of cadmium nitrate tetrahydrate dissolved in 500 ml and 80 ml methanol, respectively. After around 2 h of rigorous stirring and complete dissolution, both solutions were mixed together and further stirred for 2 h. The bulky white cadmium myristate was rinsed with methanol two times to remove unreacted chemicals or small monomers, and at the end filtered and dried under vacuum for overnight.

Synthesis of 4.5 ML CdSe core NPLs. 4.5 ML CdSe NPLs were synthesized according to the reported procedures with some modifications [124]. In a typical synthesis, 800 mg of cadmium myristate, 67 mg of Se and 60 mL of ODE were mixed in a 100 mL three-neck flask and degassed at 95 °C under vacuum. Then, the temperature was set to 237.5

°C under argon gas, and when the temperature reached around 195 °C, 200 mg of cadmium acetate dihydrate was swiftly added to the solution. The solution was kept under 237.5 °C for 6 min and, after that, quenched in a water bath while 5 ml of OA was added. The final CdSe core was cleaned by consecutive precipitation and redispersion with the addition of ethanol and centrifuge at 6000 rpm for 5 min. In the end, the CdSe core was dissolved in 20 mL of hexane and kept at cool temperature for future use.

Preparation of anion precursor. For the preparation of the anion precursor, first two solutions of Te-TOP (1 M) and Se-TOP (1 M) were prepared, and then for each preferred composition of the crown, a known amount of each solution with a total volume of 60 µL was mixed with 2 mL ODE. Later, this solution was used for the growth of the crowns.

Synthesis of 4.5 MLs CdSe/CdSeTe/CdTe core/crown/crown NPLs. 4.5 ML CdSe/CdSeTe/CdTe NPLs were synthesized in one-pot and both of the crowns were grown consecutively on CdSe core NPLs. First, a certain amount of CdSe, equivalent to 1 optical density (OD) absorption at 350 nm when 100 µL of it was dissolved in 3 mL hexane and optical length of the measurement is 1 cm, was taken, and it was precipitated and redispersed with ethanol and centrifugation for three times. The final precipitate was dissolved in 1 ml of hexane and mixed with 30 mg of cadmium acetate dihydrate, 45 µL of OA and 3.5 mL of ODE in a 50 ml three-neck flask. The solution was degassed under vacuum at room temperature for 1 h to remove the volatile species. Then, the temperature was set at 215 °C under argon gas, and at 195 °C, the anion precursor started to be injected at a rate of 2.5 ml h^{-1} with the aid of an injection pump to grow the intermediate crown. When the first injection finished, an extra 1 min of growth time was given, and then the final CdTe crown was grown on the NPLs with the injection of the second anion precursor. The composition of the anion precursor depends on the aimed ratio of Te to

Se in the crown, and its amount for each injection depends on the size of the crown that is aimed. For example, for an intermediate crown with x = 0.50, r = 1/1 and D = 1, 0.5 mL of anion precursor with an equal ratio of Te to Se is injected into the solution. After complete injection, the solution was kept at high temperature for 1 min before adding 1 mL of OA and fast quenching in the water bath. The final NPLs were precipitated by the addition of 6 mL of ethanol and centrifugation at 6000 rpm for 6 min, and then redispersed in 5 mL hexane at the end.

NPLs Characterization. All the in-solution characterizations of the NPLs were carried out via quartz cuvettes and the solutions were first diluted with hexane. Absorption spectra were collected via Agilent Cary 60 UV-Vis Spectrophotometer, and PL and photoluminescence excitation (PLE) spectra were collected with Varian Cary Eclipse at an excitation wavelength (λ_{ex}) of 400 nm. TRF measurement was carried out via Pico Quant FluoTime 200 at λ_{ex} of 375 nm and repetition rate of 2.5 MHz. TEM images were obtained using Tecnai G2 F30 microscope. XRD and XPS measurements were carried out on a drop-cast film of NPLs with a Panalytical Xpert Pro MPDand and Thermo Scientific K-Alpha X-Ray spectrometer, respectively.

Low-temperature PL and TRF measurements were performed using a home-built micro-PL setup. The NPLs were mounted in a closed cycle cryostat (Attodry 1000) with a base temperature of 3.5K. A picosecond pulsed laser diode operating at 532 nm both under CW and pulsed mode was used as an excitation source. Following the excitation, emitted PL light was collected via a low-temperature compatible microscope objective (0.82 NA) and coupled to single-mode fiber after spectrally filtered by a 550 nm long-pass filter. For TRF measurements, pulsed mode of the laser diode (500 kHz repetition rate) was used for excitation of NPLs and emitted PL light was sent to a silicon Single Photon Avalanche Diode (SPAD) with a photon timing resolution of 50ps (MPD-PDM). The

HydraHarp 400 multichannel picosecond event timer and TCSPC module (PicoQuant) was used to record PL decay curve of NPLs.

Measurement of 2-photon absorption cross-section. For the measurement of 2-photon absorption cross-section(σ_{2PA}), we employed the open-aperture Z-Scan measurement [189]. Two in-solution samples of NPLs were diluted with hexane and the measurement was carried out in a 1 mm quartz cuvette. The transmission of the laser light was measured based on the position of the samples, which is provided in the main text. In order to calculate the 2PA cross-section, the transmission was first fitted with equation S5,

$$T(z) = \frac{1}{1 + \frac{I_0 \times \beta \times l}{1 + (\frac{z}{z_0})^2}} \tag{4.1}$$

where T(z) is the transmittance based on the sample position (z), I_0 is the focal point peak intensity of the irradiance, β is the 2-photon absorption (2PA) coefficient, l is the length of the cuvette and z_0 is the Rayleigh range. After fitting the curves and calculating β, σ_{2PA} can be calculated through equation S6,

$$\sigma_{2PA} = \frac{h \times \nu \times \beta}{N_a \times d_0 \times 10^{-3}} \tag{4.2}$$

where hν is the energy of the irradiance, N_a is the Avagadro's number and d_0 is the in-solution concentration of the NPLs. In order to calculate d_0, first, the volume of the NPLs (V) were measured via TEM images and then, with the aid of ICP-MS, the molar concentration of Cd (C_{Cd}) was measured. d_0 would be

$$d_0 = \frac{C_{Cd}}{(V/V_{UC}) \times 4} \quad (4.3)$$

where V_{UC} is the volume of the zinc blende unite cell.

4.3. Results and Discussion

In our samples with the general heterostructure of CdSe/$CdSe_{1-x}Te_x$/CdTe core/crown/crown, the intermediate crown always has a band alignment with the conduction and valance band in a staggered position with respect to the core and final crown. This alignment assures that, from the energy perspective, there would be only one emission from the lowest energy path. However, as shown later, not all the samples show one peak emission, and for some samples, this dominant emission may fade away at the expense of other possible channels. The general band alignment and all the possible transitions for core/crown/crown NPLs are shown in Figure 4.1a and b, respectively. The first three excitonic transitions (T_1, T_2, and T_3) are the intrinsic feature of each domain, which show their effect as electron-heavy hole (e-hh) and electron-light hole (e-lh) peaks in the absorption spectra of the NPLs. In that regard, the e-hh and e-lh transitions for the CdSe core are denoted as T_1 and always present themselves as two peaks located at around 510 and 482 nm, respectively. For T_2 and T_3, the e-lh transition usually fades into the absorption spectra, as shown elsewhere [69], and may become prominent upon overgrowth of the domain [70]. The e-hh transition for T_2 and T_3, on the other hand, usually shows a distinct absorption peak that depends on the lateral size and composition of the domain. The corresponding position of the peaks may be so close to each other, and for some samples, these two peaks may show their presence as only one peak; however, the emission spectra confirm the co-existence of these two domains. Alongside the direct bandgap transitions, there are three possible charge transfer (CT) channels

denoted to the type-II emissions through the interfacial recombination of the excitons (Figure 4.1b). These three transitions are responsible for the long tail of the absorption spectra, and because of their spatially collective recombination nature, they produce a long-lived spectrally-broad emission.

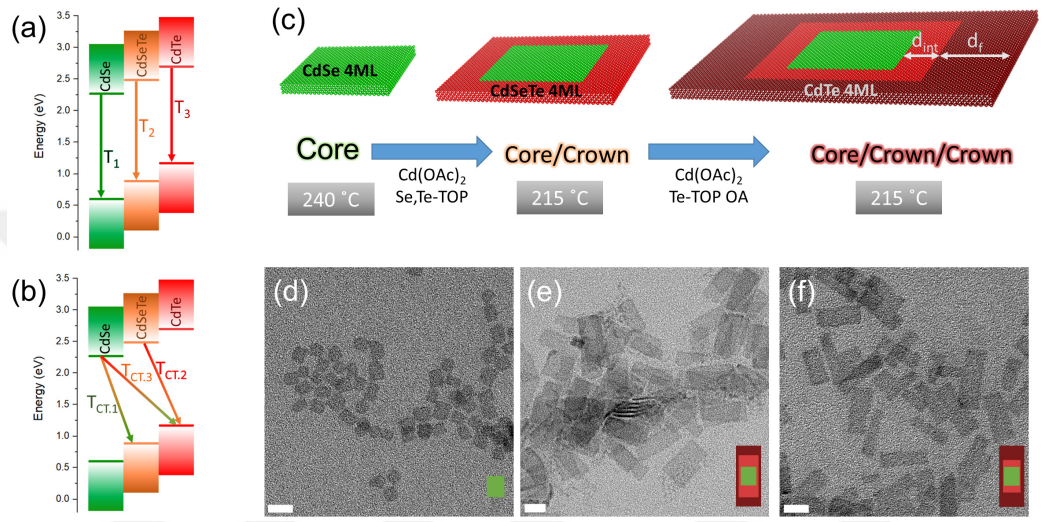

Figure 4.1. (a) Band alignment of the NPLs with the general heterostructure of CdSe/CdSeTe/CdTe core/crown/crown and all the possible direct band-edge transitions happen in one domain. (b) Same as (a) for the possible indirect type-II transitions between two different domains. (c) A schematic of the synthetic route of CdSe/CdSeTe/CdTe core/crown/crown NPLs. Starting with 4.5 ML CdSe core, two consecutive crowns were grown through a single-pot procedure where a mixture of Se-Te was injected for the first crown and then only Te was introduced to the NPLs. (d) TEM image of 4.5 ML CdSe core and (e and f) multi-crown NPLs with r equal to 3 and 0.33, respectively. All scale bars are 20 nm. Copyright 2023 WILEY-VCH Verlag GmbH & Co. KGaA, Weinheim.

The synthesis route of these multi-crown NPLs is demonstrated in Figure 4.1c. Starting with 4 monolayers (MLs) CdSe core, the first crown was grown via the introduction of

an anion mixture with the desired ratio of Se and Te alongside the Cd precursor. After a brief resting time, the second precursor of only-Te was injected into the solution to form the CdTe final crown. This approach allows us to tune the composition and size of the crowns in a relatively simple manner and engineer the final multi-crown heterostructure. The XPS spectra of CdSe/CdSeTe/CdTe core/crown/crown NPLs for three participant elements of Cd, Se and Te are shown in Figure 4.2. The excellent fit for the elements and the binding energies suggests no formation of unwanted species, or even if, they were cleared out from the ensemble after the cleaning procedure. This is especially important for the chalcogenides with a higher tendency to form unwanted subspecies [44], [190]. The XRD pattern of the NPLs with two different ratios of the intermediate crown is shown in Figure 4.3. As the share of the final crown increases, the peaks tend to shift to lower diffraction angles due to the larger lattice constant of CdTe compared to CdSe.

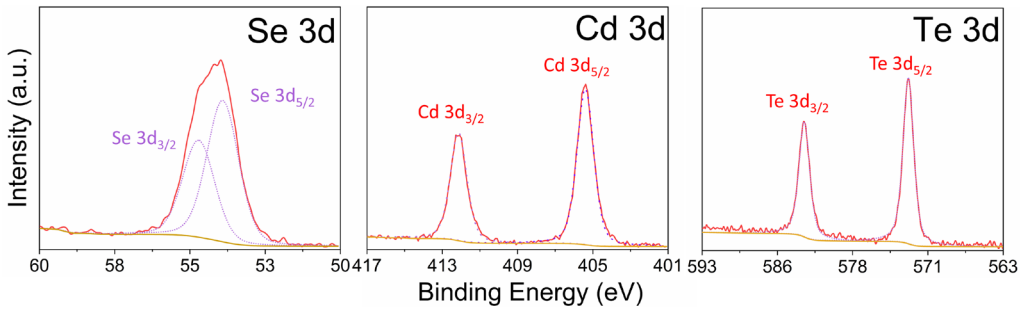

Figure 4.2. XPS spectra of CdSe/:1 CdSeTe/:3 CdTe core/crown/crown NPLs. The elemental binding energies of Cd, Se and Te, presented in the NPLs heterostructure, are measured, and the curves are fitted to the peaks to ensure the nature of the binding. Copyright 2023 WILEY-VCH Verlag GmbH & Co. KGaA, Weinheim.

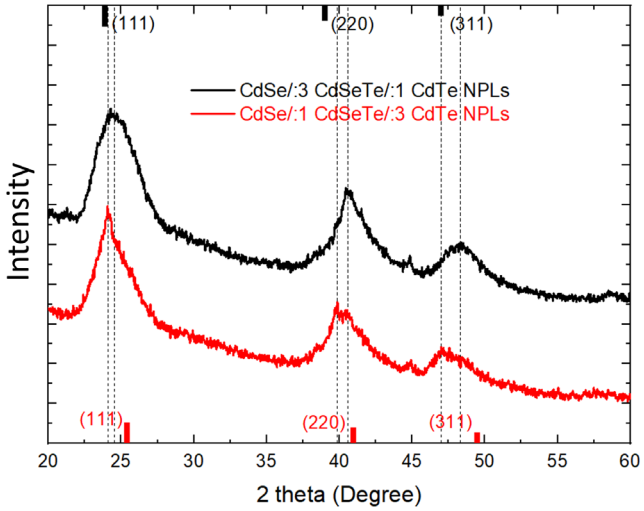

Figure 4.3. XRD patterns of CdSe/:3 CdSeTe/:1 CdTe and CdSe/:1 CdSeTe/:3 CdTe core/crown/crown NPLs with zinc blende crystal structure. The XRD peaks of bulk zinc blende CdTe (black lines at the top) and CdSe (red lines at the bottom) are included as references. As the ratio of the final crown increases, the peaks are shifted to the lower diffraction angles, which suggests a higher ratio of the final crown to the middle crown. Copyright 2023 WILEY-VCH Verlag GmbH & Co. KGaA, Weinheim.

The optical properties of the NPLs arise from the interactive combination of all the transitions discussed. Due to the constant thickness of the core, core/crown and core/crown/crown NPLs, the volume of the domains is proportional to their surface area and lateral size, which in turn depends on the injected amount of Se-Te and Te precursors. In our study, we investigate the effect of three parameters, namely, the ratio of the crowns, the intermediate crown composition and the overall size of two crowns on the electron and hole wavefunctions and the recombination dynamics in the NPLs. In the first step, we synthesized multi-crown type-II NPLs with similar compositions of the intermediate crown but having various lateral sizes. The overall size of the intermediate and final crown was kept constant, while their longitudinal ratio ($r = d_{int}/d_f$, where d_{int} and d_f are the longitudinal length of the intermediate crown and final crown, respectively,

shown in Figure 4.1c) varied to be 1/3, 1/1, and 3/1 through adjusting the injected amount of precursors. Figure 4.1d shows the transmission electron microscopy (TEM) image of the original core before the crown growth, where NPLs have a square shape with a lateral size of 12.1 ± 1.5 × 10.6 ± 1.5 nm^2. After the growth of the CdSeTe/CdTe crown, the symmetry of NPLs is disturbed, with one of the facets growing faster than the other one. These rectangular core/crown/crown NPLs have a lateral size of 16.1 ± 0.8 × 39.3 ± 3.6 nm^2 for the case of r = 3/1 (Figure 4.1e), and their size does not significantly change when r is changed to 1/3 (lateral size was measured as 17.9 ± 0.9 × 42.6 ± 3.8 nm^2 for the corresponding NPLs in Figure 4.1f). The slight change in the lateral size for these two sets of NPLs suggests very similar growth kinetic of the crowns regardless of the anion. Moreover, the huge break in the symmetry of the NPLs points to the intrinsic anisotropic growth mechanism from the length to the width of the NPLs.

To understand the position of atoms, especially Se and Te, we performed TEM-EDX mapping on multi-crown NPLs, shown in Figure 4.4. Although Cd shows a clear localization in the NPLs region, the signal from Se and Te is too low to define the exact position of the atoms, a problem that was previously reported for type-II NPLs [178].

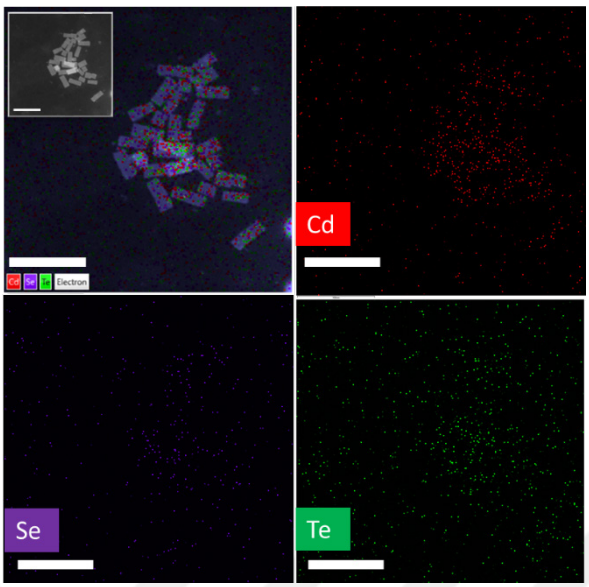

Figure 4.4. EDX mapping of CdSe/$CdSe_{0.5}Te_{0.5}$/CdTe multi-crown NPLs with r=1/3. The top left image shows the mapping of all the elements and the inset shows the TEM image. The respected element mappings are indicated for other images. The scale bars are 100 nm. Copyright 2023 WILEY-VCH Verlag GmbH & Co. KGaA, Weinheim.

Herein, we performed EDX line mapping on two isolated samples with a general structure of CdSe/$CdSe_{0.5}Te_{0.5}$/CdTe core/crown/crown and different r of 3/1 and 1/3 shown in Figure 4.5a and b, respectively. The samples were precipitated and redispersed in hexane twice to remove the unreacted chalcogenides as much as possible. As line-EDX is performed on high voltage, the NPLs are damaged during the measurement and scatter the elements to the peripheries, complicating the spatial accuracy of the mapping [64]. However, the line scans confirm the existence of three domains with high, average and low concentrations of Se corresponding to the core, intermediate crown and final crown domains, respectively. Moreover, qualitatively, the size of the intermediate (final) crown decreases (increases) for NPLs with r = 3/1 compared to NPLs with r = 1/3. The core region is slightly moved away from the center (5 nm) for one measurement, which can be due to the measurement or different crown growth on different sides.

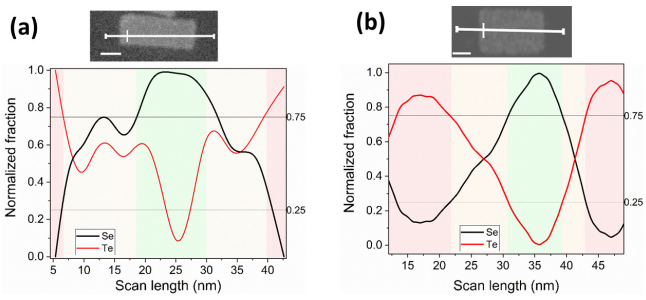

Figure 4.5. TEM-line EDX of two multi-crown NPLs with the same D=1 and different r of (a) 3/1 and (b) 1/3. The EDX line is drawn in the respective TEM images above the graphs and only the region corresponding to the actual place of the NPLs is plotted. Se and Te fractions were first calculated and then normalized between 0 and 1 to differentiate different domains. The core region was expected to have Se above 0.75 and the boundary between the intermediate crown and final crown was supposed to have 0.75 of Te (or 0.25 Se). The scale bars are 10 nm in the TEM images. Copyright 2023 WILEY-VCH Verlag GmbH & Co. KGaA, Weinheim.

To investigate the homogeneous intermediate crown growth, we took TEM images from CdSe/$CdSe_{0.5}Te_{0.5}$ core/crown NPLs after injection of 0.5 mL Se-Te-TOP precursor, shown in Figure 4.7a and b. The NPLs have a lateral size of 25 ± 1.6 × 13.7 ± 0.5 nm^2, which closely correlates to the expected size of the intermediate crown in multi-crown NPLs with D = 1.0 and r = 1/1 and indicates fast growth of the crowns compared to the time-scale of the reaction.

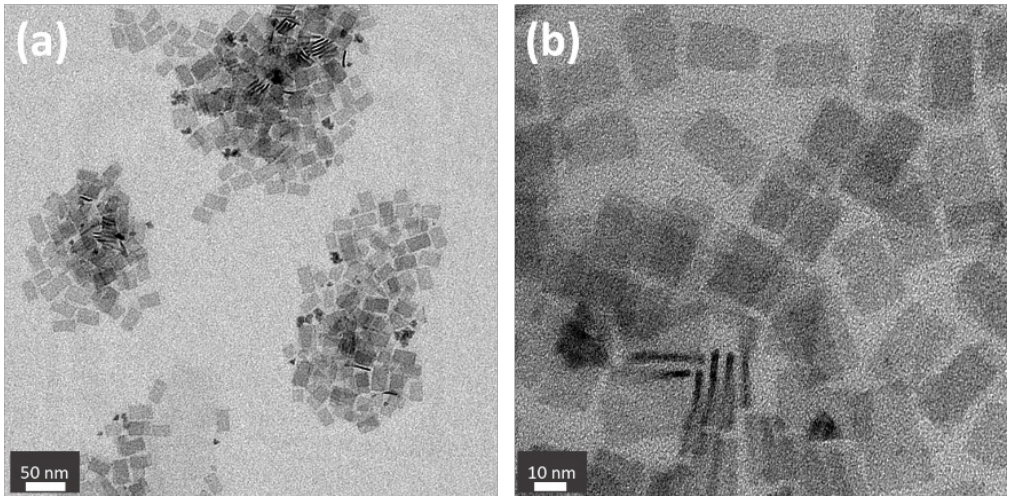

4.6. TEM images of CdSe/$CdSe_{0.5}Te_{0.5}$ core/crown NPLs after injection of 0.5 mL of Se-Te-TOP crown precursor at two different magnifications. The scale bars are 50 nm in (a) and 10 nm in (b).

Moreover, we conducted a control reaction, in which the absorption and emission spectra of aliquots of NPLs were measured after complete injection of the Se-Te-TOP precursor and further after 15 and 30 min of annealing at the synthesis temperature of the original multi-crown NPLs (215 ˚C). The absorption spectra normalized to the electron-heavy hole of the CdSe core and the PL spectra normalized to the emission peak wavelength are shown in Figure 4.7a and b, respectively. Knowing the absorption peak of each domain directly correlates to the lateral size of that domain [64], [191], all three aliquots show the same absorption spectra with no change in the optical density of the CdSeTe peak. Also, the emission spectra did not show much change from the initial aliquot, with only 2 nm of redshift after 15 min followed by 3 nm of blueshift after 30 min. These observations firmly confirm that the reaction time for the CdSeTe crown is much faster than the time scale of the reaction, in which the crown grows almost instantly after the injection of the anion precursor. Also, the NPLs are stable at high temperature for at least 30 min and does not dissolve into the reaction medium. In conclusion, after the injection

of the first anion precursor, almost all of the Se and Te are consumed and no leftover Se remains to enter the final CdTe crown.

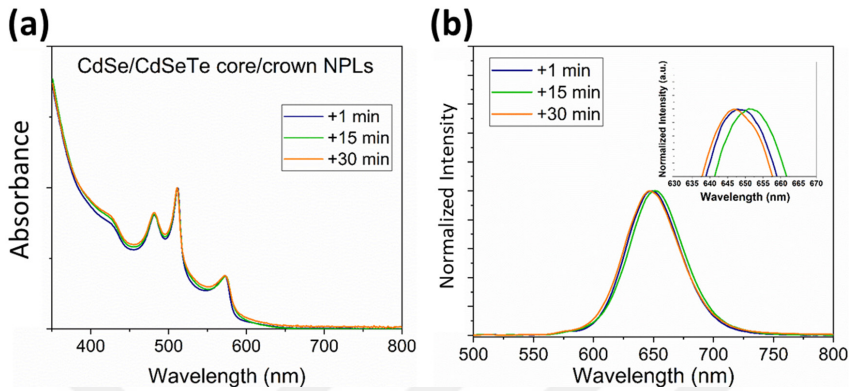

Figure 4.7. (a) Absorption and (b) emission spectra of CdSe/$CdSe_{0.5}Te_{0.5}$ core/crown NPLs after different annealing times at the synthesis temperature of 215 ˚C. The inset in (d) shows the magnified PL spectra at the peak. Copyright 2023 WILEY-VCH Verlag GmbH & Co. KGaA, Weinheim.

The absorption and emission spectra of the NPLs with varying r are shown in Figure 4.8a and b, respectively. For r = 1/3 and 1/1, the absorption spectra show two peaks at 583 and 560 nm originating from the $CdSe_{0.5}Te_{0.5}$ and CdTe domains, respectively. The e-hh absorption peak for 4.5 ML CdTe domain in the case of only CdTe core and CdSe/CdTe core/crown NPLs has been reported to be at the same wavelength [23], [192]. Incorporation of selenium in the intermediate crown has the alloying effect and it should blue-shift the e-hh of the CdSeTe domain [193]. However, while CdSe has a higher bandgap than CdTe, the shift caused by Se is due to a phenomenon known as “optical bowing” [194].

While for most semiconductor alloys, the physical properties, such as lattice constant, varies linearly with composition, the same behavior is not applicable for bandgap energy

[194], [195]. The bowing behavior of the bandgap energy can be best described by $E_{BG}(x) = xE_{BG}^{A} + (1-x)E_{BG}^{B} - bx(1-x)$, where $E_{BG}(x)$, E_{BG}^{A} and E_{BG}^{B} are bandgap energies of the semiconductor alloy and pure semiconductor A and B, respectively, and b is the optical bowing parameter [195]. The quadratic term causes deviation from linear behavior and in the case of CdSeTe alloy semiconductor, decreases its bandgap energy [196]. The origin of optical bowing is the long-range disorder in the lattice structure, which brings in locally active parameters affecting the bandgap but not the lattice constant. The change in the bandgap energy is mainly due to the varying tetrahedral bonding angle of Se/Te and Cd and different charge distributions on the anions originating in different electronegativity [197]. This effect is responsible for the nonlinear change in the e-hh peak position and has been reported to have a strong influence on CdSeTe alloys [198]. The absorption peak of CdSeTe intermediate crown in our heterostructure closely correlates with the previous reports of CdSe/CdSeTe core/crown NPLs in the literature [70], [199]. With increasing the size of the intermediate crown, the original e-hh peak of CdTe has been dissolved into the spectrum (for r = 3/1), which we believe is due to the optical bowing and lattice strain exacerbation that can be a source for optical nonlinearity.

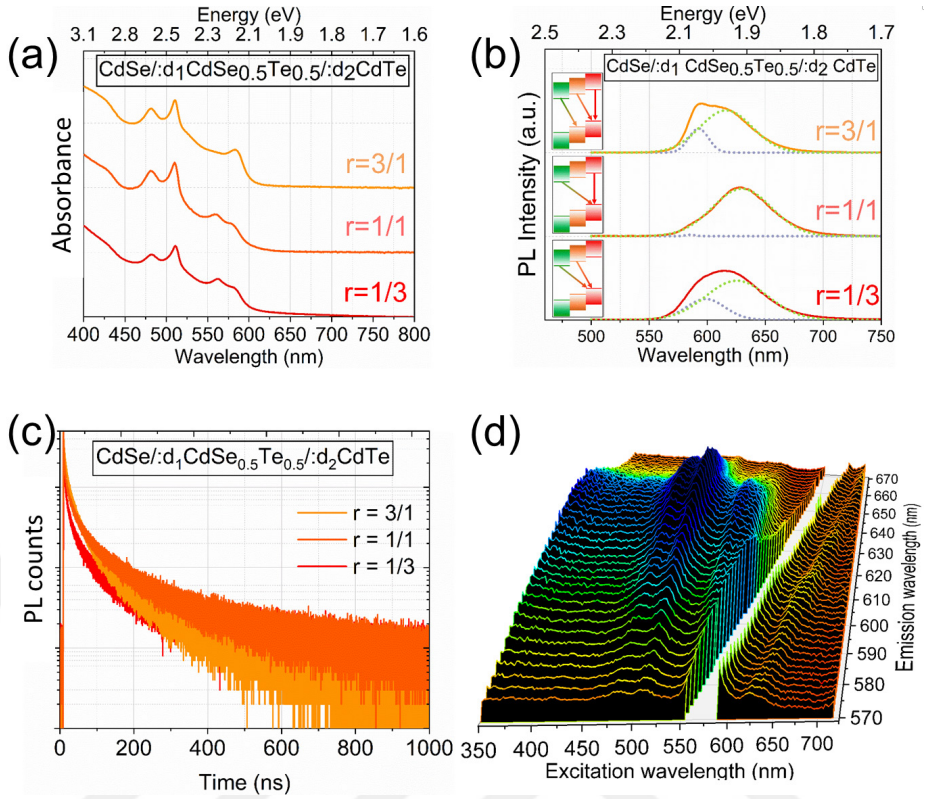

Figure 4.8. (a) Absorption profile of CdSe/CdSeTe/CdTe core/crown/crown NPLs with constant composition of the intermediate crown (Se/Te = 1) and changing ratio of intermediate to final crown, r. (b) PL profile of the same samples. The dotted curves are the deconvoluted peaks for each graph. (c) TRF decay curves at the emission peak wavelength of the NPLs. (d) PLE profile of the NPLs with r = 1 sweeping from the beginning (570 nm) to the end (670 nm) of the emission spectra. Copyright 2023 WILEY-VCH Verlag GmbH & Co. KGaA, Weinheim.

A dual emission PL is recorded for all three sets of NPLs with varying r; however, the peak profile, including position, linewidth, and peaks ratio, differs drastically for different architectures. Deconvolution of PL spectra can help to explain the origin of the emission for these multi-peak emission NPLs. The deconvoluted emission peaks for r = 1/3, 1/1, and 3/1 are shown in Figure 4.9 and the results are summarized in Table 4.1.

For NPLs with r = 3/1, one of the fitted peaks is much narrower with full-width-at-half-maximum (FWHM) of 20 nm than the other one (with FWHM of 53 nm). This narrow and higher-energy emission peak is originated from the direct recombination within one domain and has a smaller Stokes shift than the broader peak. The bicolor emissive type–II heterostructure has been reported previously for CdSe/$CdSe_xTe_{1-x}$ core/crown NPLs [70]; however, the same heterostructure in other studies shows only one emission profile when the lateral size of the crown is sufficiently large enough [199]. The reason behind these seemingly contradictory results is originated from the sensitive nature of type-II NPLs to the environment and complicated interfacial recombination dynamics. As a result, the interfacial recombination is not only dependent on the energy level of each transition but is also extremely sensitive to the size of each domain and the absolute recombination area within the nanocrystal. The configuration of locally excited exciton plays a critical role in coupling/decoupling of the neighboring exciton by Coulomb interaction and whether to block or allow specific transitions [187]. These interactions are more sophisticated for a two-crown structure, which can also spatially decide on the distance of the electron and hole and make up a dual emission.

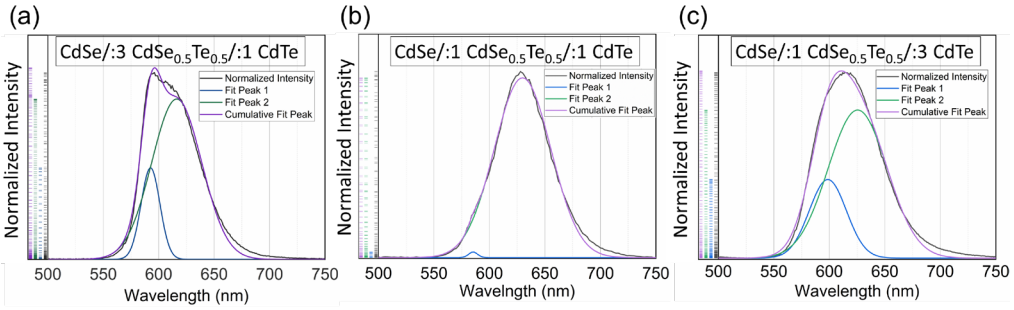

Figure 4.9. PL spectra and deconvoluted peaks for (a) CdSe/:3 $CdSe_{0.5}Te_{0.5}$/:1 CdTe, (b) CdSe/:1 $CdSe_{0.5}Te_{0.5}$/:1 CdTe and (c) CdSe/:3 $CdSe_{0.5}Te_{0.5}$/:1 CdTe core/crown/crown NPLs. Copyright 2023 WILEY-VCH Verlag GmbH & Co. KGaA, Weinheim.

Table 4.1. A summary of the peaks deconvolution results

Sample	Peak 1 position (nm)	Peak 1 FWHM (nm)	Peak 2 position (nm)	Peak 2 FWHM (nm)	Peak 1 share (%)	Peak 2 share (%)
CdSe/:3 $CdSe_{0.5}Te_{0.5}$/:1 CdTe	592.5	20.0	616.2	53.0	17.8	82.2
CdSe/:1 $CdSe_{0.5}Te_{0.5}$/:1 CdTe	585.3	19.1	629.8	61.2	13.3	86.7
CdSe/:1 $CdSe_{0.5}Te_{0.5}$/:3 CdTe	598.5	39.2	625.4	62.6	25.0	75.0

The change in the PL spectra of the samples with different architectures emphasizes the switch from one transition channel to another. The decay curves, shown in Figure 4.8c, help to reveal the dynamics behind the recombination and the active emission channel(s). The sample with r = 3/1 shows the fastest recombination rate, and with decreasing the intermediate crown size (d_{int}), the recombination slows down (decay components and lifetimes are summarized in Table 4.2). This was not predictable as the recombination distance of electron and hole in the final crown and core is increased, and it should take a longer time for them to recombine. Moreover, when the intermediate crown size further decreases, the recombination rate does not increase for r = 1/3 compared to r = 1/1.

Table 4.2. Decay Components and numerical analysis of time-resolved fluorescence from NPLs with general heterostructure of CdSe/:d_{int} $CdSe_{0.5}Te_{0.5}$/:d_f CdTe core/crown/crown for different ratios of crown sizes, r. Copyright 2023 WILEY-VCH Verlag GmbH & Co. KGaA, Weinheim.

	TRF decay components							
Sample	A_1	τ_1 (ns)	A_2	τ_2 (ns)	A_3	τ_3 (ns)	A_4	τ_4 (ns)
r = 1/3	1192	6.7	2559	1.0	83	186.1	395	36.3
r = 1/1	13900	1.3	5782	6.9	2844	36.6	595	177.7
r = 3/1	34280	1.2	20581	10.5	6157	44.9	201	372.0

	Intensity-averaged lifetime $(\frac{\sum \boldsymbol{A_i} \times \boldsymbol{\tau_i^2}}{\sum \boldsymbol{A_i} \times \boldsymbol{\tau_i}})$	Fractional emission contribution $(\frac{\boldsymbol{A_i} \times \boldsymbol{\tau_i}}{\sum \boldsymbol{A_i} \times \boldsymbol{\tau_i}})$			
Sample	τ_{avg} (ns)	$A_1 \times \tau_1$ (%)	$A_2 \times \tau_2$ (%)	$A_3 \times \tau_3$ (%)	$A_4 \times \tau_4$ (%)
r = 1/3	85.7	8	2.4	15.4	14.3
r = 1/1	86.8	6.7	14.9	38.9	39.5
r = 3/1	70.7	6.8	35.5	45.4	12.3

Deconvolution of the peaks for NPLs with r = 3/1 showed the emergence of a distinct narrow peak, which is attributed to the direct recombination in the final CdTe crown, T_3. The TRF measurement now further confirms this assumption that an element of fast-decaying recombination is due to the band-edge transition in one domain. In other words, when the separation distance of electron and hole is extensively increased, the probability of band-edge recombination of electron and hole in one domain also increases. For NPLs with r = 1/1, some portion of this T_3 transition exists, which indicates that the distance is still large enough, while for r = 1/3 NPLs, the short spatial distance of electron-hole completely turns the equilibrium in favor of type-II recombination. The minuscule change in τ_{avg} for r = 1/1 and 1/3 NPLs also points out to the shorter $T_{CT,3}$ recombination

distance of r = 1/3 NPLs vs. fast band-edge recombination of r = 1/1 NPLs. The decay curves collected at two emission wavelengths of 577 and 627 nm for NPLs with r = 1/3 (shown in Figure 4.10, and the decay components summarized in Table 4.3) indicates that the recombination rate at lower wavelength is approximately 2 times faster than the longer wavelength, which suggests the activation of other type-II transition such as $T_{CT,2}$.

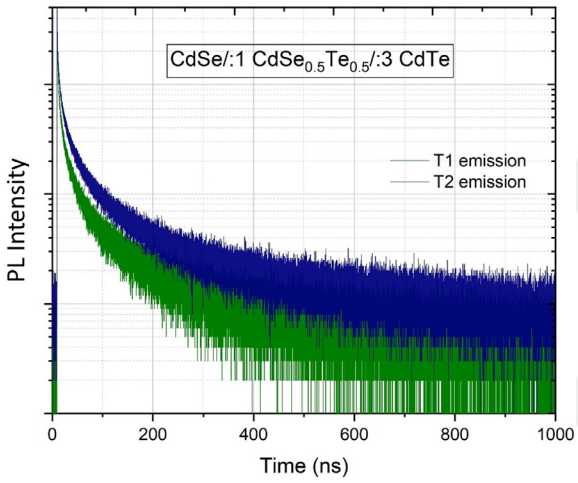

Figure 4.10. TRF decay curves of CdSe/:1 $CdSe_{0.5}Te_{0.5}$/:3 CdTe core/crown/crown NPLs recorded at two emission wavelengths of T1 = 577 nm and T2 = 627 nm. Copyright 2023 WILEY-VCH Verlag GmbH & Co. KGaA, Weinheim.

Table 4.3. A summary of the decay components.

Emission decay (nm)	**A_1**	**τ_1 (ns)**	**A_2**	**τ_2 (ns)**	**A_3**	**τ_3 (ns)**	**A_4**	**τ_4 (ns)**	**τ_{avg} (ns)**
T1 = 577	1462	3	382	21	65	135	2	1830	13
T2 = 627	1608	2	781	11	304	59	61	1835	51

The PLE for the sample with r = 1/1 is recorded for emissions between 570 and 670 nm and is presented in Figure 4.8d. For all of the emission wavelengths, the e-hh and e-lh peaks of the core are in position and two peaks of the crowns can be detected, which

shows that both crowns are actively responsible for the final type-II emission and the apparent emission at all wavelengths is not due the two different ensembles of NPLs. Based on the TEM images, the NPLs were shown to have a lateral size distribution, which can affect the active recombination channel. For core NPLs, the distribution accounts for 14.1% in the longitudinal direction and by growing two crowns, this distribution is decreased to 9.1% (for multi-crown NPLs with r = 3/1), showing a more homogenous growth of the crowns. This also shows that a big portion of the size inhomogeneity is coming from the core, while the crowns are more homogeneous in size. In an extreme case, the size distribution of the NPLs can account for part of the multi-channel emission of the NPLs by providing a mixture of two ensembles with different active recombination channels. However, throughout our experiments, the change in r from 1/3 to 1/1 and 3/1 corresponds to 25% change in the size of the crowns, which is well above the overall size distribution of the NPLs. Hence, the switches between active channels are principally due to the change in the absolute domain size. The lateral size distribution can increase the FWHM of the emission lines and contribute to peak broadening.

The extreme variation in the recombination behavior points out the great sensitivity to the size of the intermediate crown. In a broader image, the conditioning of electron and hole landscape, where both are energetically separated into different domains and then spatially recombined, decides on the preferred transition channel. The TEM images showed that after the growth of the crowns, the shape of the NPLs changes from square to rectangular. To better understand the recombination dynamics in these type-II rectangular NPLs, we further calculate the electron and hole wavefunction distribution and its dependency on the geometry of the NPLs, considering the problem of a particle in a box in 2D. While for both square and rectangular geometries, the electron charge

density remains in the core, the asymmetric shape of the multi-crown NPLs brings a disproportional hole charge density with a dominant fraction on the longitudinal edges of the final crown instead of the corners in the case of square geometry (Figure 4.11). Here, the hole wavefunction distributes solely on the long edges where the length of the final crown is higher for rectangular NPLs, while for symmetric square NPLs, it distributes on all the edges with the maximum on the corners. The electron wavefunction is centered around the core for both sets of NPLs.

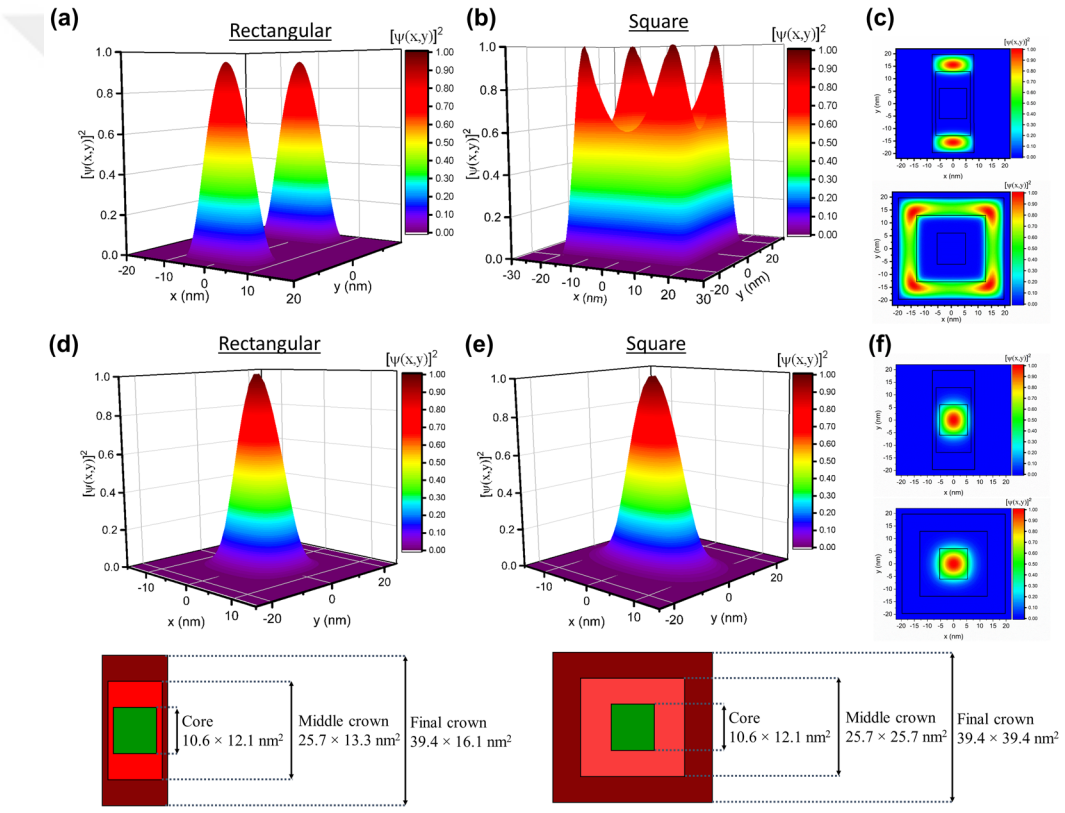

Figure 4.11. (a and b) Three-dimensional representations of hole wavefunction for CdSe/CdSeTe/CdTe core/crown/crown NPLs with rectangular and square shapes after photoexcitation, respectively. (c) 2D in-plane representations of hole wavefunction for the same rectangular (up) and square (down) NPLs. (d and e) Three-dimensional representation of electron wavefunction for rectangular and square multi-crown NPLs,

respectively, and (f) same wavefunctions for rectangular (up) and square (down) in a 2D in-plane representation. The electron wavefunction is centered around the core for both sets of NPLs. (g) Sketches of the NPLs with the size of different domains used for the theoretical calculations. Both sets of rectangular and square NPLs have an intermediate crown with x = 0.50 and r = 1/1. Copyright 2023 WILEY-VCH Verlag GmbH & Co. KGaA, Weinheim.

The higher-state electron and hole energies for rectangular CdSe/CdSeTe/CdTe core/crown/crown NPLs were calculated and shown in Figure 4.12. The electron and hole wavefunctions remain their center of position in the core and final crown, respectively, and only for higher state energies, they may diffuse into the intermediate crown or narrower edges. While the CdSe core and CdTe final crown provide the lowest energies for hole and electron, respectively, at higher energy states, the electron with lower effective mass starts to diffuse into the CdSeTe intermediate crown (n = 4) and later into the final crown (n = 23). On the other hand, the hole does not diffuse into the core even for very high energy states and it only diffuses into the thin periphery sides (n = 9) and intermediate crown (n = 14). The difference between the higher energy state electron and hole distribution is mainly due to the difference in the effective mass of the electron and the hole (Figure 4.12).

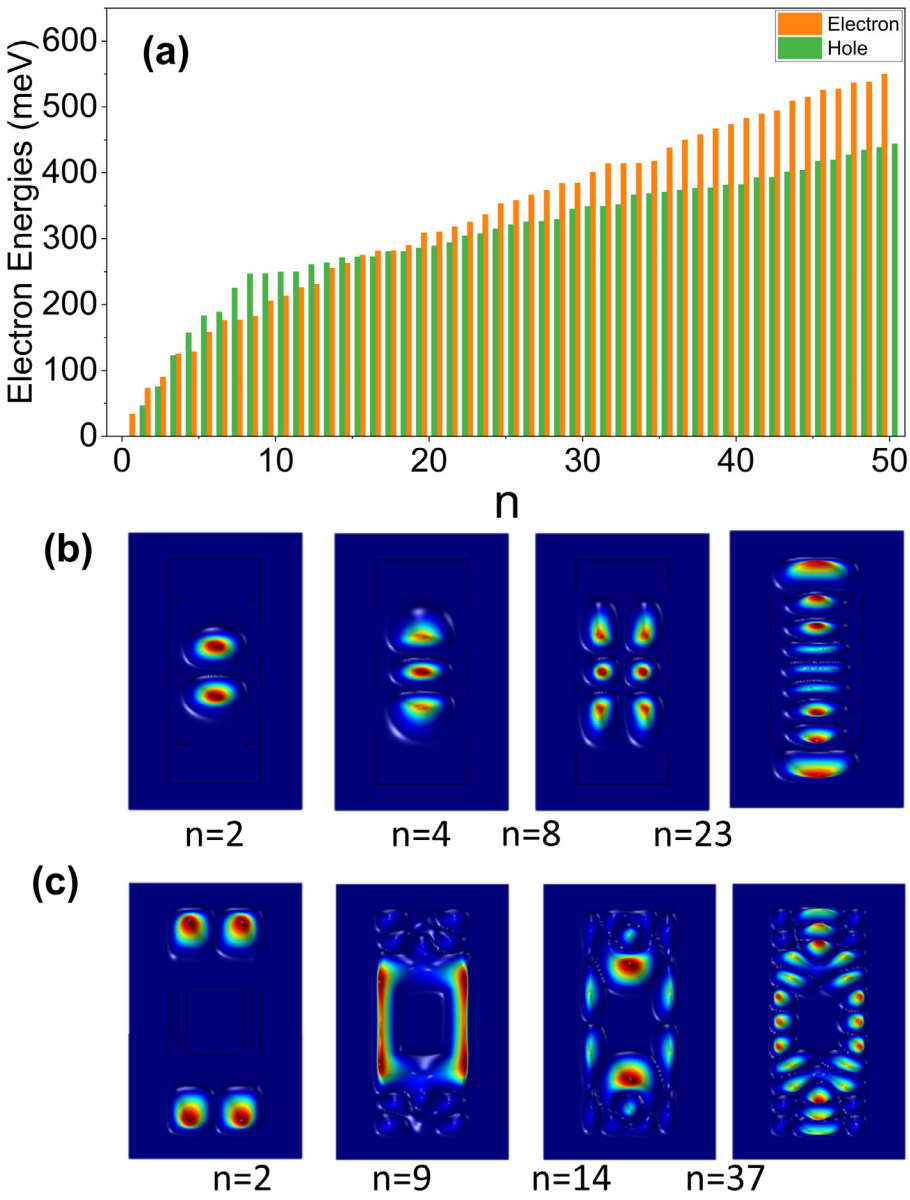

Figure 4.12. (a) Higher-state electron and hole energies for rectangular CdSe/CdSeTe/CdTe core/crown/crown NPLs. (b and c) A few representations of electron and hole wavefunction, respectively. Copyright 2023 WILEY-VCH Verlag GmbH & Co. KGaA, Weinheim.

The dependency of the electron and hole wavefunctions on the geometry of the multi-crown NPLs is shown in Figure 4.13a. The electron wavefunction does not show any

change with r due to the consistency of the core size with the lowest energy (see Figure 4.1a). However, as the size of the intermediate crown increases, which can be translated as a smaller final crown, the hole wavefunction gradually squeezes in a smaller area. The indirect type-II recombination is the result of the overlap between the two wavefunctions. The e-h overlap vs. r for three different compositions of $CdSe_{1-x}Te_x$ intermediate crown is demonstrated in Figure 4.13b, where regardless of the composition, the overlap decreases with increasing r. As we squeeze the hole wavefunction through changing r, we decrease the probability of the excitons interacting with each other at different domains; hence, the chance of direct recombination will increase, as was seen in the PL profile of the samples (Figure 4.8b and Figure 4.9).

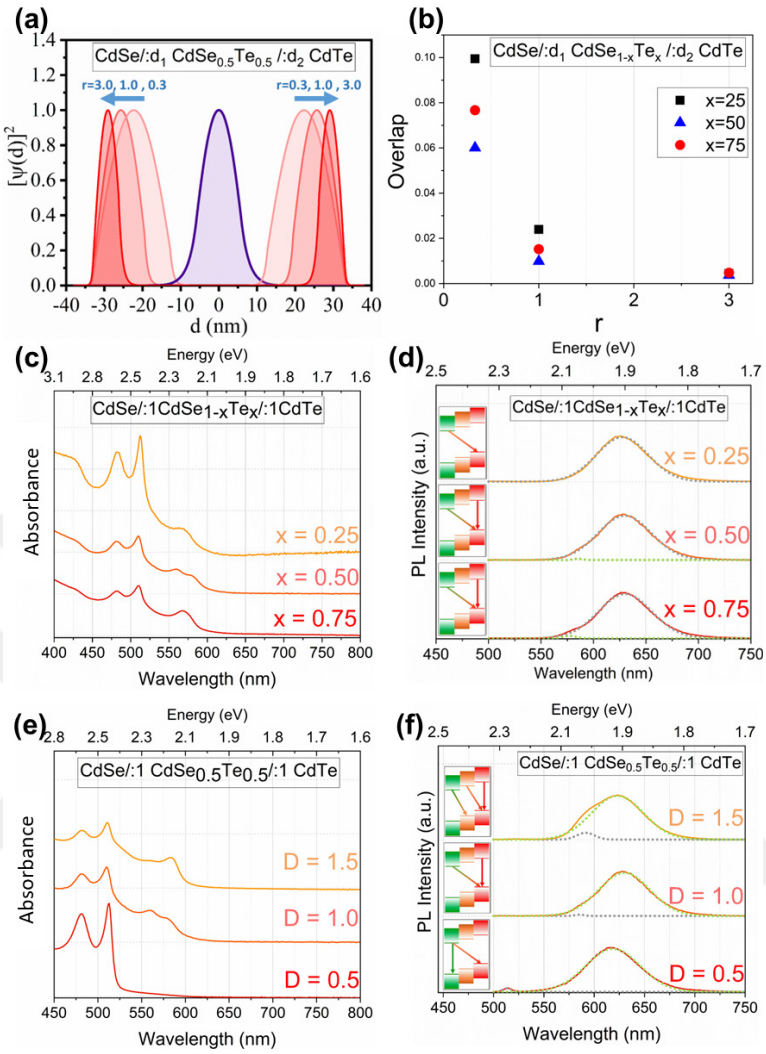

Figure 4.13. (a) Electron (purple) and hole (red) wavefunctions of the NPLs with x = 0.5 and changing r. (b) The e-h overlap extracted from the corresponding heterostructures with different r and x. (c) Absorption and (d) PL spectra of the CdSe/$CdSe_{1-x}Te_x$/CdTe core/crown/crown NPLs with different intermediate compositions. (e) Absorption and (f) PL spectra of the CdSe/:1 $CdSe_{0.5}Te_{0.5}$/:1 CdTe core/crown/crown NPLs with different collective sizes of the crowns, $D = d_{int} + d_f$. Copyright 2023 WILEY-VCH Verlag GmbH & Co. KGaA, Weinheim.

In calculating the electron and hole wavefunction distributions, the band alignment of the heterostructure was assumed to be unstrained. However, the difference between the lattice constant of the domains causes a strain, which can bend the conduction and valance band and make a local potential barrier or well in the band structure of semiconductor heterojunctions [200], [201]. The direct recombination channel in the CdTe domain points to the retention of the electron in the domain and, later, its direct recombination. Bicolor emission was previously observed for CdSe/$CdSe_{1-x}Te_x$ core/crown NPLs, in which at crown compositions near to x = 0.5, an emission line related to the CdSeTe domain emerges [70]. The strain-induced local barrier in the conduction band can prevent the electron from transferring to its lowest energy state in the CdSe domain. This strain should increase by decreasing the CdSeTe buffer layer size and amplifying the CdTe emission. However, with decreasing the size of the intermediate crown, the share of the CdTe emission decreases and then completely diminishes for r = 1/3. The observation shows that the local barrier preventing the electron transfer is not the only cause of the switching between the channels and probably not the main reason behind the retention of the electron.

Initially, the hot electron and hole do not feel the band structure; however, the electron with a lower effective mass relaxes faster than the hole. The direct recombination of retained electron and hole in the CdTe domain has a much higher rate (in the order of ns with components as fast as hundreds of picoseconds) [31] than the indirect recombination, which requires the spatial transfer of the charges. As the size of the intermediate crown increases (r = 3/1), the e-h overlap decreases and the transfer of both electron and hole to the intermediate crown becomes harder. Previously, it was shown that the carrier transfer for CdSe/CdTe/CdSe core/crown/crown NPLs with two type-II interfaces is unusually long, in the order of hundreds of ps, showing a hindrance in the

formation of the charge-separated state [178]. Also, in CdSe/CdTe core/crown NPLs, the carrier transfer from CdTe and CdSe domains can take up to 100 ps [202]. The comparable direct recombination and carrier transfer lifetimes in a type-II system enable direct recombination before charge separation.

After investigating the effect of the geometry of the crowns, we focus on the effect of the intermediate crown composition on the recombination dynamics. Herein, we changed the composition of the intermediate crown from selenium-rich to tellurium-rich at constant r = 1/1. Figure 4.13c and d show the absorption and emission spectra of three samples with nominal compositions of x = 0.25, 0.50, and 0.75, respectively, in which x is the fraction of Te. As the Se concentration increases, the share of the absorbance proportion corresponding to the CdSe e-hh peak increases relative to CdTe e-hh absorption peak. This increase is due to the smooth and gradually decreasing CdSeTe alloyed crown peak at high selenium concentrations, shown for CdSe/CdSeTe core/crown heterostructure before [70] and makes the share of CdSe core peak stronger than the crown. Increasing the amount of Se widens the bandgap of CdSeTe alloyed semiconductor with some levels of bowing effect for the composition of Te higher than 30% [186], [203]. The emission spectra of the samples seem to be almost the same for all three compositions, which strongly suggests no switch in the active transition channel. The results show that it is the size of the intermediate crown that decides on the active transition and final recombination dynamics of the NPLs, regardless of their composition. The theoretical calculations results, depicted in Figure 4.13b, suggests that at higher r, the composition of the intermediate crown has little to no effect on the e-h overlap, and only at low r it becomes decisive. Considering the long e-h separation distance, the result makes perfect sense, as the overlap is already decreased and just at short distances changing the band alignment becomes a prominent parameter. One

significant complication arising from the theoretical calculation is that the NPLs with x = 0.5 possess the lowest overlap. The intermediate crown tends to act more like a CdSe core or CdTe crown at boundary compositions. Hence, as the elemental fraction of Te in the intermediate crown gets closer to zero or 1, the prospect of indirect $T_{CT,3}$ recombination becomes stronger, and for the molar fraction of Te (x) equal to 0.5, the intermediate crown has the least nature of the core or final crown. The decay curves of the samples with different intermediate compositions are shown in Figure 4.14 and the decay components are summarized in Table 4.4. In line with the previous observations, NPLs with x = 0.5 have the fastest decay rate compared to x = 0.25 or 0.75 indicating the least type-II characteristic of the sample.

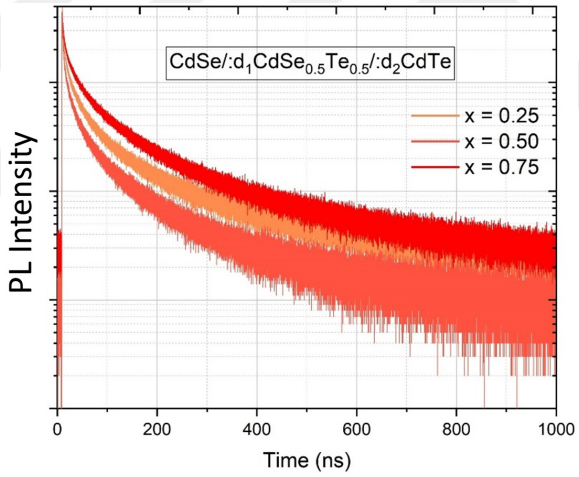

Figure 4.14. TRF decay curves of the CdSe/:1 $CdSe_{1-x}Te_x$/:1 CdTe core/crown/crown NPLs with different compositions of the intermediate crown. Copyright 2023 WILEY-VCH Verlag GmbH & Co. KGaA, Weinheim.

Table 4.4. The summary of the decay components in Figure 4.14.

	TRF decay components							
Sample	A_1	τ_1 (ns)	A_2	τ_2 (ns)	A_3	τ_3 (ns)	A_4	τ_4 (ns)
x = 0.25	16650	1.2	7069	8.6	3520	45.4	733	228.9
x = 0.50	13900	1.3	5782	6.9	2844	36.6	595	177.7
x = 0.75	12120	1.3	6034	12.1	4015	60.9	1445	238.2

	Intensity-averaged lifetime $(\frac{\sum A_i \times \tau_i}{\sum A_i})$	Fractional emission contribution $(\frac{A_i \times \tau_i}{\sum A_i \times \tau_i})$			
Sample	τ_{avg} (ns)	$A_1 \times \tau_1$ (%)	$A_2 \times \tau_2$ (%)	$A_3 \times \tau_3$ (%)	$A_4 \times \tau_4$ (%)
x = 0.25	113.2	4.8	14.9	39.2	41.1
x = 0.50	86.6	6.7	14.9	38.9	39.5
x = 0.75	144.3	2.4	10.8	36.1	50.9

Until now, the collective size of the crowns was kept constant and it was only the ratio of d_{int}/d_f that was changed. To investigate the absolute effect of crown size, we changed the collective size of the crowns, $D = d_{int} + d_f$. As the hole wavefunction only resides on the smaller edges of the NPLs, it is only the longitudinal length of the multi-crown NPLs that was taken into account. Based on the TEM images of the samples shown in Figure 4.1d-f, the absolute collective size of the crowns in the longitudinal direction is 28.8 nm, which is designated as D=1.0. With changing the amount of anion precursor injected, two sets of multi-crown NPLs with D=0.5 (14.4 nm) and D=1.5 (43.2 nm) were also synthesized. The relative size of the collective crowns to the core for these NPLs are 1.2, 2.4 and 3.8 for D = 0.5, 1.0 and 1.5, respectively. The absorption and emission spectra of three samples with the same r of 1 and the same intermediate crown composition of x = 0.50 but different D is shown in Figure 4.13e and f. When D is too small, complete interfacial separation of electron and hole does not happen, and instead, a small emission peak of CdSe emerges at 512 nm. The absorption spectrum does not show any distinct crown peak, and instead, a long tail of charge transfer extends from the e-hh peak of

CdSe to the lower energy side of the spectrum. As D increases, the absorption peaks of the two crowns become apparent, and a second peak starts to emerge for D = 1.0. The decay curves of the NPLs in Figure 4.15 (with the decay components summarized in Table 4.5) show that for the smallest collective crown size, recombination is slower than for bigger collective crowns with D = 1.0 and 1.5. This phenomenon is due to the change in the preferred recombination pathway of electron and hole. For the NPLs with larger crowns, once dormant transition channels ($T_{CT,1}$ and $T_{CT,2}$) become more and more favorable over the least energy channel of $T_{CT,3}$. For these channels with no interspace, electron and hole travel over a shorter distance, which causes a faster recombination dynamic and hence a shorter lifetime.

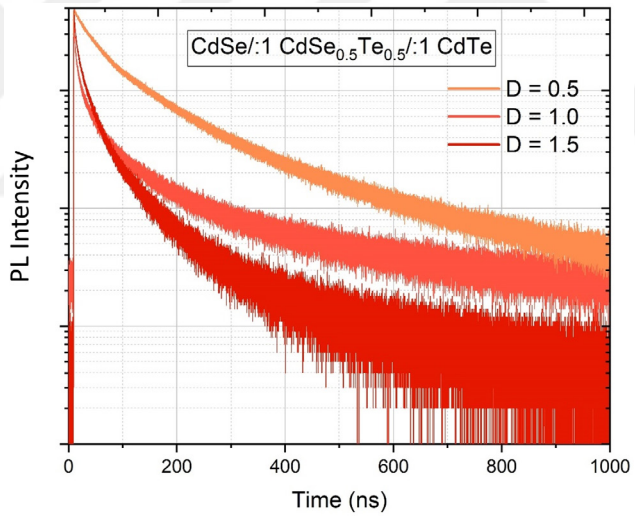

Figure 4.15. TRF decay curves of the CdSe/:1 CdSe0.5Te0.5/:1 CdTe core/crown/crown NPLs with different sizes of the collective crowns, D. Copyright 2023 WILEY-VCH Verlag GmbH & Co. KGaA, Weinheim.

Table 4.5. The summary of the decay components of the CdSe/:1 CdSe0.5Te0.5/:1 CdTe core/crown/crown NPLs with different sizes of the collective crowns, D.

Sample	TRF decay components							
	A_1	τ_1 (ns)	A_2	τ_2 (ns)	A_3	τ_3 (ns)	A_4	τ_4 (ns)
D = 0.5	2610	2.5	7220	31.4	9016	98.6	2881	295.2
D = 1.0	13900	1.3	5782	6.9	2843.7	36.6	595.0	177.7
D = 1.5	10760	1.5	9755	11.3	4941.6	43.7	334.7	205.9

Sample	Intensity-averaged lifetime $(\frac{\sum A_i \times \tau_i}{\sum A_i})$	Fractional emission contribution $(\frac{A_i \times \tau_i}{\sum A_i \times \tau_i})$			
	τ_{avg} (ns)	$A_1 \times \tau_1$ (%)	$A_2 \times \tau_2$ (%)	$A_3 \times \tau_3$ (%)	$A_4 \times \tau_4$ (%)
D = 0.5	175.3	0.4	11.5	45.1	43.2
D = 1.0	86.6	6.8	14.9	38.9	39.5
D = 1.5	60.5	4.0	26.9	52.6	16.8

Deconvolution of the PL peaks in Figure 4.16 (summarized in Table 4.6) shows that the direct recombination transition channel (with FWHM of 21.6 nm) for D = 1.5 is stronger than the case of D = 1 (Figure 4.9), while NPLs with D = 0.5 are the only ensemble with direct recombination at CdSe core with an emission peak wavelength of 513.8 nm.

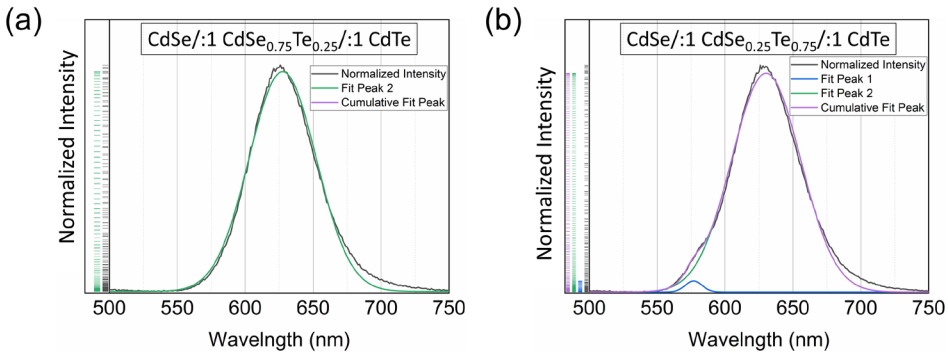

Figure 4.16. Deconvolution of the PL spectra for CdSe/:1 $CdSe_{0.75}Te_{0.25}$/:1 CdTe and CdSe/:1 $CdSe_{0.25}Te_{0.75}$/:1 CdTe core/crown/crown NPLs. Copyright 2023 WILEY-VCH Verlag GmbH & Co. KGaA, Weinheim.

Table 4.6. Summary of the peak deconvolution shown in Figure 4.16.

Sample	Peak 1 position (nm)	Peak 1 FWHM (nm)	Peak 2 position (nm)	Peak 2 FWHM (nm)	Peak 1 share (%)	Peak 2 share (%)
CdSe/:1 $CdSe_{0.75}Te_{0.25}$/:1 CdTe	-	-	629.7	60.4	-	100
CdSe/:1 $CdSe_{0.25}Te_{0.75}$/:1 CdTe	577.0	14.6	629.7	60.0	1.2	98.8

The same argument about the electron retention in the CdTe crown can be used to explain the retention of the hole in the CdSe core, which makes up for the CdSe emission. For small NPLs with D = 0.5, the bicolor PL profile consists of one CdSe band-edge emission and one type-II emission. With increasing D, the band-edge emission diminishes (Figure 4.13f), similar to the previous report of CdSe/CdTe core/crown NPLs [204]. Increasing the size of the crown would increase the lattice strain and hence put the hypothetical potential barrier in the conduction band at a higher level. However, for both of the observations enlarging the crown lead to diminish of the CdSe emission, which means the potential barrier is not the leading cause of CdSe emission. We believe that, although lattice strain can change the electron and hole potential landscapes, but the leading effect in the final e-h overlap is the geometry of the NPLs. For small-crown NPLs a higher

fraction of holes is statistically generated in the core region than in the crowns. Also, the direct recombination lifetime in the CdSe domain is fast, which gives a chance to small portion of the holes in CdSe to recombine directly before the carrier transfer to the interface and separation takes place.

Incorporation of an intermediate crown changes the band alignment of the NPLs, in which the predominant transition is dependent on the relative size of the crowns, the overall size of the crowns, and to some extent, on the energy level of the intermediate crown. In order to gain further insight into the recombination dynamics, we followed the temperature-dependent PL of CdSe/:3 $CdSe_{0.5}Te_{0.5}$/:1 CdTe NPLs, which are shown to have two emission peaks: one direct band-edge and one indirect type-II. The relative emission intensity of the two peaks is different from what was recorded in Figure 4.8b due to the change in the dielectric medium after the transfer of the NPLs from solution to drop-casted film [187]. Figure 4.17a follows the PL spectra at different temperatures. The PL peak wavelength (Figure 4.17b) blue-shifts upon decreasing the temperature due to the lattice contraction of the nanocrystal; however, the NPLs demonstrate a strange switch from dual emission to single emission. While for temperatures above 250K, two emission peaks are resolvable, one of the peaks fades away with a further decrease in the temperature. The peak deconvolution for the first three temperatures of 295, 250, and 200 K is demonstrated in Figure 4.19. The change can also be tracked from the sudden drop in the PL FWHM from 250 to 200 K presented in Figure 4.20. This behavior shows that the indirect type-II recombination channel dominates over the other competitive direct recombination channel at the CdTe crown, T_3. Conclusively, the direct recombination of the multi-crown type-II NPLs is the result of a sufficiently big intermediate crown and thermal activation.

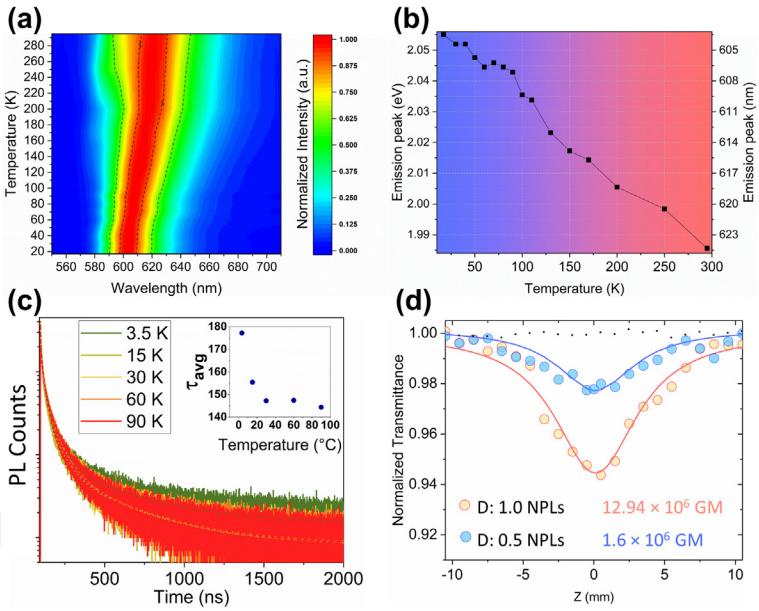

Figure 4.17. Temperature-dependent PL spectra at different temperatures and (b) emission peak position versus temperature extracted from the PL spectra for CdSe/:3 $CdSe_{0.5}Te_{0.5}$/:1CdTe core/crown/crown NPLs. (c) PL decay curves for the same samples. The inset shows the evolution of the lifetime with temperature. (d) Open-aperture z-scan graphs comparing two samples of multi-crown NPLs with the same composition (x = 0.5) and r = 1 and different collective crown sizes, D. The black scatter dots correspond to the measurement for only hexane, and the solid lines are the fittings for the samples. An increase in the size of the NPLs gives a huge rise in the two-photon absorption cross-section from 1.6×10^6 to 12.9×10^6 GM. Copyright 2023 WILEY-VCH Verlag GmbH & Co. KGaA, Weinheim.

The sudden deactivation of the direct transition channel has almost no effect on the evolution of the type-II emission peak vs. temperature (Figure 4.17b), where the peak linearly blue-shifts as temperature decreases. The temperature dependence of the photoluminescence energy was examined by fitting the PL peak energy vs. temperature with Varshni and Bose−Einstein equations both known to best explain the bandgap

energy with temperature, the values obtained for Debye temperature demonstrate high uncertainty and are far below the prediction. Both equations could be fitted with great accuracy (reduced chi-square lower than 10^{-5} for both cases), and both show linear behavior down to T = 17 K.

Varshni semiempirical relation with the general form of [205]

$$E_g(T) = E_g(0) - \frac{\alpha T^2}{T + \beta} \tag{4.4}$$

where $E_g(T)$ is the energy gap at temperature T, $E_g(0)$ is the energy gap at T = 0 K and α and β are constants that β is proportional to Debye temperature, shows that at a relatively high temperature, the change in the lattice parameter decides on the peak position, and the position would change linearly. While, for low temperatures, below Debye temperature, this behavior depends on the electron-lattice interaction and is dependent on the second order of T.

The Bose−Einstein equation was also implemented for better insight into the physics behind the temperature-dependent behavior of the NPLs. The equation with the general form of [206]

$$E_g(T) = E_g(0) - \frac{2\alpha_B}{\exp\left(\frac{\theta_E}{T}\right) - 1} \tag{4.5}$$

where α_B is the coupling force and Θ_E is the average temperature of interaction, takes the phonon-electron interaction into consideration. Θ_E is related to the Debye temperature with $\beta = (4\theta_E) / 3$.

The fitting plots and parameters are depicted and summarized in Figure 4.18 and Table 4.7, respectively. Both models predict the Debye temperature far below the real value, indicating reduced phonon-electron interaction. The linear dependency emphasizes the importance of the electron-hole distance, which is lowered through dilatation of the lattice at low temperatures. The switch from direct-indirect active channels to only indirect active channels is resulted from the reduced distance between electron and hole that happens by lowering the temperature. At this point, we believe that for our type-II NPLs the electron-phonon interaction has minimum effect on the recombination rates and marginal effect on the active indirect channels.

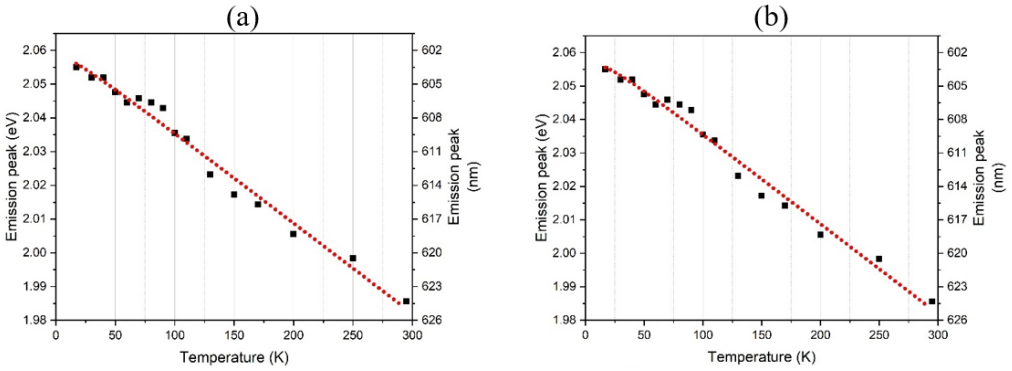

Figure 4.18. Emission peak position (scattered squares) fitted with (a) Varshni and (b) Bose−Einstein type equation for CdSe/:3 CdSe0.5Te0.5/:1 CdTe core/crown/crown NPLs.

Table 4.7. The Varshni and Bose−Einstein fitting parameters.

Varshny equation	$E_g(0)$ (eV)	α (eV/K)	β (K)
	2.05 ± 0.00	0.27 ± 0.02	16 ± 31
Bose−Einstein equation	$E_g(0)$ (eV)	α_B (eV)	Θ_E (K)
	2.05 ± 0.00	6.6 ± 6.6	49 ± 47

Negative deviation in Debye temperature has been shown for QDs compared to the bulk semiconductor and was attributed to the size dependency of the vibration of confined phonons, which decreases in frequency upon reducing the size [206]. However, for the present work, the reason behind the low estimation of the Debye temperature is the positioning of different lattices with different oscillator energies, which leads to low Debye temperatures for each component with high deviation [176], [207]. The linear dependency predicts that the exciton-phonon interaction is negligible in a broad range of temperatures, and the lattice contraction plays a bigger role in the indirect bandgap recombination of electron and hole. This was foreseeable as we show that the separated electron and hole are too sensitive to the interspacing between the core and final CdTe crown.

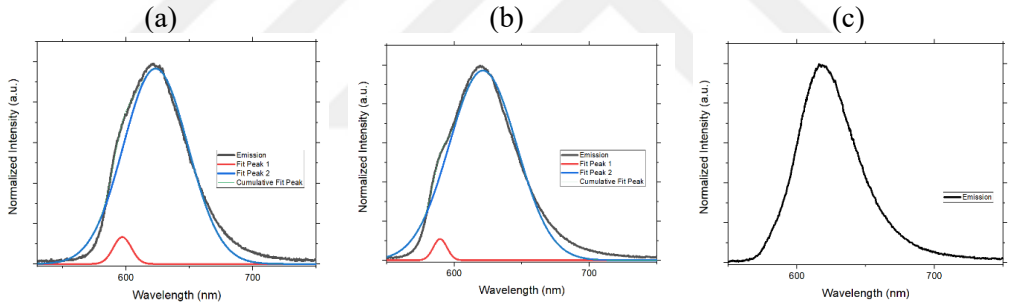

Figure 4.19. PL spectra of CdSe/:3 $CdSe_{0.5}Te_{0.5}$/:1 CdTe core/crown/crown NPLs presented in black line for three temperatures of (a) 295 K, (b) 250 K and (c) 200 K, and peaks deconvoluted (red and blue lines) for 295 and 250 K. Copyright 2023 WILEY-VCH Verlag GmbH & Co. KGaA, Weinheim.

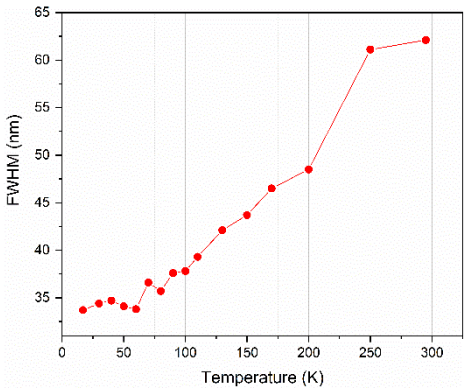

Figure 4.20. Evolution of the FWHM of the PL peak with temperature for CdSe/:3 $CdSe_{0.5}Te_{0.5}$/:1 CdTe core/crown/crown NPLs. Copyright 2023 WILEY-VCH Verlag GmbH & Co. KGaA, Weinheim.

As one of the powerful tools to understand the recombination dynamics and properties of the excitons, we also measured the temperature-dependent TRF [208]. Figure 4.17c shows the decay curves for CdSe/:3 $CdSe_{0.5}Te_{0.5}$/:1 CdTe multi-crown NPLs at low temperatures, which were fitted with a four-exponential function as the emission is originated from different type-II channels. The average lifetime (τ_{avg}) of the sample slightly increases with decreasing temperature for T > 15 K; however, a sharp increase in τ_{avg} from 155 to 177 ns occurs when T is further decreased from 15 to 3.5 K. The energy splitting (Δ) induced by the e-h exchange is responsible for the increase in the lifetime at low T, where the dark state (quasi-forbidden spin) with the lowest exciton energy level comes into effect [209], [210]. The dark state, in oppose to the bright state (spin allowed), has a much longer lifetime, which upon prevention of thermal activation at temperatures corresponding to $k_BT < \Delta$ (k_B is the Boltzmann constant) becomes effective [23], [47]. Previously, it was shown that for the CdTe/CdS core/shell QDs, the lifetime stays almost constant between 20 to 120 K [211]. The same behavior was also reported for 4.5 ML CdSe/CdTe core/crown NPLs except that at approximately T > 40 K, lifetime starts to decrease, with two distinctly opposing bright and dark decay

components [212]. In our case, the sudden increase in the lifetime comes at a much lower T; moreover, only the longest lifetime component shows a meaningful increase while the rest stay almost constant (Figure 4.21). As one of the requirements of quantum devices where it is crucial to minimize the fine structure splitting and depletion of dark excitons [213], [214], these multi-crown type-II heterostructures offer an adjustable alternative quantum system where e-h overlap dominates the e-h exchange reaction and hence the splitting [215], [216]. As we showed, with the implementation of the intermediate crown, the splitting can be finely tuned through the size and composition of the intermediate crown.

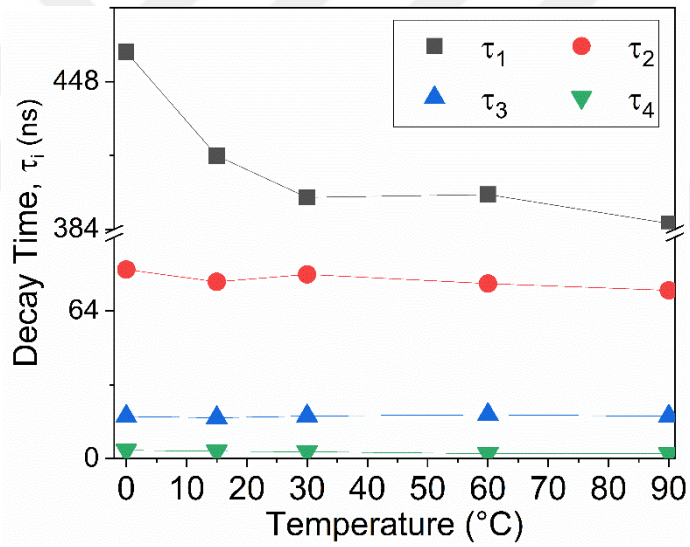

Figure 4.21. Evolution of the decay lifetimes with temperature for CdSe/:3 $CdSe_{0.5}Te_{0.5}$/:1 CdTe core/crown/crown NPLs. Copyright 2023 WILEY-VCH Verlag GmbH & Co. KGaA, Weinheim.

4.4. Summary

In this chapter, we demonstrated the design and synthesis of gradient type-II CdSe/CdSeTe/CdTe core/crown/crown NPLs and investigated their excitonic properties.

The unique electronic heterostructure of these NPLs gave rise to multiple of direct band-edge and indirect type-II channels where upon adjusting the intermediate crown, the e-h wavefunctions and the overlap between them could be adjusted, and the optical properties could be tuned. The geometry of the NPLs exhibited a far more critical factor in the final optical properties and activation/deactivation of the channels compared to the composition of the intermediate crown. We showed the sensitive nature of the active channels to the temperature that besides the conventional electron-phonon interaction, the lattice contraction can also change the overlap and hence the final emission properties. The low-temperature decay behavior of the NPLs revealed a very low dark-bright exciton splitting energy, which is originated from the localization of the electron and hole at the interface of the domains where electrons and holes can readily recombine from the many existing indirect channels. Moreover, the NPLs demonstrated an exceptionally high two-photon absorption cross-section of 12.9×10^6 GM, which scaled superlinearly with the volume of the NPLs. The result further encourages the design and usage of the gradient type-II heterostructures, especially for nonlinear applications of photodetectors, bioimaging and quantum devices.

Chapter 5

Thermodynamic Doping of Core/Shell Heteronanoplatelets

This chapter of the thesis is based on the publication "Thermodynamic Silver Doping of Core/Shell Colloidal Quantum Wells Imparted with Paramagnetic Properties Emitting at Near-Infrared" F. Shabani, M. Ahmad, S. Kumar, S. Delikanli, F. Isik, A. Bhattacharya, A. Petrou, and H. V. Demir, Chemistry of Materials 35 (11), 4159–4170 (2023). Reprinted with permission from [72]. Copyright 2023 American Chemical Society.

5.1. Motivation

The optical properties of the NPLs can best be tuned by changing the thickness and composition. The atomically precise thickness of the NPLs suppresses the inhomogeneous broadening and results in a sharp emission; however, it limits the tunability in between of discrete energy levels. In recent years different strategies have been developed to overcome this problem. Various electronic heterostructures of type-I and type-II core/crown or core/shell, alloying and doping of the NPLs have enabled fine-tuning of their emission spectrum and even extended their emission beyond their bulk

bandgap energy values [51], [92], [124], [216], [217]. In particular, doping of the NPLs with transition metals has not only served as a way of emission tuning but also opened up the possibilities of imparting magneto-optical and magneto-electronic properties [101], [218]–[220]. Due to the non-zero magnetic moment of the dopant ions, these magnetically-doped NCs demonstrate two orders of magnitude higher Zeeman splitting than the non-magnetic ones [221] which pave the way for applications such as magneto-optical gating [222], spin filtering [223], spintronics [224] and charge engineering [225].

Doping of the group II-VI nanocrystals (NCs) with isovalent manganese atoms has long been under extensive investigation and has produced a rich literature [226], [227]. Copper and, to a lower extent, silver have also been investigated as heterovalent dopants with their emissions extending to 1100 nm [36]. So far, there have been two main methods of doping: first, in situ doping or else known as kinetically-controlled doping, in which the dopant ions are incorporated during the nucleation and growth of the NCs and stay there as a result of a metastable thermodynamic condition [228]. Second, post-doping, also known as thermodynamically-controlled or diffusion-controlled doping, in which the dopant ions are introduced to previously synthesized NCs and diffuse into the structure [76], [229]. Incorporating dopant ions deep into the volume of the NCs through post-doping is a challenging process as these ions with different ionic radii, charge and coordination numbers are not favorable to form stable interstitial or substitutional sites. Moreover, the diffusion constant of these ions may be too low due to the hindrance from the lattice or insufficient chemical gradient.

Previously, it was shown that Cu and Ag impurities can replace the host Cd ions in the crystalline lattice sites through cation exchange, where the dopant ions diffuse interstitially [90] or via surface or bulk vacancies into the structure and substitute the Cd ions in the lattice [230]. For both of the proposed mechanisms, the chemical activities

(μ) of the dopant ions in the solution and the lattice play a central role in the doping level. Especially at high doping temperature, where the lattice is flexible enough, chemical activity determines the diffusion direction and equilibrium concentration of the dopant, which in many cases result in depletion of the dopant ions in a reverse exchange reaction, known as self-purification [231], [232]. Mere increase in the dopant precursor concentration is also not the best strategy as it can cause re-nucleation and destabilization of the original NCs and leads to the formation of unwanted species.

Recently, 2.5-6.5 ML CdSe NPLs have been successfully doped with silver through post-doping process. Moreels's group demonstrated high silver doping affinity even at 0 ˚C with silver acetate precursor quenching the band-edge emission [104]. Separately, Dufour et al. looked into the Ag-activated states in CdSe NPLs and concluded that the sub-band energy level of doped NPLs remains fixed in contrast to QDs [92]. While post-silver-doping of 2.5-6.5 ML CdSe NPLs seems feasible, putting a shell with different composition has been a pending challenge because it causes re-emergence of the band-edge emission after deposition of the shell [104]. This problem is usually attributed to the self-purification of the NCs possibly during the shell deposition process [76], [97], [226], [233]–[235].

In this chapter, we propose and demonstrate a high-temperature thermodynamic approach toward silver doping of core/shell NPLs with different shell compositions. This method allows us to dope the core/shell NPLs in a high dopant regime, which previously proved to be challenging due to self-purification and long diffusion distance imposed by the extra layers of shell. We investigate the effect of different shells of ZnS, CdS and alloyed CdZnS on the integrity of the NPLs during the high-temperature doping and demonstrate that the composition of the shells strongly affects the destruction process of the NPLs. NPLs with the tendency to form silver selenide islands on the surface would

undergo etching and dissolution in the irreversible doping regime. In contrast, those with no affinity of surface silver selenide islands would experience fragmentation and segmentation. Since retaining the doping process in the reversible regime is important, NPLs with alloyed CdZnS shell exhibit prolonged doping resistance and they best preserve their integrity at high temperatures. The recombination dynamics were very sensitive to the end-product doped NPLs, where the distribution of silver ions strongly determines the recombination channels and lifetimes. The silver-doped NPLs demonstrate paramagnetic properties, with the bound excitons possessing a negative Brillouin-like dependence in the presence of a magnetic field and a positive Zeeman splitting. Strongly affected by the doping dynamics, NPLs with higher doping tendencies showed enhanced paramagnetic properties.

5.2. Experimental

Materials. Cadmium nitrate tetrahydrate (≥99.0%), sodium myristate (≥99.0%), cadmium acetate dihydrate ($Cd(OAc)_2 \times 2H_2O$, 98%), cadmium acetate ($Cd(OAc)_2$, 99.995%), silver nitrate ($AgNO_3$, 99%), zinc acetate ($Zn(OAc)_2$, 99.99%), selenium (99.99%), 1-octanethiol (≥98.5%), trioctylphosphine (TOP, 90%) oleylamine (OLA, 70%), oleic acid (OA, 90%), 1-octadecene (ODE, 90%), n-hexane (≥97.0%), methanol (≥99.7%), ethanol (absolute) and toluene (≥99.5%) were purchased from Sigma Aldrich.

Synthesis of cadmium myristate. Cadmium myristate was synthesized according to a published recipe with minor modifications [122]. Separately, 31.3 g of sodium myristate was dissolved in 2.5 L of methanol and 12.3 g of cadmium nitrate tetrahydrate was dissolved in 400 mL of methanol. After that, the solutions were mixed and stirred for 4 h for a complete exchange reaction. The white precipitate was separated from methanol and unreacted species and put under vacuum to dry for 48 h.

Synthesis of 4.5 ML CdSe core NPLs. 4.5 ML CdSe core NPLs were synthesized according to a recipe in the literature [122]. In a 100 mL 3-neck flask, 340 mg of cadmium myristate, 24 mg of Se and 30 mL of ODE were mixed and degassed at 95 ˚C for one hour to remove oxygen and other volatile species. Then, the flask was flushed with Ar gas and the temperature was set to 237.5 ˚C. At around 195 ˚C, 120 mg of $Cd(OAc)_2 \times 2H_2O$ was swiftly added to the flask. The solution was kept at 237.5 ˚C for 8 min and then 1 mL of OA was injected into the solution while the flask was quenched in a water bath just after the injection. The solution was collected and diluted with hexane and centrifuged at 6,000 rpm for 6 min. Through addition of extra ethanol and centrifugation, 4.5 ML CdSe core NPLs were precipitated and redispersed in hexane.

Synthesis of CdSe/ZnS, CdSe/CdS and CdSe/CdZnS core/shell NPLs. For the synthesis of core/shell NPLs, 4.5 ML of CdSe core NPLs (with the optical density of one at λ = 350 nm, when 100 µL of the core solution is dissolved in 3 mL of hexane), 7 mL of ODE, 1 mL of OA and x mmol of $Cd(OAc)_2$ and y mmol of $Zn(OAc)_2$,where for ZnS shell x = 0.0 and y = 0.5 mmol, for CdS shell x = 0.5 and y = 0.0 mmol and x = 0.1 and y = 0.4 mmol for CdZnS shell, were mixed in a 50 ml three-neck flask and degassed at room temperature for 1.5 h. Then the solution was degassed at 80 ˚C for a further half an hour, before being flushed with argon gas. 1 mL of OLA was injected into the solution and the temperature was set to 300 ˚C. At 165 ˚C, 2.5 mL of a solution of 1-octanethiol/ODE (0.1 M) was started to be injected into the solution with the injection rate of 10 mL/h for T below 240 ˚C and 4 mL/h for T above 240 ˚C. For thick-shelled samples, the amount of injected anion precursor was doubled, and for the extra thick-shelled samples, it was increased to 6 mL. The flask was kept for an extra 15 min after complete injection and then quenched in water. The solution was diluted with hexane and then centrifuged to remove the unstable and heavy species. The NPLs were separated and collocated through

addition of extra ethanol and centrifugation and then they were redispersed in 4 mL of hexane.

Synthesis of Ag-doped CdSe/$Cd_xZn_{1-x}S$ core/shell NPLs. The doping procedure was performed on the preprepared core/shell NPLs with different shell compositions. First, a silver precursor was prepared by dissolving 0.3 mmol of $AgNO_3$ in a mixture of 150 μL of TOP and 18 mL of ODE. In a typical synthesis, 1 mL of core/shell NPLs (equivalent to a quarter of total core/shell NPLs synthesized in the previous step) and 3.5 mL of ODE were put in a three-neck flask and degassed at room temperature for 1.5 h. The solution was further degassed at 90 ˚C for 30 minutes to ensure that hexane and other volatile spices were removed. Then, the flask was flushed with argon gas and the temperature was increased to 160 ˚C. The silver precursor was injected with an injection rate of 2.5 mL/h. After injection of 1 mL of the precursor, the temperature was increased with 10 ˚C increments and a retention time of 1 min for each step. The solution was quenched in water at 240 ˚C and diluted with 5 mL hexane. Doped NPLs were precipitated by adding extra ethanol and centrifugation and redispersed in hexane for further use.

NPLs Characterization. For the in-solution characterizations, a diluted sample solution in hexane was prepared in a quartz cuvette. PL spectra at an excitation wavelength (λ_{ex}) of 400 nm and absorption profile were collected via Varian Cary Eclipse and Agilent Cary 60 UV-Vis Spectrophotometer, respectively. Time-resolved photoluminescence (TRF) decay curves were collected via Pico Quant FluoTime 200 at a repetition rate of 2.5 MHz and λ_{ex} of 375 nm. The quantum yield (QY) of the NPLs was measured using absolute QY technique with the methodology described in the literature [236]. The setup is comprised of a Hamamatsu integrating sphere, Ocean Optics Maya 2000 spectrometer and a Xenon lamp integrated with a monochromator. Transmission electron microscopy (TEM) imaging was carried out using Tecnai G2 F30 microscope. X-ray photoelectron

spectroscopy (XPS) and X-ray diffraction (XRD) measurements were done by drop-casting and evaporation of a solution of the NPLs with a Thermo Scientific K-Alpha X-Ray spectrometer and Panalytical Xpert Pro MPD, respectively. The magnetic circularly polarized luminescence (MCPL) spectroscopy was carried out according to a previous report of our group [237].

The atomic level of Ag, Cd and Zn were measured via inductively coupled plasma mass spectrometry (ICP-MS). For each sample set, the NPLs were first precipitated by adding ethanol and centrifugation and then redispersed in hexane to remove the unreacted species. The NPLs were then precipitated again and dissolved in an aqueous HNO_3 solvent to digest the NPLs and the measurement was performed on this solution by a Thermo X series II spectrometer. The calibration curves for the elements were obtained by using standard solutions with known concentrations.

5.3. Results and Discussion

A fully thermodynamically-controlled doping process requires the dopant atoms to diffuse into the lattice upon increasing the driving force and diffuse out when the driving force is reversed without disturbing the structure. Figure 5.1 is a schematic of reversible and irreversible doping processes. The concentration of dopant (host) atoms at the beginning of the process is at their highest (lowest) point inside the medium solution (excluding the NPLs). As doping of the NPLs proceeds, the dopant concentration will decrease, and at the same time, the host concentration will increase in the solution as a result of the host-dopant exchange reaction. The driving force of doping is a sum of complex interweaved factors including concentration and temperature. For example, intuitively increasing the dopant concentration should enhance the doping level; however, as was previously shown, increasing the dopant concentration reduces the

doping affinity after a certain point (one reason can be the preference for nucleation over doping) [238], Or as we will show, increasing the temperature would initially increase the doping level in the NPLs, followed by a decrease from a certain point on. A reversible (or non-destructive) doping requires the host and dopant atoms to return to their initial position through reverse exchange reaction and diffusion without affecting the structure (Figure 5.1a). The in-solution concentration of the host and dopant atoms and NPLs will be the same as the beginning in this process. On the other hand, an irreversible (or destructive) doping process is one that upon reversing the driving force, the dopant ions diffuse out of the structure but the process is not complemented with a reverse exchange reaction, or worse, it may be accompanied by dissolution or etching of the crystal. In this destructive process, the in-solution concentration of the dopant and host atoms will increase, while the number of the NPLs may decrease or NPLs may end up partially damaged (Figure 5.1b). One important aspect of this classification is that for most of the doping processes, this is the increase in the forward driving force (temperature, dopant concentration, etc.), which may hit a no-return point where the equilibrium completely changes in favor of some other phenomena such as dissolution, re-nucleation, etching, etc. In that sense, the most important factor is to keep the doping process in the reversible regime and then kinetically trap the dopant atoms in the lattice. Once the equilibrium is disturbed, the chance of doping and self-purification decrease and the NPLs may deteriorate through a destructive and irreversible process.

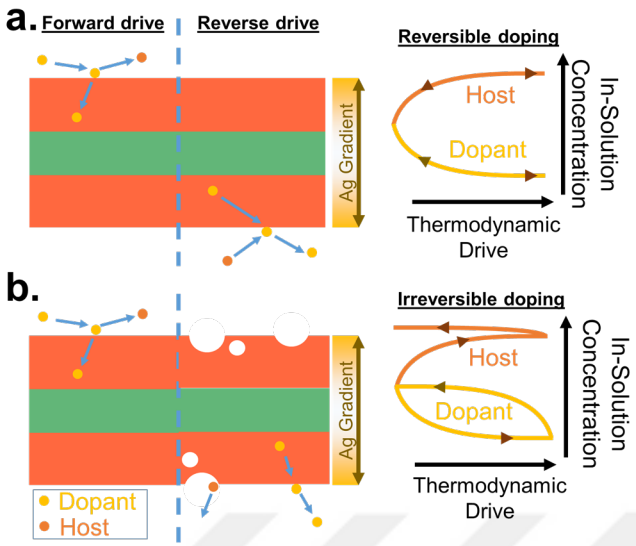

Figure 5.1. Schematics of (a) reversible non-destructive doping and (b) irreversible destructive doping. Under both regimes, increasing the driving force would decrease the in-solution dopant concentration and increase the host concentration. However, for a reversible process, the NPLs retrieve their original composition upon a decrease in the driving force through a reverse exchange reaction, while for an irreversible process, the NPLs cannot regain their initial form (composition, shape, etc.). Copyright 2023 American Chemical Society.

NPLs with hot-injection (HI) shell are known for their high-temperature stability in comparison with the room-temperature grown shell NPLs, traditionally formed through colloidal atomic layer deposition (c-ALD) technique [44], [190]. Conducting our post-doping synthesis at high temperature, these NPLs are the best choices as they can expand their crystalline structure, providing a fluid enough lattice while maintaining their integrity. To tune the shell thickness, the initial amount of anion and cation precursors during HI shell growth was kept constant and the thickness of the shell was carefully controlled by varying the growth time.

For the first set of our doping experiments, we used CdSe/ZnS core/shell NPLs with band-edge emission at 596 nm, indicating a relatively thin shell with 4 MLs of ZnS on each side (absorption and PL spectra are provided in Figure 5.2) [120].

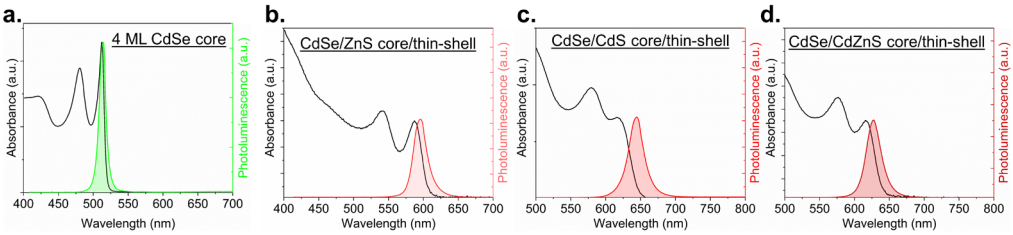

Figure 5.2. (a) Absorption and PL spectra of the initial 4.5 ML CdSe core seeds used for the proceeding shell coatings. Absorption and PL spectra of (b) CdSe/ZnS, (c) CdSe/CdS and (d) CdSe/CdZnS core/thin-shell NPLs, which were mainly used in this study for silver doping. Copyright 2023 American Chemical Society.

The evolution of the absorption spectra of the CdSe/ZnS core/shell NPLs after adding 1 mL of Ag precursor is demonstrated in Figure 5.3a. For all temperatures ranging from 160 to 240 ˚C, the first and second excitonic peaks associated with the heavy and light hole transitions remain distinct, indicating the intact 2D shape of the NPLs. As the doping temperature increases, the charge-transfer (CT) excited state starts to appear due to the fast localization of the hole, which nominally oxidizes Ag^{+} to Ag^{2+} and makes strong bonding with electrons in the conduction band, similar to previous reports on copper-doped QDs and CdSe only-core NPLs [36], [104], [239]. The CT state is not obvious at lower temperatures; however, the emission spectra (Figure 5.3j) develop dopant emission characteristics from the initial temperature of 160 ˚C, which means dopant ions diffuse into the structure even at low temperatures.

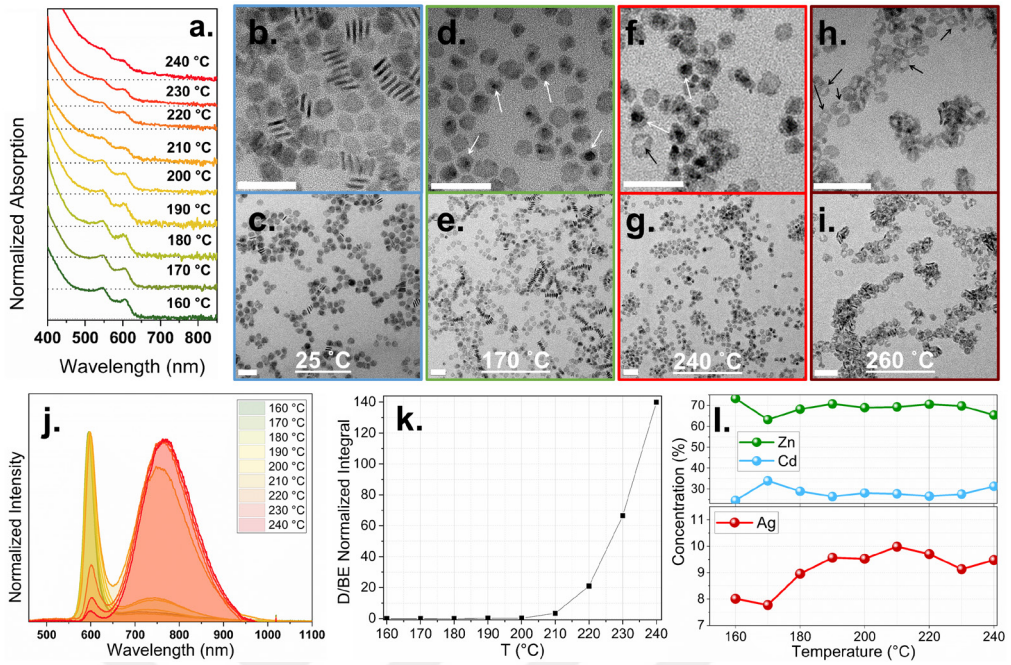

Figure 5.3. (a) Absorption profile for aliquot samples of Ag:CdSe/ZnS core/shell NPLs after complete injection of Ag precursor at 160 ˚C, taken while the doping temperature was increased from 160 to 240 ˚C. TEM images of the samples at four different temperatures of (b-c) 25 ˚C (before the injection of the doping precursor), (d-e) 170 ˚C, (f-g) 240 ˚C and (h-i) 260 ˚C. Scale bars are 50 nm. The black and white arrows show the silver selenide islands and etching sites on the NPLs, respectively. (j) Emission spectra of the aliquot samples corresponding to the NPLs in (a). The inset is a schematic showing the dependency of the position of the mid-gap states on the Ag concentration. (k) Evolution of dopant/band-edge emission ratio with increasing temperature. (l) ICP-MS analysis of Ag concentration. Copyright 2023 American Chemical Society.

We calculated the dopant to band-edge (D/BE) emission fraction simply by dividing the area below the dopant emission peak to the band-edge emission peak. The evolution of D/BE emission versus doping temperature, shown in Figure 5.3k, demonstrates a sudden increase at temperatures above 210 ˚C. However, the band-edge emission does not

completely fade away even at high doping temperatures. It is important to stress that introducing silver to the NPLs at room temperature did not yield any meaningful dopant emission (Figure 5.4), despite the previous reports in the literature for the core-only NPLs [92], [104].

Figure 5.3l shows the concentration of silver, cadmium and zinc in the NPLs determined via inductively coupled plasma mass spectrometry (ICP-MS). Ag concentration increases monotonously with increasing the temperature; however, the evolution of Ag concentration demonstrates two unusual features: First, even at a relatively lower temperature of 160 ˚C, the core/shell structure is already heavily doped with silver. This behavior is unlike the other Ag-doped core/shell samples in this study. Moreover, the increase in the concentration continues up until 210 ˚C where it reaches its maximum of 10% and then declines at higher temperatures. On the other hand, Zn and Cd keep their concentrations after the initial stage and only fluctuate around that concentration. The later drop in Ag concentration shows that the silver ions are moving out of the lattice.

There are multiple factors governing over this anomalous behavior. First, at increased temperature, the expanding crystalline structure of the NPLs grants more freedom for atoms to diffuse in the lattice structure with a higher diffusion constant (D) scaling with $\propto exp\,(-1/T)$ [240]. Moreover, the silver ions residing in the interstitial or substitutional sites act as defects that disturb the homogeneity and purity of the crystalline structure. The equilibrium number of these defects in a crystalline structure also scales up with Arrhenius dependency over temperature [240]. Both factors should principally enhance the doping of the NPLs, but in fact the doping level is decreased. The reason for the shift in the diffusion direction of silver ions from populating the NPLs at a lower T to evacuating them at a higher T is not the solid solution thermodynamic

equilibrium but the higher solubility of the silver ions in the solvent. At the minuscule Ag concentration (3.5 mM), in which the synthesis has been carried out, a small shift in the salt-liquid solubility imposes a huge change on the thermodynamic equilibrium within the NPLs, which ultimately reverses the diffusion direction of the atoms and force them out of their inherent defect sites.

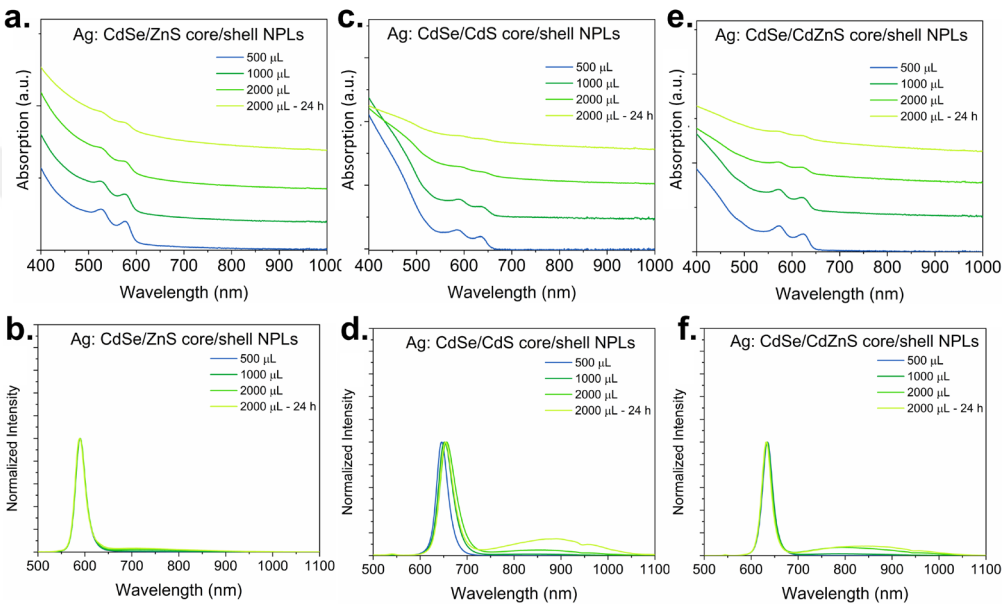

Figure 5.4. Absorption and PL evolution of (a, b) CdSe/ZnS, (c, d) CdSe/CdS and (e, f) CdSe/CdZnS core/shell NPLs doped with Ag(OAc)-ethanol (0.016 M) precursor at room temperature. Although the total amount of Ag is two times higher than the high-temperature method, the dopant emission remained insignificant after 24 h. The highest D/BE ratio achieved was 0.54 for CdSe/CdS core/shell NPLs. Copyright 2023 American Chemical Society.

As can be seen in the TEM images (Figure 5.3b-i) of the samples obtained at different temperatures, the 2D shape of the NPLs is conserved until 240 ˚C. The NPLs underwent dissolution above this temperature with almost all of them (at 260 ˚C) carved out from the center. The dissolution process has not caused any fragmentation of the NPLs as the

image does not show any size change of the NPLs. Moreover, it seems that even at lower temperatures, there are silver-rich islands on some of the NPLs (Figure 5.3d-j), which do not change in numbers significantly by increasing the temperature. Consistent with previous reports in the literature, when the concentration of the dopant ions exceeds a number, a silver metallic tip will form on the NPLs [92]. The TEM-EDS map of ZnS-shelled NPLs doped with Ag in Figure 5.5 shows that away from the islands, silver is distributed homogeneously on the NPLs. However, its concentration on the islands is much higher than in the other regions suggesting that the islands predominantly consist of silver. Also, the concentration of Cd on these islands is slightly higher, which indicates the Cd and Ag alloying. These islands are absent at 260 ˚C suggesting that they are preferably detached and are partially accountable for NPLs shape instability.

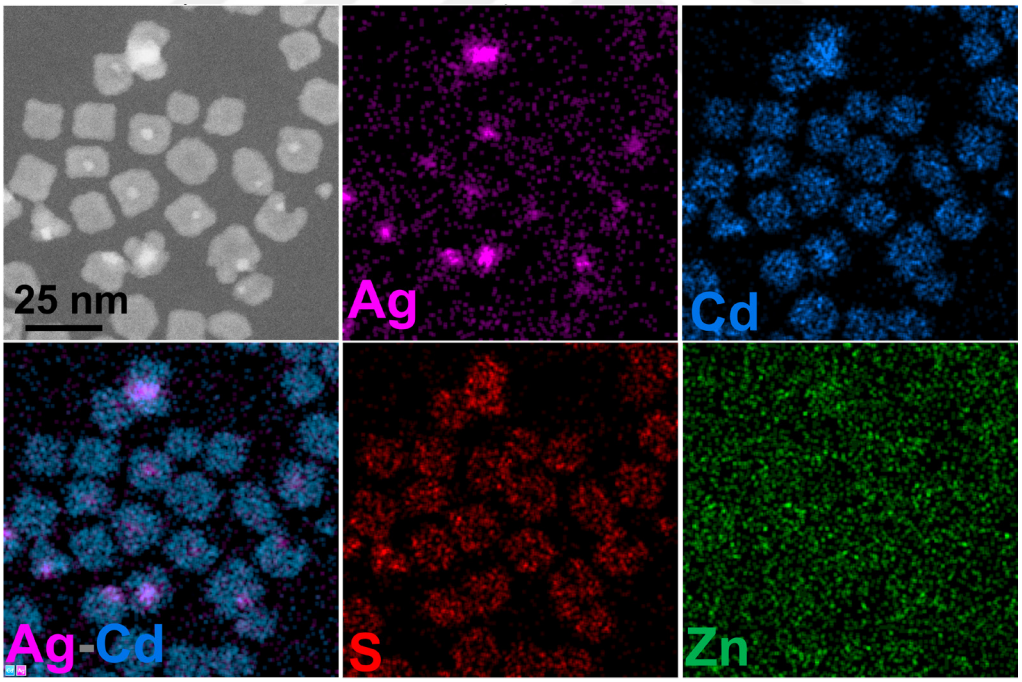

Figure 5.5. TEM-EDS maps of Cd, Zn, S, and Ag for CdSe/ZnS NPLs after doping with no washing. The silver ions are distributed homogenously in the bulk of the NPLs and the Ag concentration is much higher for brighter islands in the TEM image. The mapping

shows the islands predominantly consist of Ag with some Cd alloying. Copyright 2023 American Chemical Society.

Up until 240 ˚C, the share of dopant emission is increasing (Figure 5.3k), despite the decrease in the overall concentration of Ag (Figure 5.3l). This is due to the retention of silver inside the lattice structure that experiences difficulty to diffuse out in comparison to surface silver selenide islands. The TEM images confirm this behavior as the islands are the first silver-rich spots that are dissolved. At temperatures above 240 ˚C, the NPLs lose their entirety and the excitonic features fade away, as seen in their absorption profile in Figure 5.6.

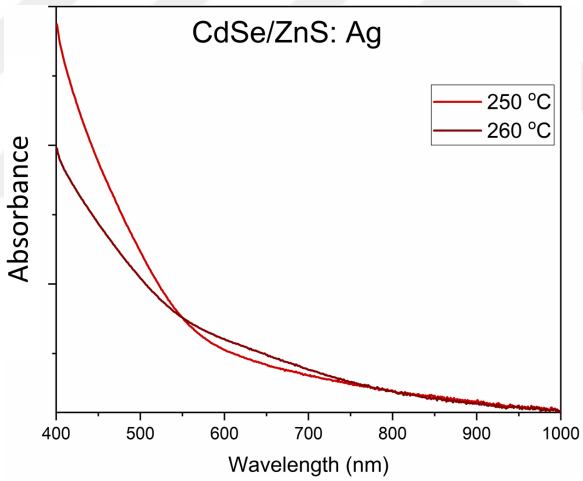

Figure 5.6. Absorption spectra of CdSe/ZnS core/thin-shell NPLs doped with Ag at 250 and 260 ˚C. Copyright 2023 American Chemical Society.

The band-edge and dopant emission peak wavelengths of the NPLs, presented in Figure 5.7, exhibit consistent red shift with increasing temperature. While the band-edge peak position is less sensitive to silver concentration (it only red-shifts from 596 to 602 nm), the dopant emission exhibits great sensitivity to the presence of silver and red-shifts from 729 nm to a maximum of 769 nm. The behavior is reasonable as the silver ions would

not alter the size of the NPLs, and hence do not affect the confinement and direct bandgap energy. However, silver ions populate the sub-band energy levels that introduce new conduction band-sub-band transition channels with lower energy. The very small red shift in the band-edge emission peak wavelength is probably due to the island formation of the NPLs at high temperatures, which produces a thickness distribution at mid-range temperatures and increases the full-width-at-half-maximum (FWHM, Table 5.1).

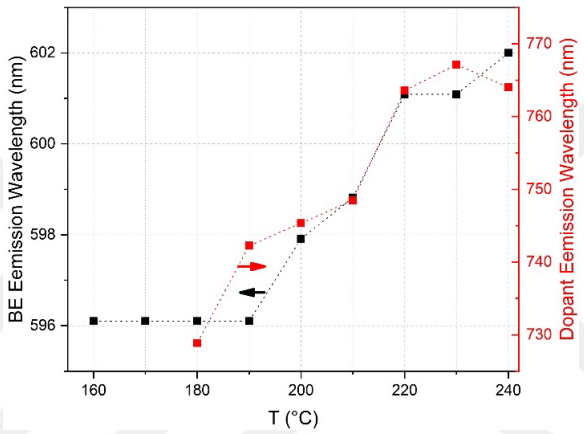

Figure 5.7. Band-edge and dopant emission peak wavelength evolution with increasing the temperature for CdSe/ZnS core/thin-shell NPLs. Copyright 2023 American Chemical Society.

Table 5.1. The summary of the emission peak wavelength and FWHM with increasing the temperature for CdSe/ZnS core/thin-shell NPLs.

Temperature (˚C)	160	170	180	190	200	210	220	230	240
BE Emission (nm)	596	596	596	596	598	599	601	601	602
BE FWHM (nm)	25	26	27	28	30	27	25	23	23
Dopant Emission (nm)	-	-	729	742	745	749	764	767	764
Dopant FWHM (nm)	-	-	95	108	109	127	132	135	137

With the same 4ML CdSe core, changing the thin shell of ZnS with CdS should not change the doping process substantially; however, CdSe/CdS core/shell NPLs follow completely different doping dynamics. For the second core/shell NPLs doping, we used CdSe/CdS core/thin-shell NPLs emitting at 652 nm (Figure 5.2c), corresponding to approximately 4-5 MLs of CdS shell on each side [119]. The red shift in the original band-edge emission wavelength from ZnS-shelled to CdS-shelled NPLs is mainly due to the smaller valance band offset between CdSe and CdS than ZnS and partially because of thicker core/shell NPLs [50]. The first difference from the case of ZnS-shelled NPLs after the introduction of Ag precursor is the decreased number of islands (Figure 5.8a-c). These islands are probably the reason for extra higher Ag concentration for ZnS-shelled NPLs in comparison to CdS-shelled NPLs, especially at low temperatures. Another fundamental difference between these two sets of NPLs is the destruction mechanism at high temperatures. While for ZnS-shelled NPLs some holes form at above 240 ˚C due to the dissolution of NPLs from preferred silver selenide domains, CdS-shelled NPLs demonstrate fragmentation and segmentation at higher temperatures. The fragmented NPLs are obvious at 260 ˚C in Figure 5.8c. Both sets of NPLs do not tolerate high doping temperatures and disintegrate but for ZnS-shelled NPLs the process involves preferred dissolution sites provided by silver selenide islands rather than the fast fracturing of CdS-shelled NPLs.

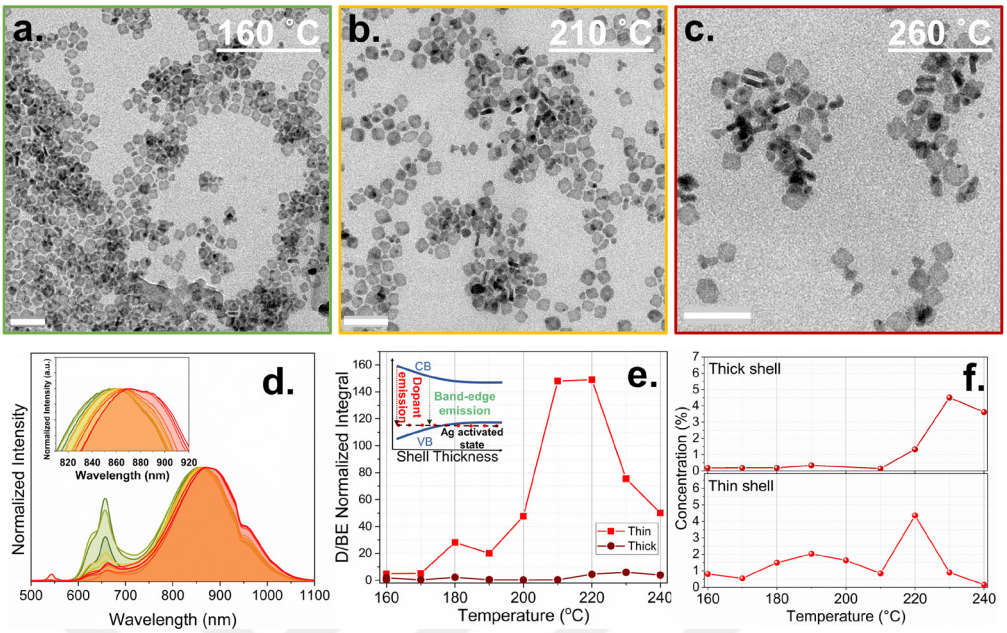

Figure 5.8. TEM images of CdSe/CdS core/shell NPLs at (a) 160 ˚C, before the injection of Ag precursor and (b, c) at 210 and 250 ˚C, respectively, after the injection of Ag precursor. Scale bars are 50 nm. (d) Evolution of PL spectra of Ag:CdSe/CdS core/shell NPLs within the temperature range of 160 (green line) to 240 ˚C (red line). The inset follows the red shift in the dopant emission with increasing the temperature. (e) D/BE emission ratio. The inset is a schematic showing the decrease in the band-edge with increasing the shell thickness. The thick-shelled samples show negligible dopant emission as the Ag-activated states are no longer inside the bandgap. (f) Ag concentration measured via ICP-MS from aliquots taken during the synthesis. For thick-shelled samples, the core/shell synthesis was prolonged and its emission was red-shifted compared to the thin-shelled NPLs due to the confinement relaxation. Copyright 2023 American Chemical Society.

The evolution of photoluminescence spectra in Figure 5.8d sheds more light on the doping kinetics of the CdS-shelled NPLs. Firstly, even at 160 ˚C, the share of dopant emission exceeds the band-edge emission and increases continuously until 220 ˚C.

However, above 220 ˚C, the band-edge emission again starts to gain prominence, as seen in Figure 5.8e (thin). The behavior is unlike the CdSe/ZnS core/shell NPLs where in spite of a much higher initial Ag concentration, the dopant emission remains negligible until 200 ˚C and also after decreasing the Ag concentration no resurgence of the band-edge emission is observed. This different behavior indicates a higher diffusion coefficient of Ag ions in the lattice of CdSe/CdS core/shell NPLs that requires less thermal energy and can enter and exit the lattice much easier. For ZnS-shelled NPLs, much of the silver concentration is coming from the surface islands but for CdS-shelled NPLs, Ag has diffused more effectively at low temperatures. The higher diffusion coefficient dictates the faster dopant emission emergence and, at the same time, leads to a higher self-purification rate and the NPLs recovery at high temperatures when the doping driving force is reversed.

To fully understand the doping process of these NPLs, we also synthesized another set of CdSe/CdS core/shell NPLs with a thicker shell. These NPLs, designated as thick, demonstrate weaker sensitivity in their emission spectra to silver concentration and their D/BE ratio does not exceed even 10 at all temperatures (Figure 5.8e), while their concentration of silver is increasing similar to the thin-shelled NPLs. Figure 5.8f demonstrates the concentration of Ag in the thin-shelled NPLs, which is in line with the PL spectra. A sudden increase in the Ag concentration at 220 ˚C is followed by a decrease at higher temperatures, similar to the ZnS-shelled NPLs, meaning self-purification is also in process. Ag concentration in thick-shelled NPLs undergoes the same sudden increase at 230 ˚C and then again decreases (Figure 5.8f). The higher doping/self-purification equilibrium temperature indicates that the diffusion time and distance required for Ag ions in thick-shelled NPLs is increased and, consequently, the whole process is shifted to higher temperatures. More importantly, increasing the shell thickness decreases the

direct bandgap energy of the NPLs, and resultantly, decreases the chance of the mid-gap states to form inside the bandgap. These thick-shelled NPLs show a minor sign of dopant emission. This observation also confirms previous reports where the silver-activated states do not depend on confinement and thickness [92]. The dopant-emission peak position for thin-shelled NPLs in Figure 5.8d (summarized in Table 5.2) exhibits consistent red shift from 852 to 862 nm. For the CdS-shelled NPLs, the peak position is much deeper in the red side of the spectra compared to ZnS-shelled NPLs with a maximum of 767 nm. Also, the red shift is merely 10 nm, in comparison to 38 nm for ZnS-shelled NPLs. Both of these differences are because of the much lower conduction band offset of CdS-shelled NPLs, which decreases the mid-gap charge transfer energy. More importantly, as the red shift in the dopant emission exhibits a significant decrease, there must be a saturation point where for tighter bandgaps, the silver mid-gap state would not fall in between the valance and conduction band. For this reason, our thick CdS-shelled NPLs did not demonstrate the same level of D/BE emission.

Table 5.2. Band-edge and dopant emission peak wavelength and FWHM for CdSe/CdS core/thin-shell NPLs. FWHM for the band-edge emission is not reported as the samples demonstrate two band-edge emission peaks due to NPLs breakage. Copyright 2023 American Chemical Society.

Temperature (°C)	160	170	180	190	200	210	220	230	240
BE emission (nm)	652	651	654	654	654	654	653	654	648
Dopant emission(nm)	852	853	852	861	862	861	861	861	861
Dopant FWHM (nm)	143	144	144	143	142	141	140	140	138

To cross-examine this hypothesis, we synthesized extra-thick CdS-shelled NPLs and tried to dope them using the same procedure. The PL evolution of these NPLs with

temperature is demonstrated in Figure 5.9a. For all of the temperatures, the share of dopant emission is less than the band-edge emission (Figure 5.9b) and increasing the temperature only seems to direct it toward zero-level.

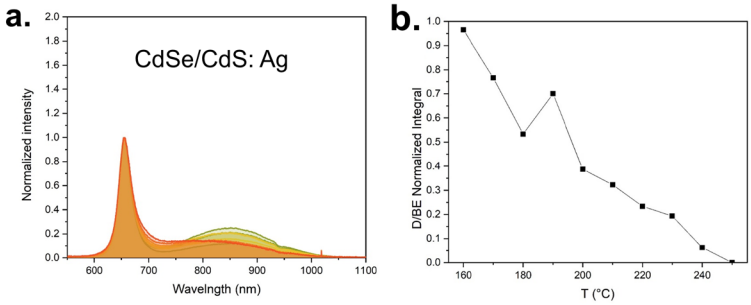

Figure 5.9. (a) PL spectra evolution between 160 ˚C (green line) and 240 ˚C (red line) and (b) D/BE emission ratio for extra-thick CdSe/CdS core/shell NPLs. Copyright 2023 American Chemical Society.

So far, it has been shown that ZnS-shelled NPLs collapse during high-temperature doping because of the formation of silver selenide islands that later act as sweet etching spots, while for CdS-shelled NPLs, the fragmentation is the leading cause of destruction. For the third set of our experiments, NPLs with thin CdZnS alloyed shell were synthesized and the same doping procedure was performed. The evolution of the PL spectra with increasing the doping temperature is shown in Figure 5.10a (summarized in Table 5.3). The original band-edge emission peak wavelength of CdZnS-shelled NPLs is between those of ZnS- and CdS-shelled NPLs (Figure 5.2d). At a low temperature of 160 ˚C, the dopant emission is completely absent, while above 220 ˚C, the dopant emission overrides the band-edge emission (Figure 5.10b, thin). The behavior is unlike the previous doped NPLs while drawing some similarities with each of them. The TEM image of these NPLs at 240 ˚C in Figure 5.10c indicates that the number of the silver selenide islands is higher than that of CdS-shelled NPLs and lower than that of the ZnS-

shelled NPLs. The D/BE emission goes to infinity (Figure 5.10b, thin), which means that Ag ions effectively diffused into the lattice and the dopant emission is not only the result of the islands on a sparse number of NPLs. The TEM image of doped NPLs at 260 ˚C, with no cleaning after sampling, is shown in Figure 5.10d. Interestingly, for these overheated NPLs, fragmentation and dissolution exist but both of them are inhibited to the highest degree. Dissolution is minimized and the fewest of the NPLs are broken and cleaved. If the broken pieces are not considered, the lateral size distribution of the NPLs is almost the same, which indicates that small pieces are part of the broken NPLs that do not exist anymore. As was expected, the silver selenide islands are completely wiped out due to their high-temperature instability that was observed for ZnS-shelled NPLs.

Table 5.3. Band-edge and dopant emission peak wavelength and FWHM for CdSe/CdZnS core/thin-shell NPLs. Copyright 2023 American Chemical Society. Copyright 2023 American Chemical Society.

Temperature (˚C)	160	170	180	190	200	210	220	230	240
BE emission (nm)	641	642	641	644	642	-	-	-	-
BE FWHM (nm)	25	26	25	25	26	-	-	-	-
Dopant emission (nm)	820	821	842	834	840	841	836	842	841
Dopant FWHM (nm)	143	143	147	145	148	147	150	154	168

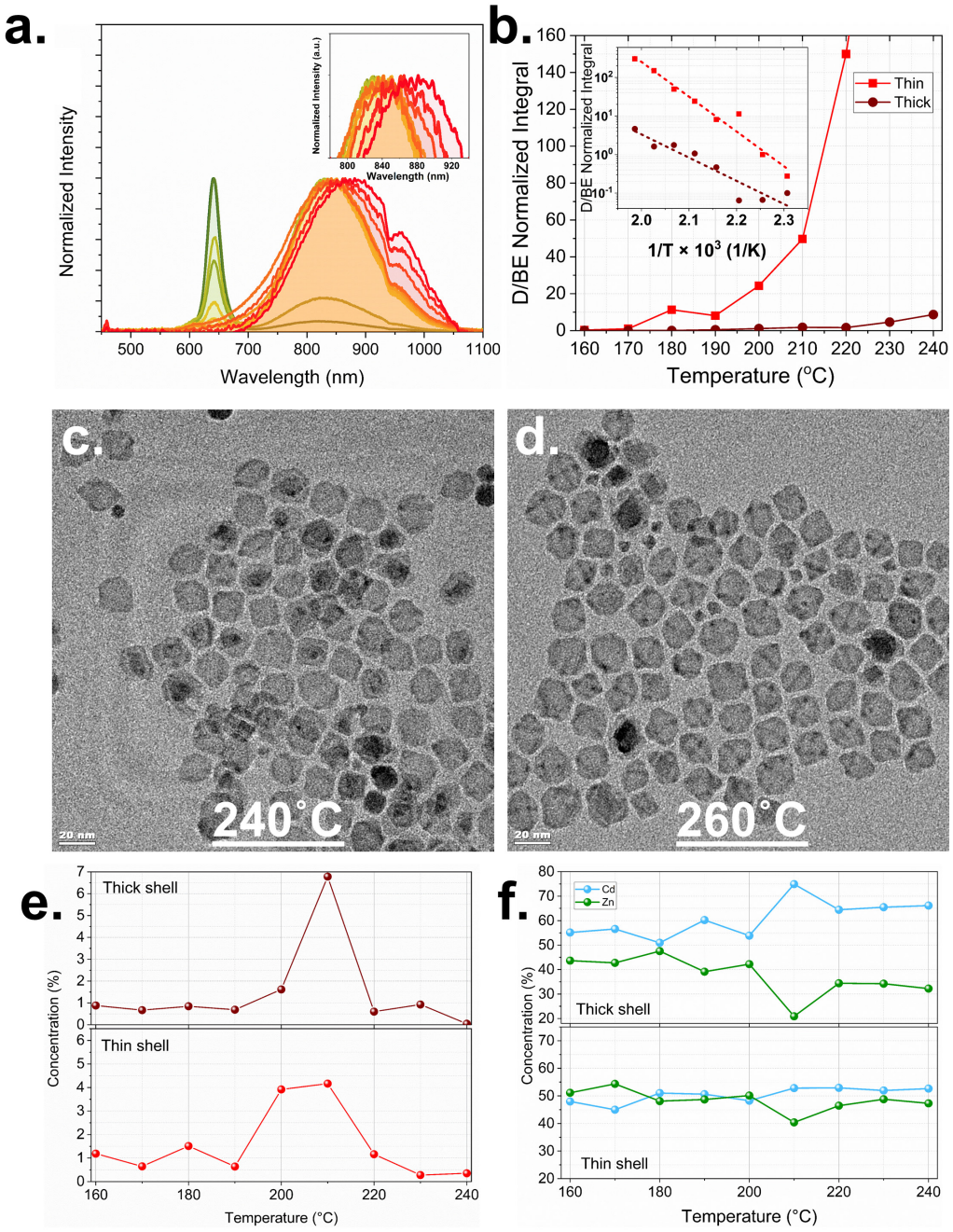

Figure 5.10. (a) PL emission spectra of CdSe/CdZnS core/shell NPLs after injection of the Ag precursor from 160 ˚C (green line) to 240 ˚C (red line). The inset follows the red shift of dopant emission with increasing temperature. (b) D/BE emission ratio for thin- and thick-shelled NPLs. The inset is the Eyring plot for the same data. (c, d) TEM images of the samples for thin CdZnS-shelled NPLs taken at 240 and 260 ˚C, respectively. (e)

Concentration of Ag and (f) Cd and Zn for CdZnS-shelled samples obtained via ICP-MS analyses. Copyright 2023 American Chemical Society.

The PLQY of the CdZnS-shell NPLs was measured at different temperatures and is shown in Figure 5.11. At lower temperatures, the PLQY is at its highest and for higher temperatures, it drops, probably due to the severe reaction condition. The high-temperature doped NPLs possess a high PLQY of 44%, with all the share of emission coming from the dopant. The PLQY goes up to a maximum of 56% for the partially doped NPLs with 90% of the PL coming from the dopant.

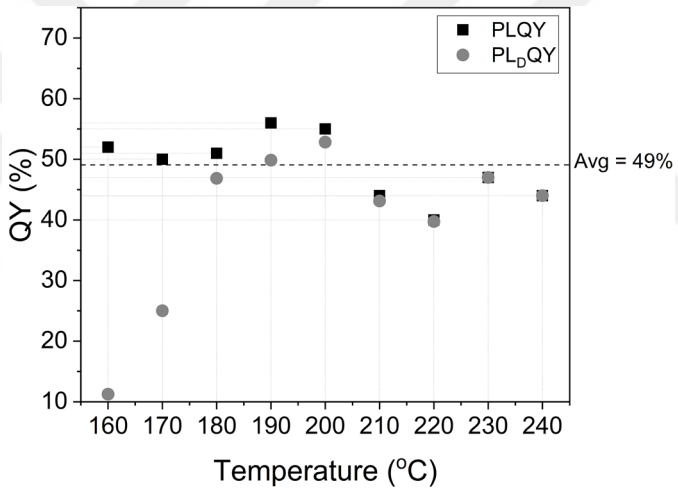

Figure 5.11. PLQY of CdSe/CdZnS core/thin-shell NPLs at different temperatures and the share of the dopant emission, in which $PL_DQY = PLQY \times D/(D+BE) \times 100$. Copyright 2023 American Chemical Society.

The crystalline structure of the CdSe/CdZnS core/shell NPLs was examined through X-ray diffraction (XRD) measurement before and after doping (Figure 5.12). Doped NPLs showed no significant change in the diffraction peak positions indicating the preservation of the original zinc blende crystalline structure. There was no trace of characteristic peaks

of either monoclinic or cubic Ag_2S and Ag_2Se to suggest nucleation of side products [241]. The XPS spectra of silver for doped CdSe/CdZnS core/shell NPLs in Figure 5.13 verifies successful doping of the NPLs with peaks at 367.88 and 373.88 eV corresponding to Ag $3d_{5/2}$ and Ag $3d_{3/2}$ orbitals, respectively. The unchanged S 2p and Se 3d XPS peak profiles and Ag 3d peaks suggest the silver ions sit in tetrahedral sites surrounded by four sulfide ions [242], [243].

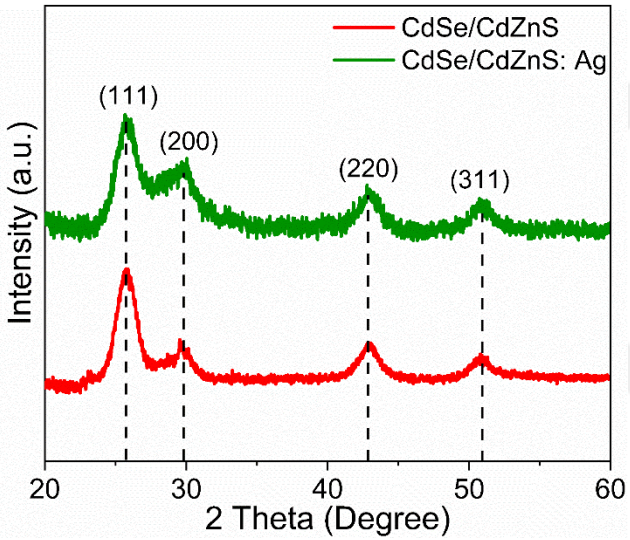

Figure 5.12. X-ray diffraction patterns of CdSe/CdZnS core/shell NPLs before and after silver doping. Copyright 2023 American Chemical Society.

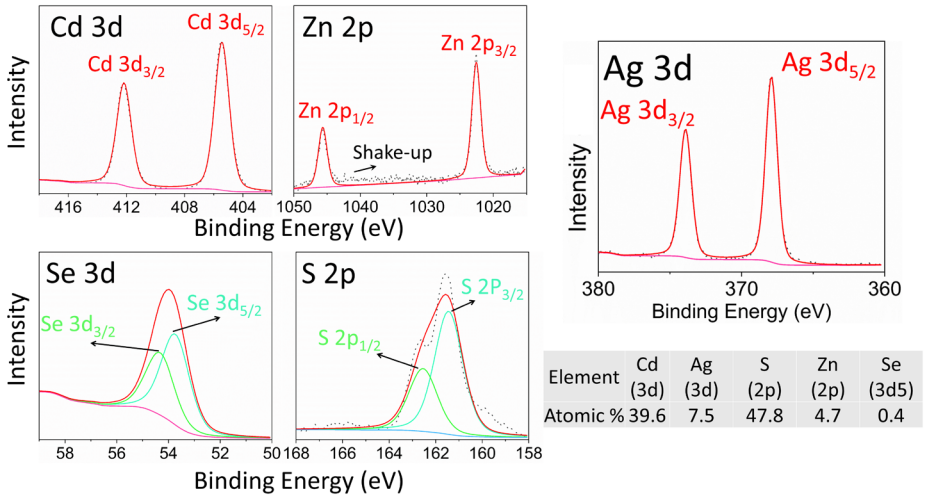

Element	Cd (3d)	Ag (3d)	S (2p)	Zn (2p)	Se (3d5)
Atomic %	39.6	7.5	47.8	4.7	0.4

Figure 5.13. High-resolution X-ray photoelectron spectroscopy (XPS) spectra of host elements of Cd 3d, Zn 2P, Se 3d, S 2P, and dopant Ag 3d states for a representative sample of CdSe/CdZnS core/thick-shell NPLs doped with silver at 240 ˚C, along with the elemental composition extracted from the XPS measurement. Copyright 2023 American Chemical Society.

For another ensemble of NPLs with thick CdZnS shell, the share of dopant emission did not increase substantially even at high temperatures (Figure 5.10b). However, if D/BE emission for thin- and thick-shelled NPLs are plotted on a semi-log scale (inset of Figure 5.10b), the increase in the dopant emission share follows similar behavior over temperature for both sets of NPLs. The absence or minimization of the dopant emission for thick-shelled NPLs happens as the silver mid-gap states are dropped out of the bandgap of the NPLs, as was shown for CdS-shelled NPLs. The linear behavior of D/BE in the semi-log plot may be an indication of the Arrhenius type of activation of the doped NPLs where D/BE $\propto exp\,(-1/T)$. The calculated slope for this linear fit (dash lines) for thin-shelled NPLs is 1.5 times higher than that of the thick-shelled NPLs. This slope in Arrhenius equation is related to the activation energy ($\propto \frac{-E_a}{RT}$, where E_a is the activation energy and R is the gas constant), which is unpredictably higher for thin-shelled NPLs

than the thick-shelled NPLs. The higher E_a implies a slower process and probably less doping.

Figure 5.10e demonstrates the concentration of silver in both sets of CdZnS-shelled NPLs. Thin-shelled NPLs have a lower Ag concentration at their highest point than the thick-shelled ones with a lower doping temperature threshold. In line with the results from D/BE emission, the higher activation energy is responsible for lower doping in the thin-shelled NPLs. This is also similar to the results in Figure 5.8e and f, where thick CdS-shelled NPLs are more doped than the thin-shelled NPLs but still possess low dopant emission. Thick NPLs provide more interstitial or substitutional sites with deeper concentration gradient over their structure, which is necessary for any diffusion process. Figure 5.10f shows that, for both sets of NPLs, Zn is preferably more prone to give its position to silver at high temperatures, which is more pronounced for thick-shelled NPLs where Ag concentration is 1.5 times higher.

Introducing ligands to the NCs during or just before the end of the synthesis is one of the conventional methods to increase the stability and performance in the colloidal synthesis of NCs. Herein, two common ligands that are used extensively in the synthesis of NPLs were added to the doped NPLs to see how they may affect the doping. For this purpose, two sets of CdSe/CdZnS core/thin-shell NPLs were taken from the mother batch for doping.

At high temperatures above 120 ˚C, the NPLs undergo partial dissolution, in which CdSe core NPLs completely dissolve in ODE at 240 ˚C [124]. However, as shown, our NPLs do not dissolve and lose their integrity even above 240 ˚C because of the protective inorganic shell layer around them. The original reason behind partial or complete

dissolution is the equilibrium concentration of metal in ODE. At the beginning of the synthesis, no Ag ions are dissolved in ODE; hence the equilibrium can be described as

$$MX \rightleftharpoons M^{2+} + X^{2-} \tag{5.1}$$

where M is Cd or Zn and X is S or Se. Addition of $AgNO_3$ (or any other metallic salt) would compensate for part of the dissolution, as solid $AgNO_3$ forms an equilibrium both with ODE and with Cd and Zn from the NPLs. The latter exchange reaction is responsible for doping of NPLs. Herein, a more comprehensive description would be

$$MX + AgNO_3 \rightleftharpoons Ag_xM_{1-x}X + Ag_{1-x}M_x(NO_3) \rightleftharpoons Ag^+ + M^{2+} + X^{2-} + NO_3^- \tag{5.2}$$

which explains why addition of $Cd(OAc)_3$ at high temperature preserves the uniformity of the NPLs, as reported elsewhere.

For the first experiment, 500 µL of oleylamine (OLA) was injected into the flask just before quenching the solution in water. OLA is known to etch the NPLs and reduce their excitonic features due to the loss of their 2D shape. It accelerates the dissolution process and reduces the destruction temperature of CdSe to 150 ˚C. OLA is also known to increase the quantum yield and colloidal stability of the NPLs due to the surface passivation. For this reason, we added OLA just before the quenching of the solution in water. Figure 5.14a demonstrates the absorption and emission peak of the NPLs after centrifugation and removal of ODE. Although the dopant emission is in place, its peak position is blue-shifted compared to the OLA-free NPLs. More importantly, the band-edge emission did not quench completely. The TEM images in Figure 5.14b and c confirm the intact 2D shape of the NPLs, with Ag concentration of 4.6%, according to energy dispersive X-Ray (EDX) measurement. The retained band-edge emission implies

that the NPLs were not doped effectively, probably due to the self-purification process that happened quickly after addition of OLA.

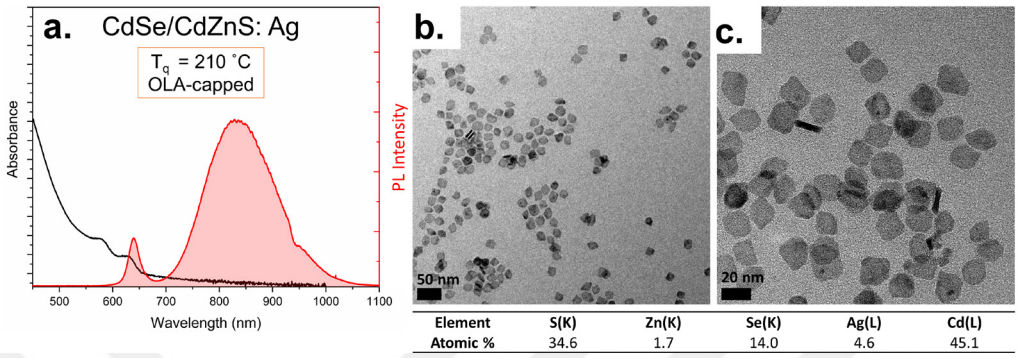

Figure 5.14. (a) Absorption (black) and emission spectra (red) of Ag-doped CdSe/CdZnS: core/thin-shell NPLs. OLA was introduced to the reaction flask just before quenching in water. (b, c) TEM images of the same NPLs with EDS analysis of the corresponding elements given below. Copyright 2023 American Chemical Society.

For the second experiment, all the reaction conditions were the same except that instead of OLA, 500 µL of oleic acid (OA) was added before quenching. The band-edge emission was effectively quenched and the dopant emission was also red-shifted (Figure 5.15a). However, complete quench of the band-edge emission was not achieved, probably due to some degrees of self-purification. The shape of the NPLs remained intact and resembled those from the previous sample (Figure 5.15b and c). However, Ag concentration is increased to 8.9%, which is two times higher than the OLA-passivated NPLs.

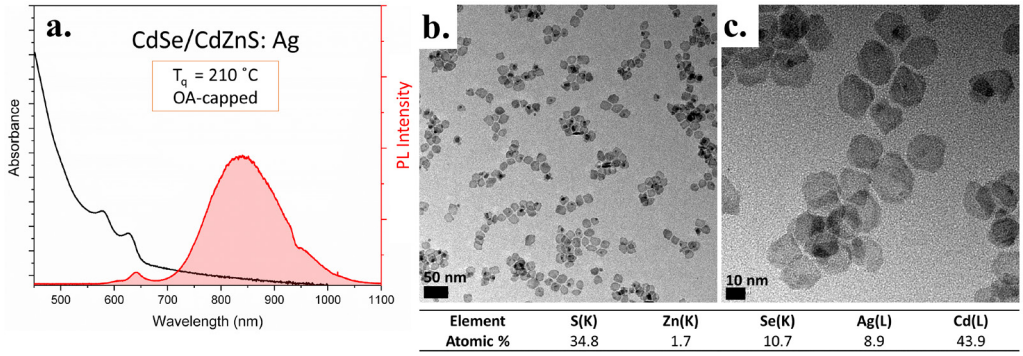

Figure 5.15. (a) Absorption (black) and emission spectra (red) of Ag:CdSe/CdZnS core/thin-shell NPLs. The flask was quenched just after addition of OA. (b, c) TEM images of the same NPLs with EDS analysis of the corresponding elements given below. Copyright 2023 American Chemical Society.

Both ligands we used possess long carbon chains with functional groups at the end. The fast self-purification of the NPLs is probably originated from these functional groups, which can further scavenge Ag atoms from the NPLs. Knowing that Ag ions are closer to the surface than the depth of the NPLs, they are more prone to be evacuated from the surface by these functional groups.

Alongside the spectral shift of the emission peak wavelength, heterovalent doping of the semiconductor NCs is known to alter the emission kinetics drastically. Here, three new sets of half-doped thin-shelled NPLs (having a dopant to band-edge PL peak intensity ratio equal to one) with three different shell compositions of ZnS, CdS and CdZnS were prepared and their emission decays were measured via time-resolved fluorescence (TRF) spectroscopy. Figure 5.16a depicts the PL decay curves for these three samples, where each curve is fitted with a three-exponential function.

It is known that even for near-unity core/shell NPLs reaching mono-exponential decay is not possible due to the existence of nonradiative recombination channels [50]. The

samples exhibit band-edge recombination lifetimes (τ_{avg}) from 4.0 to 15.4 ns, which is the characteristic lifetime of thin-shelled NPLs (details in Table 5.4a). The comparatively fastest recombination lifetime of ZnS-shelled NPLs is originated from its thinner shell, which results in lower band-edge emission wavelength and closer proximity of the electron and hole (for comparison, see the absorption and emission spectra of the initial NPLs presented in Figure 5.2).

Implementing Ag ions into the lattice opens up new channels for carrier trapping and consequently increases the recombination lifetime. Generally, a shorter recombination lifetime indicates fast nonradiative channels where trapped electrons on the surface of the NC recombine nonradiatively with hole [244], [245]. We showed that ZnS-shelled NPLs are more prone to the nucleation of silver selenide islands. These islands act as electron scavengers and accelerate electron trapping on the surface of NPLs. Moreover, ZnS-shelled NPLs undergo etching and carving, which in turn reduces the electron-hole distance. The maximum τ_{avg} for CdZnS-shelled NPLs is the result of both higher stability and lower fast nonradiative channels of these NPLs. The dopant emission decay curves for all three samples demonstrate at least two orders of magnitude longer recombination lifetime (Table 5.4b), similar to previous reports in the literature [246], [247]. For ZnS-shelled NPLs, it was shown that the PL emission has the highest energy with the least red shift for its dopant emission wavelength compared to the other two samples. The shortest τ_{avg} for its dopant emission is originated from the highest emission energy and, as a result, its shortest electron-hole recombination pathway. In accordance with the donor-acceptor pair (DAP) model, the distribution of the Ag mid-gap states implies that those electrons and holes that stand closer to each other are more affected by the Coulomb interaction and therefore recombine faster and produce higher PL quanta energy [248], [249].

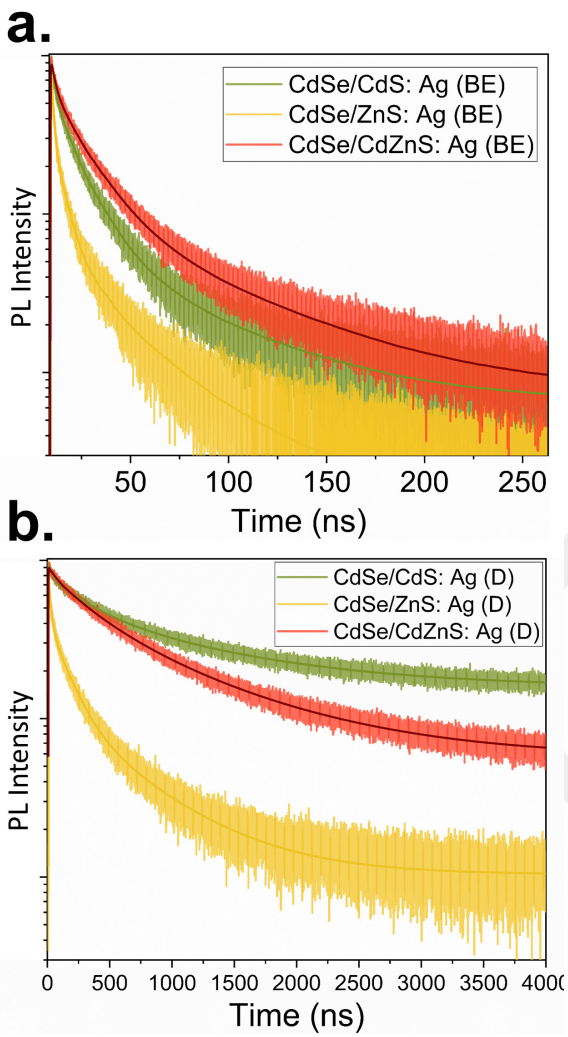

Figure 5.16. TRF decay curves of thin-shelled NPLs with respective heterostructures of CdSe/ZnS, CdSe/CdS and CdSe/CdZnS core/shell. All three samples were half-doped with Ag, in which the dopant to band-edge PL peak intensity ratio equals one: (a) band-edge emission decay after doping and (b) dopant emission decay curve. Copyright 2023 American Chemical Society.

Table 5.4. TRF decay components of half-doped thin-shelled NPLs for (a) band-edge emission and (b) dopant emission. Copyright 2023 American Chemical Society.

(a)							
Sample	τ_1 (ns)	τ_2 (ns)	τ_3 (ns)	$\frac{A_1.\tau_1}{\sum A_i.\tau_i}$ (%)	$\frac{A_2.\tau_2}{\sum A_i.\tau_i}$ (%)	$\frac{A_3.\tau_3}{\sum A_i.\tau_i}$ (%)	$\frac{\sum A_i.\tau_i}{\sum A_i}$ (ns)
Ag:CdSe/CdS (BE)	11.5	49	1.4	56.4	37.4	6.1	10.1
Ag:CdSe/ZnS (BE)	6.3	36.8	0.9	41.6	43.4	15	4.0
Ag:CdSe/CdZnS (BE)	14.8	58.1	1.8	49	46.7	4.4	15.4
(b)							
Sample	τ_1 (ns)	τ_2 (ns)	τ_3 (ns)	$\frac{A_1.\tau_1}{\sum A_i.\tau_i}$ (%)	$\frac{A_2.\tau_2}{\sum A_i.\tau_i}$ (%)	$\frac{A_3.\tau_3}{\sum A_i.\tau_i}$ (%)	$\frac{\sum A_i.\tau_i}{\sum A_i}$ (ns)
Ag:CdSe/CdS (D)	1163.8	287.9	36.3	82.6	16.3	1.1	629.1
Ag:CdSe/ZnS (D)	139.9	601.1	17.5	37.5	55.8	6.7	134.5
Ag:CdSe/CdZnS (D)	73.8	100.8	337.5	1.7	77.9	20.3	620.2

Unlike isovalent dopants such as Mn, Ag^+ ions with a full d shell are capable of capturing the photoexcited holes from the valance band of the host material. The new Ag^{2+} ions possess an unpaired electron, which gives rise to a non-zero magnetic moment and can be detected through magnetic circularly polarized luminescence (MCPL) spectroscopy [237]. To observe the effect of Ag^+ ions on the magnetization, it is essential to keep the dopant content restricted so that the band-edge emission remains strong for the measurement [101]. Using our half-doped CdSe/CdZnS core/shell NPLs, the left circularly polarized (LCP, σ_+) and right circularly polarized (RCP, σ_-) components of the PL at the band-edge were measured at T = 3 K for magnetic fields (B) up to 7 T (Figure 5.17a and b).

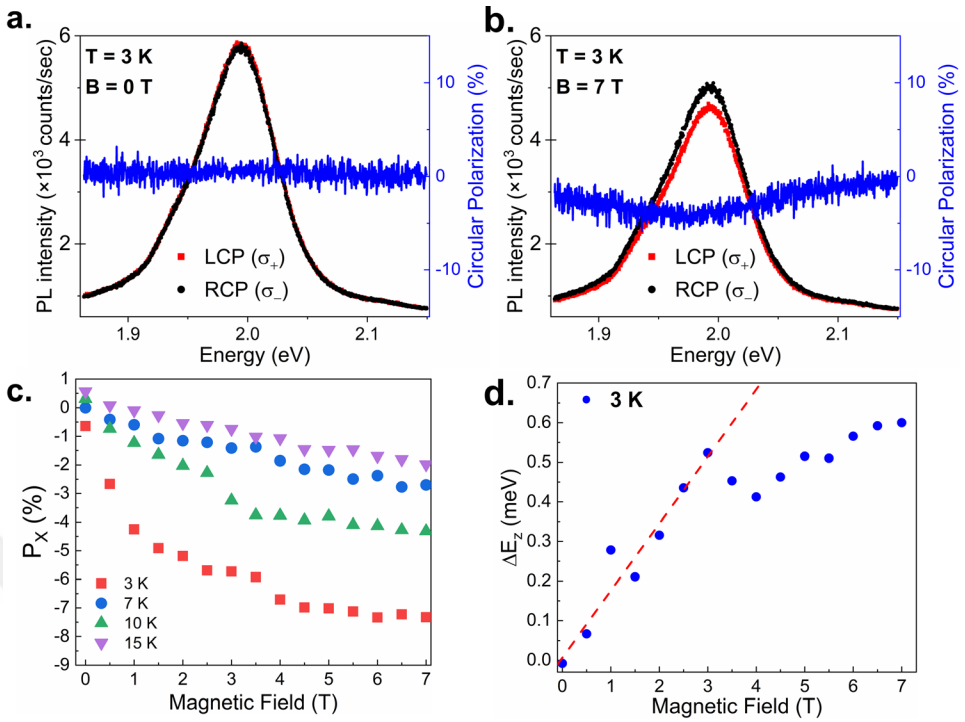

Figure 5.17. (a) Right circularly polarized (RCP) and left circularly polarized (LCP) components of photoluminescence for partially silver-doped CdSe/CdZnS core/shell NPLs at 3 K and in the absence of magnetic field. The circular polarization, shown in blue line, is almost zero in the band-edge emission vicinity. (b) Same measurement at an increased magnetic field of 7 T. The bound exciton feature, at energy P_X, demonstrates negative circular polarization. (c) P_X vs. the magnetic field (B) for a temperature range from 3 to 15 K. (d) Bound exciton Zeeman splitting (ΔE_Z) as a function of B at T = 3 K. Copyright 2023 American Chemical Society.

The temperature-dependent PL of these NPLs in the band-edge vicinity (Figure 5.18) exhibits emission peak broadening with decreasing temperature, attributed to the strain variation and interaction of band-edge excitons with the silver impurities.

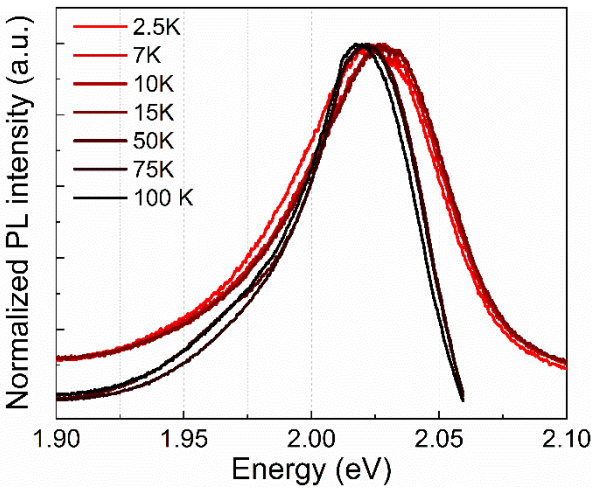

Figure 5.18. Temperature-dependent PL of partially doped CdSe/CdZnS core/shell NPLs in the band-edge vicinity. The emission peak broadening with decreasing temperature can be attributed to the strain variation and interaction of band-edge excitons with the silver impurities. The only prominent feature is coming from the bound excitons while the absence of free exciton is probably originated from the high dopant concentration. Copyright 2023 American Chemical Society.

Defining circular polarization as $(I_+ - I_-)/(I_+ + I_-) \times 100$, where I_+ and I_- are the intensities of the σ_+ and σ_-, respectively, the polarization remains zero with no apparent feature for B = 0 T. With increasing magnetic field to 7 T, a negative value of polarization related to the bound excitons was observed. The bound exciton circular polarization (P_X) as a function of the magnetic field is depicted in Figure 5.17c for a temperature range from 3 to 15 K, which follows a negative Brillouin-like dependence. This behavior is in contrast with undoped samples, which exhibited linear dependancy [237] on the magnetic field, whereas Mn-doped samples exhibit positive P_X [250]. The bound exciton Zeeman Splitting (ΔE_Z), defined as $\Delta E_Z = E_+ - E_-$ (where E_+ and E_- are the energy of σ_+ and σ_+ components, respectively), for the half-doped CdSe/CdZnS core/shell NPLs at T = 3 K is demonstrated in Figure 5.17d. With increasing B, ΔE_Z increases linearly and reaches

a saturation point at ~ 3 T. Moreover, ΔE_Z is positive ($E_+ > E_-$), which confirms the negative circular polarization ($P_X < 0$). The same MCPL measurements were carried out for the half-doped CdSe/CdS core/shell NPLs and are shown in Figure 5.19. Both sets of NPLs exhibit negative Brillouin-like temperature dependence of P_X and positive saturable ΔE_Z. However, the value for P_X and ΔE_Z for CdSe/CdZnS core/shell NPLs is roughly two times higher than that of CdSe/CdS core/shell NPLs, probably due to the enhanced diffusion of the dopant ions into the better-reserved lattice of the host NPLs. The results also provide further evidence of the existence of Ag dopants with paramagnetic properties.

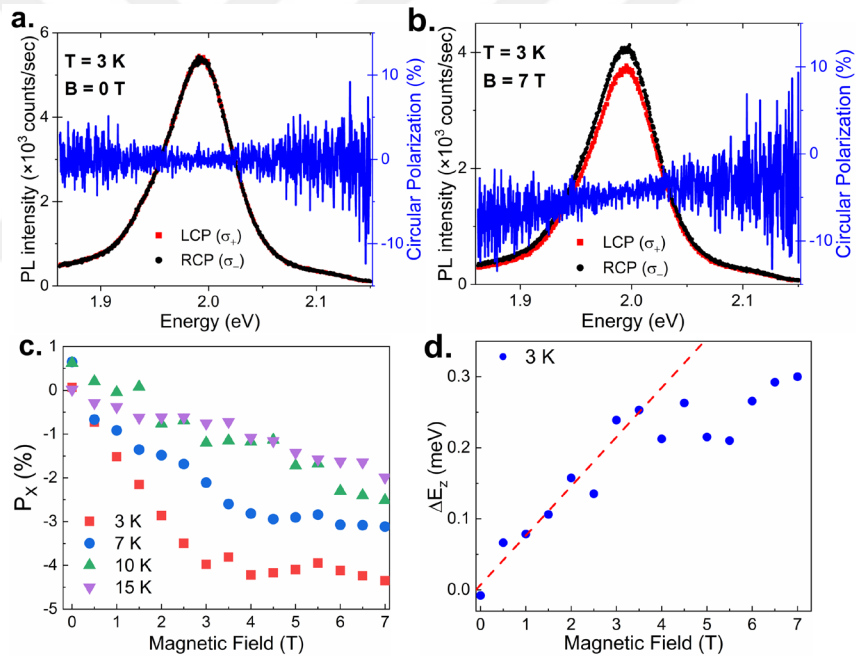

Figure 5.19. (a) RCP and LCP components in the vicinity of the band-edge emission for partially silver-doped CdSe/CdS core/shell NPLs at 3 K and in the absence of magnetic field. The circular polarization, shown in blue line, is almost zero in this vicinity. (b) Same measurement at an increased magnetic field of 7 T. The bound exciton feature at energy P_X exhibits weak circular polarization compared to the CdSe/CdZnS core/shell NPLs. (c) P_X vs. magnetic field for a temperature range between 3 and 15 K. (d) Bound

exciton Zeeman splitting (ΔE_Z) as a function of B at T = 3 K. Both P_X and ΔE_Z follow the same behavior shown for CdSe/CdZnS core/shell NPLs; however, the circular polarization is smaller and ΔE_Z is slightly shifted to higher. Copyright 2023 American Chemical Society.

5.4. Summary

To summarize this chapter, the core/shell heterostructures of CdSe-based NPLs were successfully doped with silver through a thermodynamically controlled doping procedure. We have shown that the destruction mechanism of the NPLs in the irreversible doping regime changes from dissolution and etching, for ZnS-shelled NPLs, to fragmentation and segmentation, for CdS-shelled NPLs. The NPLs with the alloyed shell of CdZnS possess the highest resistance to high-temperature doping with both destruction mechanisms active to a minimum extent. The emission spectra of the doped NPLs can be tuned through the doping level as long as the silver mid-gap state stays within the bandgap of the NPLs. Moreover, the recombination dynamics were shown to be sensitive to the distribution of dopant ions inside the heterostructure or on the surface, which is dependent on the composition of the shell. The silver-doped CdSe/CdZnS core/shell NPLs demonstrated superior paramagnetic properties with P_X and ΔE_Z roughly two times higher than CdSe/CdS core/shell NPLs, which suggests lattice preservation and lattice doping of the NPLs. These findings should encourage further investigation for spintronic applications and spin-based devices based on doped colloidal quantum wells where light-induced modulation of the properties is required.

Chapter 6

Surface-Modified Group I-III-VI Nanocrystals

6.1. Motivation

Group I-III-VI colloidal semiconductor NCs provide a versatile and flexible platform to realize NCs with a vast range of compositions and shapes. The soft crystalline structure of these NCs allows heavy alloying, doping and cation exchange, which opens the way for a diverse range of ternary compositions, such as $AgInS_2$ (AIS), $CuInS_2$ (CIS) and $CuInSe_2$ (CISe) [251]–[254], to their Al^{3+} and Mn^{3+} doped compositions [255]–[257], and further to quaternary compositions including $CuInSeS_2$ and $CuAgInS_2$ [258], [259].

The optical properties of these NCs can be optimized through engineering the shape, composition and size, which determines the bandgap energy and midgap states, and ultimately covers a broad range of the spectrum from the visible to the near-infrared, [260]–[262]. As one of the effective methods to tune and enhance the optical properties, growing an inorganic shell of CdS or ZnS is employed, similar to group II-VI NCs, which

prevents the electron and hole from reaching surface defects [263], [264]. This core/shell structure, known as type-I, can be obtained by high-temperature thermal decomposition of the precursors and subsequent nucleation and growth of the shell on the surface of the NCs. At the initial stage of the shell coating, the diffusion and exchange of the Cd and Zn tightens the quantum confinement, resulting in an apparent blue shift in the PL spectrum, and with the increasing shell size, the PL spectrum red-shifts [264], [265]. The literature of the group I-III-VI NCs is mostly focused on the seed-mediated or single-pot synthesis methods, in which the shell precursor is introduced after the core NCs are formed either in the same reaction pot or a separate one [261], [266]. However, the cation exchange method is usually employed to modify the original atoms (In, Ag, and Cu) of the group I-III-VI NCs or to obtain anisotropic shapes of NCs by full-exchange of Cd- or Zn-based NCs to capture their shape [267].

The solution-processed group I-III-VI QDs make one of the best candidates to replace the polycrystalline silicon transistor for their low process and fabrication cost [268]. While most of the studies on the solution-processed transistors were focused on the Pb- or Cd-based devices, it was not until recently the interest in engineering I-III-VI QDs started to grow [269]–[271]. Previously, it was shown that CIS and CISe QDs possess inherently *p*-type behavior due to their high number of point defects [272]. The high number of defects of these NCs is the result of incomplete miscibility of the Cu_2S-In_2S_3 solid solution, which produces defects in the lattice structure to relax the lattice strain [272] The metal vacancy in the lattice and the antisite defects of Cu_{In} (Cu instead of In) result in an extra positive charge that amplifies the *p*-type behavior [273] The metal-terminated surface of these NCs with unsaturated ligand passivation also traps the carriers and contributes to the higher positive charge [274]. The unbalanced charge of NCs, low hole mobility compared to electron mobility and bulky ligands that increase

the distance between the NCs, composition and surface modification are imperative to enhance the electronic properties and their device performance [61].

Two main strategies are employed to enhance the performance of the solution-processed electronic devices: first, exchanging the surface bulky ligands with shorter, usually inorganic, ligands, which decreases the hopping distance and increases the number of carriers per unit volume [272], [275]–[278]. Second, modification of the composition and nullification of the acceptor sites [273], [277]. The transport behavior of the NCs usually does not change with the first strategy, as the excessive positive charge is unchanged after the ligand exchange [33]. However, with the soft lattice of the group I-III-VI NCs, compositional modification is possible due to easier diffusion and exchange of the host atoms with a cation source. Previously, it was shown that by annealing the transistor in the presence of an In source, the device switches to non-degenerate *n*-type behavior with enhanced carrier mobility [273]. More recently, the ability to overhaul the charge balance of the NCs by terminating the surface with an extra anion layer has been shown, resulting in very high electron mobility comparable to Pb- and Cd-based field effect transistors [33].

In this chapter, a universal approach toward surface and composition modification of the group I-III-VI NCs is proposed and demonstrated. The method is shown for three sets of group I-III-VI NCs, namely CIS, AIS, and CISe, where upon ZnS treatment, the optical properties are tuned in the near-infrared region. The original bulky ligands of oleylamine are first replaced with S^{2-}, and the NCs are treated with a Zn precursor that covers the surface with a layer of ZnS. Moreover, the Zn^{2+} cations are shown to diffuse in the lattice and exchange with the vacancy sites or host cations. The surface treatment technique can be repeated for at least three times, in which the morphology of NCs is not changed but their size increases with each treatment cycle. The original CIS and AIS NCs

demonstrate *p*-type behavior with poor hole mobility; however, the FETs based on the surface-treated CIS and AIS NCs demonstrate a switch to *n*-type behavior with a 10^5-fold enhancement in their carrier mobility. The enhancement in the carrier mobility is originated from the decreased distance between the NCs, injection of a negative charge and nullification of the acceptor sites due to Zn treatment. The final FET devices exhibit an electron mobility of 6.99 cm V^{-1} s^{-1} and on/off ratio in the order of 10^5, comparable to the best solution-processed FETs.

6.2. Experimental

Materials. Indium(III) acetate ($In(OAc)_3$, 99.99%), copper(I) iodide (CuI, ≥99.5%), silver acetate (Ag(OAc), ReagentPlus®, 99%), zinc nitrate hexahydrate ($Zn(NO_3)_2.6H_2O$, reagent grade, 98%), cadmium nitrate tetrahydrate ($Cd(NO_3)_2.4H_2O$, ≥99.0%), ammonium sulfide solution ($(NH_4)_2S$, selenium (99.99%), sulfur (99.98%), 40-48 wt. % in H_2O), 1-dodecanethiol (DDT, ≥98.0%), oleylamine (OLA, 70%), N-methylformamide (NMF, 99%), ethanol (absolute), toluene (≥99.5%), n-hexane (≥97.0%), and acetonitrile (≥99.9 %), were purchased from Sigma Aldrich.

Synthesis of $CuInS_2$ (CIS) QDs. CIS QDs were synthesized according to a published recipe in the literature with minor modifications. Typically, 57.1 mg of CuI, 175.2 mg of $In(OAc)_3$, 32.5 mg of elemental S, 1.5 mL of DDT and 5 mL of OLA were added to a 50-mL flask. The solution was stirred intensely under vacuum in the room temperature to remove the volatile species for 30 min. After that, the flask was flushed with Ar gas and the temperature was adjusted to 180 °C to initiate the nucleation and growth of the CIS QDs. The growth was allowed for 2 min and then the flask was quenched in a water bath. The solution was collected and diluted with 6 mL of hexane and centrifuged at 6000 rpm for 6 min to remove the big particles. The QDs were precipitated from the

unreacted precursors by centrifugation and the extra addition of ethanol. Finally, the QDs were redispersed in hexane for future usage.

Synthesis of $AgInS_2$ (AIS) QDs. The AIS QDs were synthesized with the same method as CIS QDs, except that the CuI was replaced with 50.1 mg of Ag(OAc).

Synthesis of $CuInSe_2$ (CISe) QDs. For the synthesis of CISe QDs, typically, 57.1 mg of CuI, 175.2 mg of $In(OAc)_3$, 86.9 mg of elemental Se and 5 mL of OLA were added to a 50 mL flask. The solution was degassed at room temperature for 30 min and then the flask was flushed with Ar gas. Then, the temperature was adjusted to 180 °C to initiate the nucleation and growth of the QDs. The growth was allowed for 2 min, and subsequently, the flask was quenched in a water bath. The solution was collected and diluted with 5 mL of hexane and then centrifuged at 6,000 rpm for 6 min to remove the unstable particles. The supernatant was centrifuged again at 6,000 rpm for 6 min with additional ethanol to precipitate the CISe QDs. Finally, the QDs were redispersed in hexane for future usage.

Sequential MS (M: Cd or Zn) shell treatment of CIS, AIS and CISe QDs. The shell treatment for all three different sets of QDs follows the same procedure. Typically, the QDs are first precipitated and redispersed in 5 mL hexane in a centrifuge tube and 5 mL of NMF is added to the solution, which makes a biphasic solution. Then, 100 μL of $(NH_4)_2S$ was added to the solution, replacing the original ligands with a S^{2-} layer on the surface and transferring the QDs to the NMF. After 5 min of intense mixing, the hexane was removed from the solution and the QDs were precipitated through addition of toluene and centrifugation and redispersed in NMF for three times to remove the unreacted $(NH_4)_2S$ in the solution. Then, 3mL of cation precursor (zinc nitrate hexahydrate or cadmium nitrate tetrahydrate in NMF, 0.4 M) was added to the solution

and mixed intensely for approximately 20 min to form a layer of metal on the surface. To remove the unreacted precursor, the QDs were precipitated/redispersed three times by centrifugation. The anion and cation treatment were applied three times, and after each complete layer, 1 mL of OLA was added to the precipitated QDs to transfer them to hexane.

Transistor fabrication. The FET devices were fabricated for CIS and AIS QDs. The FETs typically consist of the terminals of drain, source and gate with a layer of dielectric between the gate electrode and semiconductor layer. The FETs were fabricated with a top-gate/bottom-contact architecture on a glass substrate, and Au electrodes were interdigitated on the devices. The Cr/Au (5/100 nm) source and drain interdigitated electrodes, each with a channel width of 30 mm and a length of 50 μm, were fabricated by the photolithography technique. The AIS and CIS solutions were spin-coated on the substrate of interdigitated Au electrodes. To prevent oxidization of the film, the devices were encapsulated in a glass coverslip and cured resin. The FETs were characterized under ambient conditions with a Keithley 4200 SCS.

QDs characterization. The in-solution QDs characterizations were performed on dilute samples by a quartz cuvette. The absorption and PL spectra were collected via Agilent Cary 60 UV-Vis Spectrophotometer and Varian Cary Eclipse, respectively. TRF measurement was performed by Pico Quant FluoTime 200 at an excitation wavelength of 375 nm. The XRD and XPS measurements were carried out on drop-cast film samples via Panalytical Xpert Pro MPD, and the TEM imaging was performed via Tecnai G2 F30 microscope.

Device characterization. The fabricated FETs with CIS- and AIS-based QDs were subjected to repeated measurements of their electrical characteristics recorded under

ambient conditions. The electric parameters were calculated using a standard analytical theory of FET according to the following equation:

$$I_{DS,sat} = \frac{WC_i}{2L}\mu(V_{GS} - V_{Th})^2 \quad (6.1)$$

where $I_{DS,sat}$ is the saturation source-drain current, V_{Th} is the threshold voltage, V_{GS} is the gate voltage, μ is the field-effect mobility, W and L are the channel width and length, respectively, and C_i is the insulator capacitance per unit area.

Subthreshold swing (S) is the inverse slope of the drain current versus the gate voltage in a semilog plot ($S=dV_{GS}/d(\log(I_{DS}))$. It is often used to characterize the subthreshold regime by indicating how rapidly the device switches from the OFF state to the ON state. A large value of S generally implies a large concentration of shallow traps. Subthreshold swing is also evaluated to extrapolate the maximum surface trap density (N_{Smax}) according to the relationship $N_{Smax} \approx [(S \times \log(e) \times q/k \times T)-1]C/q$, where k is the Boltzmann constant, q is the elementary charge, T is temperature, and C is the capacitance value [279].

6.3. Results and Discussion

The surface treatment method of the group I-III-VI QDs was inspired by the c-ALD technique [63]. Accordingly, the precursors for each cation and anion half-layer are introduced to the QDs separately and sequentially, and before the start of each half-layer, the unreacted precursors are removed from the medium [44], [190]. The method allows high precision on an atomic scale for shell growth and increases the radius of the QDs. Herein, the original as-synthesized QDs are capped with long-chain OLA ligands dispersible in non-polar solvents. With the introduction of the sulfur layer, the surface

polarity of the QDs changes, and the QDs are transferred to a polar solvent (in our case, NMF). Step-by-step photographs and a schematic of the surface treatment of the QDs are shown in Figure 6.1. The metal-terminated QDs have a high tendency to form ionic bonds with sulfur ions, which easily replace the surface ligands. The surface S^{2-} layer also provides high colloidal stability in polar solvent due to the negative electrostatic force. After the first half-reaction, the whole process is continued in the polar solvent. The Zn precursor of zinc nitrate in NMF (0.4 M) is added to the solution to form a complete layer of ZnS shell on the QDs. The anion and cation half-reactions can be alternatively performed to obtain the desired thickness of the shell. In the final stage, the surface of the metal-terminated QDs is passivated with OLA, and the QDs are transferred back to the non-polar solvent.

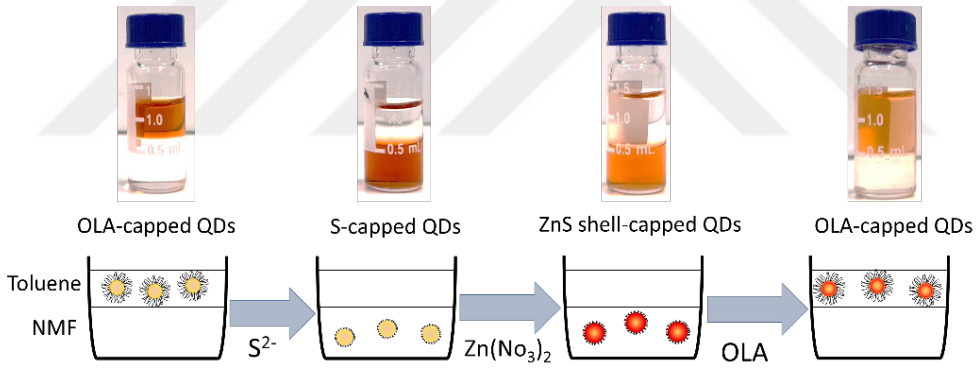

Figure 6.1. Real images of the QDs and a schematic of the half-reactions. For each step of the surface treatment, the QDs are either dispersible in the polar or non-polar solvent based on the surface polarity and ligands on the surface of the QDs.

Figures 6.2a and b show the absorption and PL spectra of the CIS QDs, respectively, for 1-3 cycles of the surface treatment. With increasing the number of the surface treatment cycles, no change in the absorption onset was observed, but the absorption increased for wavelengths below 500 nm due to the higher absorption of ZnS at higher energies [280].

The PL peak wavelength for 1 ML of ZnS demonstrates a slight blue shift, probably due to the diffusion and exchange of Zn with the host atoms. With the deposition of the S^{2-} half-layer, the PL red-shifts, which confirms the Zn diffusion in the lattice for the first layer. Moreover, with increasing the number of shells and quantum confinement relaxation, the PL spectra red-shift monotonously.

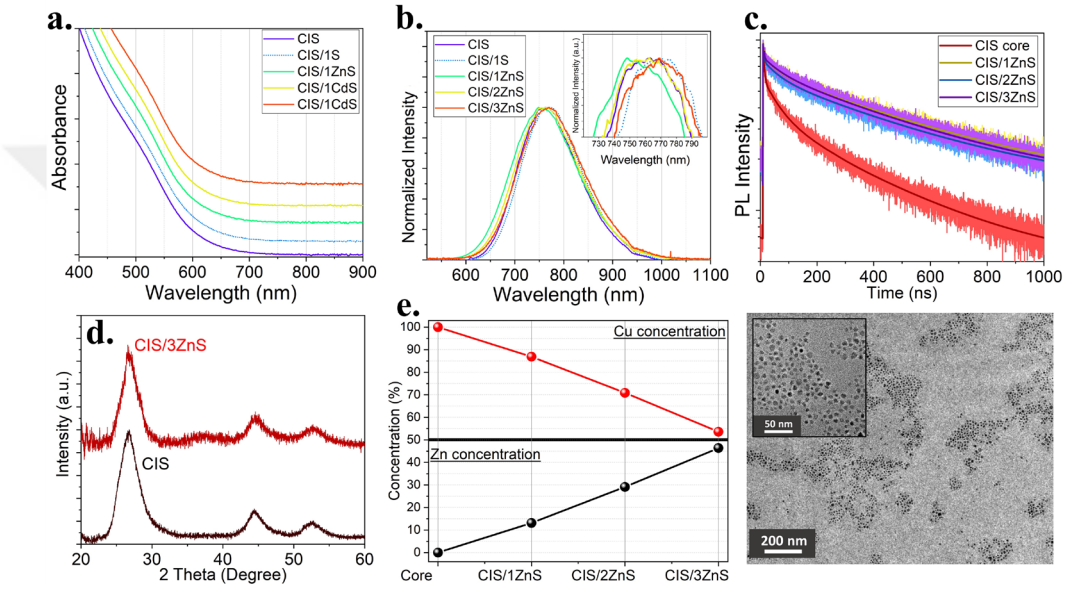

Figure 6.2. (a) Absorption and (b) PL spectra of CIS QDs before and after the shell treatment. (c) TRF decay curves and the corresponding three-exponential fits for the same samples. (d) XRD pattern of CIS and CIS/3ZnS QDs. (e) Concentration of Cu and Zn for each cycle of shell treatment. (f) TEM images of CIS/3ZnS QDs.

The recombination dynamics of the QDs, shown in Figure 6.2c, exhibits a substantial change in the decay curves before and after the surface treatment. The amplitude average lifetime (τ_{avg}) of the QDs increases from 143.1 ns for CIS QDs to 229.3 ns for CIS/1ZnS QDs, with the lifetime for the CIS/2-3 ZnS QDs being in the same range (Table 6.1). The increase in the lifetime points to better surface passivation, which inhibits the electron and hole from reaching the surface and decreases the share of nonradiative recombination

pathways. Moreover, the CIS/1S QDs (Figure 6.3) have a lifetime of 152.3 ns, close to the CIS QDs, indicating no meaningful change in the recombination dynamic [72], [103].

Table 6.1. Decay components for CIS QDs before and after the shell treatment.

Sample	τ_1 **(ns)**	τ_2 **(ns)**	τ_3 **(ns)**	$\frac{A_1.\tau_1}{\sum A_i.\tau_i}$ **(%)**	$\frac{A_2.\tau_2}{\sum A_i.\tau_i}$ **(%)**	$\frac{A_3.\tau_3}{\sum A_i.\tau_i}$ **(%)**	$\frac{\sum A_i.\tau_i}{\sum A_i}$ **(ns)**
CIS	399.7	64.1	4.8	85.8	12.8	1.4	143.1
CIS/1ZnS	571.2	55.2	1.9	97.1	2.4	0.4	229.3
CIS/2ZnS	526.3	55.3	1.7	96.6	3.0	0.5	200.8
CIS/3ZnS	532.9	61.4	1.6	96.9	2.7	0.4	210.5

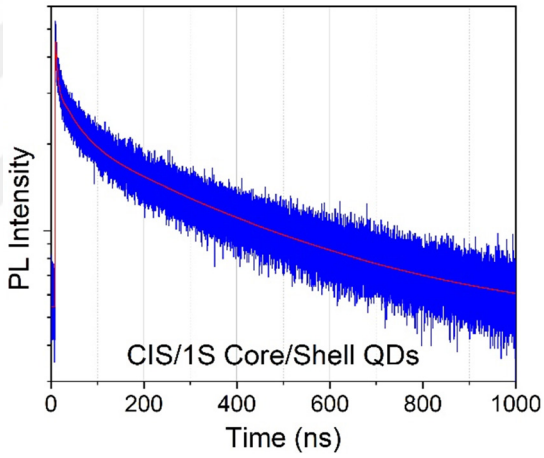

Figure 6.3. TRF decay curve of CIS QDs after the S^{2-} half-reaction. The red line is the tri-exponential fit of the curve.

The XRD analysis in Figure 6.2d explored the crystalline structure of CIS and CIS/3ZnS QDs. The chalcopyrite CIS QDs possess a lattice constant and diffraction pattern dependent on the Cu/In ratio with three prominent peaks in the diffraction pattern. Comparatively, the zinc blende crystalline structure of ZnS and chalcopyrite CIS are highly similar, differing only due to the chalcopyrite's bi-cation system, which results in

an elongated unit cell in one direction. Introduction of 3 MLs of ZnS caused a slight shift in peaks towards higher angles ($\Delta\theta = 0.2^{\circ}$ for the first peak) closer to the diffraction pattern of ZnS. Additionally, Zn treatment causes diffusion and exchange with the host atoms, filling vacancy sites and elevating the proportion of zinc blende in the structure. ICP-MS analysis, presented in Figure 6.2e, demonstrates a consistent rise in Zn concentration with each shell-treatment cycle. The radii of QDs increased statistically from an initial of 6.9 ± 1.7 nm (Figure 6.4) to 8.7 ± 1.5 nm for CIS/3ZnS (Figure 6.2f), marking a 26% increase in radius or a 100% increase in the volume of the QDs. The approximately 50% rise in Zn concentration after three cycles aligns with the 100% volume increase, indicating the shell growth.

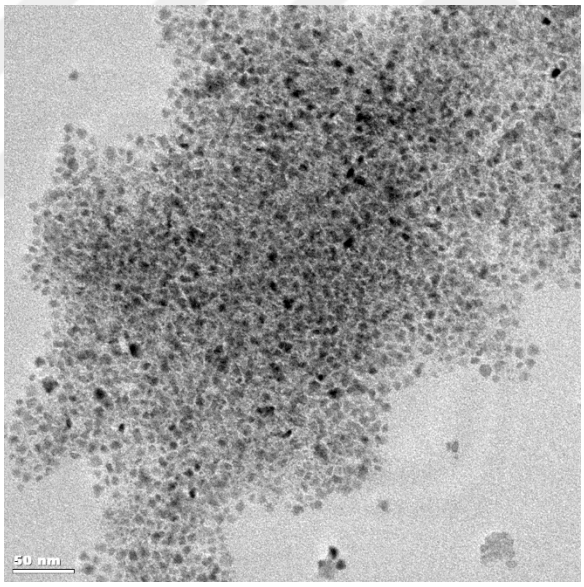

Figure 6.4. TEM image of untreated CIS QDs.

The shell treatment process was also examined for the CdS shell to demonstrate the flexibility of the method. The absorption spectra of CIS, CIS/1S and CIS/1-3CdS QDs are shown in Figure 6.5a. Similar to ZnS-treated QDs, the absorption onset did not change with increasing the number of the shell treatment cycles, while for higher

energies, the absorption increased. The PL spectra in Figure 6.5b shows that by implementing 1 ML of CdS shell, the PL peak wavelength blue-shifts due to the diffusion and exchange of the Cd in the lattice of the CIS QDs. Subsequent shell growth results in a red shift in the PL spectra, pointing to the quantum confinement relaxation. It is worth mentioning that the shift in the PL spectra is much stronger for CdS-treated than ZnS-treated QDs due to the higher chemical activity of Cd. Also, the TRF decay curves in Figure 6.5c shows that with increasing the shell thickness, initially, the lifetime decreases and subsequently it increases, with the longest lifetime belongs to the initial CIS QDs. The different behavior indicates a higher number of defects after CdS treatment compared to ZnS-treated QDs.

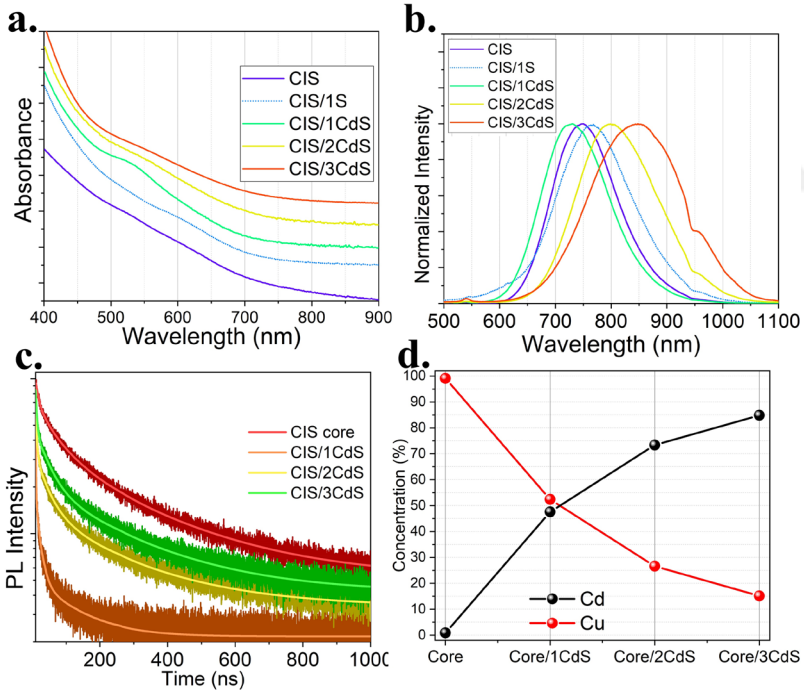

Figure 6.5. (a) Absorption and (b) PL spectra of CIS QDs before and after CdS-treatment. (c) TRF decay curve of the samples. (d) Concentration of Cd and Cu for each cycle of shell treatment.

The higher chemical reactivity of Cd can also be traced in the chemical composition of the QDs, where upon each cycle of shell treatment, the Cd concentration increases faster than Zn. In fact, the higher affinity of Cd to chalcogenides is the underlying reason for the easier synthesis procedure of Cd-based QDs and their shape engineering compared to the Zn chalcogenide QDs [130], [132]. As shown in Figure 6.5d, the Cd concentration is two times higher than Zn for the same number of treatment cycles, which also points to a higher rate of diffusion and cation exchange.

Previously, it was shown that the Cd exchange can effectively modify the charge equilibrium of CISe QDs [33]. Initially, Cd diffusion widens the bandgap; however, as shell deposition continues, the confinement relaxes, leading to a reduction in bandgap energy. Moreover, the bandgap energy and conduction band offset of CdS and CIS are lower than those of ZnS [50]. This suggests that electrons with a lower effective mass can more readily leak into the CdS shell than the ZnS shell. Consequently, even with an equal number of shell layers, CdS is anticipated to display a stronger PL red shift and offers a greater potential for PL tuning at longer wavelengths [50]. The TRF decay curves in Figure 6.5c further validate that following the initial stage of shell coating, the recombination lifetime increases due to the QD enlargement and the increased distance between the electron and hole (see detailed decay components provided in Table 6.2).

Table 6.2. Decay components for CIS QDs before and after treatment with CdS shells.

Sample	τ_1 (ns)	τ_2 (ns)	τ_3 (ns)	$\tau_{amp} \frac{\sum A_i . \tau_i}{\sum A_i}$ (ns)
CIS	399.7	64.1	4.8	143.1
CIS/1CdS	110.5	12.8	1.0	5.6
CIS/2CdS	217.6	30.3	1.4	29.1
CIS/3CdS	262.6	42.0	3.4	55.4

In the next stage, we examined the applicability of the shell treatment method for AIS and CISe QDs. Similar to CIS QDs, the absorption onset of the QDs did not show any change with the increasing number of shells (Figure 6.6a). The PL in Figure 6.6b spectra for AIS QDs before and after ZnS treatment show an initial blue shift followed by a continuous red shift due to the initial diffusion and exchange of Zn and subsequent shell growth. The red shift for AIS/1S QDs is more pronounced compared to CIS/1S (18 nm compared to 9 nm). The XRD pattern of the AIS and AIS/3ZnS QDs, in Figure 6.6d, exhibit no change in the crystalline structure of the QDs after treatment. As the first diffracted peak for AIS QDs is located at 0.8˚ higher degrees than CIS QDs, CIS/3ZnS QDs demonstrate a slight shift to lower angles, in contrast to CIS/3ZnS QDs. The real images of the AIS and CISe QDs in solution for the first cycle of shell treatment show a successful transfer of the QDs between the polar and non-polar solvents depending on the surface nature of the QDs (Figure 6.6g and h). TEM images for AIS/3ZnS and AIS QDs, provided in Figure 6.6e and Figure 6.7a, show that the QDs preserved their morphology after treatment. For CISe QDs, the morphology is slightly changed with apparent favorable growth in lateral directions (Figures 6.6f and 6.7b). The volume of the QDs increased by 50% for AIS and 55% for CISe QDs after treatment. Also, due to the multiple washing steps during the surface treatment procedure, the AIS/3ZnS QDs demonstrate a more homogeneous size distribution resulted from the filtering of smaller and larger QDs.

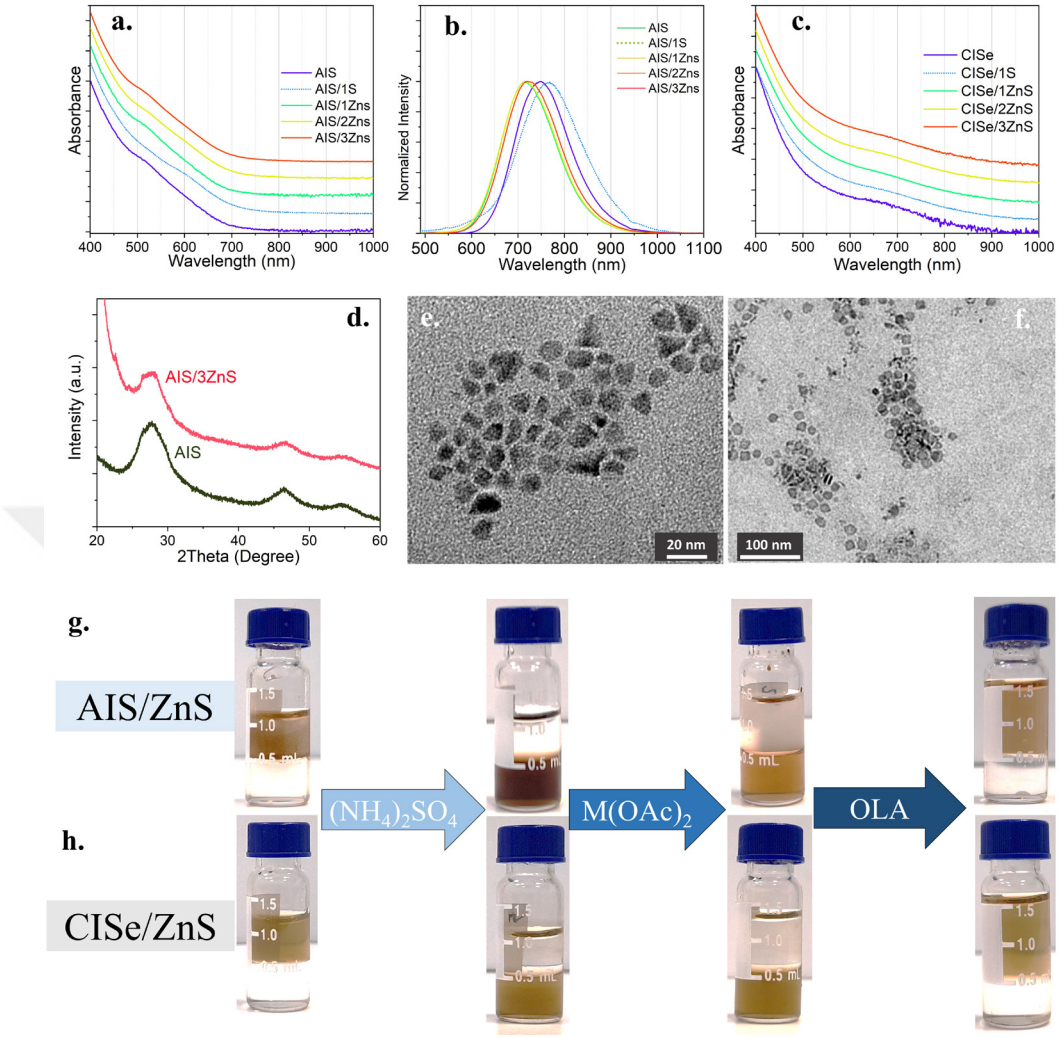

Figure 6.6. (a) Absorption and (b) emission spectra for AIS QDs, respectively, before and after surface treatment. (c) Absorption spectra of CISe QDs before and after surface treatment. (d) TEM images of AIS/3ZnS and (e) CISe/3ZnS QDs. (g and h) Real images of the AIS and CISe QDs during different stages of the surface treatment, respectively.

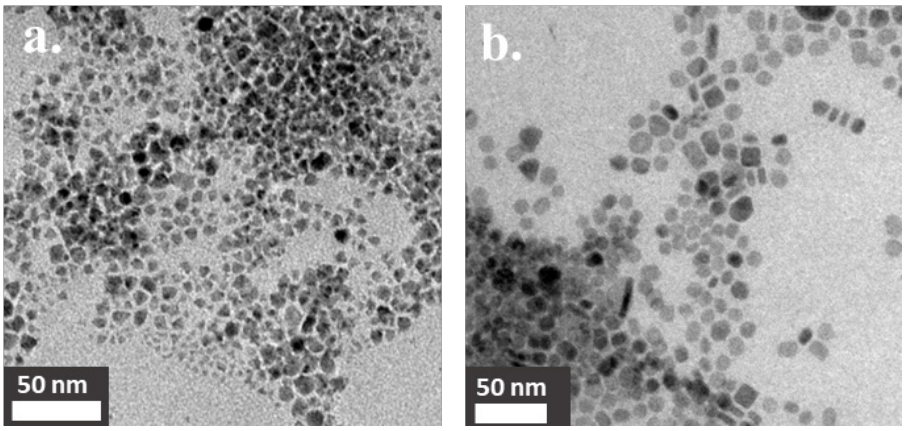

Figure 6.7. TEM images of (a) AIS and (b) CISe core QDs before the treatment.

The easy synthesis procedure and the vast and versatile compositions of the group I-III-VI QDs place them among the most promising candidates for electronic applications. Here, the surface-modified QDs were implemented in the field-effect transistor (FETs) and their electronic properties were examined. The top-gate/bottom-contact architecture of the FETs is shown in Figure 6.7a, and CIS, CIS/1S, CIS/ZnS/1S and CIS/2ZnS/1S QDs, were used as the transport layer. Similar ZnS-treated AIS QDs and CdS-treated CIS QDs were also implemented as the transport layer, and the electronic properties, especially the carrier mobility, were investigated. A cross-sectional SEM image of the CIS-FET device is shown in Figure 6.8b indicating the successful formation of the layers. The AFM images of the transport layer film in Figures 6.8h and i demonstrate a smooth film with R_{rms} (root-mean-square roughness) of 4.7 and 5.3 nm for CIS and CIS/1S FETs, respectively. The CIS-FETs did not show any change in performance after 21 days of working (Figure 6.8j).

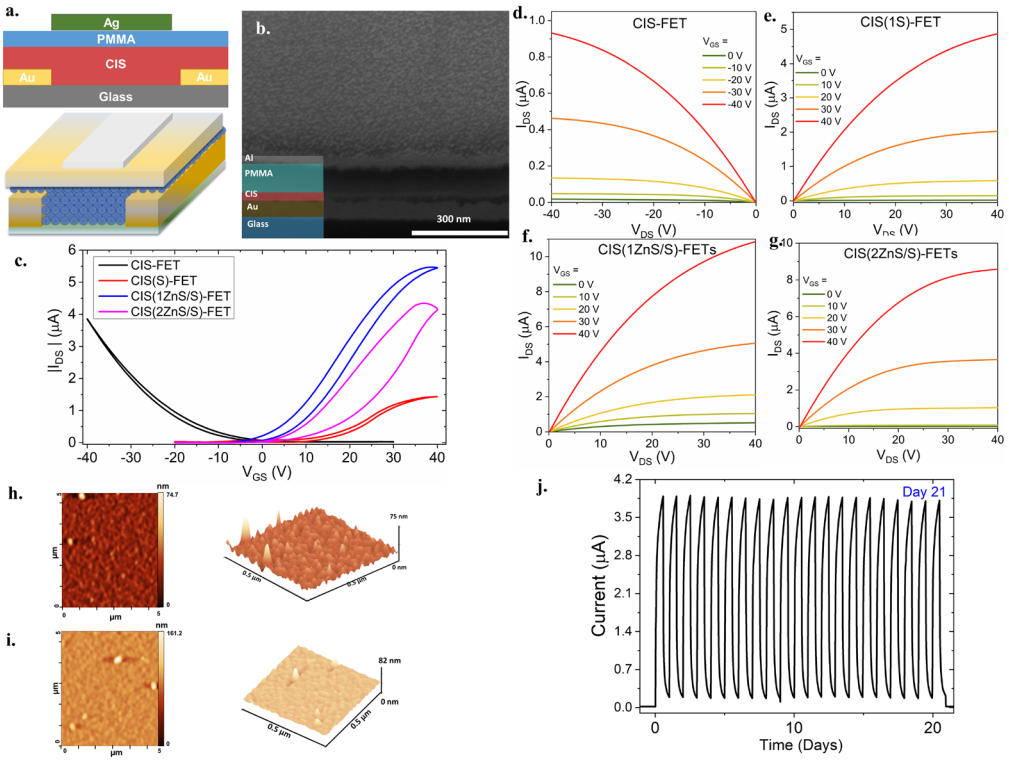

Figure 6.8. (a) QDs-FET device structure and (b) SEM image of the cross-section of this CIS-FET device. (c) I_{DS} vs I_{Gs} transfer curves for CIS-based FETs with V_{DS} = 20 V. (d) I_{DS} vs V_{DS} output characteristic curves of CIS-FETs, (e) CIS(1S)-FETs, (f) CIS(1/ZnS/S)-FETs and (g) CIS(2ZnS/S)-FETs. (h and i) AFM images for CIS and CIS/1S films, respectively. (j) Time-dependent CIS-FET measurement.

The original OLA ligands of CIS, CISe and AIS QDs are known to hinder the charge mobility and, in some cases, completely prevent the gating effect. The QDs are known for their both *p*-type and *n*-type behavior, which depends on the number and nature of the defects [34]. The deficiency in the chalcopyrite shows its effect in increased donor sites, while cation vacancy sites result in an increased number of acceptor sites. The antisite defects of In_{Cu} (Cu replaced by In) act as divalent donors, while Cu_{In} defects act as divalent acceptor sites. With the soft crystalline lattice, group I-III-VI QDs allow the

ion diffusion that is critical for tailoring the electronic properties. We showed the applicability of the surface modification method, which does not damage the morphology of the QDs. Here, we further look into the electrical properties of the untreated and treated QDs. Figures 6.8c and d show the transfer and output characteristics of the CIS-FETs, respectively, with V_{GS} varying between 0 to -40 V. The CIS-FET exhibits *p*-type behavior with a relatively poor hole mobility of 5.46×10^{-4} cm^2 $V^{-1}s^{-1}$ and a low on/off ratio of 0.8×10^2, corresponding with other reports in the literature [271], [281]. The *p*-type behavior originates in the final metal layer and excessive number of acceptor sites, which ultimately favors a higher positive charge and thus a larger number of holes compared to electrons.

Through surface treatment of the QDs, first, the long and bulky original ligands are removed, which increases the proximity of the QDs. Also, the outer sulfur layer affects the overall stoichiometry and injects an extra negative charge into the QDs. Figure 6.8e shows the output characteristics of CIS(S) FETs. The overturn of the charge balance and the increased number of the electron density causes a switch to *n*-type behavior for these transistors. The electron mobility is increased to 2.17 cm^2 V^{-1} s^{-1}, which is four orders of magnitude higher than the carrier mobility of CIS-FETs. Moreover, the on/off ratio is also increased by two orders of magnitude (Table 6.3).

The cation-poor stoichiometry of the QDs, especially deficiency of In and Cu_{In} antisites, amplifies the *p*-type behavior of the QDs [33]. Here, through decreasing the number of the cation vacancy sites or Cu_{In} antisite defects, the electron mobility can be enhanced. Figures 6.8f and g show the output characteristics of CIS(ZnS/S)-FETs and CIS(2ZnS/S)-FETs, respectively. The electron mobility after one cycle of shell treatment and termination with a sulfur layer is increased to 6.99 cm^2 V^{-1} s^{-1}, three times higher than those with no Zn treatment. Here, the diffusion of Zn and filling in the vacancy sites

and antisite defects are the leading causes of enhancement in the electron mobility of these QDs. Further treatment of the QDs with ZnS shell did not show any increase in the hole mobility, possibly due to an increase in the radius of the QDs.

The applicability of the strategy was also examined for AIS-based QDs. Figures 6.9a and b show the transfer and characteristic curves of the AIS-FET, respectively. The AIS-FETs demonstrate *p*-type degenerate behavior due to the excessive number of acceptor sites. The output characteristics of surface treated AIS-based FETs is shown in Figures 6.9c-e. When coating the QDs with a layer of S^{2-}, the FETs switch to *n*-type due to electron injection, and the carrier mobility also increases to 6.18 $cm^2 V^{-1} s^{-1}$. The behavior is similar to CIS-based FETs, where the injection of the electron and passivation of the acceptor sites for AIS(ZnS/S)-FETs possess the highest electron mobility and it does not increase by continuing the surface treatment cycles.

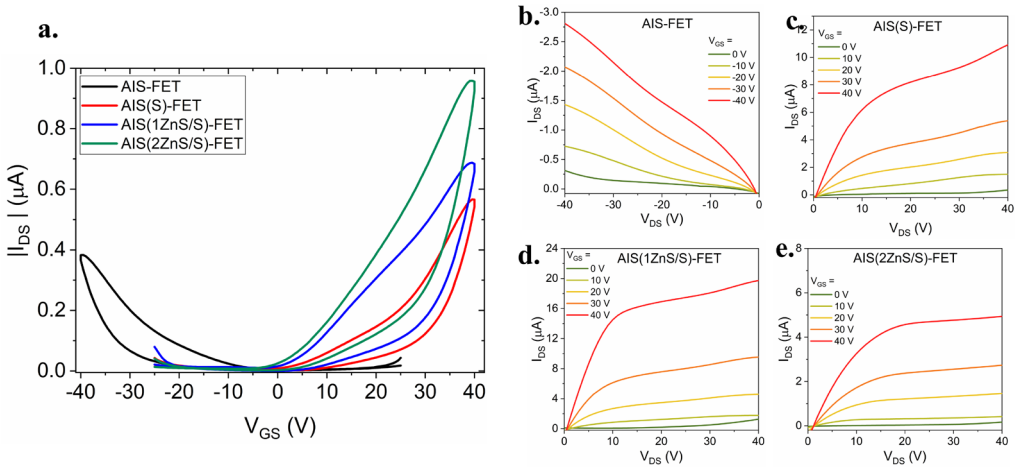

Figure 6.9. (a) Transfer characteristics of pristine and surface-treated AIS-based FETs at V_{DS} = 20 V. (b-e) Output characteristics of AIS-, AIS(1S)-, AIS(ZnS/S)- and AIS(2ZnS/S)-FETs, respectively.

The output characteristics of CIS(CdS/S)- and CIS(CIS/2CdS/S)-FETs are shown in Figures 6.10a and b, respectively, and the transfer characteristics are given in Figure 6.10c. The FETs based on the CdS-treated QDs also exhibit the same trend similar to ZnS-treated AIS- and CIS-FETs, in which one layer of CdS-shell contributes to higher electron mobility, and with the second shell, the mobility decreases.

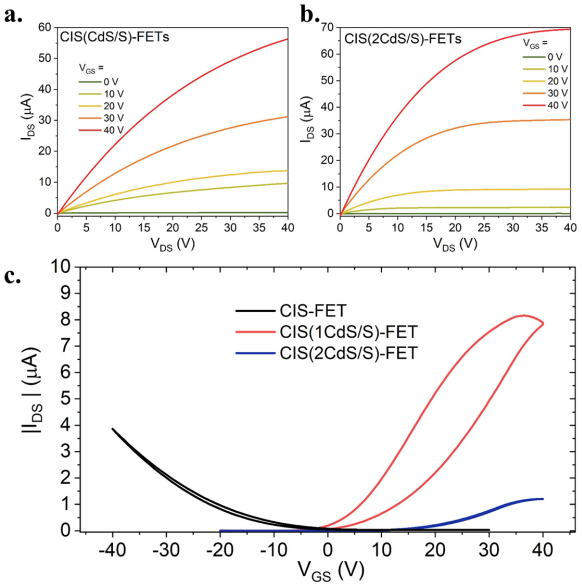

Figure 6.10. (a and b) Output characteristics of surface-treated CIS-based FETs after CdS-treatment at V_{DS} = 20 V. (c) Transfer characteristics of CIS QDs before and after CdS-treatment.

The highest μ_e achieved for CdS-treated CIS-FETs is 6.13 $cm^2 V^{-1} s^{-1}$ (up from 2.17 $cm^2 V^{-1} s^{-1}$), and 6.57 $cm^2 V^{-1} s^{-1}$ (up from 6.18 $cm^2 V^{-1} s^{-1}$) for ZnS-treated AIS-FETs, as presented in Table 6.3. These experiments demonstrate the potential diffusion of Zn and Cd into the lattice and the neutralization of vacancy or antisite defects. This aligns with earlier chemical measurements (Figures 6.2e and 6.5d), wherein the cation exchange of host ions led to a blue shift in the PL spectra, consistent with findings in other studies [282].

Table 6.3. Device characteristics of FETs based on pristine and surface-treated QDs.

FETs	μ_e/μ_h ($cm^2/V\ s$)	$I_{On/Off}$
*CIS core	5.46×10^{-4}	0.8×10^{2}
CIS/1S	2.17	3.2×10^{4}
CIS/ZnS/S	6.99	1.7×10^{5}
CIS/CdS/S	6.13	2.8×10^{3}
CIS/ZnS/ZnS/S	6.58	1.3×10^{4}
CIS/CdS/CdS/S	6.07	4.6×10^{4}
*AIS	3.44×10^{-4}	1.1×10^{5}
AIS/S	6.18	0.5×10^{3}
AIS/ZnS	6.57	1.4×10^{4}
AIS/ZnS/ZnS/S	6.17	0.4×10^{3}

μ_e and μ_h: electron and hole mobility, respectively. Numbers with a star indicate the hole mobility for *p*-type devices. $I_{On/Off}$ is the on/off current ratio.

6.4. Summary

In summary, a strategy toward surface and composition modification of group I-III-VI QDs was developed, in which a consecutive number of ZnS or CdS shells were grown on the original QDs. The optical properties, including the PL peak wavelength and recombination dynamics, can be finely tuned with ZnS treatment, while CdS treatment demonstrates a much more immense impact on the optical properties due to its lower band offset and higher Cd activity. The QDs-FETs exhibit superior electronic properties due to a combination of factors such as removal of bulky original ligands, inorganic passivation of the surface, injection of negative charge and nullification of acceptor antisite, and vacancy defects after surface modification. CIS-based FETs possess very high electron mobility of 6.99 $cm^2\ V^{-1}\ s^{-1}$ and an on/off ratio in the order of $10^{5,}$ on par with the best-reported number for solution-based transistors. We believe our synthetic route and the device strategy can pave the way for a better understanding of the carrier mobility mechanism and device performance enhancement for solution-based NCs FETs in the future.

Chapter 7

Conclusion

In this thesis, we tackled some of the fundamental challenges related to the synthesis and photophysical properties of colloidal semiconductor NCs. Motivated by the strong structure-property correlation, we employed colloidal NCs as the framework of our work and investigated different strategies of engineering complex heterostructures, doping and surface modification to enhance the properties and our understanding of the NCs. Herein, different strategies were proposed and demonstrated to further tune and enhance the optoelectronic properties of the NCs, including the PL spectral tunability, QY and linewidth, multi-channel recombination pathways, nonlinear absorption, paramagnetic properties, and carrier mobility. Considering the real-world application of the NCs, the proposed structures were tailor-made to face the needs of the industry and fulfill the missing points in the academic literature. In this chapter, a summary of the thesis and the scientific achievements are given with a prospect of the possibilities for future works and unanswered questions worthy of further investigation.

7.1. Concluding Remarks

With the focus on the structure-property relation of the colloidal NCs, in this thesis, we investigated different synthetic approaches to construct complex NCs and studied the optoelectronic properties and applications. Developing these complex NCs is only possible by developing the synthesis approach considering multiple factors, including the shape, composition, heterostructure and surface. The metal chalcogenide NCs discussed here are part of a large and growing class of colloidal NCs, which evidently reveals the high potential of these materials.

As one of the most promising NCs, 2D NPLs demonstrate exceptional properties originated from the anisotropic shape. The large absorption cross-section and the high oscillator strength combined with the synthesis versatility allow us to construct the desired structures based on the need. Keeping the shape and entirety of NPLs is always a challenge in the synthesis of more elaborated NPLs and a more comprehensive synthesis dynamics picture of the NPLs is needed. The emerging optoelectronic properties of the new NPLs can be entirely engineered differently from the constituent compositions and previously reported materials, which require closer inspection. In Chapter 3, the synthesis condition needed for extra thick NPLs was investigated. Through increasing the thickness of the NPLs, the quantum confinement was relaxed, which is essential to extend the tunability of the emission wavelength into the deep-red region. The proposed (CdSe/CdS)@(1-4 CdZnS/CdZnS) (core/crown)@(c-ALD shell-HI shell) NPLs was shown to have PL peak wavelength close to the theoretical band gap energy of the CdSe with high PLQY of 88%. The crown and the shell alongside with the long retention time at high temperature, could best keep the electron and hole confinement away from the surface, which is essential for high PLQY. Moreover, the intermediate layers alleviate the lattice strain between the CdSe core and the final ZnS

shell and allow the extra-thick shell deposition. While shell growth is the leading phenomenon during the HI, dissolution/recrystallization and cation reorganization also happen due to the lattice mismatch or Ostwald ripening. The final NPLs were used as the active materials for the LED device, which demonstrate a high EQE of 6.8% at 701 nm, on par with the best reports for the other classes of semiconductor NCs.

The combination of type-I and quasi type-II heterostructures with multiple layers of domains encapsulating the core extends the full PL coverage of the CdSe-based NPLs. In Chapter 4, the nature of the PL light was investigated by synthesizing multi-crown NPLs with many recombination pathways. The type-II nature of the NPLs entails a long lifetime and Stokes shifted PL at longer wavelengths. Herein, we proposed CdSe/CdSeTe/CdTe core/crown/crown NPLs with multiple type-II interfaces and possible direct/indirect recombination pathways. The PL profile of the NPLs was shown to be a convoluted mixture of direct recombination in one domain and indirect type-II recombination between two domains. The share of each component could be tuned by changing the geometry of the NPLs and especially the ratio between the intermediated CdSeTe and final CdTe crown, which in turn changes the overlap between the electron and hole wavefunction. While the geometry of the NPLs (ratio of the crowns and the overall size of the crowns) critically affects the final recombination pathway of the multi-crown NPLs, the composition of the middle crown possesses a much lower impact on the e-h overlap, especially for large crown NPLs. Moreover, decreasing the temperature causes a contraction of the lattice and, hence, the geometry of the NPLs, which provides another tool in the activation/deactivation of the recombination pathway. The NPLs exhibit an extremely high two-photon absorption cross-section 12.9×10^6 GM due to multiple indirect channels that facilitate nonlinear absorption with superlinear correlation with the NPLs size.

While building sophisticated heterostructures of the NPLs is a beneficial approach to tune the properties, some other desired properties cannot be fully realized only through it. Doping of the NCs with rare earth metals such as Ag and Cu can help unfold magnetic properties and PL at near-infrared region. In Chapter 5, doping dynamics of the core/shell NPLs with Ag and its dependency on the composition of the shell were investigated. As one of the major challenges, growing a shell on the already doped NPLs causes self-purification and diminishes the dopant-induced properties. Here, the core/shell NPLs with different compositions of the shell were first synthesized and then, in a separate synthesis, the Ag precursor was introduced to the NPLs. The approach allowed high doping turnover of the NPLs while preventing self-purification. The composition of the shell was shown to decide on the destruction mechanism of the NPLs in the irreversible doping regime at extra-high temperatures. The CdS-shelled NPLs demonstrate fragmentation and ZnS-shelled NPLs show etching from the preferred silver selenide sites, while the alloyed CdZnS-shell NPLs show a mixed and minimized destruction mechanism in the irreversible doping regime. The silver-activated states were sensitive to the bandgap of the NPLs, whereas for narrow bandgap NPLs of the thick-shelled NPLs, these midgap states are not positioned in the bandgap and hence not showing optical activity. Moreover, the dopant-induced PL of the NPLs has an Arrhenius type of dependency with temperature due to the same dependency of the diffusion constant of the silver atoms. The CdZnS-shelled NPLs demonstrate superior paramagnetic properties due to the preservation of the NPLs during doping at high temperature with the bound excitons possessing a negative Brillouin-like dependence in the presence of a magnetic field and a positive Zeeman splitting.

For many of the optoelectronic applications of the colloidal NCs, electronic transport properties are one of the critical performance factors. These properties, especially the

carrier mobility and the charge majority type, can best be enhanced by surface modification of the NCs and charge injection. In Chapter 6, we demonstrate a novel approach toward surface modification of the group I-III-VI NCs with a shell of ZnS. The ease of synthesis and high potential for size/shape engineering of this group of NCs make them one of the most interesting candidates for electronic applications, such as transistors. The pristine CIS NCs with *p*-type behavior suffer from very low hole mobility, which limits their performance. The *p*-type originated from the unsaturated metal-terminated surface of the NCs due to partial ligand passivation. Moreover, the hopping distance is originally high due to the long-chain ligand of OLA, which is accompanied by the high effective mass of the hole, results in low carrier mobility. Here, the long-chain ligands are replaced with a small inorganic layer of S^{2-} that decreases the hopping distance and contributes to the injection of negative charge. Inspired by the c-ALD technique, the surface can be treated with a metal layer, which puts a ZnS or CdS shell on the NCs, and the process could be repeated for at least three times. Aside from CIS NCs, this synthesis procedure was shown to be applicable for AIS and CISe NCs too, which can also be used for tailoring the optical properties. The treated NCs demonstrate an instant shift toward *n*-type behavior with a more than 10^4 times increase in the carrier mobility and a 100 times increase in the on/off ratio.

In conclusion, in this thesis, a broad range of questions related to the synthesis, optoelectronic properties and applications of the colloidal NCs were answered. The applicability of different electronic heterostructures, impurity doping and surface modification are shown, which, combined together, are critical for the next-generation solution-processed optoelectronic devices.

7.2. Future Outlook

With all the advances in the synthesis and application of colloidal NCs, still many challenges need to be better answered. To enhance the optoelectronic properties of the NCs, a better and more comprehensive image of the synthesis dynamics is needed. Here, some research challenges and ideas related to the synthesis and physical properties of the NCs for future research direction are summarized.

Mercury chalcogenide NPLs

Mercury chalcogenide (HgE) NPLs are a relatively new class of materials with the first report of the synthesis in 2016 through complete cation exchange of Hg for Cd in CdTe NPLs [283]. Beforehand, many reports of the synthesis of HgE QDs have been published in the literature through the aqueous or high-temperature metal-organic routes, resulting in monodisperse QDs with superior properties [32]. In general, the amount of research focusing on HgE NCs is far behind the other classes of inorganic NCs due to the higher reactivity of Hg, which makes it hard to control the reaction. Moreover, the zero band-gap nature of the HgE NCs makes it possible to tune the emission in the terahertz region, which is hard to measure due to a lack of proper instrumentation.

Compared to HgE QDs, HgE NPLs possess some interesting features originating in their 1D confinement. With the absence of inhomogeneous broadening that is usual for QD systems, HgE NPLs offer a narrow PL linewidth in the NIR region with acceptable PLQY. In the best number that has been reported, the FWHM of these HgTe NPLs can be as narrow as 40 nm at the PL peak wavelength of 880 nm. The materials can be tuned to longer wavelengths for high-performance applications; however, the lack of understanding of the synthesis dynamics inhibited further development of these

materials. Herein, three challenges need to be answered: first, stabilization methods of the HgE NPLs; second, heterostructures of the HgE NPLs and third, investigation of direct synthesis of HgE NPLs and the NPLs formation dynamics.

Heterostructures of the CdE-based NPLs have produced well-established literature with versatile and known methods. The same methods have not yet been shown for HgE NPLs, probably due to the low feasibility of these approaches for Hg-based NPLs. The lack of synthetic routes is partly due to the relatively unstable nature of HgE NPLs and their soft and flexible lattice that can easily undergo cation exchange. In a recent study of ours, we demonstrate that the exchange dynamics vary substantially based on the thickness of the starting CdSe core NPLs. Our experiment points to a very different dynamic of exchange reaction compared to, for example, Cu or Ag, where the exchange reaction is uniform and not sensitive to the starting material. Also, heterostructures of HgE NPLs were shown to be possible but not in the traditional ways. Here, we can develop this new synthesis method to form the heterostructures containing HgE.

One known difficulty with the HgE NPLs is their colloidal stability and high affinity of Hg oxidation. Also, the high exchange rate results in shape instability, in which the chalcogenide frame cannot hold the structure and shape irregularities start to appear due to the etching. The surface chemistry in the case of HgE is much more important than the other group of II-VI NPLs, as it enables the development of the synthesis methods and probably paves the way for conventional synthesis methods to be implemented on HgE NPLs. The applicability of carboxylic acid, alkylamine and thiol ligands has been previously shown in the literature.[283] Although the effect of surface ligands on the optical properties (PL and absorption) has been shown, the problem with the stability of the HgE NPLs still needs to be fully addressed. The instability is especially important when further synthesis (second pot) is needed. For example, in a report by Eychmüller's

group, the second pot synthesis to deposit a CdZnS shell with the hot-injection method resulted in a very broad multi-peak emission indicative of co-nucleation, dissolution and reformation of the NCs.[284] Herein, solving the stability issue of HgE NPLs and developing methods to synthesize heterostructures of HgE-based NPLs are important research directions that open new possibilities for this class of materials.

So far, all the synthesis methods of HgE NPLs are based on cation exchange and no report on the direct synthesis of HgE NPLs has been published. This is in part due to the fast nucleation and growth of the NCs even at lower temperatures, which makes it hard to control and track the reaction. The possibility of realizing HgE NPLs through cation exchange points to the chemical stability of these NPLs. However, the main question is the possible direct synthesis of HgE NPLs, which requires to first reduce the reaction rate so that following the reaction and intermediate species becomes possible. While the reaction temperature for CdE NPLs formation is above 220 ˚C and for ZnSe, it is 150 ˚C, this temperature should be further reduced for HgE NPLs. Taking advantage of different surfactant-organic metal interaction may help to better control the reaction and drive it in the preferred direction. For example, the TOP-based synthesis of HgE results in spherical QDs, using alkylamines also has the same effect, but direct usage of acetate or halides has yet not been reported. In a super-saturated medium where the transfer time is decreased substantially, the role of surface energy signifies, which can show its effect in the anisotropic shape. Herein, we can adjust the concentration of the precursors and surfactants to drive the reaction to for HgE NPLs directly. Investigation of this reaction substantially increases our perception of the underlying NPLs formation mechanism.

Nonradiative energy transfer in a 2D-to-2D system with a leaky acceptor

Nonradiative energy transfer (NRET) refers to an electromagnetic energy transfer from a donor as a high-energy emitter to an acceptor that readily absorbs its energy through a near-field dipole−dipole coupling. Förster resonance energy transfer (FRET) is one type of NRET where the exciton energy transfer rate inversely depends on the distance between the donor and acceptor. FRET energy transfer also depends on other factors, including the spectral overlap between the donor PL and acceptor absorption, absorption cross-section of the acceptor, PLQY of the donor, and the orientation of the dipoles. The shape of both donor and acceptor is a decisive factor in the FRET rate as it decides on the absorption cross-section and the orientation of the dipoles for a specific assembled system.

As discussed previously, $Cu_{2-x}S$ (CS) NCs are a broad class of colloidal NCs with known synthesis protocols. However, until recently, the control over the shape of these NCs has not been fully understood and the general shape was limited to semi-spherical quantum dots. New synthesis protocols enabled 2D hexagonal CS NPLs with well-defined edges [285]. The tight bandgap of CS NCs and the relaxed confinement of the thick CS NPLs means an extended range of absorption toward the near-infrared region and possibly emission in the same region. However, the crystalline structure of these NCs is filled with point defects of vacancies, which trap the hole and contribute to the nonradiative fast decay, limiting the long wavelength emission. The defective and soft crystalline structure of CS NCs provides an ideal framework to further implement other cations and heal the defects. Group III cations, such as In^{3+} and Ga^{3+}, are the most known cations to heal these vacancy sites, resulting in the known $CuInS_2$ and $CuGaS_2$ NCs. Moreover, the slow diffusion and vacancy implementation rate makes it possible to tune the number of vacancies and, hence, the number of nonradiative channels.

The importance of the FRET process in light-generation, -harvesting and -sensing and the unknown nature of the FRET for a system of defective acceptor with a tunable number of sinking channels makes it essential to answer the question about the FRET dynamics. Previously, several studies have been carried out on the colloidal NCs FRET dynamics with some levels of confinement, including from NPLs to NPLs, from NPLs to graphene and graphene oxide and QDs to transition metal chalcogenides. No study, however, has been reported on the FRET dynamics for a system with a tunable sinking source and the effect it may have on the FRET rate and distance.

The TEM images of the CS NPLs in Figure 7.1a show a 2D hexagonal shape of the NPLs before any exchange reaction. After the introduction of In, the vacancy sites in the lattice structure are filled with In with no change in the morphology of the NPLs (Figure 7.1b) [285]. The pristine CS NPLs feature a peak in their absorption spectrum (Figure 7.1c) due to the localized surface plasmon resonance (LSPR) resulting from the vacancy sites. The plasmonic effect induces an electric field [286]–[287], which in turn affect the non-radiative energy transfer. As the number of vacancy sites increases, the LSPR peak increases and blue-shifts, while for the NPLs with no vacancy site, the peak completely fades away.

The In exchange reaction allows healing of the vacancy sites and, hence, tuning the LSPR peak. The same diffusion and healing process is also possible by introducing Cu or S-exchanging ligands that turn the equilibrium to more Cu-rich compositions. As the surface of the CS and CIS NCs is passivated with organic non-polar ligands, it is possible to self-assemble them in a face-down configuration (Figure 7.1d). The vacancy-varied layer of CIS NPLs acts as the acceptor. A dielectric layer of TiO_2 can be deposited on this acceptor layer and the donor of 2D CdSe-based NPLs is deposited on the dielectric layer as the donor layer (Figure 7.1d). In this configuration, the thickness of the TiO_2 and

the number of vacancy sites can be tuned with great accuracy to assess the FRET dynamics for a system with an acceptor of a sinking nature. As the FRET rate depends on the PLQY of the donor layer, highly efficient CdSe/CdS core/crown NPLs emitting in the absorption region of the CIS NPLs can be used. The absorption of the CS and CIS NPLs is compared with the emission spectrum of the core/crown NPLs in Figure 7.1e and f.

The FRET rate and distance can best be assessed by the time-resolved fluorescent spectroscopy, in which upon an increase in the rate, the lifetime of the emissive donor increases and the FRET rate (Γ_{FRET}) can be calculated by

$$\Gamma_{FRET} = 1/\tau_{FRET} = 1/\tau_{DA} - 1/\tau_{D} \quad (7.1)$$

where τ_D and τ_{DA} are the lifetimes of the donor in the absence and presence of the acceptor, respectively. Similarly, the FRET efficiency can be calculated by $\eta_{FRET} = 1 - (\tau_{DA}/\tau_D)$. With decreasing the distance between the donor and the acceptor, the FRET rate and efficiency increase; however, one factor that has not been fully investigated in such systems is the effect of the vacancy-induced LSPR peak for the acceptor layer. The vacancy sites in the CIS NPLs effectively introduce new sinking channels with fast decaying nature that completely change the FRET dynamics. To the best of our knowledge, this effect has been overlooked in similar studies and has not been investigated.

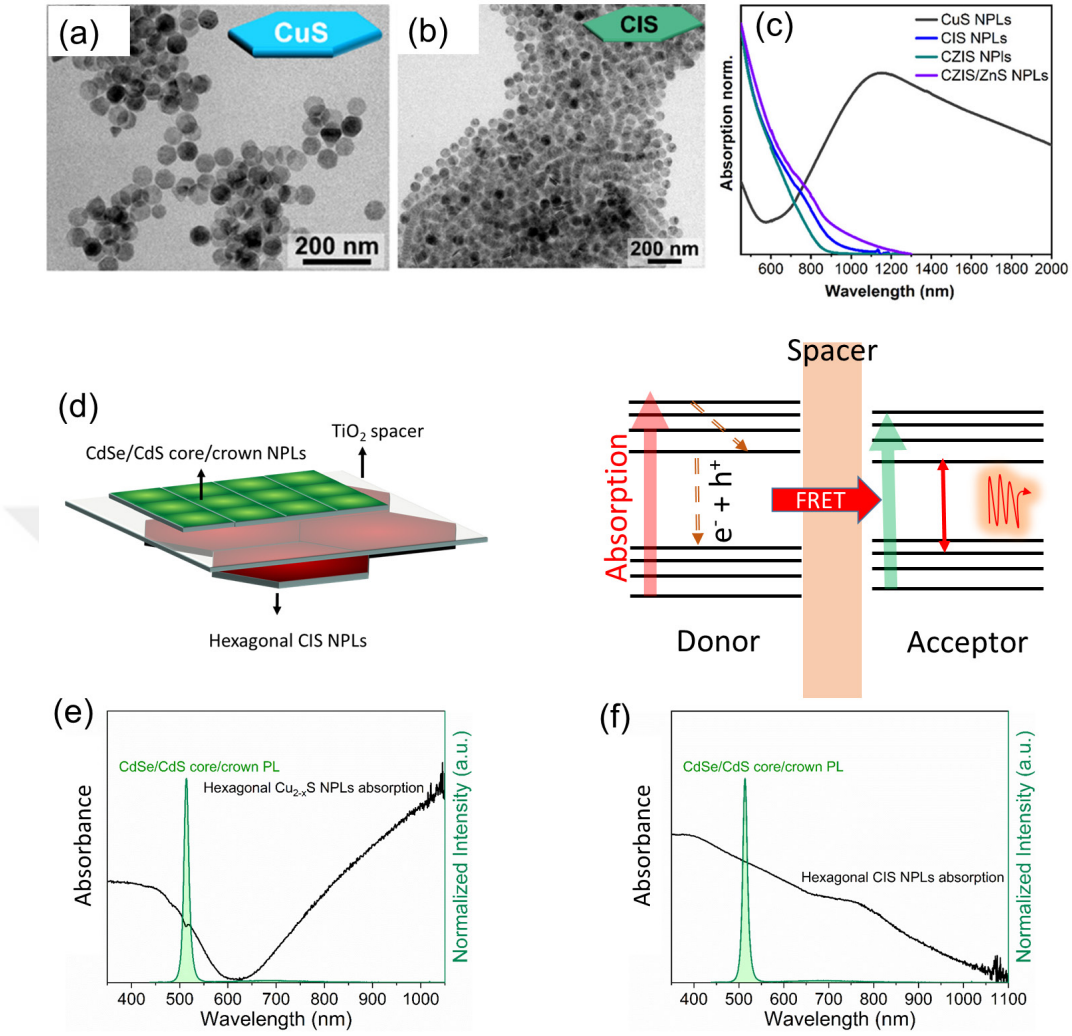

Figure 7.1. TEM images of CS NPLs (a) before and (b) after the In treatment. (c) Absorption spectra of CS and CIS NPLs. Adapted from ref. [285]. Copyright 2023 American Chemical Society. (d) A proposed schematic of the energy transfer system consisting CdSe/CdS core/crown NPLs donor and CIS NPLs acceptor. (e and f) PL spectra of the donor and the absorption spectra of the CS and CIS NPLs acceptor, respectively.

The final aim of this proposed study is to answer the important question of the defect-induced sinking channel in the FRET rate, efficiency and distance. All these three factors would change upon the introduction of the sinking channel. The scaling power of the

FRET ($1/d^n$) may also change through the introduction of the sinking channel due to the dipole-dipole interaction variation by the LSPR. Through this study, it is also of strong interest to investigate the electric field intensity distribution at the NPL sites depending on the orientation and the overlap of the NPLs.

Another interesting study is to calculate the vacancy equilibrium number and healing dynamics through the diffusion of the In to these sites, which can be obtained through X-ray absorption fine structure/X-ray fluorescence spectroscopy.

7.3. Thesis Contributions to the Literature

The first author/equal contribution publications during the thesis study include:

- Shabani, F., Ahmad, M., Kumar, S., Delikanli, S., Isik, F., Bhattacharya, A., Petrou, A. and Demir, H.V., **2023**. Thermodynamic Silver Doping of Core/Shell Colloidal Quantum Wells Imparted with Paramagnetic Properties Emitting at Near-Infrared. *Chemistry of Materials*, vol. 35, no. 11, pp. 4159–4170, 2023.
- Shabani, F., Martinez, P.L.H., Shermet, N., Korkut, H., Sarpkaya, I., Dehghanpour Baruj, H., Delikanli, S., Isik, F., Durmusoglu, E.G. and Demir, H.V., **2023**. Gradient Type-II CdSe/CdSeTe/CdTe Core/Crown/Crown Heteronanoplatelets with Asymmetric Shape and Disproportional Excitonic Properties. *Small*, vol. 19, no. 11, p. 2205729, 2023.
- Hu, S., Shabani, F., Liu, B., Zhang, L., Guo, M., Lu, G., Zhou, Z., Wang, J., Huang, J.C., Min, Y. and Xue, Q., **2022**. High-performance deep red colloidal quantum well light-emitting diodes enabled by the understanding of charge dynamics. *ACS Nano*, *ACS Nano*, vol. 16, no. 7, pp. 10840–10851, 2022.
- Shabani, F., Dehghanpour Baruj, H., Yurdakul, I., Delikanli, S., Gheshlaghi, N., Isik, F., Liu, B., Altintas, Y., Canımkurbey, B. and Demir, H.V., **2022**. Deep-Red-Emitting Colloidal Quantum Well Light-Emitting Diodes Enabled through a

Complex Design of Core/Crown/Double Shell Heterostructure," *Small*, vol. 18, no. 8, p. 2106115.

Other contributing publications include:

- Delikanli, S., Canimkurbey, B., Hernández-Martínez, P.L., Shabani, F., Isik, A.T., Ozkan, I., Bozkaya, I., Bozkaya, T., Isik, F., Durmusoglu, E.G. and Izmir, M., **2023**. On the Rational Design of Core/(Multi)-Crown Type-II Heteronanoplatelets. *Journal of the American Chemical Society*, vol. 145, p. 2023.
- Baruj, H.D., Yurdakul, I., Canimkurbey, B., Isik, A.T., Shabani, F., Delikanli, S., Shendre, S., Erdem, O., Isik, F. and Demir, H.V., **2023**. Highly-directional, highly-efficient solution-processed light-emitting diodes of all-face-down oriented colloidal quantum wells. *Small*, vol. 19, no 29, p. 2206582.
- Isik, A.T., Shabani, F., Isik, F., Kumar, S., Delikanli, S. and Demir, H.V., **2023**. Simultaneous Dual-Color Amplified Spontaneous Emission and Lasing from Colloidal Quantum Well Gain Media in their Own Layered Waveguide and Cavity. *Laser & Photonics Reviews*, vol. 17, no 9, p. 2300091.
- Durmusoglu, E.G., Hu, S., Hernandez-Martinez, P.L., Izmir, M., Shabani, F., Guo, M., Gao, H., Isik, F., Delikanli, S., Sharma, V.K. and Liu, B., **2023**. High External Quantum Efficiency Light-Emitting Diodes Enabled by Advanced Heterostructures of Type-II Nanoplatelets. *ACS Nano*, vol. 17, no. 8, pp. 7636–7644.
- İzmir, M., Durmusoglu, E.G., Sharma, M., Shabani, F., Isik, F., Delikanli, S., Sharma, V.K. and Demir, H.V., **2023**. Near-infrared emission from CdSe-based nanoplatelets induced by ytterbium doping. *The Journal of Physical Chemistry C*, vol. 127, no. 8, pp. 4210–4217.
- Dikmen, Z., Işık, A.T., Bozkaya, İ., Baruj, H.D., Canımkurbey, B., Shabani, F., Ahmad, M. and Demir, H.V., **2023**. Vertically oriented self-assembly of colloidal CdSe/CdZnS quantum wells controlled via hydrophilicity/lipophilicity balance: optical gain of quantum well stacks for amplified spontaneous emission and random lasing. *Nanoscale*, vol. 15, pp. 9745-9751.
- Azizov, R., Sinev, I., Işık, F., Shabani, F., Pushkarev, A., Yurdakul, I., Delikanli, S., Demir, H.V. and Makarov, S., **2022**. Direct laser writing of resonant periodic

nanostructures in thin light-emitting films of CdSe/CdZnS core/shell nanoplatelets. *Applied Physics Letters*, vol. 121, no. 22, pp. 223301.

- Erdem, T., Soran-Erdem, Z., Isik, F., Shabani, F., Yazici, A.F., Mutlugün, E., Gaponik, N. and Demir, H.V., **2022**. Color Enrichment Solids of Spectrally Pure Colloidal Quantum Wells for Wide Color Span in Displays. *Advanced Optical Materials*, vol. 10, no. 14, pp. 2200161.
- Delikanli, S., Isik, F., Durmusoglu, E.G., Erdem, O., Shabani, F., Canimkurbey, B., Kumar, S., Baruj, H.D. and Demir, H.V., **2022**. Observation of optical gain from aqueous quantum well heterostructures in water. *Nanoscale*, vol. 14, no. 40, pp.14895-14901.
- Foroutan-Barenji, S., Shabani, F., Isik, A.T., Dikmen, Z. and Demir, H.V., **2022**. All-colloidal parity–time-symmetric microfiber lasers balanced between the gain of colloidal quantum wells and the loss of colloidal metal nanoparticles. *Nanoscale*, vol. 14, no. 37, pp. 13755-13762.
- Razeghi, M., Üstünçelik, M., Shabani, F., Demir, H.V. and Kasırga, T.S., **2022**. Plasmon-enhanced photoresponse of single silver nanowires and their network devices. *Nanoscale Horizons*, vol. 7, no. 14, pp. 396-402.
- İzmir, M., Sharma, A., Shendre, S., Durmusoglu, E.G., Sharma, V.K., Shabani, F., Baruj, H.D., Delikanli, S., Sharma, M. and Demir, H.V., **2021**. Blue-emitting CdSe nanoplatelets enabled by sulfur-alloyed heterostructures for light-emitting diodes with low turn-on voltage. *ACS Applied Nano Materials*, vol. 5, no. 1, pp. 1367-1376.
- Delikanli, S., Isik, F., Shabani, F., Baruj, H.D., Taghipour, N. and Demir, H.V., **2021**. Ultralow Threshold Optical Gain Enabled by Quantum Rings of Inverted Type-I CdS/CdSe Core/Crown Nanoplatelets in the Blue. *Advanced Optical Materials*, vol. 9, no. 8, pp. 2002220.
- Gheshlaghi, N., Foroutan-Barenji, S., Erdem, O., Altintas, Y., Shabani, F., Humayun, M.H. and Demir, H.V., **2021**. Self-Resonant Microlasers of Colloidal Quantum Wells Constructed by Direct Deep Patterning. *Nano Letters*, vol. 21, no. 11, pp. 4598–4605.
- Delikanli, S., Erdem, O., Isik, F., Dehghanpour Baruj, H., Shabani, F., Yagci, H.B., Durmusoglu, E.G. and Demir, H.V., **2021**. Ultrahigh Green and Red Optical Gain Cross Sections from Solutions of Colloidal Quantum Well Heterostructures. *The Journal of Physical Chemistry Letters*, vol. 12, no. 9, pp. 2177–2182.

- Humayun, M.H., Hernandez-Martinez, P.L., Gheshlaghi, N., Erdem, O., Altintas, Y., Shabani, F. and Demir, H.V., **2021**. Near-Field Energy Transfer into Silicon Inversely Proportional to Distance Using Quasi-2D Colloidal Quantum Well Donors. *Small*, vol. 17, no. 41, p. 2103524.
- Altintas, Y., Liu, B., Hernandez-Martinez, P.L., Gheshlaghi, N., Shabani, F., Sharma, M., Wang, L., Sun, H., Mutlugun, E. and Demir, H.V., **2020**. Spectrally Wide-Range-Tunable, Efficient, and Bright Colloidal Light-Emitting Diodes of Quasi-2D Nanoplatelets Enabled by Engineered Alloyed Heterostructures. *Chemistry of Materials*, vol. 32, no. 18, pp. 7874–7883.
- Ebrahimi, E., Irfan, M., Shabani, F., Kocak, Y., Karakurt, B., Erdem, E., Demir, H.V. and Ozensoy, E., **2020**. Core-crown Quantum Nanoplatelets with Favorable Type-II Heterojunctions Boost Charge Separation and Photocatalytic NO Oxidation on TiO2. *ChemCatChem*, vol. 12, no. 24, pp. 6329–6343.

Bibliography

[1] A. I. Ekimov, A. L. Efros, and A. A. Onushchenko, “Quantum size effect in semiconductor microcrystals,” *Solid State Commun.*, vol. 56, no. 11, pp. 921–924, 1985.

[2] L. E. Brus, “Electron–electron and electron-hole interactions in small semiconductor crystallites: The size dependence of the lowest excited electronic state,” *J. Chem. Phys.*, vol. 80, no. 9, pp. 4403–4409, 1984.

[3] C. B. Murray, D. J. Norris, and M. G. Bawendi, “Synthesis and Characterization of Nearly Monodisperse CdE (E = S, Se, Te) Semiconductor Nanocrystallites,” *J. Am. Chem. Soc*, vol. 115, pp. 8706–8715, 1993.

[4] A. R. C. Osypiw, S. Lee, S.-M. Jung, S. Leoni, P. M. Smowton, B. Hou, J. M. Kim, and G. A. J. Amaratunga, “Solution-processed colloidal quantum dots for light emission,” *Mater. Adv.*, vol. 3, no. 17, pp. 6773–6790, 2022.

[5] Y. Shu, X. Lin, H. Qin, Z. Hu, Y. Jin, and X. Peng, “Quantum Dots for Display Applications,” *Angew. Chem.*, vol. 132, no. 50, pp. 22496–22507, 2020.

[6] S. Jiang, A. Van Dyk, A. Maurice, J. Bohling, D. Fasano, and S. Brownell, “Design colloidal particle morphology and self-assembly for coating applications.,” *Chem. Soc. Rev.*, vol. 46, no. 12, pp. 3792–3807, 2017.

[7] Y. Pu, F. Cai, D. Wang, J.-X. Wang, and J.-F. Chen, “Colloidal Synthesis of Semiconductor Quantum Dots toward Large-Scale Production: A Review,” *Ind. Eng. Chem. Res.*, vol. 57, no. 6, pp. 1790–1802, 2018.

[8] “NobelPrize.org.” Accessed: Oct. 17, 2023. [Online]. Available: https://www.nobelprize.org/prizes/chemistry.

[9] J. Zhang, Y. Tang, K. Lee, and M. Ouyang, “Tailoring light–matter–spin interactions in colloidal hetero-nanostructures,” *Nature*, vol. 466, no. 7302, pp. 91–95, 2010.

[10] M. Liu, N. Yazdani, M. Yarema, M. Jansen, V. Wood, and E. H. Sargent, “Colloidal quantum dot electronics,” *Nat. Electron.*, vol. 4, no. 8, pp. 548–558, 2021.

[11] T. Kim, D. Shin, M. Kim, H. Kim, E. Cho, M. Choi, J. Kim, E. Jang, and S. Jeong, “Development of Group III-V Colloidal Quantum Dots for Optoelectronic Applications,” *ACS Energy Lett.*, vol. 8, no. 1, pp. 447–456, 2023.

[12] A. P. Litvin, I. V. Martynenko, F. Purcell-Milton, A. V. Baranov, A. V. Fedorov, and Y. K. Gun’ko, “Colloidal quantum dots for optoelectronics,” *J. Mater. Chem.*, vol. 5, no. 26, pp. 13252–13275, 2017.

[13] S. B. Brichkin and V. F. Razumov, “Colloidal quantum dots: synthesis, properties and applications,” *Russian Chemical Reviews*, vol. 85, no. 12, pp. 1297–1312, 2016.

[14] J. Zhang, S. Zhang, Y. Zhang, O. A. Al-Hartomy, S. Wageh, A. G. Al-Sehemi, Y. Hao, L. Gao, H. Wang, and H. Zhang, “Colloidal Quantum Dots: Synthesis, Composition, Structure, and Emerging Optoelectronic Applications,” *Laser Photon Rev.*, vol. 17, no. 3, p. 2200551, 2023.

[15] M. J. Enright and B. M. Cossairt, “Synthesis of tailor-made colloidal semiconductor heterostructures,” *Chem. Commun.*, vol. 54, no. 52, pp. 7109–7122, 2018.

[16] J. M. Pietryga, Y. S. Park, J. Lim, A. F. Fidler, W. K. Bae, S. Brovelli, and V. I. Klimov, “Spectroscopic and device aspects of nanocrystal quantum dots,” *Chem. Rev.*, vol. 116, no. 18, pp. 10513–10622, 2016.

[17] V. I. Klimov, “Spectral and dynamical properties of multiexcitons in semiconductor nanocrystals,” *Annu. Rev. Phys. Chem.*, vol. 58, pp. 635–673, 2007.

[18] D. A. Wheeler, J. Z. Zhang, D. A. Wheeler, and J. Z. Zhang, “Exciton Dynamics in Semiconductor Nanocrystals,” *Adv. Mater.*, vol. 25, no. 21, pp. 2878–2896, 2013.

[19] T. Qiao, D. Parobek, D. H. Son, and D. H. Son, “Photons and charges from colloidal doped semiconductor quantum dots,” *J. Mater. Chem.*, vol. 7, no. 47, pp. 14788–14797, 2019.

[20] A. M. Smith and S. Nie, “Semiconductor nanocrystals: Structure, properties, and band gap engineering,” *Acc. Chem. Res.*, vol. 43, no. 2, pp. 190–200, 2010.

[21] A. R. Tao, S. Habas, and P. Yang, “Shape Control of Colloidal Metal Nanocrystals,” *Small*, vol. 4, no. 3, pp. 310–325, 2008.

[22] J. Sung Son, J. Ho Yu, S. Gu Kwon, J. Lee, J. Joo, T. Hyeon, J. S. Son, J. H. Yu, S. G. Kwon, T. Hyeon, J. Lee, and J. Joo, “Colloidal Synthesis of Ultrathin Two-Dimensional Semiconductor Nanocrystals,” *Adv. Mater.*, vol. 23, no. 28, pp. 3214–3219, 2011.

[23] S. Ithurria, M. D. Tessier, B. Mahler, R. P. S. M. Lobo, B. Dubertret, and A. L. Efros, “Colloidal nanoplatelets with two-dimensional electronic structure,” *Nat. Mater.*, vol. 10, no. 12, pp. 936–941, 2011.

[24] J. Cui, Y. E. Panfil, S. Koley, D. Shamalia, N. Waiskopf, S. Remennik, I. Popov, M. Oded, and U. Banin, “Colloidal Quantum Dot Molecules Manifesting Quantum Coupling at Room Temperature,” *Nat. Commun.*, pp. 1–34, 2019.

[25] G. A. Drake, L. P. Keating, and M. Shim, “Design Principles of Colloidal Nanorod Heterostructures,” *Chem. Rev.*, vol. 123, no. 7, pp. 3761–3789, 2023.

[26] D. V. Talapin, J. S. Lee, M. V. Kovalenko, and E. V. Shevchenko, “Prospects of colloidal nanocrystals for electronic and optoelectronic applications,” *Chem. Rev.*, vol. 110, no. 1, pp. 389–458, 2010.

[27] X. Peng, “An essay on synthetic chemistry of colloidal nanocrystals,” *Nano. Res.*, vol. 2, no. 6, pp. 425–447, 2009.

[28] S. V Gaponenko and H. V. Demir, *Applied Nanophotonics*. 2018.

[29] B. K. Ridley, “Quantum Processes in Semiconductors,” *Quantum Processes in Semiconductors*, 2013.

[30] M. C. Hanna and A. J. Nozik, “Solar conversion efficiency of photovoltaic and photoelectrolysis cells with carrier multiplication absorbers,” *J. Appl. Phys.*, vol. 100, no. 7, p. 74510, 2006.

[31] L. T. Kunneman, J. M. Schins, S. Pedetti, H. Heuclin, F. C. Grozema, A. J. Houtepen, B. Dubertret, and L. D. A. Siebbeles, “Nature and decay pathways of photoexcited states in CdSe and CdSe/CdS nanoplatelets,” *Nano. Lett.*, vol. 14, no. 12, pp. 7039–7045, 2014.

[32] C. Gréboval, A. Chu, N. Goubet, C. Livache, S. Ithurria, and E. Lhuillier, “Mercury Chalcogenide Quantum Dots: Material Perspective for Device Integration,” *Chem. Rev.*, vol. 121, no. 7, pp. 3627–3700, 2021.

[33] C. Pang, S. Hu, C. Guo, J. Wang, S. Zou, Z. Pan, J. Liu, L. Shen, N. Bao, H. Ning, A. Gupta, and Z. Gong, “High-Performance Inorganically Connected $CuInSe_2$ Nanocrystal Thin-Film Transistors and Integrated Circuits Based on the Solution Process of Colloidal Synthesis, Ligand Exchange, and Surface Treatment,” *Chem. Mater.*, vol. 33, no. 22, pp. 8775–8785, 2021.

[34] H. J. Yun, J. Lim, J. Roh, D. C. J. Neo, M. Law, and V. I. Klimov, “Solution-processable integrated CMOS circuits based on colloidal $CuInSe_2$ quantum dots,” *Nat. Commun.*, vol. 11, no. 1, p. 5280, 2020.

[35] M. Nasilowski, B. Mahler, E. Lhuillier, S. Ithurria, and B. Dubertret, “Two-Dimensional Colloidal Nanocrystals,” *Chem. Rev.*, vol. 116, no. 18, pp. 10934–10982, 2016.

[36] K. E. Knowles, K. H. Hartstein, T. B. Kilburn, A. Marchioro, H. D. Nelson, P. J. Whitham, and D. R. Gamelin, “Luminescent Colloidal Semiconductor Nanocrystals Containing Copper: Synthesis, Photophysics, and Applications,” *Chem. Rev.*, vol. 116, no. 18, pp. 10820–10851, 2016.

[37] C. Coughlan, M. Ibáñez, O. Dobrozhan, A. Singh, A. Cabot, and K. M. Ryan, “Compound copper chalcogenide nanocrystals,” *Chem. Rev.*, vol. 117, no. 9, pp. 5865–6109, 2017.

[38] L. Jing, S. V. Kershaw, Y. Li, X. Huang, Y. Li, A. L. Rogach, and M. Gao, “Aqueous Based Semiconductor Nanocrystals,” *Chem. Rev.*, vol. 116, no. 18, pp. 10623–10730, 2016.

[39] C. Pu, H. Qin, Y. Gao, J. Zhou, P. Wang, and X. Peng, “Synthetic Control of Exciton Behavior in Colloidal Quantum Dots,” *J. Am. Chem. Soc.*, vol. 139, no. 9, pp. 3302–3311, 2017.

[40] J. Van Embden, A. S. R. Chesman, and J. J. Jasieniak, “The heat-up synthesis of colloidal nanocrystals,” *Chem. Mater.*, vol. 27, no. 7, pp. 2246–2285, 2015.

[41] T. H. Yang, Y. Shi, A. Janssen, and Y. Xia, “Surface Capping Agents and Their Roles in Shape-Controlled Synthesis of Colloidal Metal Nanocrystals,” *Angew. Chem.*, vol. 59, no. 36, pp. 15378–15401, 2020.

[42] A. Riedinger, F. D. Ott, A. Mule, S. Mazzotti, P. N. Knüsel, S. J. P. Kress, F. Prins, S. C. Erwin, and D. J. Norris, “An intrinsic growth instability in isotropic materials leads to quasi-two-dimensional nanoplatelets,” *Nat. Mater.*, vol. 16, no. 7, pp. 743–748, 2017.

[43] F. D. Ott, A. Riedinger, D. R. Ochsenbein, P. N. Knüsel, S. C. Erwin, M. Mazzotti, and D. J. Norris, “Ripening of Semiconductor Nanoplatelets,” *Nano. Lett.*, vol. 17, no. 11, pp. 6870–6877, 2017.

[44] F. Shabani, H. Dehghanpour Baruj, I. Yurdakul, S. Delikanli, N. Gheshlaghi, F. Isik, B. Liu, Y. Altintas, B. Canımkurbey, and H. V. Demir, “Deep-Red-Emitting Colloidal Quantum Well Light-Emitting Diodes Enabled through a Complex Design of Core/Crown/Double Shell Heterostructure,” *Small*, vol. 18, no. 8, p. 2106115, 2022.

[45] C. Burda, X. Chen, R. Narayanan, and M. A. El-Sayed, “Chemistry and properties of nanocrystals of different shapes.,” *Chem. Rev.*, vol. 105, no. 4, pp. 1025–102, 2005.

[46] P. Reiss, M. Protière, and L. Li, “Core/shell semiconductor nanocrystals,” *Small*, vol. 5, no. 2, pp. 154–168, 2009.

[47] P. C. Sercel and A. L. Efros, “Band-Edge Exciton in CdSe and Other II-VI and III-V Compound Semiconductor Nanocrystals - Revisited,” *Nano. Lett.*, vol. 18, no. 7, pp. 4061–4068, 2018.

[48] S. Delikanli, F. Isik, F. Shabani, H. D. Baruj, N. Taghipour, and H. V. Demir, “Ultralow Threshold Optical Gain Enabled by Quantum Rings of Inverted Type-I CdS/CdSe Core/Crown Nanoplatelets in the Blue,” *Adv. Opt. Mater.*, vol. 9, no. 8, p. 2002220, 2021.

[49] C. H. Chuang, S. S. Lo, G. D. Scholes, and C. Burda, “Charge separation and recombination in CdTe/CdSe core/shell nanocrystals as a function of shell coverage: Probing the onset of the quasi type-II regime,” *J. Phys. Chem. Lett.*, vol. 1, no. 17, pp. 2530–2535, 2010.

[50] Y. Altintas, B. Liu, P. L. Hernández-Martínez, N. Gheshlaghi, F. Shabani, M. Sharma, L. Wang, H. Sun, E. Mutlugun, and H. V. Demir, “Spectrally Wide-Range-Tunable, Efficient, and Bright Colloidal Light-Emitting Diodes of Quasi-2D Nanoplatelets Enabled by Engineered Alloyed Heterostructures,” *Chem. Mater.*, vol. 32, no. 18, pp. 7874–7883, 2020.

[51] F. Shabani, P. L. H. Martinez, N. Shermet, H. Korkut, I. Sarpkaya, H. Dehghanpour Baruj, S. Delikanli, F. Isik, E. G. Durmusoglu, and H. V. Demir, "Gradient Type-II CdSe/CdSeTe/CdTe Core/Crown/Crown Heteronanoplatelets with Asymmetric Shape and Disproportional Excitonic Properties," *Small*, vol. 19, no. 11, p. 2205729, 2023.

[52] S. Delikanli, B. Canimkurbey, P. L. Hernández-Martínez, F. Shabani, A. T. Isik, I. Ozkan, I. Bozkaya, T. Bozkaya, F. Isik, E. G. Durmusoglu, M. Izmir, H. Akgun, and H. V. Demir, "On the Rational Design of Core/(Multi)-Crown Type-II Heteronanoplatelets," *J. Am. Chem. Soc.*, vol. 145, p. 2023, 2023.

[53] E. G. Durmusoglu, S. Hu, P. L. Hernandez-Martinez, M. Izmir, F. Shabani, M. Guo, H. Gao, F. Isik, S. Delikanli, V. K. Sharma, B. Liu, and H. V. Demir, "High External Quantum Efficiency Light-Emitting Diodes Enabled by Advanced Heterostructures of Type-II Nanoplatelets," *ACS Nano*, vol. 17, no. 8, pp. 7636–7644, 2023.

[54] L. E. Shea-Rohwer, J. E. Martin, X. Cai, B. Xu, B. Cai, M. Liu, al -, H. Shen, Y. Zheng, H. Wang, W. Xu, L. Qian, Y. Yang, A. Titov, J. Hyvonen, and L. Song Li, "Highly efficient near-infrared light-emitting diodes by using type-II CdTe/CdSe core/shell quantum dots as a phosphor," *Nanotechnology*, vol. 24, no. 47, p. 475603, 2013.

[55] A. V. Antanovich, A. V. Prudnikau, D. Melnikau, Y. P. Rakovich, A. Chuvilin, U. Woggon, A. W. Achtstein, and M. V. Artemyev, "Colloidal synthesis and optical properties of type-II CdSe-CdTe and inverted CdTe-CdSe core-wing heteronanoplatelets," *Nanoscale*, vol. 7, no. 17, pp. 8084–8092, 2015.

[56] Y. Kelestemur, B. Guzelturk, O. Erdem, M. Olutas, K. Gungor, and H. V. Demir, "Platelet-in-Box Colloidal Quantum Wells: CdSe/CdS@CdS Core/Crown@Shell Heteronanoplatelets," *Adv. Funct. Mater.*, vol. 26, no. 21, pp. 3570–3579, 2016.

[57] H. Zhu, N. Song, W. Rodríguez-Córdoba, and T. Lian, "Wave function engineering for efficient extraction of up to nineteen electrons from one CdSe/CdS quasi-type II quantum dot," *J. Am. Chem. Soc.*, vol. 134, no. 9, pp. 4250–4257, 2012.

[58] M. A. Hines and P. Guyot-Sionnest, "Synthesis and characterization of strongly luminescing ZnS-capped CdSe nanocrystals," *J. Phys. Chem.*, vol. 100, no. 2, pp. 468–471, 1996.

[59] B. O. Dabbousi, J. Rodriguez-Viejo, F. V. Mikulec, J. R. Heine, H. Mattoussi, R. Ober, K. F. Jensen, and M. G. Bawendi, "(CdSe)ZnS core-shell quantum dots: Synthesis and characterization of a size series of highly luminescent nanocrystallites," *J. Phys. Chem. B*, vol. 101, no. 46, pp. 9463–9475, 1997.

[60] X. Peng, M. C. Schlamp, A. V. Kadavanich, and A. P. Alivisatos, "Epitaxial growth of highly luminescent CdSe/CdS core/shell nanocrystals with photostability and electronic accessibility," *J. Am. Chem. Soc.*, vol. 119, no. 30, pp. 7019–7029, 1997.

[61] N. Gheshlaghi, S. Foroutan-Barenji, O. Erdem, Y. Altintas, F. Shabani, M. H. Humayun, and H. V. Demir, "Self-Resonant Microlasers of Colloidal Quantum Wells Constructed by Direct Deep Patterning," *Nano. Lett.*, vol. 21, no. 11, pp. 4598–4605, 2021.

[62] S. Delikanli, F. Isik, E.G. Durmusoglu, O. Erdem, F. Shabani, B. Canimkurbey, S. Kumar, H.D. Baruj, and H.V. Demir, "Observation of optical gain from aqueous quantum well heterostructures in water," *Nanoscale*. vol. 14, no. 40, pp. 14895-901, 2022.

[63] S. Ithurria and D. V. Talapin, "Colloidal Atomic Layer Deposition (c-ALD) using self-limiting reactions at nanocrystal surface coupled to phase transfer between polar and nonpolar media," *J. Am. Chem. Soc.*, vol. 134, no. 45, pp. 18585–18590, 2012.

[64] A. H. Khan, G. H. V. Bertrand, A. Teitelboim, C. Sekhar M., A. Polovitsyn, R. Brescia, J. Planelles, J. I. Climente, D. Oron, and I. Moreels, "CdSe/CdS/CdTe Core/Barrier/Crown Nanoplatelets: Synthesis, Optoelectronic Properties, and Multiphoton Fluorescence Upconversion," *ACS Nano*, 2020.

[65] E. Ebrahimi, M. Irfan, F. Shabani, Y. Kocak, B. Karakurt, E. Erdem, H. V. Demir, and E. Ozensoy, "Core-crown Quantum Nanoplatelets with Favorable Type-II Heterojunctions Boost Charge Separation and Photocatalytic NO Oxidation on TiO2," *ChemCatChem*, vol. 12, no. 24, pp. 6329–6343, 2020.

[66] C. M. Tyrakowski, A. Shamirian, C. E. Rowland, H. Shen, A. Das, R. D. Schaller, and P. T. Snee, "Bright Type II Quantum Dots," *Chem. Mater.*, vol. 27, no. 21, pp. 7276–7281, 2015.

[67] S. Yadav, A. Singh, and S. Sapra, "Long-Lived Emission in Type-II CdS/ZnSe Core/Crown Nanoplatelet Heterostructures," *J. Phys. Chem. C*, vol. 121, no. 48, pp. 27241–27246, 2017.

[68] H. McDaniel, P. E. Heil, C. L. Tsai, K. Kim, and M. Shim, "Integration of type II nanorod heterostructures into photovoltaics," *ACS Nano*, vol. 5, no. 9, pp. 7677–7683, 2011.

[69] S. Pedetti, S. Ithurria, H. Heuclin, G. Patriarche, and B. Dubertret, "Type-II CdSe/CdTe core/crown semiconductor nanoplatelets," *J. Am. Chem. Soc.*, vol. 136, no. 46, pp. 16430–16438, 2014.

[70] M. Dufour, V. Steinmetz, E. Izquierdo, T. Pons, N. Lequeux, E. Lhuillier, L. Legrand, M. Chamarro, T. Barisien, and S. Ithurria, "Engineering bicolor emission in 2D core/crown CdSe/$CdSe_{1-x}Te_x$ nanoplatelet heterostructures using band-offset tuning," *J. Phys. Chem. C*, vol. 121, no. 39, pp. 24816–24823, 2017.

[71] M. Sharma, S. Delikanli, and H. V. Demir, "Two-Dimensional CdSe-Based Nanoplatelets: Their Heterostructures, Doping, Photophysical Properties, and Applications," *Proc. IEEE*, vol. 108, no. 5, pp. 655–675, 2020.

[72] F. Shabani, M. Ahmad, S. Kumar, S. Delikanli, F. Isik, A. Bhattacharya, A. Petrou, and H. V. Demir, "Thermodynamic Silver Doping of Core/Shell Colloidal

Quantum Wells Imparted with Paramagnetic Properties Emitting at Near-Infrared," *Chem. Mater.*, vol. 35, no. 11, pp. 4159–4170, 2023.

[73] E. M. Chan, M. A. Marcus, S. Fakra, M. ElNaggar, R. A. Mathies, and A. Paul Alivisatos, "Millisecond kinetics of nanocrystal cation exchange using microfluidic X-ray absorption spectroscopy," *J. Phys. Chem. A*, vol. 111, no. 49, pp. 12210–12215, 2007.

[74] A. L. Routzahn and P. K. Jain, "Luminescence Blinking of a Reacting Quantum Dot," *Nano. Lett.*, vol. 15, no. 4, pp. 2504–2509, 2015.

[75] A. L. Routzahn and P. K. Jain, "Single-nanocrystal reaction trajectories reveal sharp cooperative transitions," *Nano. Lett.*, vol. 14, no. 2, pp. 987–992, 2014.

[76] V. A. Vlaskin, C. J. Barrows, C. S. Erickson, and D. R. Gamelin, "Nanocrystal diffusion doping," *J. Am. Chem. Soc.*, vol. 135, no. 38, pp. 14380–14389, 2013.

[77] D. H. Son, S. M. Hughes, Y. Yin, and A. Paul Alivisatos, "Cation Exchange Reactions in Ionic Nanocrystals," *Science*, vol. 306, no. 5698, pp. 1009–1012, 2004.

[78] J. B. Rivest and P. K. Jain, "Cation exchange on the nanoscale: an emerging technique for new material synthesis, device fabrication, and chemical sensing," *Chem. Soc. Rev.*, vol. 42, no. 1, pp. 89–96, 2012.

[79] L. De Trizio and L. Manna, "Forging colloidal nanostructures via cation exchange reactions," *Chem. Rev.*, vol. 116, no. 18, pp. 10852–10887, 2016.

[80] G. D. Moon, S. Ko, Y. Xia, and U. Jeong, "Chemical transformations in ultrathin chalcogenide nanowires," *ACS Nano*, vol. 4, no. 4, pp. 2307–2319, 2010.

[81] R. D. Robinson, B. Sadtler, D. O. Demchenko, C. K. Erdonmez, L. W. Wang, and A. P. Alivisatos, "Spontaneous superlattice formation in nanorods through partial cation exchange," *Science*, vol. 317, no. 5836, pp. 355–358, 2007.

[82] D. O. Demchenko, R. D. Robinson, B. Sadtler, C. K. Erdonmez, A. P. Alivisatos, and L. W. Wang, "Formation mechanism and properties of CdS-Ag_2S nanorod superlattices," *ACS Nano*, vol. 2, no. 4, pp. 627–636, 2008.

[83] P. H. C. Camargo, Y. H. Lee, U. Jeong, Z. Zou, and Y. Xia, "Cation exchange: A simple and versatile route to inorganic colloidal spheres with the same size but different compositions and properties," *Langmuir*, vol. 23, no. 6, pp. 2985–2992, 2007.

[84] S. Jeong, J. H. Han, J. T. Jang, J. W. Seo, J. G. Kim, and J. Cheon, "Transformative two-dimensional layered nanocrystals," *J. Am. Chem. Soc.*, vol. 133, no. 37, pp. 14500–14503, 2011.

[85] K. Huang, W. Deng, R. Dai, X. Wang, Q. Xiong, Q. Yuan, X. Jiang, X. Yuan, and X. Xiong, "Ultrasensitive speciation analysis of silver ions and silver nanoparticles with a CdSe quantum dots immobilized filter by Cation exchange reaction," *Microchemical Journal*, vol. 135, pp. 74–80, 2017.

[86] J. Yao, S. Schachermeyer, Y. Yin, and W. Zhong, “Cation exchange in ZnSe nanocrystals for signal amplification in bioassays,” *Anal. Chem.*, vol. 83, no. 1, pp. 402–408, 2011.

[87] K. Huang, K. Xu, J. Tang, L. Yang, J. Zhou, X. Hou, and C. Zheng, “Room Temperature Cation Exchange Reaction in Nanocrystals for Ultrasensitive Speciation Analysis of Silver Ions and Silver Nanoparticles,” *Anal. Chem.*, vol. 87, no. 13, pp. 6584–6591, 2015.

[88] B. Mao, C. H. Chuang, F. Lu, L. Sang, J. Zhu, and C. Burda, “Study of the partial Ag-to-Zn cation exchange in $AgInS_2$/ZnS nanocrystals,” *J. Phys. Chem. C*, vol. 117, no. 1, pp. 648–656, 2013.

[89] D. Deng, L. Qu, and Y. Gu, “Near-infrared broadly emissive $AgInSe_2$/ZnS quantum dots for biomedical optical imaging,” *J. Mater. Chem. C*, vol. 2, no. 34, pp. 7077–7085, 2014.

[90] F. D. Ott, L. L. Spiegel, D. J. Norris, and S. C. Erwin, “Microscopic theory of cation exchange in CdSe nanocrystals,” *Phys Rev Lett*, vol. 113, no. 15, 2014.

[91] M. Casavola, M. A. Van Huis, S. Bals, K. Lambert, Z. Hens, and D. Vanmaekelbergh, “Anisotropic cation exchange in PbSe/CdSe core/shell nanocrystals of different geometry,” *Chem. Mater.*, vol. 24, no. 2, pp. 294–302, 2012.

[92] M. Dufour, E. Izquierdo, C. Livache, B. Martinez, M. G. Silly, T. Pons, E. Lhuillier, C. Delerue, and S. Ithurria, “Doping as a Strategy to Tune Color of 2D Colloidal Nanoplatelets,” *ACS Appl. Mater. Interfaces*, vol. 11, no. 10, pp. 10128–10134, 2019.

[93] Y. Lin, Q. Zhou, D. Tang, R. Niessner, H. Yang, and D. Knopp, “Silver Nanolabels-Assisted Ion-Exchange Reaction with CdTe Quantum Dots Mediated Exciton Trapping for Signal-On Photoelectrochemical Immunoassay of Mycotoxins,” *Anal. Chem.*, vol. 88, no. 15, pp. 7858–7866, 2016.

[94] A. Sahu, M. S. Kang, A. Kompch, C. Notthoff, A. W. Wills, D. Deng, M. Winterer, C. D. Frisbie, and D. J. Norris, “Electronic impurity doping in CdSe nanocrystals,” *Nano. Lett.*, vol. 12, no. 5, pp. 2587–2594, 2012.

[95] S. J. Ding, S. Liang, F. Nan, X. L. Liu, J. H. Wang, L. Zhou, X. F. Yu, Z. H. Hao, and Q. Q. Wang, “Synthesis and enhanced fluorescence of Ag doped CdTe semiconductor quantum dots,” *Nanoscale*, vol. 7, no. 5, pp. 1970–1976, 2015.

[96] A. R. Freyer, P. C. Sercel, Z. Hou, B. H. Savitzky, L. F. Kourkoutis, A. L. Efros, and T. D. Krauss, “Explaining the Unusual Photoluminescence of Semiconductor Nanocrystals Doped via Cation Exchange,” *Nano. Lett.*, vol. 19, no. 7, pp. 4797–4803, 2019.

[97] J. Liu, Q. Zhao, J. L. Liu, Y. S. Wu, Y. Cheng, M. W. Ji, H. M. Qian, W. C. Hao, L. J. Zhang, X. J. Wei, S. G. Wang, J. T. Zhang, Y. Du, S. X. Dou, and H. S. Zhu, “Heterovalent-Doping-Enabled Efficient Dopant Luminescence and Controllable

Electronic Impurity Via a New Strategy of Preparing II-VI Nanocrystals," *Adv. Mater.*, vol. 27, no. 17, pp. 2753–2761, 2015.

[98] A. Freyer, T. M. Tumiel, M. Smeaton, B. H. Savitzky, L. F. Kourkoutis, and T. D. Krauss, "Heterogeneity in Cation Exchange Ag^+ Doping of CdSe Nanocrystals," *ACS Nanoscience Au*, vol. 3, no. 4, pp. 280–285, 2023.

[99] K. E. Hughes, K. H. Hartstein, and D. R. Gamelin, "Photodoping and Transient Spectroscopies of Copper-Doped CdSe/CdS Nanocrystals," *ACS Nano*, vol. 12, no. 1, pp. 718–728, 2018.

[100] D. Morgan and D. F. Kelley, "Role of Surface States in Silver-Doped CdSe and CdSe/CdS Quantum Dots," *The J. Phys. Chem. C*, vol. 122, no. 19, pp. 10627–10636, 2018.

[101] V. Pinchetti, Q. Di, M. Lorenzon, A. Camellini, M. Fasoli, M. Zavelani-Rossi, F. Meinardi, J. Zhang, S. A. Crooker, and S. Brovelli, "Excitonic pathway to photoinduced magnetism in colloidal nanocrystals with nonmagnetic dopants," *Nat. Nanotechnol.*, vol. 13, no. 2, pp. 145–151, 2017.

[102] H. D. Nelson, S. O. M. Hinterding, R. Fainblat, S. E. Creutz, X. Li, and D. R. Gamelin, "Mid-Gap States and Normal vs Inverted Bonding in Luminescent Cu^+- and Ag^+-Doped CdSe Nanocrystals," *J. Am. Chem. Soc.*, vol. 139, no. 18, pp. 6411–6421, 2017.

[103] M. H. Humayun, P. L. Hernandez-Martinez, N. Gheshlaghi, O. Erdem, Y. Altintas, F. Shabani, and H. V. Demir, "Near-Field Energy Transfer into Silicon Inversely Proportional to Distance Using Quasi-2D Colloidal Quantum Well Donors," *Small*, vol. 17, no. 41, p. 2103524, 2021.

[104] A. H. Khan, V. Pinchetti, I. Tanghe, Z. Dang, B. Martín-García, Z. Hens, D. Van Thourhout, P. Geiregat, S. Brovelli, and I. Moreels, "Tunable and Efficient Red to Near-Infrared Photoluminescence by Synergistic Exploitation of Core and Surface Silver Doping of CdSe Nanoplatelets," *Chem. Mater.*, vol. 31, no. 4, pp. 1450–1459, 2019.

[105] B. Liu, M. Sharma, J. Yu, L. Wang, S. Shendre, A. Sharma, M. Izmir, S. Delikanli, Y. Altintas, C. Dang, H. Sun, and H. V. Demir, "Management of electroluminescence from silver-doped colloidal quantum well light-emitting diodes," *Cell. Rep. Phys. Sci.*, vol. 3, no. 5, p. 100860, 2022.

[106] W. S. Lee, Y. G. Kang, M. Sharma, Y. M. Lee, S. Jeon, A. Sharma, H. V. Demir, M. J. Han, W. K. Koh, and S. J. Oh, "Ligand Exchange and Impurity Doping in 2D CdSe Nanoplatelet Thin Films and Their Applications," *Adv. Electron. Mater.*, vol. 8, no. 1, p. 2100739, 2022.

[107] A. C. Berends, M. J. J. Mangnus, C. Xia, F. T. Rabouw, and C. De Mello Donega, "Optoelectronic Properties of Ternary I-III-VI_2 Semiconductor Nanocrystals: Bright Prospects with Elusive Origins," *J. Phys. Chem. Lett.*, vol. 10, no. 7, pp. 1600–1616, 2019.

[108] X. J. Wu, X. Huang, X. Qi, H. Li, B. Li, and H. Zhang, "Copper-based ternary and quaternary semiconductor nanoplates: Templated synthesis, characterization, and photoelectrochemical properties," *Angew. Chem.*, vol. 53, no. 34, pp. 8929–8933, 2014.

[109] L. Chen, H. Hu, Y. Chen, J. Gao, and G. Li, "Plasmonic $Cu_{2-x}S$ nanoparticles: a brief introduction of optical properties and applications," *Mater. Adv.*, vol. 2, no. 3, pp. 907–926, 2021.

[110] Z. Long, W. Zhang, J. Tian, G. Chen, Y. Liu, and R. Liu, "Recent research on the luminous mechanism, synthetic strategies, and applications of $CuInS_2$ quantum dots," *Inorg. Chem. Front.*, vol. 8, no. 4, pp. 880–897, 2021.

[111] H. Zhong, S. S. Lo, T. Mirkovic, Y. Li, Y. Ding, Y. Li, and G. D. Scholes, "Noninjection Gram-Scale Synthesis of Monodisperse Pyramidal $CuInS_2$ Nanocrystals and Their Size-Dependent Properties," *ACS Nano*, vol. 4, no. 9, pp. 5253–5262, 2010.

[112] B. Chen, W. Zheng, F. Chun, X. Xu, Q. Zhao, and F. Wang, "Synthesis and hybridization of $CuInS_2$ nanocrystals for emerging applications," *Chem. Soc. Rev.*, vol. 52, no. 23, pp. 8374–8409, 2023.

[113] P. Reiss, M. Carrière, C. Lincheneau, L. Vaure, and S. Tamang, "Synthesis of Semiconductor Nanocrystals, Focusing on Nontoxic and Earth-Abundant Materials," *Chem. Rev.*, vol. 116, no. 18, pp. 10731–10819, 2016.

[114] O. Stroyuk, A. Raevskaya, and N. Gaponik, "Solar light harvesting with multinary metal chalcogenide nanocrystals.," *Chem. Soc. Rev.*, vol. 47, no. 14, pp. 5354–5422, 2018.

[115] N. Moghaddam, C. Dabard, M. Dufour, H. Po, X. Xu, T. Pons, E. Lhuillier, and S. Ithurria, "Surface Modification of CdE (E: S, Se, and Te) Nanoplatelets to Reach Thicker Nanoplatelets and Homostructures with Confinement-Induced Intraparticle Type I Energy Level Alignment," *J. Am. Chem. Soc.*, vol. 143, no. 4, pp. 1863–1872, 2021.

[116] W. Cho, S. Kim, I. Coropceanu, V. Srivastava, B. T. Diroll, A. Hazarika, I. Fedin, G. Galli, R. D. Schaller, and D. V. Talapin, "Direct Synthesis of Six-Monolayer (1.9 nm) Thick Zinc-Blende CdSe Nanoplatelets Emitting at 585 nm," *Chem. Mater.*, vol. 30, no. 20, pp. 6957– 6960, 2018.

[117] S. Christodoulou, J. I. Climente, J. Planelles, R. Brescia, M. Prato, B. Martín-Garciá, A. H. Khan, and I. Moreels, "Chloride-Induced Thickness Control in CdSe Nanoplatelets," *Nano. Lett.*, vol. 18, no. 10, pp. 6248–6254, 2018.

[118] A. Chu, C. Livache, S. Ithurria, and E. Lhuillier, "Electronic structure robustness and design rules for 2D colloidal heterostructures," *J. Appl. Phys.*, vol. 123, no. 3, p. 035701, 2018.

[119] A. Hazarika, I. Fedin, L. Hong, J. Guo, V. Srivastava, W. Cho, I. Coropceanu, J. Portner, B. T. Diroll, J. P. Philbin, E. Rabani, R. Klie, and D. V. Talapin, "Colloidal Atomic Layer Deposition with Stationary Reactant Phases Enables

Precise Synthesis of 'Digital' II–VI Nano-heterostructures with Exquisite Control of Confinement and Strain," *J. Am. Chem. Soc.*, vol. 141, no. 34, pp. 13487–13496, 2019.

[120] A. Polovitsyn, Z. Dang, J. L. Movilla, B. Martín-García, A. H. Khan, G. H. V. Bertrand, R. Brescia, and I. Moreels, "Synthesis of Air-Stable CdSe/ZnS Core-Shell Nanoplatelets with Tunable Emission Wavelength," *Chem. Mater.*, vol. 29, no. 13, pp. 5671–5680, 2017.

[121] C. Meerbach, R. Tietze, S. Voigt, V. Sayevich, V. M. Dzhagan, S. C. Erwin, Z. Dang, O. Selyshchev, K. Schneider, D. R. T. Zahn, V. Lesnyak, and A. Eychmüller, "Brightly Luminescent Core/Shell Nanoplatelets with Continuously Tunable Optical Properties," *Adv. Opt. Mater.*, vol. 7, no. 7, p. 1801478, 2019.

[122] M. D. Tessier, P. Spinicelli, D. Dupont, G. Patriarche, S. Ithurria, and B. Dubertret, "Efficient exciton concentrators built from colloidal core/crown CdSe/CdS semiconductor nanoplatelets," *Nano. Lett.*, vol. 14, no. 1, pp. 207–213, 2014.

[123] M. D. Tessier, B. Mahler, B. Nadal, H. Heuclin, S. Pedetti, and B. Dubertret, "Spectroscopy of colloidal semiconductor core/shell nanoplatelets with high quantum yield," *Nano. Lett.*, vol. 13, no. 7, pp. 3321–3328, 2013.

[124] A. A. Rossinelli, A. Riedinger, P. Marqués-Gallego, P. N. Knüsel, F. V. Antolinez, and D. J. Norris, "High-temperature growth of thick-shell CdSe/CdS core/shell nanoplatelets," *Chem. Commun.*, vol. 53, no. 71, pp. 9938–9941, 2017.

[125] Y. Altintas, U. Quliyeva, K. Gungor, O. Erdem, Y. Kelestemur, E. Mutlugun, M. V. Kovalenko, and H. V. Demir, "Highly Stable, Near-Unity Efficiency Atomically Flat Semiconductor Nanocrystals of CdSe/ZnS Hetero-Nanoplatelets Enabled by ZnS-Shell Hot-Injection Growth," *Small*, vol. 15, no. 8, p. 1804854, 2019.

[126] L. Zhao, L. Hu, and X. Fang, "Growth and device application of CdSe nanostructures," *Adv. Funct. Mater.*, vol. 22, no. 8, pp. 1551–1566, 2012.

[127] Y. Chen, J. Vela, H. Htoon, J. L. Casson, D. J. Werder, D. A. Bussian, V. I. Klimov, and J. A. Hollingsworth, "'Giant' multishell CdSe nanocrystal quantum dots with suppressed blinking," *J. Am. Chem. Soc.*, vol. 130, no. 15, pp. 5026–5027, 2008.

[128] C. Galland, S. Brovelli, W. K. Bae, L. A. Padilha, F. Meinardi, and V. I. Klimov, "Dynamic hole blockade yields two-color quantum and classical light from dot-in-bulk nanocrystals," *Nano. Lett.*, vol. 13, no. 1, pp. 321–328, 2013.

[129] S. Brovelli, W. K. Bae, C. Galland, U. Giovanella, F. Meinardi, and V. I. Klimov, "Dual-color electroluminescence from dot-in-bulk nanocrystals," *Nano. Lett.*, vol. 14, no. 2, pp. 486–494, 2014.

[130] A. A. Rossinelli, H. Rojo, A. S. Mule, M. Aellen, A. Cocina, E. De Leo, R. Schäublin, and D. J. Norris, "Compositional Grading for Efficient and

Narrowband Emission in CdSe-Based Core/Shell Nanoplatelets," *Chem. Mater.*, vol. 31, no. 22, pp. 9567–9578, 2019.

[131] J. Zhang, Y. Sun, S. Ye, J. Song, and J. Qu, "Heterostructures in Two-Dimensional CdSe Nanoplatelets: Synthesis, Optical Properties, and Applications," *Chem. Mater.*, vol. 32, no. 22, pp. 9490–9507, 2020.

[132] H.D. Baruj, I. Bozkaya, B. Canimkurbey, A.T. Isik, F. Shabani, S. Delikanli, S. Shendre, O. Erdem, F. Isik, H.V. Demir, "Highly-Directional, Highly-Efficient Solution-Processed Light-Emitting Diodes of All-Face-Down Oriented Colloidal Quantum Well Self-Assembly," Small, vol. 19, no. 29, pp. 2206582.

[133] H. Lu, G. M. Carroll, N. R. Neale, and M. C. Beard, "Infrared quantum dots: Progress, challenges, and opportunities," *ACS Nano*, vol. 13, no. 2, pp. 939–953, 2019.

[134] P. Vashishtha, S. Bishnoi, C. H. A. Li, M. Jagadeeswararao, T. J. N. Hooper, N. Lohia, S. B. Shivarudraiah, M. S. Ansari, S. N. Sharma, and J. E. Halpert, "Recent Advancements in Near-Infrared Perovskite Light-Emitting Diodes," *ACS Appl. Electron. Mater.*, vol. 2, no. 11, pp. 3470–3490, 2020.

[135] S. Foroutan-Barenji, F. Shabani, A.T. Isik, Z. Dikmen, and H.V. Demir, "All-colloidal parity–time-symmetric microfiber lasers balanced between the gain of colloidal quantum wells and the loss of colloidal metal nanoparticles," *Nanoscale*. vol. 14, no. 37, pp. 13755-62, 2022.

[136] R. Azizov, I. Sinev, F. Işık, F. Shabani, A. Pushkarev, I. Yurdakul, S. Delikanli, H.V. Demir, and S. Makarov, "Direct laser writing of resonant periodic nanostructures in thin light-emitting films of CdSe/CdZnS core/shell nanoplatelets," Appl. Phys. Lett., vol. 121, no. 22, pp. 223301, 2022.

[137] Y. Zheng and X. Zhu, "Recent Progress in Emerging Near-Infrared Emitting Materials for Light-Emitting Diode Applications," *Organic Materials*, vol. 2, no. 04, pp. 253–281, 2020.

[138] D. Hertel, H. Marechal, D. A. Tefera, W. Fan, and R. Hicks, "A low-cost VIS-NIR true color night vision video system based on a wide dynamic range CMOS imager," *IEEE Intelligent Vehicles Symposium, Proceedings*, pp. 273–278, 2009.

[139] A. M. Smith, M. C. Mancini, and S. Nie, "Bioimaging: Second window for in vivo imaging," *Nat. Nanotechnol.*, vol. 4, no. 11, pp. 710–711, 2009.

[140] G. H. V. Bertrand, A. Polovitsyn, S. Christodoulou, A. H. Khan, and I. Moreels, "Shape control of zincblende CdSe nanoplatelets," *Chem. Commun.*, vol. 52, no. 80, pp. 11975–11978, 2016.

[141] L. Biadala, F. Liu, M. D. Tessier, D. R. Yakovlev, B. Dubertret, and M. Bayer, "Recombination dynamics of band edge excitons in quasi-two-dimensional cdse nanoplatelets," *Nano. Lett.*, vol. 14, no. 3, pp. 1134–1139, 2014.

[142] T. Erdem, Z. Soran-Erdem, F. Isik, F. Shabani, A.F. Yazici, E. Mutlugün, N. Gaponik, and H.V. Demir, "Color Enrichment Solids of Spectrally Pure Colloidal

Quantum Wells for Wide Color Span in Displays," *Adv. Opt. Mat.*, vol. 10, no. 14, pp. 2200161, 2022.

[143] D. V. Talapin, J. H. Nelson, E. V. Shevchenko, S. Aloni, B. Sadtler, and A. P. Alivisatos, "Seeded growth of highly luminescent CdSe/CdS nanoheterostructures with rod and tetrapod morphologies," *Nano. Lett.*, vol. 7, no. 10, pp. 2951–2959, 2007.

[144] N. J. Borys, M. J. Walter, J. Huang, D. V. Talapin, and J. M. Lupton, "The role of particle morphology in interfacial energy transfer in CdSe/CdS heterostructure nanocrystals," *Science*, vol. 330, no. 6009, pp. 1371–1374, 2010.

[145] R. Xie, U. Kolb, J. Li, T. Basché, and A. Mews, "Synthesis and characterization of highly luminescent CdSe-core CdS/Zn 0.5Cd0.5S/ZnS multishell nanocrystals," *J. Am. Chem. Soc.*, vol. 127, no. 20, pp. 7480–7488, 2005.

[146] I. Fedin and D. V. Talapin, "Colloidal CdSe Quantum Rings," *J. Am. Chem. Soc.*, vol. 138, no. 31, pp. 9771–9774, 2016.

[147] B. Liu, M. Sharma, J. Yu, S. Shendre, C. Hettiarachchi, A. Sharma, A. Yeltik, L. Wang, H. Sun, C. Dang, *et al.*, "Light-Emitting Diodes with Cu-Doped Colloidal Quantum Wells: From Ultrapure Green, Tunable Dual-Emission to White Light," *Small*, vol. 15, no. 38, p. 1901983, 2019.

[148] E. M. Miller, D. M. Kroupa, J. Zhang, P. Schulz, A. R. Marshall, A. Kahn, S. Lany, J. M. Luther, M. C. Beard, C. L. Perkins, and J. Van De Lagemaat, "Revisiting the Valence and Conduction Band Size Dependence of PbS Quantum Dot Thin Films," *ACS Nano*, vol. 10, no. 3, pp. 3302–3311, 2016.

[149] X. Dai, Z. Zhang, Y. Jin, Y. Niu, H. Cao, X. Liang, L. Chen, J. Wang, and X. Peng, "Solution-processed, high-performance light-emitting diodes based on quantum dots," *Nature*, vol. 515, no. 7525, pp. 96–99, 2014.

[150] M. İzmir, A. Sharma, S. Shendre, E.G. Durmusoglu, V.K. Sharma, F. Shabani, H.D. Baruj, S. Delikanli, M. Sharma, and H.V. Demir, "Blue-emitting CdSe nanoplatelets enabled by sulfur-alloyed heterostructures for light-emitting diodes with low turn-on voltage," *ACS Appl. Nano Mater.*, vol. 5, no. 1, pp. 1367-1376, 2021.

[151] L. Qian, Y. Zheng, J. Xue, and P. H. Holloway, "Stable and efficient quantum-dot light-emitting diodes based on solution-processed multilayer structures," *Nat Photonics.*, vol. 5, no. 9, pp. 543–548, 2011.

[152] Q. Zeng, Z. Xu, C. Zheng, Y. Liu, W. Chen, T. Guo, F. Li, C. Xiang, Y. Yang, W. Cao, X. Xie, X. Yan, L. Qian, and P. H. Holloway, "Improving Charge Injection via a Blade-Coating Molybdenum Oxide Layer: Toward High-Performance Large-Area Quantum-Dot Light-Emitting Diodes," *ACS Appl. Mater. Interfaces*, vol. 10, no. 9, pp. 8258–8264, 2018.

[153] I. Lignos, V. Morad, Y. Shynkarenko, C. Bernasconi, R. M. Maceiczyk, L. Protesescu, F. Bertolotti, S. Kumar, S. T. Ochsenbein, N. Masciocchi, A. Guagliardi, C. J. Shih, M. I. Bodnarchuk, A. J. Demello, and M. V. Kovalenko,

"Exploration of Near-Infrared-Emissive Colloidal Multinary Lead Halide Perovskite Nanocrystals Using an Automated Microfluidic Platform," *ACS Nano*, vol. 12, no. 6, pp. 5504–5517, 2018.

[154] Y. Tian, C. Zhou, M. Worku, X. Wang, Y. Ling, H. Gao, Y. Zhou, Y. Miao, J. Guan, and B. Ma, "Highly Efficient Spectrally Stable Red Perovskite Light-Emitting Diodes," *Adv. Mater.*, vol. 30, no. 20, p. 1707093, 2018.

[155] X. Shen, Y. Zhang, S. V. Kershaw, T. Li, C. Wang, X. Zhang, W. Wang, D. Li, Y. Wang, M. Lu, L. Zhang, C. Sun, D. Zhao, G. Qin, X. Bai, W. W. Yu, and A. L. Rogach, "Zn-Alloyed CsPbI 3 Nanocrystals for Highly Efficient Perovskite Light-Emitting Devices," *Nano. Lett.*, vol. 19, no. 3, pp. 1552–1559, 2019.

[156] B. Han, B. Cai, Q. Shan, J. Song, J. Li, F. Zhang, J. Chen, T. Fang, Q. Ji, X. Xu, and H. Zeng, "Stable, Efficient Red Perovskite Light-Emitting Diodes by (α, δ)-$CsPbI_3$ Phase Engineering," *Adv. Funct. Mater.*, vol. 28, no. 47, p. 1804285, 2018.

[157] J. Si, Y. Liu, Z. He, H. Du, K. Du, D. Chen, J. Li, M. Xu, H. Tian, H. He, D. Di, C. Lin, Y. Cheng, J. Wang, and Y. Jin, "Efficient and High-Color-Purity Light-Emitting Diodes Based on in Situ Grown Films of $CsPbX_3$ (X = Br, I) Nanoplates with Controlled Thicknesses," *ACS Nano*, vol. 11, no. 11, pp. 11100–11107, 2017.

[158] M. Lu, J. Guo, S. Sun, P. Lu, J. Wu, Y. Wang, S. V. Kershaw, W. W. Yu, A. L. Rogach, and Y. Zhang, "Bright CsPbI3 Perovskite Quantum Dot Light-Emitting Diodes with Top-Emitting Structure and a Low Efficiency Roll-Off Realized by Applying Zirconium Acetylacetonate Surface Modification," *Nano. Lett.*, vol. 20, no. 4, pp. 2829–2836, 2020.

[159] J. Pan, Y. Shang, J. Yin, M. De Bastiani, W. Peng, I. Dursun, L. Sinatra, A. M. El-Zohry, M. N. Hedhili, A. H. Emwas, O. F. Mohammed, Z. Ning, and O. M. Bakr, "Bidentate Ligand-Passivated CsPbI 3 Perovskite Nanocrystals for Stable Near-Unity Photoluminescence Quantum Yield and Efficient Red Light-Emitting Diodes," *J. Am. Chem. Soc.*, vol. 140, no. 2, pp. 562–565, 2018.

[160] X. Zhang, C. Sun, Y. Zhang, H. Wu, C. Ji, Y. Chuai, P. Wang, S. Wen, C. Zhang, and W. W. Yu, "Bright Perovskite Nanocrystal Films for Efficient Light-Emitting Devices," *J. Phys. Chem. Lett.*, vol. 7, no. 22, pp. 4602–4610, 2016.

[161] S. Zhang, C. Yi, N. Wang, Y. Sun, W. Zou, Y. Wei, Y. Cao, Y. Miao, R. Li, Y. Yin, N. Zhao, J. Wang, and W. Huang, "Efficient Red Perovskite Light-Emitting Diodes Based on Solution-Processed Multiple Quantum Wells," *Adv. Mater.*, vol. 29, no. 22, p. 1606600, 2017.

[162] G. Li, J. Huang, H. Zhu, Y. Li, J. X. Tang, and Y. Jiang, "Surface Ligand Engineering for Near-Unity Quantum Yield Inorganic Halide Perovskite QDs and High-Performance QLEDs," *Chem. Mater.*, vol. 30, no. 17, pp. 6099–6107, 2018.

[163] M. Lu, X. Zhang, Y. Zhang, J. Guo, X. Shen, W. W. Yu, and A. L. Rogach, "Simultaneous Strontium Doping and Chlorine Surface Passivation Improve

Luminescence Intensity and Stability of CsPbI3 Nanocrystals Enabling Efficient Light-Emitting Devices," *Adv. Mater.*, vol. 30, no. 50, p. 1804691, 2018.

[164] X. Zhang, M. Lu, Y. Zhang, H. Wu, X. Shen, W. Zhang, W. Zheng, V. L. Colvin, and W. W. Yu, "PbS Capped CsPbI3 Nanocrystals for Efficient and Stable Light-Emitting Devices Using p- i- n Structures," *ACS Cent Sci*, vol. 4, no. 10, pp. 1352–1359, 2018.

[165] J. Mao, H. Lin, F. Ye, M. Qin, J. M. Burkhartsmeyer, H. Zhang, X. Lu, K. S. Wong, and W. C. H. Choy, "All-Perovskite Emission Architecture for White Light-Emitting Diodes," *ACS Nano*, vol. 12, no. 10, pp. 10486–10492, 2018.

[166] J. Chang, S. Zhang, N. Wang, Y. Sun, Y. Wei, R. Li, C. Yi, J. Wang, and W. Huang, "Enhanced Performance of Red Perovskite Light-Emitting Diodes through the Dimensional Tailoring of Perovskite Multiple Quantum Wells," *J. Phys. Chem. Lett.*, vol. 9, no. 4, pp. 881–886, 2018.

[167] G. Li, F. W. R. Rivarola, N. J. L. K. Davis, S. Bai, T. C. Jellicoe, F. De La Peña, S. Hou, C. Ducati, F. Gao, R. H. Friend, N. C. Greenham, and Z. K. Tan, "Highly Efficient Perovskite Nanocrystal Light-Emitting Diodes Enabled by a Universal Crosslinking Method," *Adv. Mater.*, vol. 28, no. 18, pp. 3528–3534, 2016.

[168] H. Hu, T. Salim, B. Chen, and Y. M. Lam, "Molecularly Engineered Organic-Inorganic Hybrid Perovskite with Multiple Quantum Well Structure for Multicolored Light-Emitting Diodes," *Sci Rep*, vol. 6, no. 1, pp. 1–8, 2016.

[169] X. Liu, S. Zhao, W. Gu, Y. Zhang, X. Qiao, Z. Ni, X. Pi, and D. Yang, "Light-Emitting Diodes Based on Colloidal Silicon Quantum Dots with Octyl and Phenylpropyl Ligands," *ACS Appl. Mater. Interfaces*, vol. 10, no. 6, pp. 5959–5966, 2018.

[170] A. P. Alivisatos, "Perspectives on the physical chemistry of semiconductor nanocrystals," *J. Phys. Chem.*, vol. 100, no. 31, pp. 13226–13239, 1996.

[171] S. Kim, B. Fisher, H. J. Eisler, and M. Bawendi, "Type-II quantum dots: CdTe/CdSe(core/shell) and CdSe/ZnTe(core/shell) heterostructures," *J. Am. Chem. Soc.*, vol. 125, no. 38, pp. 11466–11467, 2003.

[172] D. Mourad, J. P. Richters, L. Gérard, R. André, J. Bleuse, and H. Mariette, "Determination of valence-band offset at cubic CdSe/ZnTe type-II heterojunctions: A combined experimental and theoretical approach," *Phys Rev B Condens Matter Mater Phys*, vol. 86, no. 19, pp. 1–10, 2012.

[173] S. S. Lo, T. Mirkovic, C. H. Chuang, C. Burda, and G. D. Scholes, "Emergent properties resulting from type-II band alignment in semiconductor nanoheterostructures," *Adv. Mater.*, vol. 23, no. 2, pp. 180–197, 2011.

[174] R. Ghosh Chaudhuri and S. Paria, "Core/shell nanoparticles: Classes, properties, synthesis mechanisms, characterization, and applications," *Chem. Rev.*, vol. 112, no. 4, pp. 2373–2433, 2012.

[175] S. Delikanli, O. Erdem, F. Isik, H. Dehghanpour Baruj, F. Shabani, H. B. Yagci, E. G. Durmusoglu, and H. V. Demir, "Ultrahigh Green and Red Optical Gain Cross Sections from Solutions of Colloidal Quantum Well Heterostructures," *J. Phys. Chem. Lett.*, vol. 12, no. 9, pp. 2177–2182, 2021.

[176] V. Steinmetz, J. I. Climente, R. Pandya, J. Planelles, F. Margaillan, Y. Puttisong, M. Dufour, S. Ithurria, A. Sharma, G. Lakhwani, L. Legrand, F. Bernardot, C. Testelin, M. Chamarro, A. W. Chin, A. Rao, and T. Barisien, "Emission State Structure and Linewidth Broadening Mechanisms in Type-II CdSe/CdTe Core–Crown Nanoplatelets: A Combined Theoretical–Single Nanocrystal Optical Study," *The J. Phys. Chem. C*, vol. 124, no. 31, pp. 17352–17363, 2020.

[177] Q. Li, K. Wu, J. Chen, Z. Chen, J. R. McBride, and T. Lian, "Size-Independent Exciton Localization Efficiency in Colloidal CdSe/CdS Core/Crown Nanosheet Type-I Heterostructures," *ACS Nano*, vol. 10, no. 3, pp. 3843–3851, 2016.

[178] C. Dabard, V. Guilloux, C. Gréboval, H. Po, L. Makke, N. Fu, X. Z. Xu, M. G. Silly, G. Patriarche, E. Lhuillier, T. Barisien, J. I. Climente, B. T. Diroll, and S. Ithurria, "Double-crowned 2D semiconductor nanoplatelets with bicolor power-tunable emission," *Nature Communications 2022 13:1*, vol. 13, no. 1, pp. 1–10, 2022.

[179] W. Y. Wu, M. Li, J. Lian, X. Wu, E. K. L. Yeow, M. H. Jhon, and Y. Chan, "Efficient color-tunable multiexcitonic dual wavelength emission from type II semiconductor tetrapods," *ACS Nano*, vol. 8, no. 9, pp. 9349–9357, 2014.

[180] S. Kaniyankandy, S. Rawalekar, S. Verma, and H. N. Ghosh, "Ultrafast hole transfer in CdSe/ZnTe type II core-shell nanostructure," *J. Phys. Chem. C*, vol. 115, no. 5, pp. 1428–1435, 2011.

[181] M. Jones, S. Kumar, S. S. Lo, and G. D. Scholes, "Exciton trapping and recombination in type ii CdSe/CdTe nanorod heterostructures," *J. Phys. Chem. C*, vol. 112, no. 14, pp. 5423–5431, 2008.

[182] S. Kumar, M. Jones, S. S. Lo, and G. D. Scholes, "Nanorod heterostructures showing photoinduced charge separation," *Small*, vol. 3, no. 9, pp. 1633–1639, 2007.

[183] Y. Liu, C. Zhang, H. Zhang, R. Wang, Z. Hua, X. Wang, J. Zhang, and M. Xiao, "Broadband optical non-linearity induced by charge-transfer excitons in type-II CdSe/ZnTe nanocrystals," *Adv. Mater.*, vol. 25, no. 32, pp. 4397–4402, 2013.

[184] Y. Wang, Q. Wang, X. Zhan, F. Wang, M. Safdar, and J. He, "Visible light driven type II heterostructures and their enhanced photocatalysis properties: A review," *Nanoscale*, vol. 5, no. 18, pp. 8326–8339, 2013.

[185] J. Bang, B. Chon, N. Won, J. Nam, T. Joo, and S. Kim, "Spectral switching of type-II quantum dots by charging," *J. Phys. Chem. C*, vol. 113, no. 16, pp. 6320–6323, 2009.

[186] R. Tenne, S. Pedetti, M. Kazes, S. Ithurria, L. Houben, B. Nadal, D. Oron, and B. Dubertret, "From dilute isovalent substitution to alloying in CdSeTe

nanoplatelets," *Physical Chemistry Chemical Physics*, vol. 18, no. 22, pp. 15295–15303, 2016.

[187] S. S. Lo, Y. Khan, M. Jones, and G. D. Scholes, "Temperature and solvent dependence of CdSe/CdTe heterostructure nanorod spectra," *J Chem Phys*, vol. 131, no. 8, 2009.

[188] H. Laheld, "Excitons in type-II quantum dots: Finite offsets," *Phys Rev B*, vol. 52, no. 4, pp. 2697–2703, 1995.

[189] M. Olutas, B. Guzelturk, Y. Kelestemur, A. Yeltik, S. Delikanli, and H. V. Demir, "Lateral size-dependent spontaneous and stimulated emission properties in colloidal CdSe nanoplatelets," *ACS Nano*, vol. 9, no. 5, pp. 5041–5050, 2015.

[190] S. Hu, F. Shabani, B. Liu, L. Zhang, M. Guo, G. Lu, Z. Zhou, J. Wang, J. C. Huang, Y. Min, Q. Xue, H. V. Demir, and C. Liu, "High-Performance Deep Red Colloidal Quantum Well Light-Emitting Diodes Enabled by the Understanding of Charge Dynamics," *ACS Nano*, vol. 16, no. 7, pp. 10840–10851, 2022.

[191] V. Dzhagan, A. G. Milekhin, M. Y. Valakh, S. Pedetti, M. Tessier, B. Dubertret, and D. R. T. Zahn, "Morphology-induced phonon spectra of CdSe/CdS nanoplatelets: core/shell vs. core–crown," *Nanoscale*, vol. 8, no. 39, pp. 17204–17212, 2016.

[192] R. Pandya, R. Y. S. Chen, A. Cheminal, M. Dufour, J. M. Richter, T. H. Thomas, S. Ahmed, A. Sadhanala, E. P. Booker, G. Divitini, F. Deschler, N. C. Greenham, S. Ithurria, and A. Rao, "Exciton-Phonon Interactions Govern Charge-Transfer-State Dynamics in CdSe/CdTe Two-Dimensional Colloidal Heterostructures," *J. Am. Chem. Soc.*, vol. 140, pp. 14097–14111, 2018.

[193] N. N. Schlenskaya, Y. Yao, T. Mano, T. Kuroda, A. V. Garshev, V. F. Kozlovskii, A. M. Gaskov, R. B. Vasiliev, and K. Sakoda, "Scroll-like Alloyed CdS_xSe_{1-x} Nanoplatelets: Facile Synthesis and Detailed Analysis of Tunable Optical Properties," *Chem. Mater.*, vol. 29, no. 2, pp. 579–586, 2017.

[194] R. E. Bailey and S. Nie, "Alloyed semiconductor quantum dots: Tuning the optical properties without changing the particle size," *J. Am. Chem. Soc.*, vol. 125, no. 23, pp. 7100–7106, 2003.

[195] J. E. Bernard and A. Zunger, "Optical bowing in zinc chalcogenide semiconductor alloys," vol. 34.

[196] B. I. MacDonald, A. Martucci, S. Rubanov, S. E. Watkins, P. Mulvaney, and J. J. Jasieniak, "Layer-by-Layer Assembly of Sintered $CdSe_xTe_{1-x}$ Nanocrystal Solar Cells," *ACS Nano*, vol. 6, no. 7, pp. 5995–6004, 2012.

[197] C. S. Schnohr, "Compound semiconductor alloys: From atomic-scale structure to bandgap bowing," *Appl Phys Rev*, vol. 2, no. 3, p. 031304, 2015.

[198] P. P. Ingole, G. B. Markad, D. Saraf, L. Tatikondewar, O. Nene, A. Kshirsagar, and S. K. Haram, "Band gap bowing at nanoscale: Investigation of CdS_xSe_{1-x}

alloy quantum dots through cyclic voltammetry and density functional theory," *J. Phys. Chem. C*, vol. 117, no. 14, pp. 7376–7383, 2013.

[199] Y. Kelestemur, B. Guzelturk, O. Erdem, M. Olutas, T. Erdem, C. F. Usanmaz, K. Gungor, and H. V. Demir, "$CdSe/CdSe_{1-x}Te_x$ Core/Crown Heteronanoplatelets: Tuning the Excitonic Properties without Changing the Thickness," *J. Phys. Chem. C*, vol. 121, no. 8, pp. 4650–4658, 2017.

[200] J. Luo, J. Luo, Z. Zheng, Z. Zheng, S. Yan, M. Morgan, X. Zu, X. Xiang, and W. Zhou, "Photocurrent Enhanced in UV-vis-NIR Photodetector Based on CdSe/CdTe Core/Shell Nanowire Arrays by Piezo-Phototronic Effect," *ACS Photonics*, vol. 7, no. 6, pp. 1461–1467, 2020.

[201] S. C. Rai, K. Wang, J. Chen, J. K. Marmon, M. Bhatt, S. Wozny, Y. Zhang, and W. Zhou, "Enhanced Broad Band Photodetection through Piezo-Phototronic Effect in CdSe/ZnTe Core/Shell Nanowire Array," *Adv. Electron. Mater.*, vol. 1, no. 4, p. 1400050, 2015.

[202] K. Wu, Q. Li, Y. Jia, J. R. McBride, Z. X. Xie, and T. Lian, "Efficient and ultrafast formation of long-lived charge-transfer exciton state in atomically thin cadmium selenide/cadmium telluride type-II heteronanosheets," *ACS Nano*, vol. 9, no. 1, pp. 961–968, 2015.

[203] S. H. Wei, S. B. Zhang, and A. Zunger, "First-principles calculation of band offsets, optical bowings, and defects in CdS, CdSe, CdTe, and their alloys," *J. Appl. Phys.*, vol. 87, no. 3, pp. 1304–1311, 2000.

[204] Y. Kelestemur, M. Olutas, S. Delikanli, B. Guzelturk, M. Z. Akgul, and H. V. Demir, "Type-II colloidal quantum wells: CdSe/CdTe core/crown heteronanoplatelets," *J. Phys. Chem. C*, vol. 119, no. 4, pp. 2177–2185, 2015.

[205] Y. P. Varshni, "Temperature dependence of the energy gap in semiconductors," *Physica*, vol. 34, no. 1, pp. 149–154, 1967.

[206] B. Pejova, B. Abay, and I. Bineva, "Temperature dependence of the band-gap energy and sub-band-gap absorption tails in strongly quantized ZnSe nanocrystals deposited as thin films," *J. Phys. Chem. C*, vol. 114, no. 36, pp. 15280–15291, 2010.

[207] V. Kumar, V. Jha, and A. K. Shrivastava, "Debye temperature and melting point of II-VI and III-V semiconductors," *Crystal Research and Technology*, vol. 45, no. 9, pp. 920–924, 2010.

[208] A. V Rodina and A. L. Efros, "Radiative recombination from dark excitons in nanocrystals: Activation mechanisms and polarization properties," *Phys Rev B*, vol. 93, p. 155427, 2016.

[209] D. Valerini, A. Cretí, M. Lomascolo, L. Manna, R. Cingolani, and M. Anni, "Temperature dependence of the photoluminescence properties of colloidal CdSeZnS core/shell quantum dots embedded in a polystyrene matrix," *Phys Rev B Condens Matter Mater Phys*, vol. 71, no. 23, pp. 1–6, 2005.

[210] D. Norris, A. L. Efros, and M. Rosen, “Size dependence of exciton fine structure in CdSe quantum dots,” *Phys Rev B*, vol. 53, no. 24, p. 16347, 1996.

[211] T. Watanabe, K. Takahashi, K. Shimura, and D. Kim, “Influence of carrier localization at the core/shell interface on the temperature dependence of the Stokes shift and the photoluminescence decay time in CdTe/CdS type-II quantum dots,” *Phys Rev B*, vol. 96, no. 3, p. 035305, 2017.

[212] R. Scott, S. Kickhöfel, O. Schoeps, A. Antanovich, A. Prudnikau, A. Chuvilin, U. Woggon, M. Artemyev, and A. W. Achtstein, “Temperature dependent radiative and non-radiative recombination dynamics in CdSe-CdTe and CdTe-CdSe type II hetero nanoplatelets,” *Physical Chemistry Chemical Physics*, vol. 18, no. 4, pp. 3197–3203, 2016.

[213] R. Winik, D. Cogan, Y. Don, I. Schwartz, L. Gantz, E. R. Schmidgall, N. Livneh, R. Rapaport, E. Buks, and D. Gershoni, “On-demand source of maximally entangled photon pairs using the biexciton-exciton radiative cascade,” *Phys Rev B*, vol. 95, no. 23, p. 235435, 2017.

[214] H. H. Fang, J. Yang, S. Adjokatse, E. Tekelenburg, M. E. Kamminga, H. Duim, J. Ye, G. R. Blake, J. Even, and M. A. Loi, “Band-Edge Exciton Fine Structure and Exciton Recombination Dynamics in Single Crystals of Layered Hybrid Perovskites,” *Adv. Funct. Mater.*, vol. 30, no. 6, p. 1907979, 2020.

[215] A. Granados Del Águila, E. Groeneveld, J. C. Maan, C. De Mello Donegá, and P. C. M. Christianen, “Effect of Electron-Hole Overlap and Exchange Interaction on Exciton Radiative Lifetimes of CdTe/CdSe Heteronanocrystals,” *ACS Nano*, vol. 10, no. 4, pp. 4102–4110, 2016.

[216] R. Pandya, V. Steinmetz, Y. Puttisong, M. Dufour, W. M. Chen, R. Y. S. Chen, T. Barisien, A. Sharma, G. Lakhwani, A. Mitioglu, P. C. M. Christianen, L. Legrand, F. Bernardot, C. Testelin, A. W. Chin, S. Ithurria, M. Chamarro, and A. Rao, “Fine Structure and Spin Dynamics of Linearly Polarized Indirect Excitons in Two-Dimensional CdSe/CdTe Colloidal Heterostructures,” *ACS Nano*, vol. 13, no. 9, pp. 10140–10153, 2019.

[217] A.T. Isik, F. Shabani, F. Isik, S. Kumar, S. Delikanli, and H.V. Demir, “Simultaneous Dual-Color Amplified Spontaneous Emission and Lasing from Colloidal Quantum Well Gain Media in their Own Layered Waveguide and Cavity,” Laser & Photonics Rev., vol. 17, no. 9, pp. 2300091, 2023.

[218] L. Wang, Z. Chen, G. Liang, Y. Li, R. Lai, T. Ding, and K. Wu, “Observation of a phonon bottleneck in copper-doped colloidal quantum dots,” *Nature Communications 2019 10:1*, vol. 10, no. 1, pp. 1–8, 2019.

[219] D. J. Norris, A. L. Efros, and S. C. Erwin, “Doped nanocrystals,” *Science*, vol. 319, no. 5871, pp. 1776–1779, 2008.

[220] N. Pradhan, S. Das Adhikari, A. Nag, and D. D. Sarma, “Luminescence, Plasmonic, and Magnetic Properties of Doped Semiconductor Nanocrystals,” *Angew. Chem. International Edition*, vol. 56, no. 25, pp. 7038–7054, 2017.

[221] R. Beaulac, P. I. Archer, S. T. Ochsenbein, and D. R. Gamelin, "Mn^{2+}-Doped CdSe Quantum Dots: New Inorganic Materials for Spin-Electronics and Spin-Photonics," *Adv. Funct. Mater.*, vol. 18, no. 24, pp. 3873–3891, 2008.

[222] F. Muckel, C. J. Barrows, A. Graf, A. Schmitz, C. S. Erickson, D. R. Gamelin, and G. Bacher, "Current-Induced Magnetic Polarons in a Colloidal Quantum-Dot Device," *Nano. Lett.*, vol. 17, no. 8, pp. 4768–4773, 2017.

[223] J. Dehnel, Y. Barak, I. Meir, A. K. Budniak, A. P. Nagvenkar, D. R. Gamelin, and E. Lifshitz, "Insight into the Spin Properties in Undoped and Mn-Doped CdSe/CdS-Seeded Nanorods by Optically Detected Magnetic Resonance," *ACS Nano*, vol. 14, no. 10, pp. 13478–13490, 2020.

[224] R. Hu, Z. Wu, Y. Zhang, D. R. Yakovlev, P. Liang, G. Qiang, J. Guo, T. Jia, Z. Sun, M. Bayer, and D. Feng, "Long-Lived Negative Photocharging in Colloidal CdSe Quantum Dots Revealed by Coherent Electron Spin Precession," *J. Phys. Chem. Lett.*, vol. 10, no. 17, pp. 4994–4999, 2019.

[225] C. Capitani, V. Pinchetti, G. Gariano, B. Santiago-González, C. Santambrogio, M. Campione, M. Prato, R. Brescia, A. Camellini, F. Bellato, F. Carulli, A. Anand, M. Zavelani-Rossi, F. Meinardi, S. A. Crooker, and S. Brovelli, "Quantized Electronic Doping towards Atomically Controlled 'Charge-Engineered' Semiconductor Nanocrystals," *Nano. Lett.*, vol. 19, pp. 1307–1317, 2019.

[226] R. Buonsanti and D. J. Milliron, "Chemistry of Doped Colloidal Nanocrystals," *Chem. Mater*, vol. 28, p. 34, 2013.

[227] C. J. Barrows, P. Chakraborty, L. M. Kornowske, and D. R. Gamelin, "Tuning equilibrium compositions in colloidal $Cd_{1-x}Mn_xSe$ nanocrystals using diffusion doping and cation exchange," *ACS Nano*, vol. 10, no. 1, pp. 910–918, 2016.

[228] A. M. Jawaid, S. Chattopadhyay, D. J. Wink, L. E. Page, and P. T. Snee, "Cluster-seeded synthesis of doped CdSe:Cu^+ quantum dots," *ACS Nano*, vol. 7, no. 4, pp. 3190–3197, 2013.

[229] M. Izmir, E.G. Durmusoglu, M. Sharma, F. Shabani, F. Isik, S. Delikanli, V.K. Sharma, and H.V. Demir, "Near-infrared emission from CdSe-based nanoplatelets induced by ytterbium doping," *J. Phys. Chem. C*, vol. 127, no. 8, pp. 4210-4217, 2023.

[230] V. Lesnyak, R. Brescia, G. C. Messina, and L. Manna, "Cu Vacancies Boost Cation Exchange Reactions in Copper Selenide Nanocrystals," *J. Am. Chem. Soc.*, vol. 137, no. 29, pp. 9315–9323, 2015.

[231] J. Zhang, Q. Di, J. Liu, B. Bai, J. Liu, M. Xu, and J. Liu, "Heterovalent doping in colloidal semiconductor nanocrystals: Cation-exchange-enabled new accesses to tuning dopant luminescence and electronic impurities," *J. Phys. Chem. Lett.*, vol. 8, no. 19, pp. 4943–4953, 2017.

[232] D. Chen, R. Viswanatha, G. L. Ong, R. Xie, M. Balasubramaninan, and X. Peng, "Temperature dependence of 'elementary processes' in doping semiconductor nanocrystals," *J. Am. Chem. Soc.*, vol. 131, no. 26, pp. 9333–9339, 2009.

[233] S. C. Erwin, L. Zu, M. I. Haftel, A. L. Efros, T. A. Kennedy, and D. J. Norris, "Doping semiconductor nanocrystals," *Nature*, vol. 436, no. 7047, pp. 91–94, 2005.

[234] R. Viswanatha, S. Brovelli, A. Pandey, S. A. Crooker, and V. I. Klimov, "Copper-doped inverted core/shell nanocrystals with 'permanent' optically active holes," *Nano. Lett.*, vol. 11, no. 11, pp. 4753–4758, 2011.

[235] B. Bai, M. Xu, J. Li, S. Zhang, C. Qiao, J. Liu, and J. Zhang, "Dopant Diffusion Equilibrium Overcoming Impurity Loss of Doped QDs for Multimode Anti-Counterfeiting and Encryption," *Adv. Funct. Mater.*, pp. 2100286–2100287, 2021.

[236] M. Sharma, K. Gungor, A. Yeltik, M. Olutas, B. Guzelturk, Y. Kelestemur, T. Erdem, S. Delikanli, J. R. McBride, and H. V. Demir, "Near-Unity Emitting Copper-Doped Colloidal Semiconductor Quantum Wells for Luminescent Solar Concentrators," *Adv. Mater.*, vol. 29, no. 30, pp. 1–10, 2017.

[237] A. Najafi, M. Sharma, S. Delikanli, A. Bhattacharya, J. R. Murphy, J. Pientka, A. Sharma, A. P. Quinn, O. Erdem, S. Kattel, Y. Kelestemur, M. V Kovalenko, W. D. Rice, H. V. Demir, and A. Petrou, "Light-Induced Paramagnetism in Colloidal Ag^{+}-Doped CdSe Nanoplatelets," *J. Phys. Chem. Lett.*, vol. 12, no. 11, pp. 2892–2899, 2021.

[238] M. Sharma, K. Gungor, A. Yeltik, M. Olutas, B. Guzelturk, Y. Kelestemur, T. Erdem, S. Delikanli, J. R. McBride, and H. V. Demir, "Near-Unity Emitting Copper-Doped Colloidal Semiconductor Quantum Wells for Luminescent Solar Concentrators," *Adv. Mater.*, vol. 29, no. 30, pp. 1–10, 2017.

[239] L. Yang, K. E. Knowles, A. Gopalan, K. E. Hughes, M. C. James, and D. R. Gamelin, "One-Pot Synthesis of Monodisperse Colloidal Copper-Doped CdSe Nanocrystals Mediated by Ligand-Copper Interactions," *Chem. Mater.*, vol. 28, no. 20, pp. 7375–7384, 2016.

[240] R. Abbaschian and R. E. Reed-Hill, *Physical Metallurgy Principles - SI Version*. Cengage Learning, 2009.

[241] D. Wang, T. Xie, Q. Peng, and Y. Li, "Ag, Ag_2S, and Ag_2Se nanocrystals: Synthesis, assembly, and construction of mesoporous structures," *J. Am. Chem. Soc.*, vol. 130, no. 12, pp. 4016–4022, 2008.

[242] T. Kim, J. Park, Y. Hong, A. Oh, H. Baik, and K. Lee, "Janus to Core-Shell to Janus: Facile Cation Movement in $Cu_{2-x}S/Ag_2S$ Hexagonal Nanoplates Induced by Surface Strain Control," *ACS Nano*, vol. 13, no. 10, pp. 11834–11842, 2019.

[243] Y. Du, B. Xu, T. Fu, M. Cai, F. Li, Y. Zhang, and Q. Wang, "Near-infrared photoluminescent Ag_2S quantum dots from a single source precursor," *J. Am. Chem. Soc.*, vol. 132, no. 5, pp. 1470–1471, 2010.

[244] Z. Dikmen, A.T. Işık, İ. Bozkaya, H.D. Baruj, B. Canımkurbey B, F. Shabani, M. Ahmad, and H.V. Demir, "Vertically oriented self-assembly of colloidal CdSe/CdZnS quantum wells controlled via hydrophilicity/lipophilicity balance: optical gain of quantum well stacks for amplified spontaneous emission and random lasing," *Nanoscale*. vol. 15, pp. 9745-9751, 2023.

S. O. M. Hinterding, B. B. V. Salzmann, S. J. W. Vonk, D. Vanmaekelbergh, B. M. Weckhuysen, E. M. Hutter, and F. T. Rabouw, "Single Trap States in Single CdSe Nanoplatelets," *ACS Nano*, vol. 15, no. 4, pp. 7216–7225, 2021.

[245] M. A. Boles, D. Ling, T. Hyeon, and D. V Talapin, "The surface science of nanocrystals," *Nat. Mater.*, vol. 15, no. 3, p. 364, 2016.

[246] T. Galle, M. Kazes, R. Hübner, J. Lox, M. Samadi Khoshkhoo, L. Sonntag, R. Tietze, V. Sayevich, D. Oron, A. Koitzsch, V. Lesnyak, and A. Eychmüller, "Colloidal Mercury-Doped CdSe Nanoplatelets with Dual Fluorescence," *Chem. Mater.*, vol. 31, no. 14, pp. 5065–5074, 2019.

[247] F. Ali, S. Das, S. Banerjee, B. G. Maddala, G. Rana, and A. Datta, "Intense photoluminescence from Cu-doped CdSe nanotetrapods triggered by ultrafast hole capture," *Nanoscale*, vol. 13, no. 33, pp. 14228–14235, 2021.

[248] N. Chestnoy, T. D. Harris, R. Hull, and L. E. Brus, "Luminescence and photophysics of cadmium sulfide semiconductor clusters: the nature of the emitting electronic state," *J. Phys. Chem.*, vol. 90, no. 15, pp. 3393–3399, 2002.

[249] O. Stroyuk, A. Raevskaya, N. Gaponik, O. Selyshchev, V. Dzhagan, S. Schulze, and D. R. T. Zahn, "Origin of the Broadband Photoluminescence of Pristine and Cu^{+}/Ag^{+}-Doped Ultrasmall CdS and CdSe/CdS Quantum Dots," *J. Phys. Chem. C*, vol. 122, no. 18, pp. 10267–10277, 2018.

[250] E. V. Shornikova, D. R. Yakovlev, D. O. Tolmachev, V. Y. Ivanov, I. V. Kalitukha, V. F. Sapega, D. Kudlacik, Y. G. Kusrayev, A. A. Golovatenko, S. Shendre, S. Delikanli, H. V. Demir, and M. Bayer, "Magneto-Optics of Excitons Interacting with Magnetic Ions in CdSe/CdMnS Colloidal Nanoplatelets," *ACS Nano*, vol. 14, no. 7, pp. 9032–9041, 2020.

[251] A. D. P. Leach and J. E. Macdonald, "Optoelectronic Properties of $CuInS_2$ Nanocrystals and Their Origin," *J. Phys. Chem. Lett.*, vol. 7, no. 3, pp. 572–583, 2016.

[252] V. Sousa, B. F. Gonçalves, M. Franco, Y. Ziouani, N. González-Ballesteros, M. Fátima Cerqueira, V. Yannello, K. Kovnir, O. I. Lebedev, and Y. V. Kolen'Ko, "Superstructural Ordering in Hexagonal $CuInSe_2$ Nanoparticles," *Chem. Mater.*, vol. 31, no. 1, pp. 260–267, 2019.

[253] T. Feurer, R. Carron, G. Torres Sevilla, F. Fu, S. Pisoni, Y. E. Romanyuk, S. Buecheler, and A. N. Tiwari, "Efficiency Improvement of Near-Stoichiometric $CuInSe_2$ Solar Cells for Application in Tandem Devices," *Adv Energy Mater*, vol. 9, no. 35, p. 1901428, 2019.

[254] A. Hirase, Y. Hamanaka, and T. Kuzuya, “Ligand-Induced Luminescence Transformation in AgInS2 Nanoparticles: From Defect Emission to Band-Edge Emission,” *J. Phys. Chem. Lett.*, vol. 11, no. 10, pp. 3969–3974, 2020.

[255] J. Chen, Y. Li, L. Wang, T. Zhou, and R. J. Xie, “Achieving deep-red-to-near-infrared emissions in Sn-doped Cu–In–S/ZnS quantum dots for red-enhanced white LEDs and near-infrared LEDs,” *Nanoscale*, vol. 10, no. 20, pp. 9788–9795, 2018.

[256] J. H. Kim, K. H. Kim, S. Y. Yoon, Y. Kim, S. H. Lee, H. S. Kim, and H. Yang, “Tunable Emission of Bluish Zn-Cu-Ga-S Quantum Dots by Mn Doping and Their Electroluminescence,” *ACS Appl. Mater. Interfaces*, vol. 11, no. 8, pp. 8250–8257, 2019.

[257] P. Rao, W. Yao, Z. Li, L. Kong, W. Zhang, and L. Li, “Highly stable CuInS2@ZnS:Al core@shell quantum dots: the role of aluminium self-passivation,” *Chem. Commun.*, vol. 51, no. 42, pp. 8757–8760, 2015.

[258] K. E. Hughes, S. R. Ostheller, H. D. Nelson, and D. R. Gamelin, “Copper’s role in the photoluminescence of $Ag_{1-x}Cu_xInS_2$ nanocrystals, from copper-doped $AgInS_2$ ($x \sim 0$) to $CuInS_2$ ($x = 1$),” *Nano. Lett.*, vol. 19, no. 2, pp. 1318–1325, 2019.

[259] H. Mcdaniel, A. Y. Koposov, S. Draguta, N. S. Makarov, M. Pietryga, and V. I. Klimov, “Simple yet Versatile Synthesis of $CuInSe_xS_{2-x}$ Quantum Dots for Sunlight Harvesting,” *J Phys Chem*, vol. 118, pp. 16987–16994, 2014.

[260] O. Yarema, D. Bozyigit, I. Rousseau, L. Nowack, M. Yarema, W. Heiss, and V. Wood, “Highly luminescent, size- and shape-tunable copper indium selenide based colloidal nanocrystals,” *Chem. Mater.*, vol. 25, no. 18, pp. 3753–3757, 2013.

[261] S. Y. Yoon, J. H. Kim, E. P. Jang, S. H. Lee, D. Y. Jo, Y. Kim, Y. R. Do, and H. Yang, “Systematic and Extensive Emission Tuning of Highly Efficient Cu-In-S-Based Quantum Dots from Visible to Near Infrared,” *Chem. Mater.*, vol. 31, no. 7, pp. 2627–2634, 2019.

[262] O. Yarema, M. Yarema, D. Bozyigit, W. M. M. Lin, and V. Wood, “Independent Composition and Size Control for Highly Luminescent Indium-Rich Silver Indium Selenide Nanocrystals,” *ACS Nano*, vol. 9, no. 11, pp. 11134–11142, 2015.

[263] Z. Wang, X. Zhang, W. Xin, D. Yao, Y. Liu, L. Zhang, W. Liu, W. Zhang, W. Zheng, B. Yang, and H. Zhang, “Facile Synthesis of Cu-In-S/ZnS Core/Shell Quantum Dots in 1-Dodecanethiol for Efficient Light-Emitting Diodes with an External Quantum Efficiency of 7.8%,” *Chem. Mater.*, vol. 30, no. 24, pp. 8939–8947, 2018.

[264] L. Li, A. Pandey, D. J. Werder, B. P. Khanal, J. M. Pietryga, and V. I. Klimov, “Efficient synthesis of highly luminescent copper indium sulfide-based core/shell nanocrystals with surprisingly long-lived emission,” *J. Am. Chem. Soc.*, vol. 133, no. 5, pp. 1176–1179, 2011.

[265] A. S. Portniagin, J. Ning, S. Wang, Z. Li, A. A. Sergeev, S. V Kershaw, X. Zhong, and A. L. Rogach, "Monodisperse $CuInS_2$/CdS and $CuInZnS_2$/CdS Core–Shell Nanorods with a Strong Near-Infrared Emission," *Adv. Opt. Mater.*, vol. 10, no. 8, p. 2102590, 2022.

[266] A. C. Berends, F. T. Rabouw, F. C. M. Spoor, E. Bladt, F. C. Grozema, A. J. Houtepen, L. D. A. Siebbeles, and C. De Mello Donegá, "Radiative and Nonradiative Recombination in $CuInS_2$ Nanocrystals and $CuInS_2$-Based Core/Shell Nanocrystals," *J. Phys. Chem. Lett.*, vol. 7, no. 17, pp. 3503–3509, 2016.

[267] W. Van Der Stam, E. Bladt, F. T. Rabouw, S. Bals, and C. De Mello Donega, "Near-Infrared Emitting $CuInSe_2$/$CuInS_2$ Dot Core/Rod Shell Heteronanorods by Sequential Cation Exchange," *ACS Nano*, vol. 9, no. 11, pp. 11430–11438, 2015.

[268] T. Shimoda, Y. Matsuki, M. Furusawa, T. Aoki, I. Yudasaka, H. Tanaka, H. Iwasawa, D. Wang, M. Miyasaka, and Y. Takeuchi, "Solution-processed silicon films and transistors," *Nature 2006 440:7085*, vol. 440, no. 7085, pp. 783–786, 2006.

[269] J. Zhu, M. C. Hersam, J. Zhu, and M. C. Hersam, "Assembly and Electronic Applications of Colloidal Nanomaterials," *Adv. Mater.*, vol. 29, no. 4, p. 1603895, 2017.

[270] C. R. Kagan, "Flexible colloidal nanocrystal electronics," *Chem. Soc. Rev.*, vol. 48, no. 6, pp. 1626–1641, 2019.

[271] S. Draguta, H. Mcdaniel, V. I. Klimov, S. Draguta, H. Mcdaniel, and V. I. Klimov, "Tuning Carrier Mobilities and Polarity of Charge Transport in Films of $CuInSe_xS_{2-x}$ Quantum Dots," *Adv. Mater.*, vol. 27, no. 10, pp. 1701–1705, 2015.

[272] S. Draguta, H. Mcdaniel, V. I. Klimov, S. Draguta, H. Mcdaniel, and V. I. Klimov, "Tuning Carrier Mobilities and Polarity of Charge Transport in Films of $CuInSe_xS_{2-x}$ Quantum Dots," *Adv. Mater.*, vol. 27, no. 10, pp. 1701–1705, 2015.

[273] H. J. Yun, J. Lim, A. S. Fuhr, N. S. Makarov, S. Keene, M. Law, J. M. Pietryga, and V. I. Klimov, "Charge-Transport Mechanisms in $CuInSe_xS_{2-x}$ Quantum-Dot Films," *ACS Nano*, vol. 12, no. 12, pp. 12587–12596, 2018.

[274] I. Du Fossé, S. Ten Brinck, I. Infante, and A. J. Houtepen, "Role of Surface Reduction in the Formation of Traps in n-Doped II-VI Semiconductor Nanocrystals: How to Charge without Reducing the Surface," *Chem. Mater.*, vol. 31, no. 12, pp. 4575–4583, 2019.

[275] Y. Liu, J. Tolentino, M. Gibbs, R. Ihly, C. L. Perkins, Y. Liu, N. Crawford, J. C. Hemminger, and M. Law, "PbSe quantum dot field-effect transistors with air-stable electron mobilities above 7 $cm^2\ V^{-1}\ s^{-1}$," *Nano. Lett.*, vol. 13, no. 4, pp. 1578–1587, 2013.

[276] H. McDaniel, N. Fuke, N. S. Makarov, J. M. Pietryga, and V. I. Klimov, "An integrated approach to realizing high-performance liquid-junction quantum dot

sensitized solar cells," *Nature Communications 2013 4:1*, vol. 4, no. 1, pp. 1–10, 2013.

[277] H. Wang, D. J. Butler, D. B. Straus, N. Oh, F. Wu, J. Guo, K. Xue, J. D. Lee, C. B. Murray, and C. R. Kagan, "Air-Stable CuInSe2 Nanocrystal Transistors and Circuits via Post-Deposition Cation Exchange," *ACS Nano*, vol. 13, no. 2, pp. 2324–2333, 2019.

[278] X. Fan, D. Kneppe, V. Sayevich, H. Kleemann, A. Tahn, K. Leo, V. Lesnyak, and A. Eychmüller, "High-Performance Ultra-Short Channel Field-Effect Transistor Using Solution-Processable Colloidal Nanocrystals," *J Phys Chem Lett*, vol. 10, no. 14, pp. 4025–4031, 2019.

[279] A. Rolland, J. Richard, J. P. Kleider, and D. Mencaraglia, "Electrical Properties of Amorphous Silicon Transistors and MIS-Devices: Comparative Study of Top Nitride and Bottom Nitride Configurations," *J Electrochem Soc*, vol. 140, no. 12, pp. 3679–3683, 1993.

[280] E. Bennett, M. W. Greenberg, A. J. Jordan, L. S. Hamachi, S. Banerjee, S. J. L. Billinge, and J. S. Owen, "Size Dependent Optical Properties and Structure of ZnS Nanocrystals Prepared from a Library of Thioureas," *Chem. Mater.*, vol. 34, no. 2, pp. 706–717, 2022.

[281] H. J. Yun, J. Lim, A. S. Fuhr, N. S. Makarov, S. Keene, M. Law, J. M. Pietryga, and V. I. Klimov, "Charge-Transport Mechanisms in $CuInSe_xS_{2-x}$ Quantum-Dot Films," *ACS Nano*, vol. 12, no. 12, pp. 12587–12596, 2018.

[282] T. J. Macdonald, Y. J. Mange, M. Dewi, A. McFadden, W. M. Skinner, and T. Nann, "Cation exchange of aqueous $CuInS_2$ quantum dots," *CrystEngComm*, vol. 16, no. 40, pp. 9455–9460, 2014.

[283] E. Izquierdo, A. Robin, S. Keuleyan, N. Lequeux, E. Lhuillier, and S. Ithurria, "Strongly Confined HgTe 2D Nanoplatelets as Narrow Near-Infrared Emitters," *J. Am. Chem. Soc.*, vol. 138, no. 33, pp. 10496–10501, 2016.

[284] A. Mitrofanov, A. Prudnikau, F. Di Stasio, N. Weiß, R. Hübner, A. M. Dominic, K. B. L. Borchert, V. Lesnyak, and A. Eychmüller, "Near-Infrared-Emitting $Cd_xHg_{1-x}Se$-Based Core/Shell Nanoplatelets," *Chem. Mater.*, vol. 33, no. 19, pp. 7693–7702, 2021.

[285] J. F. L. Lox, Z. Dang, M. Lê Anh, E. Hollinger, and V. Lesnyak, "Colloidal Cu-Zn-In-S-Based Disk-Shaped Nanocookies," *Chem. Mater.*, vol. 31, no. 8, pp. 2873–2883, 2019.

[286] M. Razeghi, M. Üstünçelik, F. Shabani, H.V. Demir, and T.S. Kasırga, "Plasmon-enhanced photoresponse of single silver nanowires and their network devices," *Nanoscale Horiz.*, vol. 7, no. 4, pp. 396-402, 2022.